



Marshall, Ross James (2017) Synthesis, characterisation and postsynthetic modification of zirconium and hafnium metal-organic frameworks. PhD thesis.

<http://theses.gla.ac.uk/8177/>

Copyright and moral rights for this work are retained by the author

A copy can be downloaded for personal non-commercial research or study, without prior permission or charge

This work cannot be reproduced or quoted extensively from without first obtaining permission in writing from the author

The content must not be changed in any way or sold commercially in any format or medium without the formal permission of the author

When referring to this work, full bibliographic details including the author, title, awarding institution and date of the thesis must be given

Enlighten:Theses  
<http://theses.gla.ac.uk/>  
theses@gla.ac.uk

# **Synthesis, Characterisation and Postsynthetic Modification of Zirconium and Hafnium Metal-Organic Frameworks**

Ross James Marshall



University  
of Glasgow

Doctor of Philosophy  
School of Chemistry  
University of Glasgow

March 2017

## **Declaration**

This thesis has been written and compiled by the author, Ross James Marshall, who has carried out the research at the University of Glasgow between 2013 and 2017 under the supervision of Dr Ross Forgan. Where collaborative results have been included in this thesis the input of others has been acknowledged. Parts of this thesis have been published in peer-reviewed journals and at the start of each chapter reference to the relevant publications is given.

## Abstract

Metal-organic frameworks (MOFs) are multidimensional coordination networks comprised of metal nodes separated by organic linkers that have received widespread interest over the past 10-15 years, mainly attributable to their permanent porosity, leading to potential application in areas such as gas capture and storage, catalysis and drug delivery. The judicious choice of both the organic and inorganic constituents of MOFs enables vast opportunities for framework design, leading to materials with intrinsically variable structures and properties.

This thesis focuses on the self-assembly and functionalisation of Zr and Hf MOFs demonstrating unique structural, physical and mechanical properties, while also improving fundamental aspects such as their syntheses.

Following an introduction to prototypical MOF structures, their applications, coordination modulation and postsynthetic modification (specifically of Zr MOFs) in Chapter 1, in Chapter 2 amino acids are investigated as synthetic modulators for the syntheses of a range of Zr and Hf MOFs with different pore dimensions and functionality. Surprisingly it is found that upon addition of small amounts of L-proline to synthetic mixtures, the crystallinity of the products is dramatically improved and fine-tuning reaction conditions results in single crystals, a task that is routinely difficult for Zr and Hf MOFs. A range of experimental techniques are used to demonstrate that the amino acid modulated MOFs are phase pure, porous and thermally stable. Accessing single crystals of Zr MOFs, either with rigid (linear) or flexible (kinked) ligands, allows specialised techniques such as high-pressure single crystal X-ray diffraction and nanoindentation to be used to show that ligand flexibility imparts the MOFs with greater overall mechanical stability. To further investigate the effect of flexibility within Zr and Hf MOFs, extended carboxylate based ligands were designed and synthesised by Sonogashira cross couplings. The length of the bridging organic ligands was varied, with alkene, alkyne and butadiyne derivatives obtained. Incorporation of the series of ligands into Zr and Hf MOFs results in highly porous frameworks, and when the longest ligand is used 2-fold interpenetrated MOFs are obtained.



When contained within Zr and Hf MOFs, the integral unsaturated sites of the extended ligands are potential sites for chemical transformation. In Chapter 3, it is shown that the integral unsaturated sites can be halogenated, resulting in a mechanical contraction as the hybridisation of the integral carbon atoms is altered during the transformation, ultimately affecting ligand length and geometry. Using the Zr-alkyne MOF (**Zr-L9**) as a typical example, then addition of chloroform solutions containing Br<sub>2</sub> to the MOF transforms the alkyne units to dibromoalkene units, with the overall ligand geometry changing from linear to kinked. The transformation proceeds stereoselectively, resulting exclusively in the *trans*-dibromoalkene, while the solution-phase reaction of the free ligand results in a mixture of both the *cis* and *trans* isomers. Enhanced stereoselectivity is obtained as a result of mixed-phase reactivity, with the topological constraints of the MOF reducing the conformational freedom of the ligands. The transformation is possible in a rare single-crystal to single-crystal manner, with the cubic unit cell edge *a* contracting by ~0.38 Å (3.7% reduction in volume), proving the high mechanical stability of the MOFs. The facile addition of bromine across the integral unsaturated sites suggested the potential of the MOFs for vapour phase iodine capture. An interpenetrated Zr MOF demonstrates an I<sub>2</sub> storage capacity of 279% w/w through a combination of both physisorption (compact organisation of I<sub>2</sub> within the pores) and chemisorption (reactivity of the integral unsaturated sites). The very high iodine uptake suggests that the MOFs could be used for the sequestration of radioactive iodine released from nuclear accidents.

In Chapter 4, a series of interpenetrated Zr and Hf MOFs containing functionalised ligands, with pendant methyl, fluorine, naphthalene or benzothiadiazole moieties are reported. Twelve MOFs are synthesised, eleven of them as single crystals and it is found that they demonstrate interesting structural behaviour under different external stimuli. High pressure crystallography reveals that in the unfunctionalised derivative (**Hf-L11**), the phenylene core of the ligands twists by ~90° upon application of pressure, enabling bifurcated hydrogen bonds to form between the two interpenetrated nets, resulting in an overall stabilisation of the material. When pendant methyl groups are incorporated onto the ligands, a structural perturbation is observed where the ligands twist out of the plane of conjugation to minimise steric interactions in the ambient structure. Variable temperature powder X-ray diffraction and solid state fluorescence emission spectroscopy reveal that the ligands are able to rotate to adopt a linear geometry, resulting in a structural change and an associated change of symmetry. Fluorescence emission spectroscopy is used to probe host-guest interactions,

investigating the effect of a range of analytes on the MOFs solid-state fluorescence, with sensitive emission behaviour upon wetting suggesting their possible use as water vapour sensors.

To sum up, enhanced synthetic capabilities of Zr and Hf MOFs has been achieved by adding small quantities of L-proline to their syntheses. This synthetic methodology enabled access to highly porous Zr and Hf MOFs containing unsaturated functionality that can be postsynthetically halogenated and is potentially useful for the capture and storage of radioactive iodine released during nuclear disasters. Incorporating a diverse range of functionality within a series of interpenetrated MOFs modifies their physical properties, specifically their hydrophobicity and solid state fluorescence behaviour. Therefore, this thesis covers modulation, postsynthetic modification and functionalisation of Zr and Hf MOFs.

## Acknowledgements

I have truly enjoyed my time as a PhD student in the School of Chemistry at the University of Glasgow and have made a lot of friends along the way.

I must first thank my supervisor Dr Ross Forgan for his continued support and guidance over the years. We have worked well together and the freedom Ross has given me has allowed me to focus on projects that I have found interesting.

Also to the members of the Forgan Group – past and present – thanks for making the lab an enjoyable environment to work. In particular, I would like to thank François, Isábel and Sarah as they've been here most of the way through my PhD. Our 'holiday' in America was certainly an experience I won't forget, for instance, going on the longest bike run possible and Sarah setting the oven on fire in the apartment in LA!

Undergraduate students Colin Murphie and Sarah Griffin must be thanked for their contribution to aspects of the work discussed in this thesis during their final year research placements in the group.

Though not an expert, I would be considerably less knowledgeable about crystallography if it wasn't for Claire Wilson, so thanks a lot Claire! On that note, thanks to the National Crystallography Service in Southampton for data collections, especially of the tiny crystals. I must also thank Jim Gallagher, Andy Monaghan and David Adam who have helped me over the years with SEM, TGA and NMR.

From our squatting days in the Soddy Lab and then onto our lane in the Chemical Biology Lab, I would like to thank the Cronin, Symes and Liskamp groups for being our neighbours and letting me 'borrow' things from time to time.

Thanks to our collaborators Stephen Moggach and Claire Hobday for making the trips to Diamond enjoyable, I loved the nightshift, honest. Also special thanks to Tom Bennett, David Fairen-Jimenez, Carole Morrison, Barry Blight and their research groups for collaborating with us, your skills and techniques have been invaluable to our success.

Though offering little advice on chemistry issues, I am grateful to my Mum for her continued support and encouragement. Also thanks to the rest of my family for helping me along my way. Last but not least, thank you Zoe for being by my side – you have supported me in many more ways than you will ever realise (you were a perfect practice audience for my presentations). I would not have enjoyed my PhD as much if I did not have such an enjoyable home life – thanks for that and I'm sure we'll spend many more happy times together.

The EPSRC, University of Glasgow, Royal Society and Royal Society of Chemistry are acknowledged for their financial support.

## Contents

<b>Declaration.....</b>	<b>i</b>
<b>Abstract.....</b>	<b>ii</b>
<b>Acknowledgements .....</b>	<b>v</b>
<b>Contents .....</b>	<b>vii</b>
<b>Abbreviations .....</b>	<b>xi</b>
<b>Chapter 1 .....</b>	<b>1</b>
<b>1.1 Metal-Organic Frameworks .....</b>	<b>3</b>
<b>1.2 Applications of MOFs.....</b>	<b>8</b>
1.2.1 Gas Capture and Storage.....	8
1.2.2 Catalysis .....	10
1.2.3 Drug Delivery .....	13
<b>1.3 Zr Metal-Organic Frameworks .....</b>	<b>15</b>
<b>1.4 Coordination Modulation.....</b>	<b>20</b>
<b>1.5 Postsynthetic Modification .....</b>	<b>29</b>
1.5.1 Covalent Postsynthetic Modification of Zr MOFs.....	29
1.5.2 Integral Postsynthetic Modification of Zr MOFs.....	40
<b>1.6 References .....</b>	<b>43</b>
<b>Chapter 2 .....</b>	<b>52</b>
<b>2.1 Introduction.....</b>	<b>54</b>
<b>2.2 Aims.....</b>	<b>56</b>
<b>2.3 Amino Acid Modulation .....</b>	<b>58</b>
<b>2.4 Bulk Synthesis of Zr and Hf MOFs Containing L5-L8.....</b>	<b>67</b>
<b>2.5 Microwave Assisted Synthesis of Zr-L6.....</b>	<b>72</b>
<b>2.6 Single Crystal Synthesis of Zr and Hf MOFs Containing L5-L8.....</b>	<b>74</b>
<b>2.7 Design and Synthesis of Extended Ligands .....</b>	<b>77</b>
<b>2.8. Synthesis of Zr and Hf MOFs Containing L9-L11 .....</b>	<b>79</b>

<b>2.9 Conclusions and Future Work.....</b>	<b>85</b>
<b>2.10 Experimental .....</b>	<b>87</b>
2.10.1 General Experimental Remarks .....	87
2.10.2 Amino Acid Modulation of Zr MOFs Containing L1-L8.....	88
2.10.3 Amino Acid Modulation of Hf MOFs Containing L1-L8.....	89
2.10.4 Zr-L6 and Hf-L6 L-Proline/HCl Modulator Comparison .....	89
2.10.5 Zr-L6 L-Proline Concentration Investigation .....	90
2.10.6 Bulk Synthesis of Zr and Hf MOFs Containing L5-L8 .....	90
2.10.7 Microwave Assisted Synthesis of Zr-L6.....	91
2.10.8 Single Crystal Synthesis of Zr-L6, Zr-L7, Zr-L8, Hf-L6 and Hf-L7 .....	91
2.10.9 Extended Ligand Synthesis.....	94
2.10.10 Bulk Synthesis Zr and Hf MOFs Containing L9-L11 .....	99
2.10.11 Single Crystal Synthesis of Zr and Hf MOFs Containing L9-L11 .....	100
<b>2.11 References.....</b>	<b>104</b>
<b>Chapter 3 .....</b>	<b>108</b>
<b>3.1 Introduction.....</b>	<b>110</b>
<b>3.2 Aims.....</b>	<b>112</b>
<b>3.3 Bulk Postsynthetic Bromination of Zr-L8 .....</b>	<b>114</b>
<b>3.4 Alternative Bulk Postsynthetic Bromination of Zr-L8.....</b>	<b>117</b>
<b>3.5 Single-Crystal Postsynthetic Bromination of Zr-L8 .....</b>	<b>120</b>
<b>3.6 Attempted Synthesis of a Zr MOF Containing etdb.....</b>	<b>122</b>
<b>3.7 Bulk Postsynthetic Bromination of Zr-L9 and Hf-L9 .....</b>	<b>123</b>
<b>3.8 Single Crystal Postsynthetic Bromination of Zr-L9 and Hf-L9 .....</b>	<b>129</b>
<b>3.9 Solution Phase Bromination of L9-Me<sub>2</sub>, L10-Me<sub>2</sub> and L11-Me<sub>2</sub> .....</b>	<b>132</b>
<b>3.10 Postsynthetic Bromination of Zr-L10 .....</b>	<b>136</b>
<b>3.11 Bulk Postsynthetic Bromination of Zr-L11 and Hf-L11 .....</b>	<b>140</b>
<b>3.12 Single Crystal Postsynthetic Bromination of Zr-L11 and Hf-L11 .....</b>	<b>145</b>
<b>3.13 Postsynthetic Iodination of Zr-L8, Zr-L9, Zr-L10 and Zr-L11.....</b>	<b>147</b>

<b>3.14 Conclusions and Future Work.....</b>	<b>150</b>
<b>3.15 Experimental .....</b>	<b>152</b>
3.15.1 General Experimental Remarks .....	152
3.15.2 Ligand Synthesis .....	153
3.15.3 Ligand Brominations.....	155
3.15.4 Bulk MOF Synthesis .....	157
3.15.5 Bulk Postsynthetic Bromination of Zr-L8, Zr-L9, Hf-L9, Zr-L10, Zr-L11 and Hf-L11 .....	158
3.15.6 Single Crystal Postsynthetic Bromination of Zr-L8, Zr-L9, Hf-L9, Zr-L10, Zr-L11 and Hf-L11 .....	160
3.15.7 Iodine Uptake Experiments of Zr-L8, Zr-L9, Zr-L10 and Zr-L11.....	162
<b>3.16 References .....</b>	<b>166</b>
<b>Chapter 4 .....</b>	<b>169</b>
<b>4.1 Introduction.....</b>	<b>171</b>
<b>4.2 Aims.....</b>	<b>173</b>
<b>4.3 Ligand Design and Synthesis .....</b>	<b>175</b>
<b>4.4 Bulk Synthesis of Interpenetrated Zr and Hf MOFs.....</b>	<b>176</b>
<b>4.5 Single Crystal Synthesis of Interpenetrated Zr and Hf MOFs.....</b>	<b>178</b>
<b>4.6 Zr-L12 Structural Investigation .....</b>	<b>181</b>
<b>4.7 Thermal Analysis .....</b>	<b>184</b>
<b>4.8 Surface Area and Pore Size Distribution Analysis .....</b>	<b>186</b>
<b>4.9 Solid State UV-Vis Spectroscopy .....</b>	<b>190</b>
<b>4.10 Solid State Fluorescence Emission Spectroscopy .....</b>	<b>194</b>
<b>4.11 Conclusions and Future Work.....</b>	<b>200</b>
<b>4.12 Experimental .....</b>	<b>202</b>
4.12.1 General Experimental Remarks .....	202
4.12.2 Ligand Synthesis .....	204
4.12.3 Bulk Synthesis of Zr and Hf MOFs Containing L12-L17 .....	213
4.12.4 Single Crystal Synthesis of Zr and Hf MOFs Containing L12-L17 .....	217

<b>4.13 References .....</b>	<b>224</b>
<b>Chapter 5 .....</b>	<b>227</b>
<b>5.1 Conclusions.....</b>	<b>229</b>
<b>5.2 References .....</b>	<b>235</b>
<b>Chapter 6 .....</b>	<b>236</b>
<b>6.1 Chapter 2 Supplementary Material .....</b>	<b>238</b>
<b>6.2 Chapter 3 Supplementary Material .....</b>	<b>258</b>
<b>6.3 Chapter 4 Supplementary Material .....</b>	<b>264</b>



## Abbreviations

Å	angstrom
~	approximately
δ	chemical shift
°	degrees
°C	degrees Celsius
λ	wavelength
aq.	aqueous
BET	Brunauer–Emmett–Teller theory
br s	broad singlet
ca.	<i>circa</i> (approximately)
calc	calculated
CCDC	Cambridge crystallographic data centre
CHCl <sub>3</sub>	chloroform
CI	chemical ionisation
CuAAC	copper-catalysed azide-alkyne cycloaddition
d	doublet
DCM	dichloromethane
DFT	density functional theory
DMF	<i>N,N</i> -dimethylformamide
DMSO	dimethylsulfoxide
DPT	<i>N,N'</i> -diphenylthiourea
e.g.	for example
eq	equivalent
ESI	electrospray ionisation
<i>et al.</i>	and others
EtOAc	ethyl acetate
EtOH	ethanol
eV	electronvolt
expt	experimental
g	gram
GPa	gigapascal

HCl	hydrochloric acid
HRMS	high-resolution mass spectroscopy
Hz	hertz
IR	infrared spectroscopy
IRMOF	isoreticular metal-organic framework
$J$	dipole-dipole coupling
K	Kelvin
M	moles per litre
$m/z$	mass to charge ratio
MeCN	acetonitrile
MeOH	methanol
mg	milligram
ml	millilitre
mM	milli moles per litre
mmol	millimole
MOF	metal-organic framework
$M_r$	molecular weight
MTV-MOF	multivariate metal-organic framework
mW	milliwatt
n/a	not applicable
NBS	<i>N</i> -bromosuccinimide
nm	nanometre
NMR	nuclear magnetic resonance spectroscopy
no.	number
PABA	<i>para</i> -aminobenzoic acid
ppm	parts per million
PSD	pore size distribution
PSE	postsynthetic exchange
PSM	postsynthetic modification
PSP	photoinduced postsynthetic polymerisation
PXRD	powder X-ray diffraction
QSDFT	quenched solid density functional theory
QY	quantum yield
Ref.	reference

s	singlet
SA	surface area
SAV	solvent accessible volume
Scm <sup>-1</sup>	siemens per centimetre
SCSC	single-crystal to single-crystal
SCXRD	single crystal X-ray diffraction
SEM	scanning electron microscopy
SS-UV-Vis	solid-state ultraviolet-visible spectroscopy
TCP	tetrakis(4-carboxyphenyl)porphyrin
TEA	triethylamine
TFA	trifluoroacetic acid
TGA	thermogravimetric analysis
THF	tetrahydrofuran
UV-Vis	ultraviolet-visible spectroscopy
V	volume
vs	versus

# Chapter 1

## Introduction

**This Chapter is adapted in part from the following publication:**

Postsynthetic Modification of Zirconium Metal-Organic Frameworks

*Eur. J. Inorg. Chem.*, **2016**, 4310–4331.

**R. J. Marshall** and R. S. Forgan

## Contents

<b>Chapter 1 .....</b>	<b>1</b>
<b>1.1 Metal-Organic Frameworks .....</b>	<b>3</b>
<b>1.2 Applications of MOFs.....</b>	<b>8</b>
1.2.1 Gas Capture and Storage.....	8
1.2.2 Catalysis.....	10
1.2.3 Drug Delivery .....	13
<b>1.3 Zr Metal-Organic Frameworks .....</b>	<b>15</b>
<b>1.4 Coordination Modulation.....</b>	<b>20</b>
<b>1.5 Postsynthetic Modification .....</b>	<b>29</b>
1.5.1 Covalent Postsynthetic Modification of Zr MOFs.....	29
1.5.2 Integral Postsynthetic Modification of Zr MOFs.....	40
<b>1.6 References .....</b>	<b>43</b>

## 1.1 Metal-Organic Frameworks

Metal-organic frameworks,<sup>1-4</sup> commonly abbreviated to MOFs, are a class of hybrid materials containing both inorganic and organic constituents connected to form multi-dimensional structures. The term ‘MOF’ first appeared in the literature around 1995,<sup>5</sup> although other acronyms are frequently used to refer to the same types of materials, including porous coordination polymers (PCPs)<sup>6</sup> and porous coordination networks (PCNs)<sup>7</sup> amongst others. MOFs are commonly named after the institution where they are discovered, with NOTT,<sup>8</sup> MIL<sup>9</sup> and UiO<sup>10</sup> families of materials being named so because they were discovered by researchers in Nottingham, Institute Lavoisier and the University of Oslo, respectively. According to IUPAC recommendations a MOF is defined as ‘a Coordination Polymer (or alternatively Coordination Network) with an open framework containing potential voids’.<sup>11</sup>

The periodic arrangement of inorganic nodes and bridging organic ligands results in crystalline framework materials with intrinsic porosity. There are an inordinate number of theoretical MOFs due to the large diversity of metal ions and bridging organic ligands that can be combined. The most well-known MOF is MOF-5,<sup>12</sup> which contains  $\text{Zn}_4\text{O}$  clusters separated by terephthalate ligands (Figure 1.1).

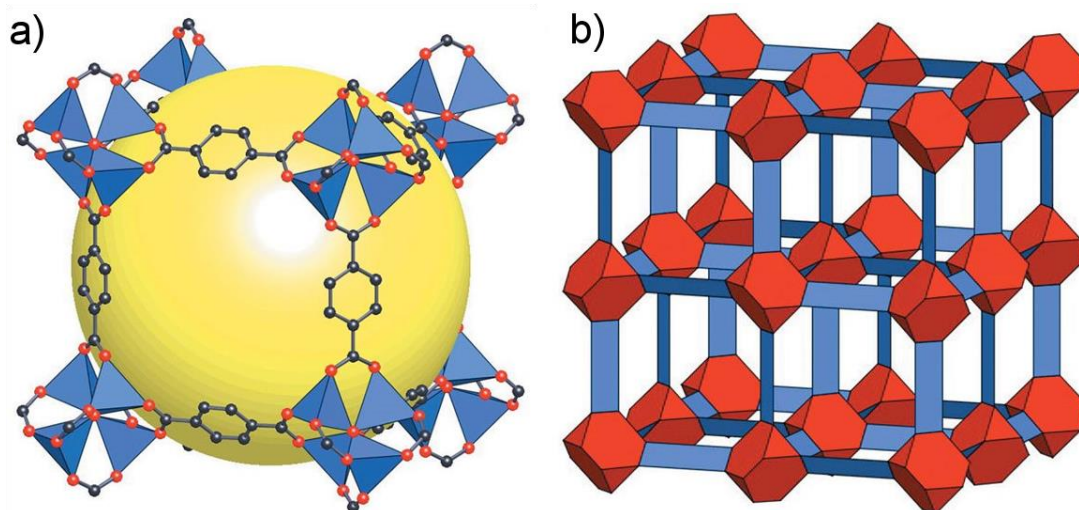


**Figure 1.1.** Two different structural representations of  $[\text{Zn}_4\text{O}(\text{terephthalate})_3]_n$ , more commonly known as MOF-5. a) Terephthalate ligands bridge the inorganic  $\text{Zn}_4\text{O}$  clusters, which are shown in polyhedral form, while the yellow sphere represents the void space of the framework. b) Schematic representation of the overall framework structure. Reproduced (modified) with permission from Ref.<sup>13</sup> Copyright (2003) Nature Publishing Group.

In MOF-5 and the majority of MOFs reported the bridging organic ligands contain carboxylate functional groups that act as points of attachment to the inorganic metal clusters. The structural features of MOFs allow them to be predesigned, known as reticular chemistry, and by judiciously selecting the inorganic and organic components materials with desired topologies, structures and properties can be obtained.<sup>13</sup> Reticular chemistry is ultimately responsible for the large number of MOFs known to date: an isorecticular series based on MOF-5 (the IRMOF series) was one of the first to be discovered.<sup>14,15</sup> An isorecticular series of MOFs contain the same underlying connectivity and as a result they share the same overall framework structure. The IRMOF series contains ligands of varying lengths and/or with pendant functionality, allowing functionalised materials for specific applications to be realised (Figure 1.2).

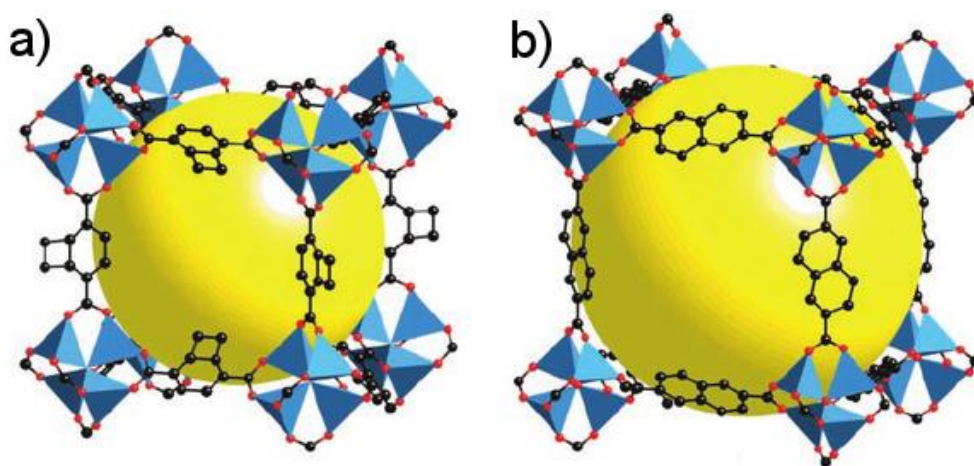


**Figure 1.2.** Portion of the solid-state structures of a) IRMOF-6 and b) IRMOF-8 which are analogues of MOF-5 that contain functionalised and extended ligands respectively. Reproduced (modified) with permission from Ref.<sup>14</sup> Copyright (2009) Royal Society of Chemistry.

The ability to design and predict MOF structures is advantageous when specific materials are required however, the expected structures are not always obtained and this is particularly true when the length of the bridging ligand is varied. As the length of the bridging ligand increases then provided the MOFs are part of an isorecticular series it is obvious that their porosity will also increase. This is true to a certain extent, although there is a critical point and when the length of the bridging ligand increases beyond a certain length framework interpenetration occurs.<sup>16</sup> Framework interpenetration describes the phenomenon whereby the pore space of a MOF is sufficient that one framework (or multiple frameworks depending

on the level of interpenetration) can grow within the void space of another independent framework (Figure 1.3).<sup>17</sup>

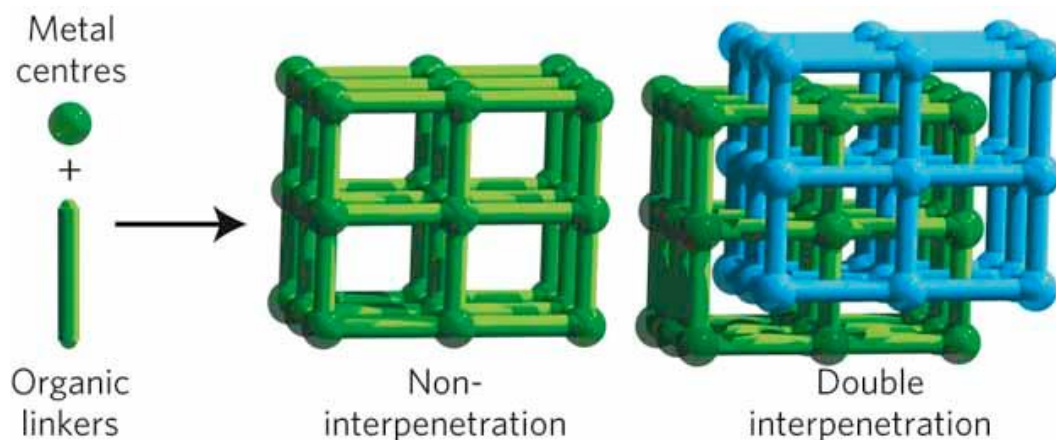


**Figure 1.3.** Schematic representation of non-interpenetrated and doubly interpenetrated MOFs. Interpenetration reduces the porosity of the MOF, as the second framework occupies the pore space of the first framework. The two independent frameworks are coloured green and blue. Reproduced (modified) with permission from Ref.<sup>17</sup> Copyright (2012) Nature Publishing Group.

There are a number of reported strategies to control the degree of interpenetration of MOFs, including refinement of reaction parameters<sup>18</sup> and template directed synthesis.<sup>19</sup> In some cases both interpenetrated and non-interpenetrated structures are known for the same MOF.<sup>20</sup> Framework interpenetration not only relies on the length of the bridging ligand, but it is also determined by the steric bulk of the ligand.<sup>21,22</sup> Interpenetration was initially considered to be a drawback as it results in a reduction of porosity however, it has been discovered that the reduction in pore diameter can be particularly useful for some applications, such as CO<sub>2</sub> capture.<sup>17,23,24</sup>

Another well-known MOF is [Cu<sub>3</sub>(btc)<sub>2</sub>(H<sub>2</sub>O)<sub>3</sub>]<sub>n</sub> (btc = 1,3,5-benzenetricarboxylate) or more commonly HKUST-1 (Figure 1.4a). The framework contains Cu<sup>2+</sup> paddlewheel units, with each Cu atom connected by 4 oxygen atoms of the bridging organic ligands and a water molecule fills the coordination sphere (Figure 1.4b). The framework contains 1 nm pores, with terminal water molecules projecting into the pores and upon dehydration they can be replaced with other molecules, such as pyridine causing a colour change and ultimately altering the pore texture.<sup>25</sup>



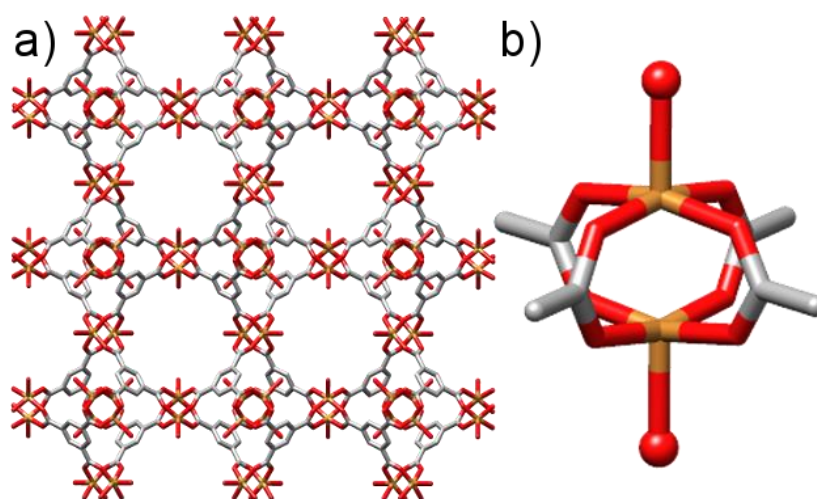


**Figure 1.4.** a) Portion of the solid-state structure of HKUST-1. b) Cu paddlewheel found in HKUST-1, with the oxygen atoms of the terminal water molecules highlighted as spheres. Redrawn from CCDC deposition 943008.<sup>26</sup>

The copper paddlewheel cluster found in HKUST-1 is a very prevalent coordination geometry and subsequently it forms the nodes of many reported MOFs, not only with copper but also commonly with zinc<sup>27</sup> and nickel.<sup>28</sup> However, the axial positions are not always capped by terminal water molecules and if the correct combination of ligands are used then ‘pillared MOFs’ are obtained, whereby 2-dimensional sheets (carboxylate based ligands) are connected into 3 dimensions, typically by nitrogen donating ligands (Figure 1.5).<sup>29,30</sup>

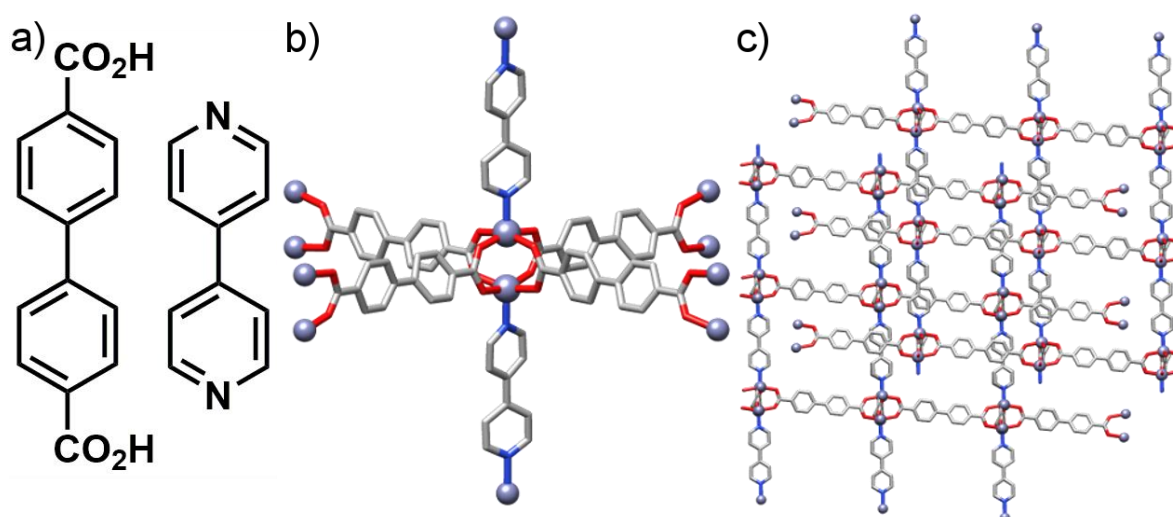


**Figure 1.5.** a) Carboxylate and nitrogen based ligands that are connected by b) Zn paddle wheel units to form c) a 3-dimensional 2-fold interpenetrated pillared MOF. Redrawn from CCDC deposition 857740.<sup>31</sup>

Furthermore, it is not only possible to use the paddlewheel motif to incorporate multiple ligands into a single framework; it is also possible to directly assemble materials containing more than one type of carboxylate based ligand. The combination of multiple ligands results in mixed-ligands or multivariate MOFs (MTV-MOFs) and by combining a number of different functional units highly specialised materials can be obtained. This concept was applied to MOF-5 type materials and up to eight different terephthalate based ligands could be incorporated into a single framework via direct synthetic methods (Figure 1.6).<sup>32</sup>

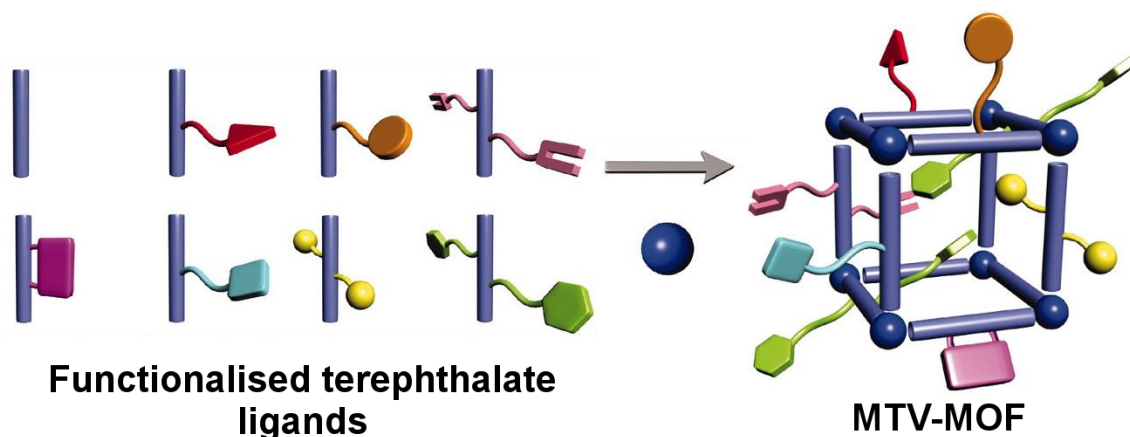


**Figure 1.6** Schematic representation of eight different terephthalate based ligands that can be used to construct a MTV-MOF with the same underlying topology as the parent MOF-5. Reproduced (modified) with permission from Ref.<sup>32</sup> Copyright (2010) American Association for the Advancement of Science.

It is usually not possible to control the ratio of ligands incorporated into MTV-MOFs during direct synthesis however, secondary ligands can be introduced into pre-synthesised MOFs by postsynthetic exchange (PSE).<sup>33,34</sup> Briefly, PSE is a process where the solid phase MOF undergoes ligand exchange, resulting in incorporation of secondary ligands by substitution of the parent ligand while maintaining crystallinity.

In some cases, such as the recently discovered MUF-77 series of MOFs, which contain both linear and trigonal carboxylate based ligands, the ligand ratio is rigid and is controlled by the MOF topology. Functionalisation of the trigonal ligands results in an isorecticular series, and by incorporating alkyl chains of varying lengths onto the ligand scaffold differences in their water vapour stabilities and gas adsorption capacities were obtained.<sup>35</sup>

It is clear from the examples discussed within that there are a diverse range of MOF structures possible, and that the judicious choice of framework constituents can be used to predesign and direct the synthesis of materials with dramatically different structures and properties. As-synthesised MOFs usually contain occluded solvent molecules within their pores and therefore activation procedures are required for their removal while maintaining the framework structure. Activation procedures typically involve solvent exchange for a more volatile solvent which can then be removed either under vacuum or by thermal treatment, while freeze drying and supercritical CO<sub>2</sub> exchange are also routinely used.<sup>36</sup> The porosity of MOFs has been responsible for the majority of the interest they have received and subsequently they have been investigated for use in a number of applications.

## **1.2 Applications of MOFs**

MOFs have received increasing amounts of interest over the past 15 years and they have been investigated for potential use in a number of applications, including gas capture and storage,<sup>37-40</sup> catalysis,<sup>41-44</sup> and drug delivery.<sup>45-47</sup> A small overview of pertinent examples of each of these applications will be discussed in the following sections.

### **1.2.1 Gas Capture and Storage**

The porosity of MOFs is normally evaluated by collecting N<sub>2</sub> adsorption and desorption isotherms at 77 K, then Brunauer–Emmett–Teller (BET) theory is used to calculate a surface area (SA).<sup>48</sup> The SAs of MOFs are usually very high, typically thousands of square metres per gram. Routine SA analysis of MOFs is useful, even if the structure is known as the SA can be used to ensure the framework is completely activated. Considering their porosity and ability to take up large volumes of N<sub>2</sub>, it is not surprising that much of the application driven research of MOFs has focused on their potential use as gas capture materials. There are large numbers of reports that investigate the potential of MOFs for the capture and sequestration of gases such as CO<sub>2</sub>,<sup>39</sup> H<sub>2</sub>,<sup>38,49</sup> and CH<sub>4</sub>.<sup>50</sup> Researchers have developed methods to maximise the uptake of the desired gas molecules, with interpenetrated MOFs<sup>17,23</sup> and those containing open-metal sites<sup>51,52</sup> holding great promise as both phenomena have been shown to result in greater interactions between the framework and the adsorbate.

The well-known MOF-74 series,<sup>51</sup> alternatively known as CPO-27<sup>53</sup> and  $M_2(\text{dobdc})$ <sup>52</sup> (where  $M = \text{Mg, Mn, Fe, Co, Ni, Cu}$  or  $\text{Zn}$  and  $\text{dobdc} = 2,5\text{-dioxido-1,4-benzenedicarboxylate}$ ), have been extensively studied for gas storage applications due to their exceptionally high concentration of exposed metal sites. The as-synthesised MOFs contain one bound solvent molecule per metal ion, although the framework is easily desolvated by heating under reduced pressure to present coordinatively unsaturated metals centres with square pyramidal geometry. Following previous discussions on the ability to design and modify MOFs, the Long group proceeded to synthesise a series of structurally very similar materials containing the *meta* substituted 4,6-dioxido-1,3-benzenedicarboxylate ligand.<sup>54</sup> The MOFs were named  $M_2(m\text{-dobdc})$  and an isorecticular series containing  $\text{Mg, Mn, Fe, Co}$  and  $\text{Ni}$  ions were reported (Figure 1.7a). Both series of MOFs contain one-dimensional hexagonal pores with helical chains of  $M^{2+}$  centres running parallel to the crystallographic  $c$  axis. Despite only subtle structural changes, which are caused by the altered regioisomerism of the ligand, this alters the ligand field of the metals and results in altered  $\text{H}_2$  binding enthalpies.

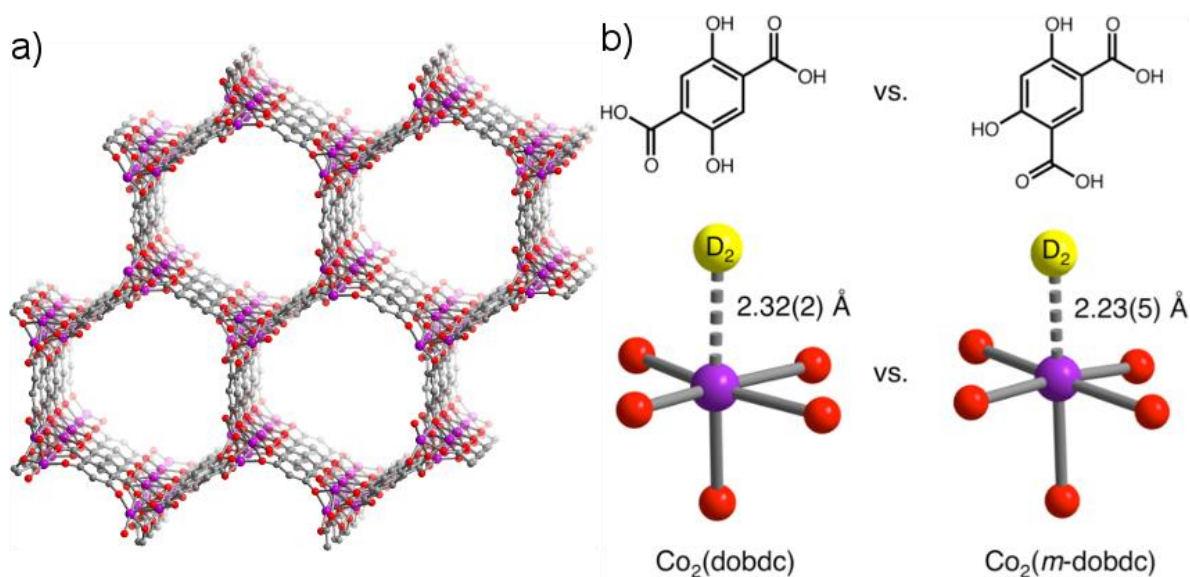


**Figure 1.7.** a) Portion of the solid state structure of  $\text{Co}_2(m\text{-dobdc})$ . b) Comparison of the *para* and *meta* substituted dihydroxy ligands used to construct  $M_2(\text{dobdc})$  and  $M_2(m\text{-dobdc})$  respectively alongside the observed binding distances between the metal ions and  $\text{D}_2$  molecules, calculated using neutron powder diffraction. Reproduced (modified) with permission from Ref.<sup>54</sup> Copyright (2014) American Chemical Society.

Despite the structural similarities between the two series of materials, the exposed metal ions in the  $M_2(m\text{-dobdc})$  series have a higher charge density, with the shorter  $\text{D}_2$  binding distance

measured by neutron powder diffraction confirming that hydrogen binds more strongly to the open metal sites within the *meta* materials (Figure 1.7b). This is further confirmed by comparing the isosteric heats of H<sub>2</sub> adsorption, which are between 0.4-1.5 kJ mol<sup>-1</sup> greater for the *meta* substituted materials (for each respective metal). This is a powerful example highlighting that small structural changes to MOFs, in this case induced through ligand regioisomerism, can dramatically alter their properties.

### 1.2.2 Catalysis

The highly ordered arrangement and porosity of MOFs has resulted in their consideration as heterogeneous catalysts for a wide variety of transformations.<sup>55-57</sup> The catalytic activity of framework materials was investigated as early as 1994,<sup>58</sup> while the ability to tune the chemical functionality and structure of MOFs allows them to be tailored to suit specific catalytic transformations.<sup>41</sup> The porosity of MOFs enables the transport of reagents and products to and from the catalytic sites. There are four main considerations that must be addressed when designing/synthesising a catalytic MOF: (i) the MOF must be sufficiently stable that upon activation its channels remain open, (ii) the MOF must contain a catalytic centre relevant to the transformation in mind, (iii) the MOF must be stable under the catalytic conditions, and (iv) the MOF should be recyclable to allow numerous catalytic cycles to occur. Points (i), (iii) and (iv) are all related and are determined in the main by the stability of the MOF and this has seen an increase in research towards MOFs with improved stabilities, such as Zr MOFs<sup>10</sup> (See Section 1.3), although catalyst deactivation and leaching are not related to MOF stability but can also result in a loss of activity.

There are a number of strategies that can be used to synthesise MOFs with catalytic centres, including open metal sites, functional sites on the ligand scaffold, encapsulation of catalytic species within the pores (such as noble-metal nanoparticles), semiconductor photocatalysis (if the metal clusters have the correct electronic configuration), postsynthetic modification of pendant functionality and finally grafting of catalytic species to the metal clusters (Figure 1.8).<sup>44</sup>

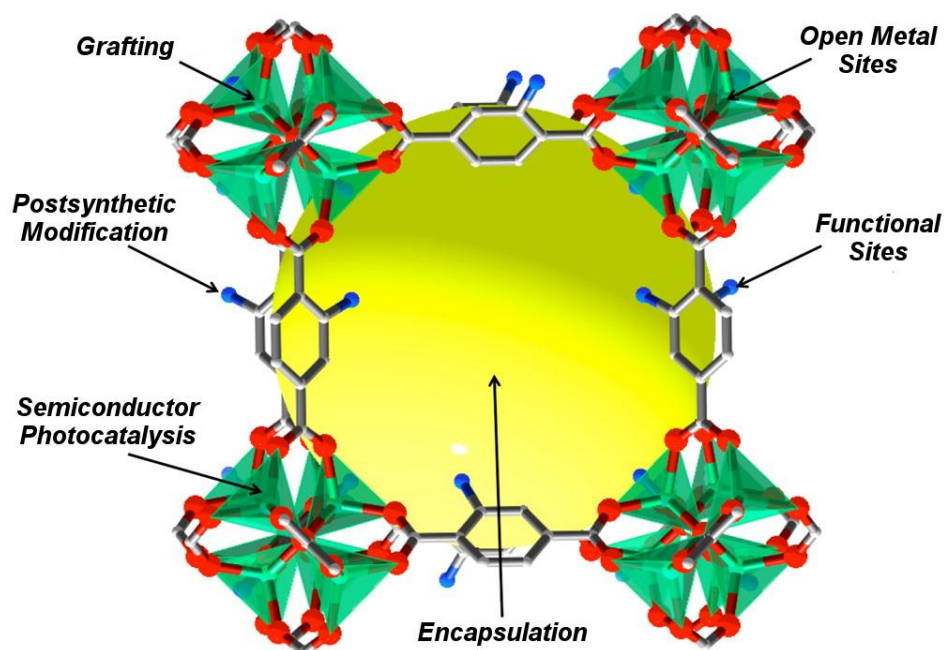


**Figure 1.8.** Representation of an exemplary MOF, highlighting different routes available for the introduction of catalytic sites. Reproduced (modified) with permission from Ref.<sup>44</sup> Copyright (2014) American Chemical Society.

In 2007, Kitagawa *et al.* reported a 2-fold interpenetrated Cd MOF containing a tridentate pyridyl based ligand with integral amide moieties.<sup>59</sup> The resulting MOF was found to be dynamic, contracting and expanding upon desolvation and resolution in DMF, while in the crystal structure H<sub>2</sub>O molecules were hydrogen bonded to the amide groups. This suggested the potential accessibility and reactivity of the amide functionality and subsequently it was found that the amide groups interacted with alcohols. In light of this, the authors decided to investigate the ability of the amide groups within the MOF to act as catalysts for Knoevenagel condensation reactions between benzaldehyde and a variety of substrates (Figure 1.9).



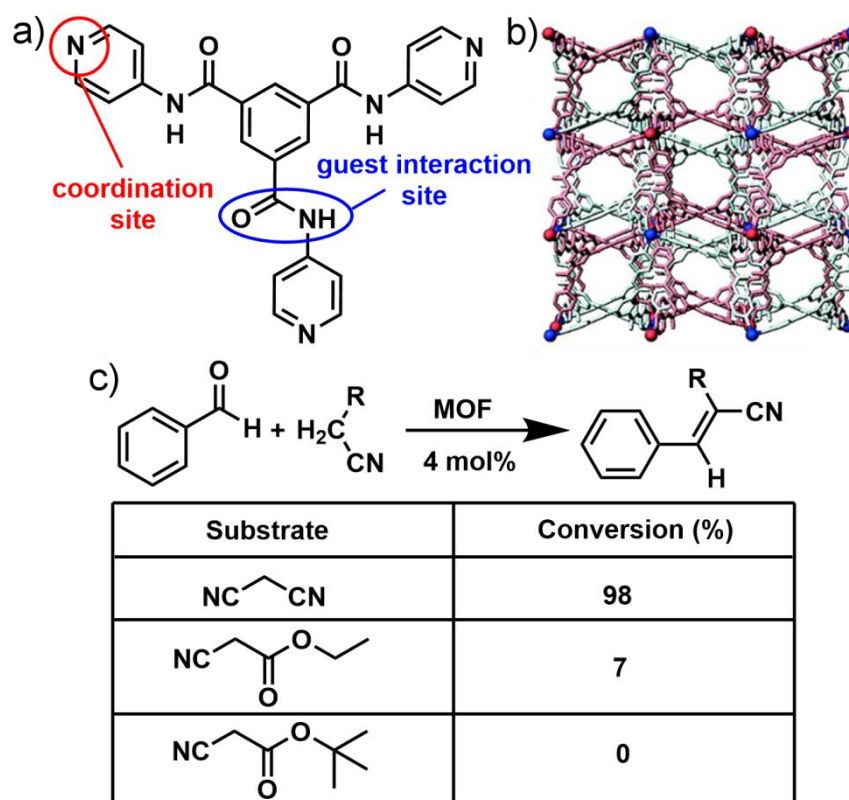


**Figure 1.9.** a) The amide containing tridentate pyridyl based ligand that forms b) a 2-fold interpenetrated 3-dimensional MOF with Cd. c) Schematic representation of the catalytic transformation investigated using the amide containing MOF, alongside the percentage conversion obtained with three different substrates of varying size. Reproduced (modified) with permission from Ref.<sup>59</sup> Copyright (2007) American Chemical Society.

The amide containing Cd MOF was very efficient for the base-catalysed Knoevenagel condensation between benzaldehyde and malononitrile, while control reactions with  $\text{Cd}(\text{NO}_3)_2 \cdot 4\text{H}_2\text{O}$  and the free ligand showed negligible catalytic activity (the amide groups of the ligand are not accessible as they are involved in intermolecular hydrogen bonding). Spatial separation of the amide functionality within the pores of the Cd MOF results in an effective catalyst, and this is further evidenced by the observed size based selectivity (the % conversion decreases with larger substrates), confirming that the catalysis occurs within the pores and not merely on the MOF surface. Furthermore, the catalyst could be recovered and showed good recyclability.

It should also be pointed out that extensive research has been performed in the quest of enantioselective MOF catalysts,<sup>43,60</sup> which are usually synthesised containing homochiral

ligands, or alternatively syntheses are performed in the presence of a chiral influence (e.g. an L-aspartate containing ionic liquid).<sup>61,62</sup> The first example of an enantioselective catalytic MOF was POST-1, which is a Zn MOF containing an enantiopure ligand derived from D-tartaric acid, although a very modest enantioselectivity of 8% was obtained during a transesterification reaction.<sup>63</sup> Since then there have been multiple reports of homochiral MOFs, containing for instance chiral BINOL based ligands,<sup>64</sup> and the reader is directed to references 43 and 60 for a more comprehensive overview of the subject.

### 1.2.3 Drug Delivery

MOFs have been realised as potential candidates for biomedical applications, for instance as drug delivery systems<sup>45,46</sup> and also as MRI contrast agents.<sup>47</sup> The chemical and structural tunability of MOFs allows them to be designed to meet the requirements of the desired application,<sup>13</sup> while more importantly this also enables fine control of their cytotoxicity.<sup>65</sup> It is well-known that MOFs demonstrate low chemical stabilities,<sup>66</sup> but this can be advantageous for drug delivery systems. The MOF has to remain intact for long enough to reach the target area of the body then in-situ degradation of the MOF releases the cargo from the pores to deliver the desired therapeutic effect. The M<sup>III</sup> carboxylate based MOFs, typically known as MIL materials, have received widespread interest as drug delivery systems, especially the Fe<sup>III</sup> analogues due to their low cytotoxicity.<sup>67</sup> During a study on flexible MIL-53 materials, ibuprofen was loaded into the MOFs by a simple impregnation technique and in both the Cr<sup>III</sup> and Fe<sup>III</sup> analogues ibuprofen loadings of ~20% were achieved.<sup>68</sup> MIL-53(Cr) was used as a proof of concept material during the study in spite of its well-known toxicity. Powder X-ray diffraction (PXRD), density functional theory (DFT) simulations, as well as nuclear magnetic resonance (NMR) and infrared (IR) spectroscopies were used to determine the precise loading and location of the ibuprofen within the MOFs (Figure 1.10a). The release of ibuprofen from the MOFs was then determined using high performance liquid chromatography (HPLC) analysis by employing simulated body fluid (similar inorganic composition to human plasma) at 37 °C to mimic physiological conditions. The release of ibuprofen from the MOFs is surprisingly slow, taking around 3 weeks to be completely liberated, resulting in a steady and controlled release (Figure 1.10b).



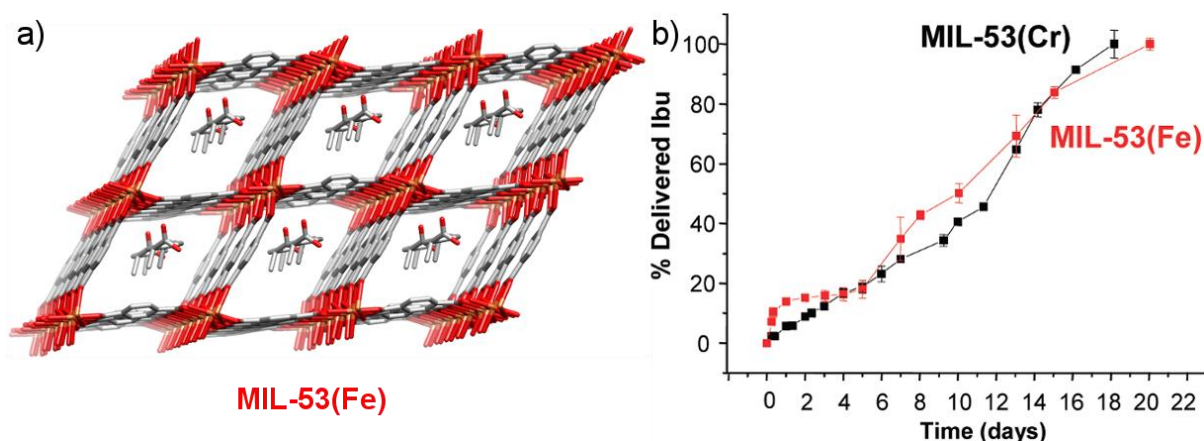


**Figure 1.10.** a) Representation of the DFT optimised structure of ibuprofen loaded MIL-53(Fe) where ibuprofen is confined within the pores through hydrogen bonding and van der Waals interactions. b) Release profiles of ibuprofen from MIL-53(Fe) and MIL-53(Cr) under simulated physiological conditions, showing a slow release over ~21 days. Reproduced (modified) with permission from Ref.<sup>68</sup> Copyright (2008) American Chemical Society.

The low cytotoxicity of Fe carboxylate frameworks has resulted in a large amount of interest in this area.<sup>45</sup> In 2009, Lin *et al.* decided to study the related Fe carboxylate, MIL-101, for imaging and drug delivery applications.<sup>69</sup> The authors synthesised a mixed ligand version of the MOF containing both terephthalate (82.6%) and amino-terephthalate (17.4%) ligands, while PXRD was used to confirm that the MIL-101 topology was retained. The amine handle of the mixed ligand MOF was used as a platform for the covalent attachment of either a BODIPY dye or a cisplatin prodrug. Release profiles revealed that both the BODIPY dye and cisplatin prodrug were released very quickly from the MOFs, suggesting their instability under simulated physiological conditions. To overcome this phenomenon the MIL-101 particles containing the covalently attached biomolecules were coated with a layer of silica, providing them with enhanced physiological stability. The  $t_{1/2}$  release times were increased by ~11.5 times for the cisplatin prodrug derivative and by ~6.5 times for the BODIPY derivative, resulting in a slower and more controlled release. The silica coating thus improves the stability of the MOFs, rendering them more useful for biomedical applications. The chemical tunability of MOFs allows fine control of their structures and properties and as new MOFs are discovered they may become potential candidates for biomedical applications, a field which is likely to receive increasing interest over the coming years.

To summarise, MOFs have been investigated and subsequently have shown great promise for use in a number of applications, although only few examples have been shown here to keep in line with the theme of this thesis. However, the take-home message from this section is that the designability of MOFs enables fine-control over their structures and properties allowing specialised materials suited to the application in mind to be obtained. The main drawback of MOFs for application based use is their low stabilities, although in the example discussed by Lin *et al.* it has been shown that coating MOF particles with silica, results in hybrid materials offering greatly improved stabilities. Another approach to increase the stabilities of MOFs is to design more robust frameworks, and Zr MOFs<sup>10</sup> are among the most stable MOFs known and hence they have been receiving increased amounts of interest in recent years.

### 1.3 Zr Metal-Organic Frameworks

Zirconium MOFs were first reported in the literature in 2008 by Lillerud *et al.* and they have received increasing interest since.<sup>10,70</sup> The MOFs were named UiO-66, UiO-67 and UiO-68 and were part of an isorecticular series containing terephthalate, biphenyl dicarboxylate and terphenyl dicarboxylate bridging ligands respectively. UiO-66 type MOFs contain  $\text{Zr}_6\text{O}_4(\text{OH})_4$  clusters that are 12-connected by bridging organic ligands, resulting in 3-dimensional porous architectures containing both tetrahedral (smaller) and octahedral (larger) pores (Figure 1.11). Initially, the structures of UiO-66 MOFs had to be solved from powder X-ray diffraction (PXRD) data as single crystals could not be obtained. However, coordination modulation (see Section 1.4) has greatly improved the synthetic capabilities of Zr MOFs, allowing single crystals to be isolated and their solid state structures have since been confirmed by single crystal X-ray diffraction.

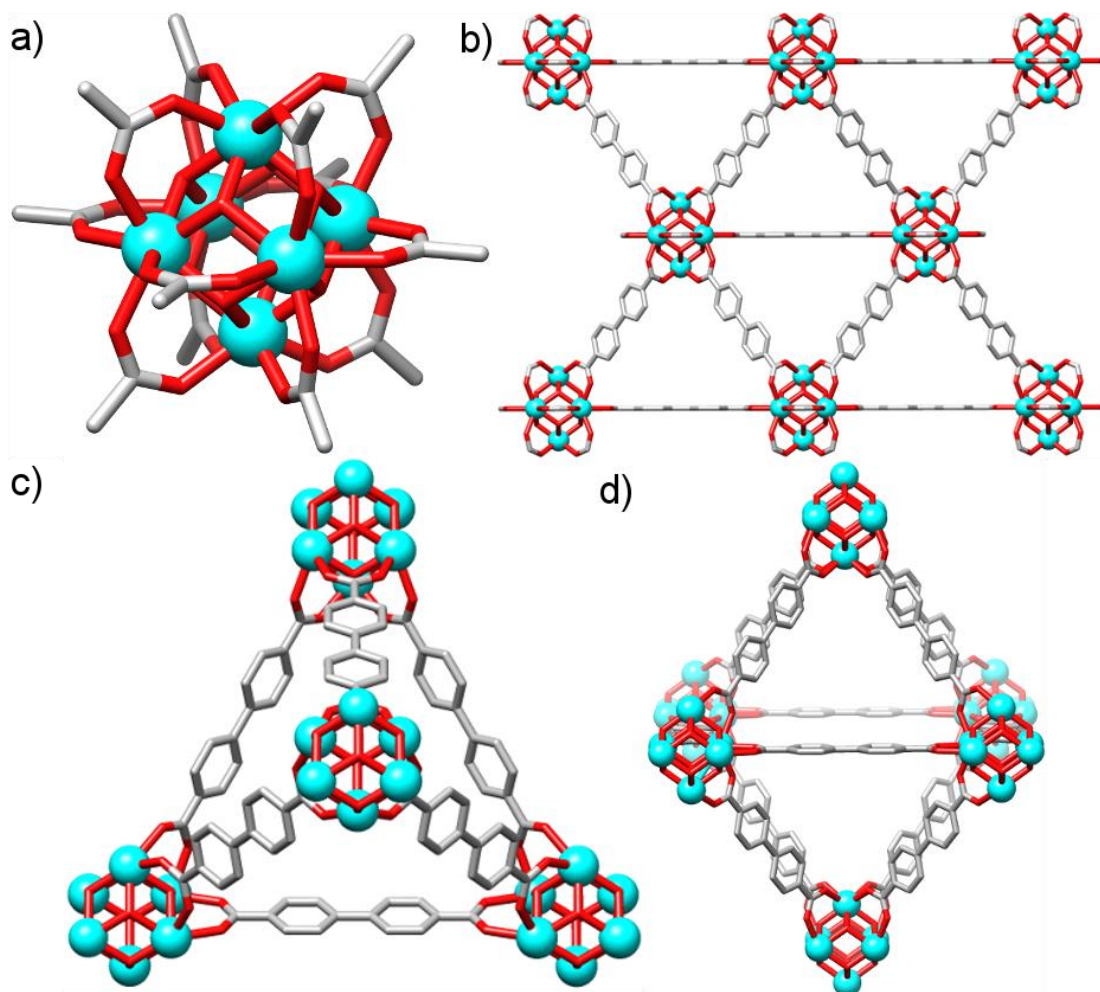


**Figure 1.11.** a) Representation of the  $\text{Zr}_6\text{O}_4(\text{OH})_4(\text{R}-\text{CO}_2)_{12}$  cluster that is found in UiO-66 type MOFs alongside b) a portion of the solid state structure of UiO-67, highlighting the connection of the  $\text{Zr}_6$  clusters by the bridging ligands. Representation of the c) tetrahedral and d) octahedral pores found within UiO-67. Redrawn from CCDC deposition 1441659.<sup>71</sup>

As the length of the bridging ligand increases the MOFs' pore volume increases, however the overall framework structure is unaltered and all UiO-66 type MOFs crystallise in the highly symmetric  $Fm-3m$  space group (they form part of an isorecticular series). There have been many reports on derivatives of UiO-66 type MOFs containing functionalised bridging organic ligands.<sup>70,72</sup> UiO-66 type MOFs are typically obtained when linear dicarboxylate ligands are used, however Serre *et al.* showed that using higher synthesis temperatures alternative structures can be obtained. The so called MIL-140 series of MOFs contain 1-dimensional Zr oxide chains and 1-dimensional porous channels while demonstrating high thermal and mechanical stabilities.<sup>73</sup>

Interpenetrated UiO-66 derivatives are known and are based on extended linear dicarboxylate ligands. Until recently, interpenetrated Zr MOFs were known only with 4,4'-[1,4-phenylenebis(ethyne-2,1-diyl)]-dibenzoate ligands containing three phenylene and two alkyne units (Figure 1.12a).<sup>74-77</sup> The extended ligands result in sufficient pore space that the resulting structures are 2-fold interpenetrated (Figure 1.12b) and functionalisation of the central phenylene ring, either by direct synthesis or postsynthetic modification (PSM – see Section 1.5), resulted in an isorecticular series of MOFs (Figure 1.12c).

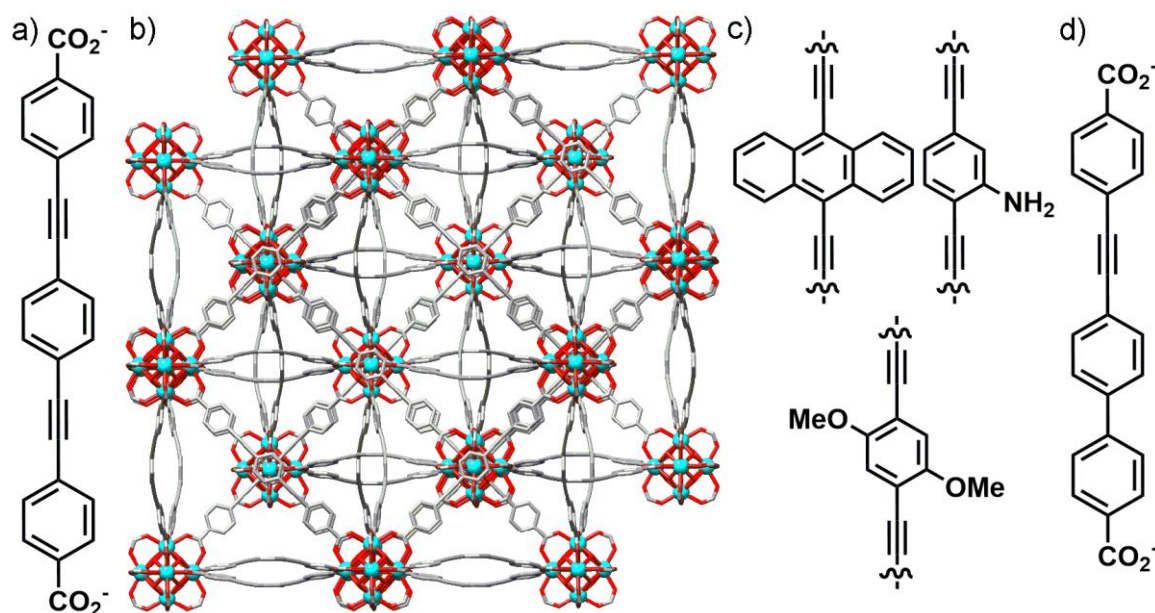


**Figure 1.12.** a) The extended 4,4'-[1,4-phenylenebis(ethyne-2,1-diyl)]-dibenzoate ligand and b) a portion of the solid state structure of the 2-fold interpenetrated MOF that it forms with Zr (Redrawn from CCDC deposition 1443196).<sup>78</sup> c) Representative examples of the functionalised cores of the isorecticular series of interpenetrated Zr MOFs and d) the slightly shorter ligand that has recently been shown to also result in 2-fold interpenetrated Zr MOFs.

A study was performed to determine the critical ligand length required for the switchover from UiO-66 to interpenetrated Zr MOFs, and it was found that the slightly shorter ligand containing three phenylene units and only one alkyne unit (Figure 1.12d) also resulted in 2-fold interpenetrated materials.<sup>79</sup> The 2-fold interpenetration slightly reduces the symmetry of the MOFs with the space group changing from *Fm-3m* to *Fd-3m*, although considering each independent framework it is clear that the interpenetrated MOFs are UiO-66 isomers, sharing the same framework connectivity. However, occupation of the octahedral pores by the interpenetrating framework results in smaller tetrahedral pores alongside the larger

tetrahedral pores. Recently an anthracene containing derivative was reported (Figure 1.12c) and although 2-fold interpenetration was maintained the symmetry was slightly altered due to favourable  $\pi$ - $\pi$  stacking interactions of the ligands.<sup>75</sup>

Alternative structural topologies have been obtained with ligands presenting different binding geometries. Trigonal tricarboxylate based ligands have been shown to form either 2-dimensional<sup>80</sup> or 3-dimensional<sup>81-83</sup> Zr MOFs, although in these cases lower connected Zr<sub>6</sub> clusters result (Figure 1.13a). The altered geometry of the ligand results in 6-connected Zr<sub>6</sub> clusters rather than the 12-connected clusters observed in UiO-66 type MOFs and the free coordination sites are capped by either solvent molecules and/or monocarboxylate modulators (coordination modulation – see Section 1.4). Interestingly, changing the terminal modulators attached to the Zr<sub>6</sub> clusters changes the inter-layer separation<sup>80</sup> which allows the porosity to be regulated.<sup>83</sup>

Planar tetracarboxylate based ligands have been used for the construction of Zr MOFs and in the specific case of tetrakis(4-carboxyphenyl)porphyrin (TCPP) Zr MOFs containing typical Zr<sub>6</sub> clusters have been obtained (Figure 1.13b),<sup>84,85</sup> while alternatively it has been shown to result in a MOF containing Zr<sub>8</sub> clusters that were previously unknown in both cluster and MOF chemistry.<sup>86</sup> The presence of porphyrin units presents opportunities for the incorporation of secondary metals and it was shown that the Fe metallated MOF is an effective peroxidase mimic during the oxidation of a number of substrates.<sup>84</sup>



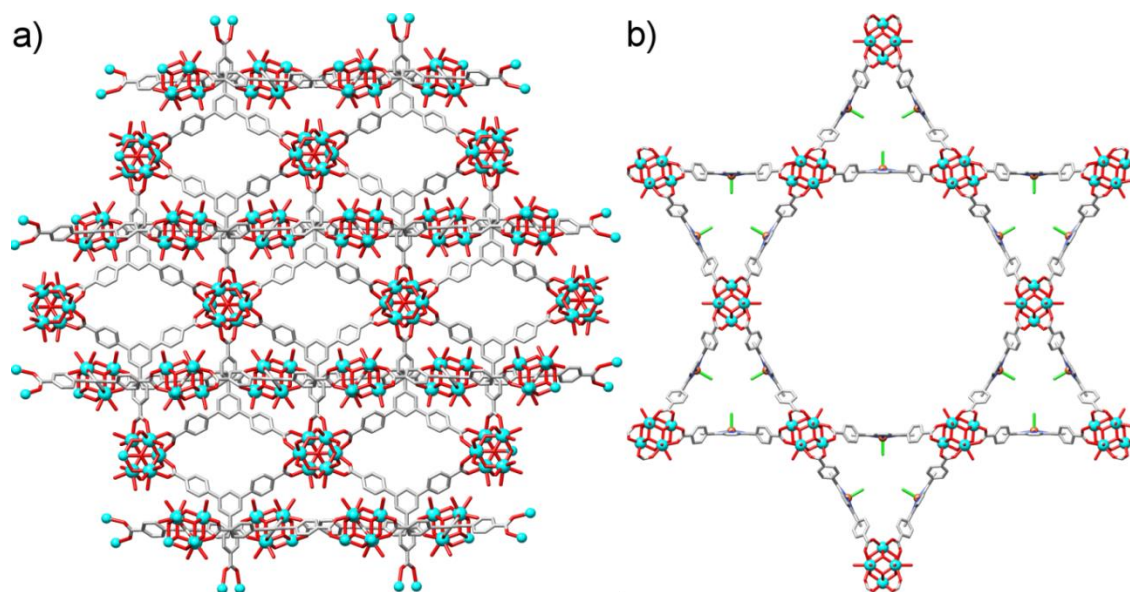


**Figure 1.13.** Portions of the solid state structures of a) a trigonal tricarboxylate containing MOF  $[\text{Zr}_6\text{O}_4(\text{OH})_4(\text{btb})_6(\text{OH})_6(\text{H}_2\text{O})_6]_n$ , where btb = benzene-1,3,5-tribenzoate and b) a planar tetracarboxylate based MOF  $[\text{Zr}_6(\text{OH})_8(\text{FeCl-TCPP})_2]_n$ . Redrawn from CCDC depositions 1000802<sup>81</sup> and 893545<sup>84</sup> in turn.

Alternatively, a tetracarboxylate pyrene based ligand was used to construct an 8-connected Zr MOF commonly known as NU-1000.<sup>87</sup> NU-1000 has been extensively investigated for a range of cluster modifications as a result of the lower connectivity of the  $\text{Zr}_6$  clusters and the presence of terminal OH and  $\text{H}_2\text{O}$  ligands. Postsynthetic exchange of the terminal ligands has been carried out using a process the authors call solvent assisted ligand incorporation.<sup>33</sup> Incorporating perfluorinated alkanes using this procedure increased both the water stability and  $\text{CO}_2$  uptake capacities of the NU-1000 materials.<sup>88,89</sup> Similar to the incorporation of organic compounds, metallation of the  $\text{Zr}_6$  clusters of NU-1000 has been investigated and it was found that the nickel metallated material is an efficient catalyst for the oligomerisation of ethylene.<sup>90</sup> Tetrahedral carboxylate based ligands have been used to construct Zr MOFs,<sup>91</sup> and when 4,4',4'',4'''-methanetetrayltetrabenzoic acid is used Zr MOFs containing either 8-connected or 12-connected  $\text{Zr}_6$  clusters have been obtained.<sup>82</sup>

To summarise, the different structure types of Zr MOFs containing linear, trigonal and tetrahedral carboxylate based ligands have been discussed. Interpenetrated Zr MOFs have been obtained when extended linear dicarboxylate ligands have been used, while it should be

noted that Zr MOFs containing phenolate<sup>92</sup> and phosphonate<sup>93</sup> based ligands have been reported infrequently.

The reason for the high interest in Zr MOFs is their improved thermal<sup>94</sup> and mechanical<sup>95-97</sup> stabilities compared with traditional late transition metal containing MOFs, resulting in their potential use in a number of applications.<sup>70</sup> UiO-66 type MOFs have been constructed with hafnium,<sup>98,99</sup> thorium,<sup>100</sup> uranium<sup>101</sup> cerium<sup>102</sup>, europium,<sup>103</sup> terbium<sup>103</sup> and yttrium<sup>103</sup> clusters although no titanium derivative has of yet been obtained. The most promising of these MOFs are the Hf derivatives which display very similar properties to their Zr counterparts. Many recent reports discuss both Zr and Hf MOFs in concert,<sup>76,104</sup> due to their similar syntheses and properties, and it is anticipated that interest in Hf MOFs will increase. Despite their similar properties, hafnium MOFs are useful for diffraction purposes as they scatter more strongly and this is particularly important for challenging single crystal X-ray diffraction experiments. The improved stabilities of Zr and Hf MOFs are attributable to the resilient coordination bonds between the hard metal ions and the carboxylate oxygen atoms. However, the hard-hard interactions between the metal and the ligand make their syntheses troublesome, as the fast crystallisation kinetics often result in the isolation of amorphous solids without long-range order. In order to access crystalline, phase-pure Zr and Hf MOFs it was clear that new synthetic procedures had to be developed and in 2011 Behrens *et al.* applied coordination modulation to Zr MOFs for the first time.

## 1.4 Coordination Modulation

Coordination modulation describes the deliberate addition of foreign compounds to MOF syntheses and typically they influence the crystallinity, size and morphology of the resulting products (Figure 1.14).<sup>105-107</sup> Modulators are typically monodentate organic compounds, such as acetic, benzoic or formic acid, and their competitive coordination towards the metal clusters influences the coordination equilibrium, allowing the directed syntheses of MOF particles with alternative morphologies. Accessing MOF crystals with different morphologies results in different concentrations of exposed facets and this can ultimately control the materials' physical properties. The ability to control the surface chemistry of MOF particles is still in its infancy however, it is becoming a topic of interest.<sup>108</sup>

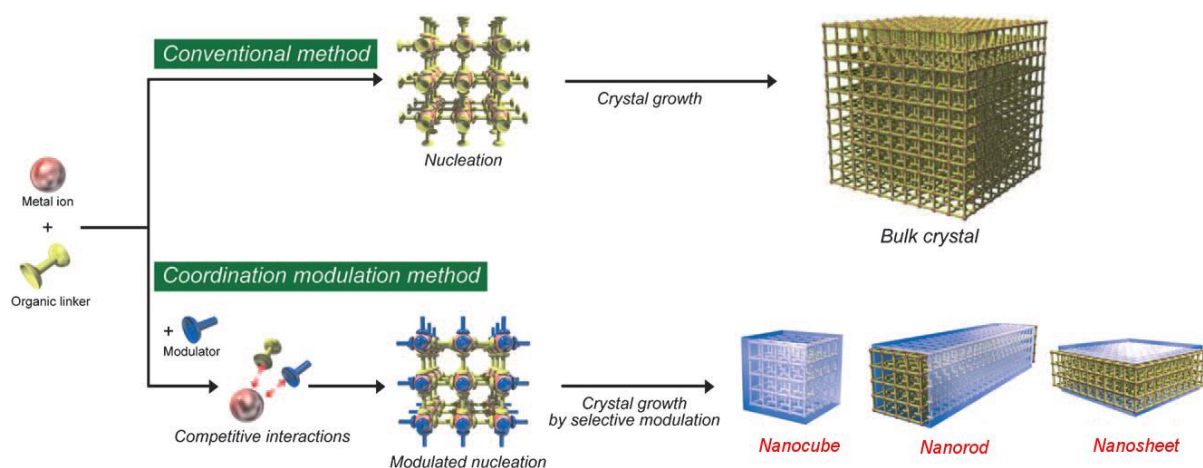


**Figure 1.14.** Schematic representation comparing conventional and coordination modulated MOF syntheses. The directed synthesis of different MOF morphologies is shown by selective modulation of crystal facets in a certain direction. Reproduced (modified) with permission from Ref.<sup>107</sup> Copyright (2009) Wiley-VCH.

One of the first examples of coordination modulation was reported by Kitagawa *et al.* where they described the modulation of an anisotropic Cu framework using acetic acid.<sup>107</sup> The material used to demonstrate the coordination modulation technique was a pillared MOF comprising 2-dimensional equatorial sheets based on carboxylate containing ligands, with the layers pillared into the third dimension by nitrogen containing ligands. Using acetic acid the authors found that they were able to inhibit the extended growth of the carboxylate based layers and instead preferentially grow the material along the axis containing the nitrogen ligands. In this context, acetic acid acts as a capping agent, subsequently favouring the growth of the material in one direction. This resulted in the isolation of nanorods that demonstrated not only improved crystallinity compared with bulk samples prepared by conventional solvothermal methods but also improved N<sub>2</sub> and CO<sub>2</sub> uptakes.<sup>107</sup>

Unlike early examples of coordination modulation where the selective attachment of modulators in certain directions is believed to result in directional growth of MOF particles (capping behaviour – see Figure 1.14), different behaviours are found upon addition of modulators to the syntheses of Zr MOFs. During the first modulation study of Zr MOFs, benzoic acid, acetic acid and water were investigated as modulators for the syntheses of a variety of UiO-66 type materials.<sup>109</sup> It was found that the addition of modulators altered the size and morphology of the crystals while also improving crystallinity, presumably by



controlling the nucleation rate through competitive coordination between the monocarboxylate and the bridging ligand for attachment to the Zr clusters.<sup>110</sup> It is reasonable to assume that there exists competitive coordination between the monocarboxylate and the bridging ligand as 12 connected  $Zr_6$  clusters containing monodentate carboxylates, such as  $Zr_6O_4(OH)_4(OMc)_{12}$  (where OMc = methacrylate) are known. Indeed it has been shown that using  $Zr_6O_4(OH)_4(OMc)_{12}$  as a Zr source, substitution of methacrylate ligands by muconic acid successfully resulted in the formation of a UiO-66 isomer, proving the labile nature of the Zr-carboxylate bond.<sup>111</sup>

The dramatic enhancement in crystallinity upon gradually increasing the number of equivalents of benzoic acid added to the syntheses of UiO-67 (Zr MOF containing biphenyl dicarboxylate ligands) is evident from both PXRD and SEM analysis (Figure 1.15).<sup>109</sup>

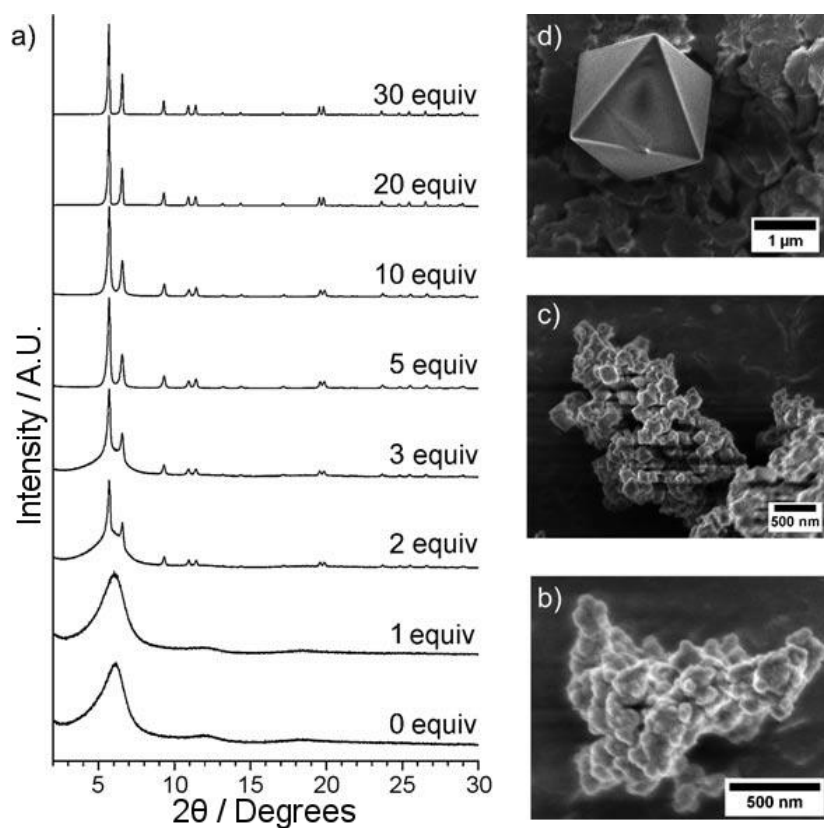


**Figure 1.15.** a) PXRD patterns of UiO-67 synthesised in the presence of varying amounts of benzoic acid. SEM images of the materials synthesised in the presence of b) 0, c) 3 and d) 30 equivalents of benzoic acid show a transition from small aggregates to individual octahedral crystals around 2  $\mu\text{m}$  in size. Reproduced (modified) with permission from Ref.<sup>109</sup> Copyright (2011) Wiley-VCH.

As part of the same study the authors investigated the use of benzoic acid (30 equivalents) and water (3 equivalents) as modulators during the synthesis of UiO-68-NH<sub>2</sub>, which contains amino-terphenyldicarboxylate bridging ligands (Figure 1.16a). UiO-68-NH<sub>2</sub> was chosen for the modulation studies over the parent UiO-68 material due to the improved solubility of the amine functionalised ligand and also due to the potential for postsynthetic modification by covalent transformation of the pendant amine handle. Surprisingly, under the modulation conditions examined, large single crystals (~100  $\mu$ m in size) of UiO-68-NH<sub>2</sub> were obtained (Figure 1.16b), allowing greater structural information to be obtained from the first single crystal structure of a Zr MOF (Figure 1.16c).

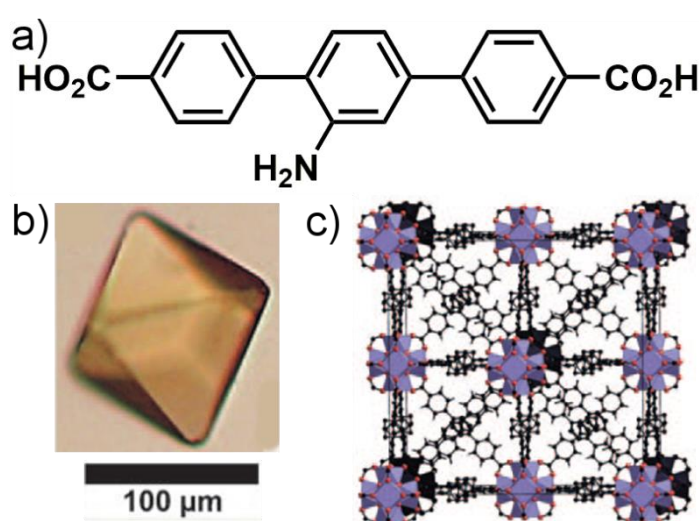


**Figure 1.16.** a) Structure of the amino-terphenyldicarboxylic acid ligand used to construct UiO-68-NH<sub>2</sub>. Benzoic acid/water modulation of UiO-68-NH<sub>2</sub> resulted in b) X-ray quality single crystals allowing c) the first single crystal structure of a Zr MOF to be obtained. Reproduced (modified) with permission from Ref.<sup>109</sup> Copyright (2011) Wiley-VCH.

The single crystal X-ray structure of UiO-68-NH<sub>2</sub> confirmed that the structures previously predicted for UiO-66 type MOFs from powder X-ray diffraction data were correct. UiO-68-NH<sub>2</sub> crystallises in the *Fm-3m* space group and contains both tetrahedral and octahedral pores. Accessing single crystals of Zr MOFs is highly advantageous as it allows their structures to be determined relatively easily without the need for complex modelling and structure prediction software/expertise. The synthesis of single crystals of Zr MOFs is still relatively difficult despite advances in coordination modulation. This is exemplified by the fact that despite their discovery in 2008<sup>10</sup> UiO-66 and UiO-67 were not obtained as single crystals until 2014<sup>112</sup> and furthermore UiO-68 (the parent sample and not functionalised

derivatives) has never been synthesised as single crystals suitable for X-ray diffraction. Accessing single crystals of Zr MOFs is useful for specialised techniques such as single crystal nanoindentation and high-pressure single crystal X-ray diffraction that can be used to determine their mechanical properties.<sup>71</sup> Even in cases where it is not possible to access single crystals of Zr MOFs by coordination modulation the ability to produce bulk, phase pure, highly crystalline samples has transformed the field, such that modulators are now accepted as an essential component during synthesis and in many cases modulators have provided access to otherwise unobtainable Zr MOFs.<sup>113,114</sup> The scope of modulators used during the synthesis of Zr MOFs has been expanded to include hydrochloric acid,<sup>115</sup> formic acid,<sup>116</sup> hydrofluoric acid,<sup>117</sup> trifluoroacetic acid (TFA)<sup>118</sup> and recently amino acids<sup>119,120</sup> (amino acid modulation forms the second chapter of this thesis) amongst others.

During the syntheses of Zr MOFs it is difficult to predict how the modulator will affect the materials structural properties and this is determined by the level of modulator incorporation. Synthetic modulators are known to promote defects,<sup>94,121,122</sup> which are predominantly caused by missing linkers/clusters. Defects alter the physical and structural properties of MOFs, and although they may have initially been considered to be problematic it has now been realised that they can result in improved properties for specific applications.<sup>122</sup> For instance, using hydrochloric acid as a modulator during the synthesis of a range of UiO-66 type MOFs, higher than expected N<sub>2</sub> uptakes were recorded as a result of defects and subsequently the creation of mesopores. In extreme cases it was found that the experimental surface areas of the MOFs were in agreement with predicted surface areas where four of the twelve ligands were missing.<sup>115</sup> Similarly, when acetic acid was used as a modulator during the synthesis of UiO-66, definitive evidence of missing linkers and the creation of mesopores was obtained from high-resolution neutron powder diffraction (Figure 1.17a).<sup>123</sup> The defect concentration was altered by varying the amount of acetic acid, causing visible changes to the colour of the material while the pore volume increased by ~150% and the surface area by ~60% (Figure 1.17b).

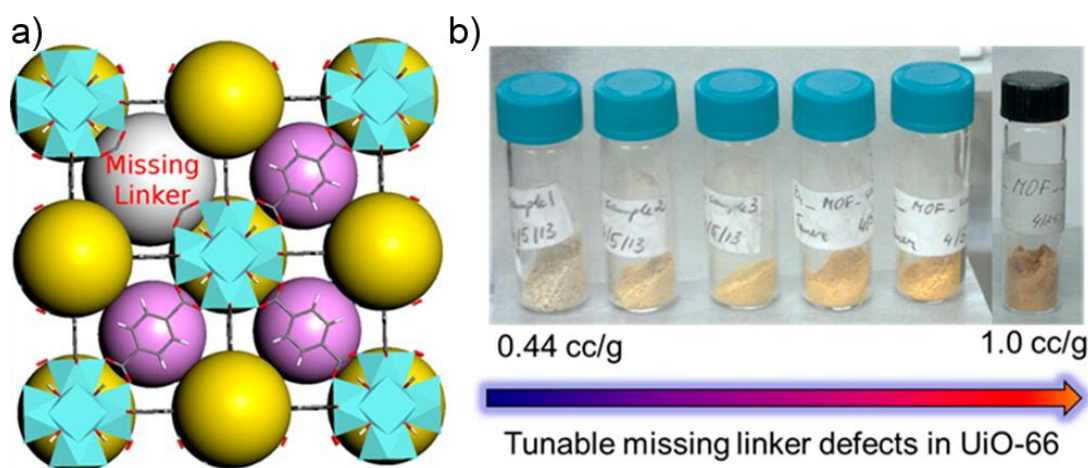


**Figure 1.17.** a) Schematic representation of a missing linker defect in UiO-66, resulting in a mesopore which is represented by a light grey sphere. b) The defect concentration could be tuned by varying the acetic acid concentration, resulting in different gas uptake capacities. Reproduced (modified) with permission from Ref.<sup>123</sup> Copyright (2013) American Chemical Society.

Considering the potential to improve the gas uptake capacities of Zr MOFs through the creation of defects, which appear to be promoted by the use of synthetic modulators, this area has received large amounts of interest and recently defects have been characterised on the molecular level using single crystal X-ray diffraction.<sup>116</sup> Recently, a comprehensive study performed by Lillerud *et al.* attempted to rationalise the use of routinely employed modulators and their effect on the porosity and composition of the resulting materials.<sup>124</sup> The authors found that the concentration of defects in UiO-66 could be systematically tuned, increasing with respect to modulator concentration and/or acidity. The defectivity was determined from the measured increase in BET surface area of the materials relative to UiO-66 synthesised in the absence of a modulator (Figure 1.18).

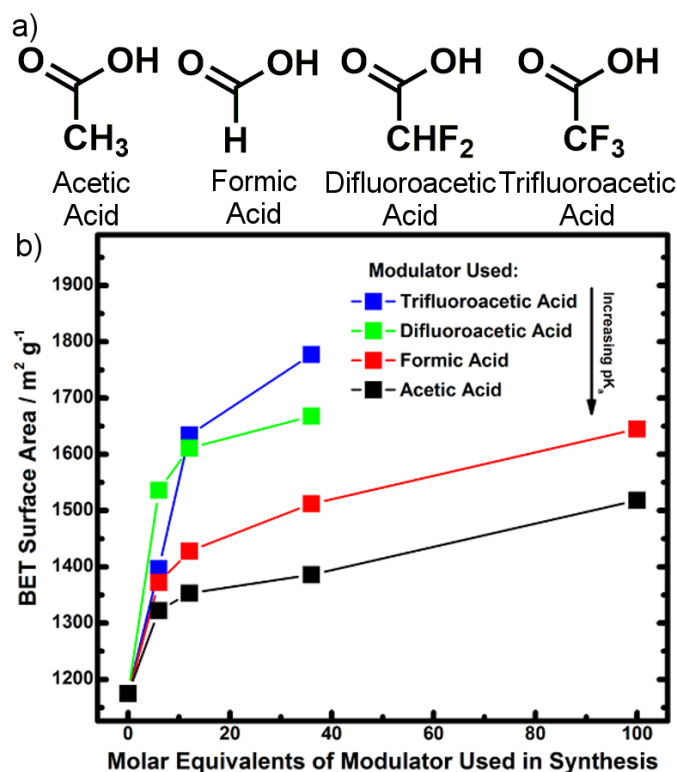


**Figure 1.18.** a) Chemical structures of modulators routinely employed during the synthesis of Zr MOFs and b) a comparison of the BET surface areas of UiO-66 samples synthesised with each of the modulators and at different concentrations. Reproduced (modified) with permission from Ref.<sup>124</sup> Copyright (2016) American Chemical Society.

Under the conditions examined the prominent defect type was found to be missing clusters, with capping formate (from the reaction *N,N*-dimethylformamide) and modulator molecules found to complete the coordination sphere of the  $\text{Zr}_6$  clusters (from dissolution NMR experiments). It was hypothesised that as the acidity of the modulator increases then it is more competitive with the bridging organic ligand and a higher concentration of defects are obtained. Similar results were also found and reported by Bennett *et al.* where higher equivalents of less acidic modulators had to be added to the synthesis of UiO-66 to achieve similar levels of modulator incorporation.<sup>125</sup> The most acidic modulator investigated during the study was TFA, resulting in the inclusion of trifluoroacetate molecules within the framework by attachment to the  $\text{Zr}_6$  clusters at defect sites. While it is frequently reported that modulators and/or defects result in altered gas uptake capacities, the trifluoroacetate containing UiO-66 material was found to be more mechanically robust compared with conventionally prepared UiO-66 samples, and this was thought to be due to stronger Zr-carboxylate bonds caused by an electron withdrawing effect of the bound TFA molecules.

The increased mechanical stability of the trifluoroacetate containing material was revealed through its ability to resist collapse under ball milling for at least 10 times longer duration.

An interesting study was conducted by Vos *et al.* whereby UiO-66 was synthesised using a combination of hydrochloric acid (HCl) and TFA, resulting in highly crystalline materials.<sup>118</sup> The resulting materials were subsequently investigated as catalysts for the “ene”-type cyclisation of citronellal to isopulegol (Figure 1.19a).

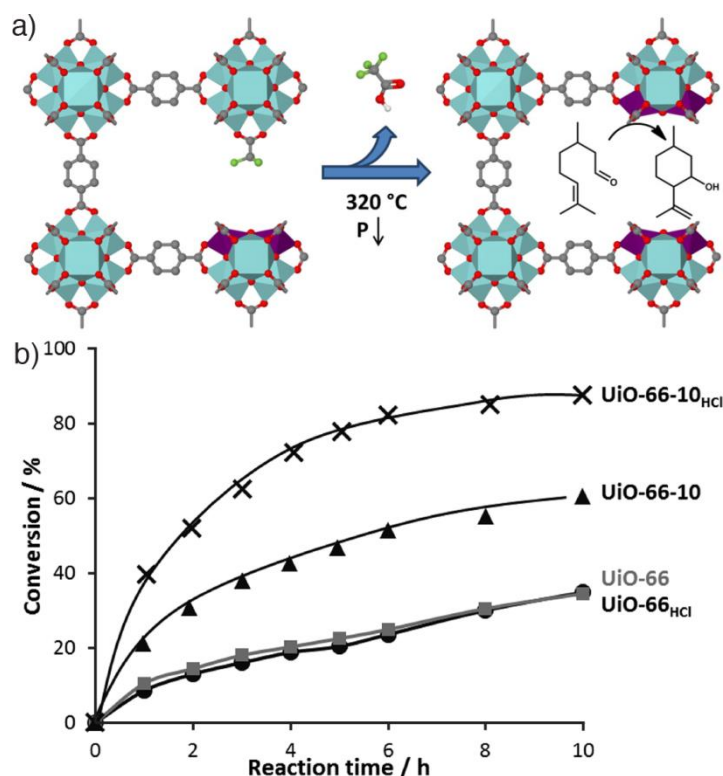


**Figure 1.19.** a) Schematic showing thermal removal of TFA from defects in UiO-66 to create a Lewis Acid catalyst for citronellal cyclisation. b) Comparison of conversion versus time for different samples, with the most defective MOF being the most catalytic. Reproduced (modified) with permission from Ref.<sup>118</sup> Copyright (2013) American Chemical Society.

UiO-66-10<sub>HCl</sub>, that is UiO-66 synthesised in the presence of 10 equivalents of TFA and 1 equivalent of HCl, was observed to contain both physisorbed and cluster bound TFA from thermal analysis and <sup>19</sup>F solid-state NMR spectroscopy. Thermal treatment of UiO-66-10<sub>HCl</sub> was followed by *in-situ* IR spectroscopy, revealing that dehydroxylation of the Zr<sub>6</sub> clusters begins prior to removal of trifluoroacetate, although the two processes occur simultaneously at higher temperatures. Postsynthetic thermal treatment results in Zr<sub>6</sub>O<sub>8</sub>(terephthalate)<sub>4</sub> – a

highly defective material containing  $\text{Zr}_6$  clusters surrounded by 8 carboxylates rather than the usual 12 – which has a high number of Lewis acid ( $\text{Zr}^{\text{IV}}$ ) sites and increased pore dimensions. This results in dramatically improved catalytic performances as  $\text{UiO-66-10}_{\text{HCl}}$  is considerably more active in the cyclisation of citronellal to isopulegol (Figure 1.19b). Overall, this example highlights that coordination modulation has been used to provide access to an otherwise unobtainable UiO-66 type material that demonstrates greatly improved catalytic activities.

During a study by Gutov *et al.* UiO-67 was synthesised in the presence of either formic, benzoic, trifluoroacetic, acetic or hydrochloric acid.<sup>121</sup> The modulated materials were found to contain cluster bound modulators in line with other group's findings however, it was subsequently revealed that the modulators could be postsynthetically substituted. A variety of substitutions were performed, and for instance in the HCl modulated sample, where  $\text{OH}^-$  ions are expected to cap the cluster, exchange with organic acids was useful for determination of the defect concentration by dissolution NMR experiments. Interestingly, the modulators could be exchanged for L-proline hydrochloride, which may result in chiral materials useful for enantioselective applications. Rather than substitution by monodentate organic molecules, 'repairing' the crystals by introducing biphenyldicarboxylic acid resulted in substitution of the modulators for the bridging ligand and the resulting crystals were of sufficient quality for single crystal X-ray diffraction.

To discuss all of the papers detailing coordination modulation would be unfeasible as it is widely employed for the synthesis of Zr MOFs however, pertinent examples have been discussed. The use of modulators is closely linked with the creation of defects, and a combination of both phenomena has been shown to change the materials properties, for instance altering their gas uptake capacities and also their mechanical stabilities. In the last example it has been shown that cluster bound modulators can be postsynthetically exchanged for other monocarboxylate molecules or the crystals can effectively be repaired by introducing the bridging organic ligand at the defect sites. Postsynthetic exchange, and more widely postsynthetic modification (PSM), is becoming an increasingly popular route for the synthesis of highly specialised Zr MOFs and an overview of current literature detailing covalent PSM of Zr MOFs is provided in Section 1.5.1.

## 1.5 Postsynthetic Modification

A large number of MOFs are synthesised via direct synthetic routes<sup>126</sup> however, as more complex structures are sought alternative synthetic routes have been developed to overcome the limitations of direct synthesis. Postsynthetic modification (PSM) – carrying out chemical transformation<sup>127-129</sup> or exchange<sup>34,130-132</sup> on pre-synthesised materials whilst maintaining their desired characteristics – has emerged as a powerful route to introduce functionality into MOFs. The true potential of PSM is realised in cases where this technique is the only method by which desired materials can be accessed. Advances in the scope of transformations performed are reported frequently and they usually fall into one of the following categories: covalent modifications, surface modifications, metallations, linker and metal exchange, and cluster modifications. The large interest towards the PSM of MOFs has resulted in significant research in this field and the topic has been comprehensively reviewed.<sup>127,129,133</sup> During the initial period of interest towards functionalisation of MOFs by PSM Zr MOFs were in their infancy and therefore other families of MOFs were investigated. However, improved synthetic capabilities increased access to Zr MOFs and they started to become prime candidates.<sup>134,135</sup> The tolerance of Zr MOFs towards harsh chemical<sup>136,137</sup> and mechanical<sup>71,95,96,125,138</sup> conditions makes them ideal platforms for a wide variety of transformations.

PSM of Zr MOFs will be the focus herein, firstly highlighting examples of covalent transformations then the few examples of integral PSM will be discussed. In Chapter 3, PSM of Zr MOFs has been extended to include the stereoselective and quantitative halogenation of integral unsaturated alkene and alkyne units. There are multiple interesting transformations that do not fall into either of these two categories and, in particular, cluster modifications are becoming increasingly important in Zr MOFs,<sup>88,139</sup> however they are out of the scope of this thesis. Should the reader be interested in a more comprehensive understanding of PSM of Zr MOFs, then they are directed to our review article on this subject.<sup>140</sup>

### 1.5.1 Covalent Postsynthetic Modification of Zr MOFs

The vast majority of reported postsynthetic modification protocols are based upon the reactivity of pendant functional moieties on the backbone of the organic linker of the MOF,



with amine groups often exploited due to the wealth of chemical transformations possible (Figure 1.20). The first amine containing Zr MOF, UiO-66-NH<sub>2</sub>, with chemical composition [Zr<sub>6</sub>O<sub>4</sub>(OH)<sub>4</sub>(bdc-NH<sub>2</sub>)<sub>6</sub>]<sub>n</sub> (where bdc-NH<sub>2</sub> is 2-amino-1,4-benzenedicarboxylate) was described independently by the groups of Tilstet<sup>134</sup> and Cohen<sup>135</sup> in 2010. Both groups subsequently demonstrated the postsynthetic reactivity of the pre-installed amine handle through reactions with a variety of acid anhydrides, resulting in amide functionalised pores. The liquid phase reactions (chlorinated solvents, varying times) were followed by a number of experimental techniques, including IR and <sup>1</sup>H NMR spectroscopies, which provide evidence of the percentage conversion, whilst PXRD was used to demonstrate retention of crystallinity, highlighting the high chemical stability of Zr MOFs. It was observed that the greatest conversion was achieved with smaller anhydrides, likely due to pore size based restrictions.

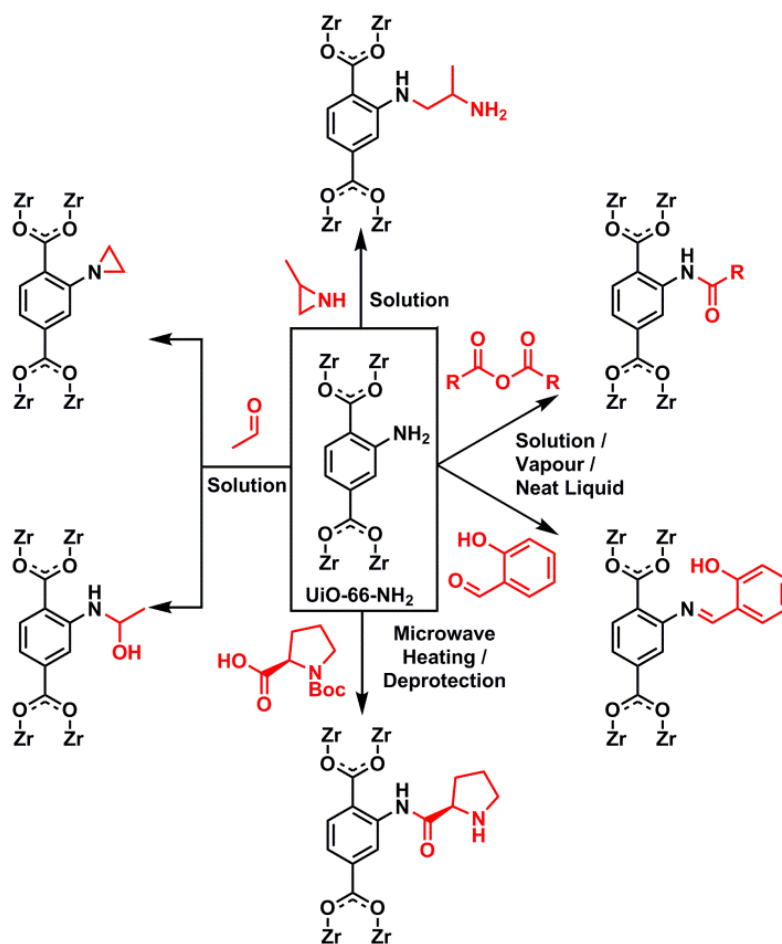


**Figure 1.20.** Examples of covalent postsynthetic modifications of pendant amine units in UiO-66-NH<sub>2</sub>.

In 2012, the PSM of UiO-66-NH<sub>2</sub> with acid anhydrides was extended to investigate the feasibility of vapour phase reactivity.<sup>141</sup> The authors report that the vapour method provides access to the amide modified MOFs with improved conversions in reduced timescales. Aside from acid anhydrides, the reactivity of UiO-66-NH<sub>2</sub> with vapour phase salicylaldehyde was also demonstrated, resulting in an imine functionalised MOF. Although only modest conversion was achieved, this still outperformed the corresponding liquid phase reaction (ca. 29% vs. 10%).

In a later report, UiO-66-NH<sub>2</sub> reactivity was investigated through reaction with neat reagents, under relatively harsh conditions (100 °C) compared to previous work.<sup>142</sup> PSM of UiO-66-NH<sub>2</sub> with acetic anhydride was successfully demonstrated using this method, achieving 98% conversion in as little as 10 minutes. The authors report that PSM with carboxylic acids in some cases leads to decomposition of the framework, postulating that this is due to postsynthetic ligand exchange owing to the free coordinating groups present on the reactive species. A study of UiO-66-NH<sub>2</sub> by Yaghi *et al.* suggested, through solid state <sup>15</sup>N NMR spectroscopy measurements, that the MOF is actually comprised of both the free amine (bdc-NH<sub>2</sub>) and ammonium chloride (bdc-NH<sub>3</sub><sup>+</sup>Cl<sup>-</sup>) ligands in a 2:1 ratio.<sup>143</sup> PSM with acetaldehyde was subsequently investigated, resulting in conversions of up to 70%, although both the hemiaminal and aziridine products were obtained, representing the kinetic and thermodynamic products respectively, and a further heating process could alter their relative ratios. These early reports have therefore provided foundations detailing the feasibility of potential transformations on the amine handle of UiO-66-NH<sub>2</sub>, although recent attention has focused on improving the materials properties, to enable their successful use in desired applications.

Wang *et al.* studied the PSM of UiO-66-NH<sub>2</sub> with 2-methylaziridine, yielding the corresponding MOF containing alkylamine lined pores in a 28% yield.<sup>144</sup> It was found that the modified material was an efficient catalyst for Knoevenagel condensations, as the alkylamine is able to successfully activate the aldehyde by forming an imine. In a typical reaction between benzaldehyde and malononitrile at room temperature in toluene, the yield of the reaction was improved from 5% to 97% in the presence of UiO-66-NH<sub>2</sub> and the alkylamine tagged UiO-66-NH<sub>2</sub> respectively. The authors also report that IRMOF-3 – a Zn MOF containing bdc-NH<sub>2</sub> – does not withstand the postsynthetic modification, highlighting

the high chemical stability of Zr MOFs. Indeed, the alkylamine modified UiO-66-NH<sub>2</sub> catalyst was recycled five times without a loss of activity.

The free carboxylic acid groups of amino acids/peptides enable them to be coupled with UiO-66-NH<sub>2</sub>, resulting in covalent functionalisation of the MOFs with a number of substrates. *tert*-Butoxycarbamate (Boc) protected enantiopure amino acids/peptides were coupled with UiO-66-NH<sub>2</sub> using a microwave assisted coupling procedure to prevent racemisation.<sup>145</sup> The microwave assisted procedure results in higher yields of modification; during the coupling of UiO-66-NH<sub>2</sub> with L-proline <2% conversion was achieved using 96 hours of conventional heating at 37 °C, although 10% conversion was observed when coupled using microwave heating at 80 °C for 20 minutes. The coupling of dipeptides with UiO-66-NH<sub>2</sub> was also investigated, although essentially no conversion was observed, likely due to size-based restrictions. Importantly, PXRD analysis of UiO-66-NH-Pro (the PSM product after Boc deprotection) reveals that the MOF is able to withstand the chemical conditions encountered during the modification/deprotection, suggesting that better conversion may have been obtained if a Zr MOF bearing an amine group with larger pores was used.

UiO-66-NH<sub>2</sub> has been subjected to PSM with methacrylic anhydride, resulting in 67% conversion, evidenced from <sup>1</sup>H NMR spectra of HF digests of the MOF, which was also in good agreement with elemental analysis results.<sup>146</sup> The methacrylate functionality was then used in further transformations (Figure 1.21a), where the modified MOF nanoparticles were mixed with butyl methacrylate (BMA) and the photo initiator phenylbis(2,4,6-trimethylbenzoyl)phosphine oxide, and then irradiated with UV light for several minutes. This photoinduced postsynthetic polymerisation (PSP) process results in a square shaped polymer which can be peeled from the Teflon surface as a stand-alone membrane (Figure 1.21b).

CO<sub>2</sub> adsorption isotherms were used to prove the permanent porosity of the membrane, thus confirming that the MOF pores were not loaded with self-polymerised BMA (PBMA) polymer. The CO<sub>2</sub> uptake capacity of the PSP membrane was found to exceed that of a blend of PBMA/MOF (both containing 20% MOF), demonstrating the improved properties that the PSP membranes offer. Scanning electron microscopy (SEM) reveals that the initial modification with methacrylic anhydride is required, as the resulting membrane contains well-dispersed MOF nanoparticles. This was not true for a PSP membrane synthesised using

non-modified UiO-66-NH<sub>2</sub> that formed conglomerates on the polymer surface. The PSP derived membrane was also investigated for its ability to separate Cr<sup>IV</sup> ions from an aqueous solution, with a first cycle retention of 80% and a separation capacity of 8 mg/g, which was a dramatic improvement compared with the other materials investigated.

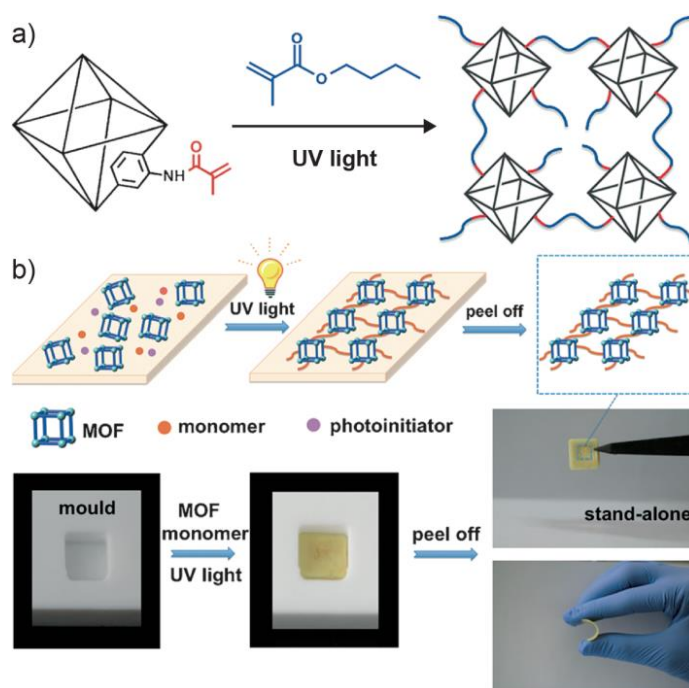


**Figure 1.21.** a) Postsynthetic polymerisation (PSP) of UiO-66-NH<sub>2</sub> functionalised with methacrylic anhydride. b) Representation of the PSP process used in the construction of stand-alone membranes, starting from UiO-66-NH<sub>2</sub>. Reproduced (modified) with permission from Ref.<sup>146</sup> Copyright (2015) Wiley-VCH.

The wealth of covalent transformations performed on UiO-66-NH<sub>2</sub> prompted investigations into the potential reactivity of other pendant groups with UiO-66-Br one of the first examples to be studied. UiO-66-Br was obtained by direct synthesis using 2-bromo-1,4-benzenedicarboxylate (Br-bdc) and then postsynthetic cyanation with CuCN in DMF produced UiO-66-CN, which the authors report to be difficult to obtain via direct synthesis.<sup>147</sup> The modification was explored via two synthetic routes, using either conventional or microwave heating, with microwave assisted cyanation resulting in conversion rates as high as 90%. These results suggest that aryl bromide substitution may be a route for incorporation of a range of functional groups that may be difficult to incorporate during direct synthesis.

Interpenetrated Zr MOFs have also been investigated as platforms for covalent PSM of pendant functionality.<sup>74</sup> One such MOF containing pendant furan moieties was functionalised by Diels-Alder cycloadditions with a variety of substrates (Figure 1.22a); reaction with maleimide, *N*-methylmaleimide or *N*-phenylmaleimide resulted in conversions of 98%, 99% and 89%, in turn, whilst modest *exo/endo* selectivities of 24%, 16% and 17% were observed.<sup>148</sup>

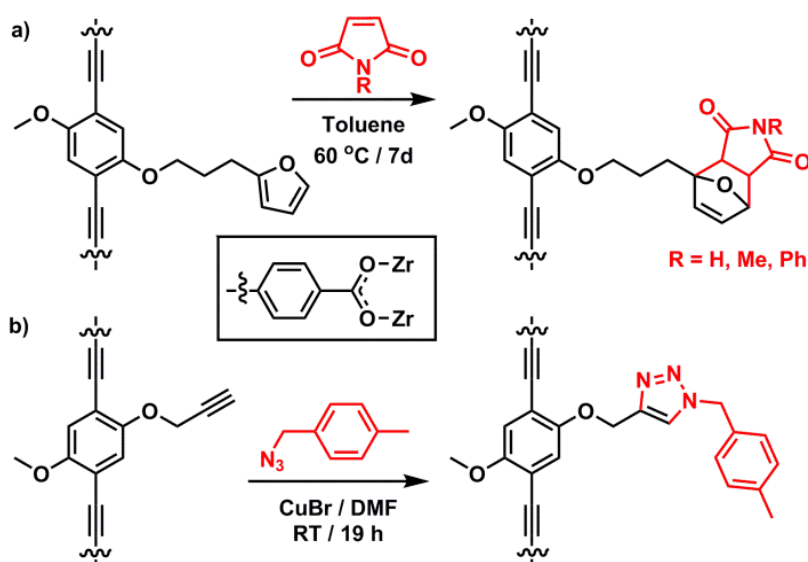


**Figure 1.22.** Schematic illustration of a) Diels-Alder cycloaddition, and b) Cu-catalysed azide-alkyne cycloaddition, both carried out postsynthetically on substituted interpenetrated Zr MOFs.

The authors also report the copper-catalysed azide-alkyne cycloaddition (CuAAC) of another member of the series bearing pendant propargyl moieties. The alkyne units were reacted with 4-methylbenzyl azide, using typical Cu<sup>I</sup>-catalysed conditions, resulting in 98% formation of the triazole product at room temperature (Figure 1.22b). This methodology can be viewed as an attractive route for the functionalisation of MOF pores under mild conditions, provided that the Cu<sup>I</sup> can be efficiently removed after modification. Pendant alkyne functionalities have also been incorporated within a UiO-68 analogue containing 2',5'-diethynyl-*p*-terphenyl-4,4''-dicarboxylate ligands.<sup>149</sup> The high porosity of the MOF enables the CuAAC reaction to proceed quantitatively with a number of substrates, namely azidoethane, azidoacetate and azidomethylbenzene, resulting in triazole functionalised MOFs with maintained porosity and crystallinity.

In a similar manner, other groups have focused on the synthesis of Zr MOFs containing pendant azide groups, which are likewise available for PSM by CuAAC. Zhou *et al.* reported the single crystal structures of a series of UiO-68 type MOFs containing terphenyl dicarboxylate ligands, bearing either two or four pendant methyl or azidomethyl functional groups on the central benzene ring.<sup>150</sup> By judiciously adjusting the molar ratios of the ligands in the synthetic mixture, mixed-ligand MOFs with azide loadings of 0, 25, 50, 75 and 100% were obtained. The MOFs containing various azide loadings were reacted with propargyl alcohol, as well as a variety of other alkyne substrates (Figure 1.23a). The introduction of nucleophilic hydroxyl groups results in improved CO<sub>2</sub>/N<sub>2</sub> selectivity performances when compared to the parent azide containing MOFs.

In another report, the UiO-68 type MOF containing two pendant azide groups was postsynthetically modified with a tetra-acetylene crosslinker under typical CuAAC conditions. The acetylene containing compound was observed to bridge the organic ligands of the MOF, resulting in the formation of a cross linked MOF whilst retaining crystallinity. The authors then selectively destroyed the metal coordination bonds within the cross linked MOF by reacting with hydrochloric acid. The resulting polymer gels were insoluble and retained the shape of the original crystals, hence the MOFs were able to act as a template towards polymer gels with predesigned architectures.<sup>151</sup>

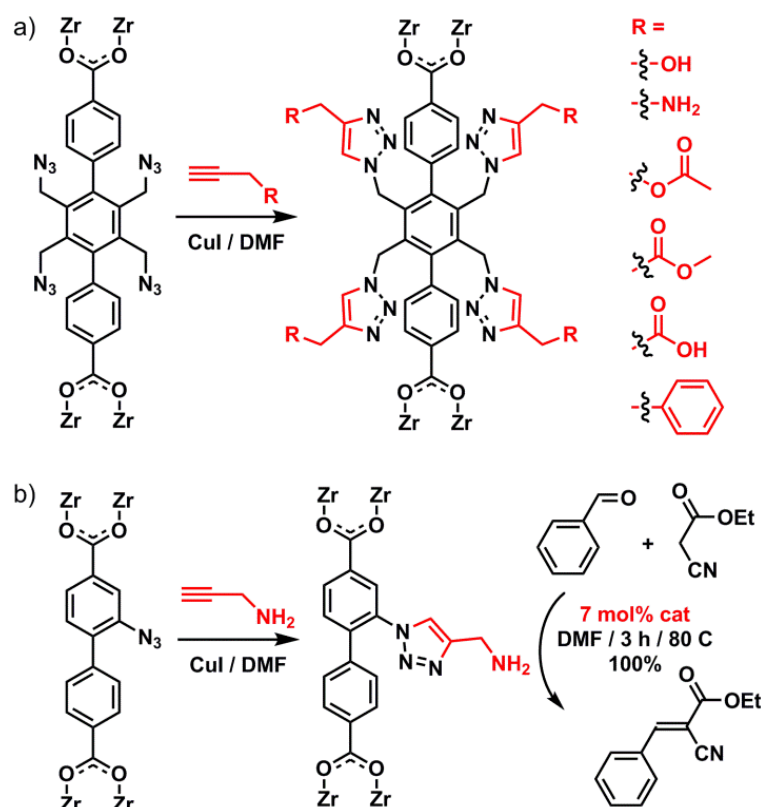


**Figure 1.23.** a) Tetra-azido containing Zr MOFs undergoing Cu-catalysed azide-alkyne cycloaddition with a variety of substrates. b) Functionalisation of UiO-67-N<sub>3</sub> with propargylamine to produce a catalyst for the Knoevenagel condensation between benzaldehyde and ethyl cyanoacetate.

UiO-67-N<sub>3</sub>, which contains 2-azidobiphenyl-4,4'-dicarboxylate, has been prepared, although the reaction temperature had to be reduced to 80 °C as conventional synthetic methods (140 °C) resulted in thermal cyclisation of the ligand to 9*H*-carbazole-2,7-dicarboxylate *in situ*.<sup>152</sup> This phenomenon also results in poor thermal stability of the MOF, as thermal cyclisation results in a bent ligand geometry that cannot be accommodated by the framework, resulting in collapse of the overall network structure. Low chemical stability was also observed, with crystallinity lost when the MOF was immersed in common organic solvents, however framework integrity was retained in DMF, allowing CuAAC reactions with alkyne substrates to be performed. Quantitative conversion was observed when the MOF was modified with methyl propiolate, 3-butyn-1-ol and propargylamine, and interestingly the modified products demonstrated improved chemical and thermal stabilities when compared with the parent framework. The pendant amine groups of the propargylamine modified framework were an efficient catalyst for the Knoevenagel condensation between benzaldehyde and ethyl

cyanoacetate (Figure 1.23b), with the MOF sufficiently stable to be reused for multiple catalytic cycles.

UiO-68-allyl, comprising 2',5'-bis(allyloxy)-*p*-terphenyl-4,4''-dicarboxylate ligands, was synthesised and subject to PSM by thiol-ene radical addition, through near quantitative reaction of the allyl moiety with ethanethiol under UV light in the presence of 2,2-dimethoxy-2-phenylacetophenone as a photoinitiator (Figure 1.24).<sup>153</sup> Thiol-ene and thiol-yne additions represent very useful routes to access functionalised MOFs, as they allow the mild insertion of a variety of functional groups across unsaturated double and triple bonds, although success thus far has been limited to pendant moieties.<sup>154</sup>

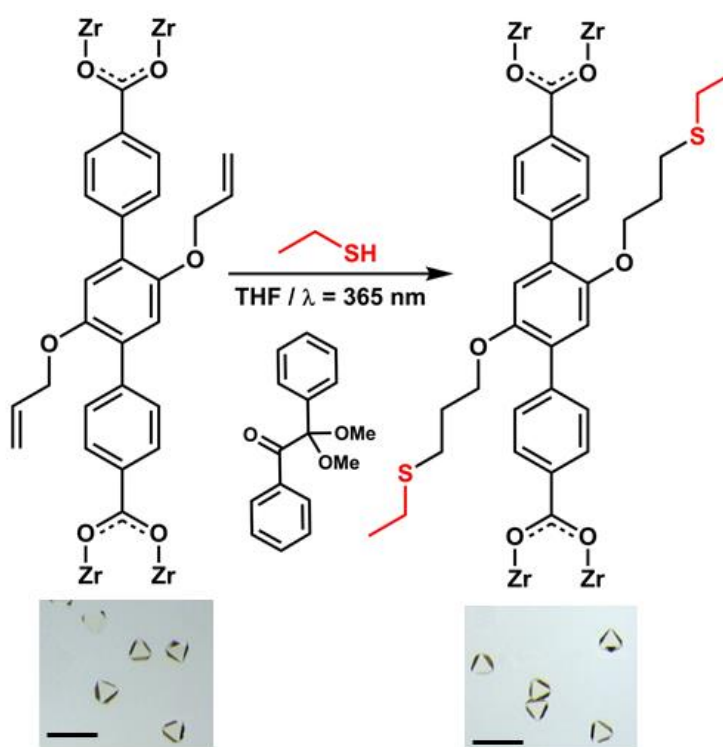


**Figure 1.24.** Schematic illustration of the thiol-ene radical addition of ethanethiol to UiO-68-allyl, with the single crystal images highlighting that the crystals remain intact during the transformation (scale bar = 200  $\mu\text{m}$ ). Reproduced (modified) with permission from Ref.<sup>153</sup> Copyright (2015) Elsevier.

MOFs bearing pendant carboxylic acid or sulfonic acid groups are of broad interest as they have been shown to result in improved characteristics including enhanced  $\text{CO}_2$  selectivity<sup>155,156</sup> and proton conductivity.<sup>157</sup> These additional acidic groups provide potential sites for attachment to metal ions, which in many cases disrupts direct MOF formation, and



so the introduction of acidic groups onto the backbone of the MOF has been investigated by a postsynthetic oxidation approach. To generate sulfonic acid moieties, UiO-66-(SH)<sub>2</sub> was synthesised directly from 1,4-dicarboxybenzene-2,5-dithiol, then the MOF was subjected to harsh chemical conditions: an aqueous 30% H<sub>2</sub>O<sub>2</sub> solution for oxidation of the thiol groups, followed by an acidic solution for protonation, resulting in quantitative conversion to UiO-66-(SO<sub>3</sub>H)<sub>2</sub> (Figure 1.25a).<sup>158</sup> The postsynthetic process was completed in as little as 90 minutes, resulting in quantitative conversion, while PXRD was used to prove the retention of crystallinity of the MOF. Introduction of the acidic sulfonic groups greatly improved the hydrophilicity of the MOF, which was beneficial for proton conduction. UiO-66-(SO<sub>3</sub>H)<sub>2</sub> demonstrated an excellent superprotonic conductivity of  $8.4 \times 10^{-2} \text{ S cm}^{-1}$  at 80 °C and 90% relative humidity, and an activation energy for proton transfer of 0.32 eV (Figure 1.25b). The proton conductivity of UiO-66-(SO<sub>3</sub>H)<sub>2</sub> is comparable to the performance of Nafion, a perfluorinated polymer membrane that is the most effective electrolyte known, and as such this material could potentially be incorporated into proton-exchange membrane fuel cells as an alternative energy technology.

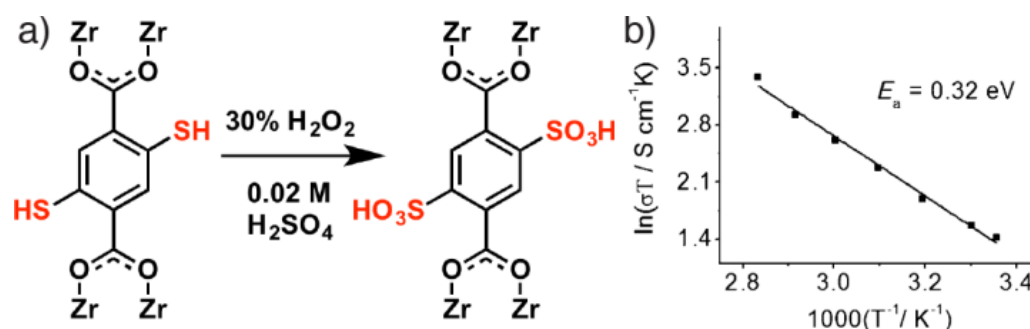


**Figure 1.25.** a) Schematic illustration of the postsynthetic oxidation of thiol units to form sulfonic acid groups. b) An Arrhenius plot of UiO-66-(SO<sub>3</sub>H)<sub>2</sub> at 90% relative humidity, revealing an activation of energy of 0.32 eV for proton conduction. Reproduced (modified) with permission from Ref.<sup>158</sup> Copyright (2015) Wiley-VCH.

Clet *et al.* were however, able to successfully synthesise UiO-66-(CO<sub>2</sub>H) and UiO-66-(CO<sub>2</sub>H)<sub>2</sub>, bearing one or two free carboxylic acid groups respectively within the pores, via a direct water-based synthetic route.<sup>159</sup> Interestingly it was found that heating the solids under vacuum results in formation of anhydride bridges between carboxylic acid groups on adjacent ligands, as evidenced by FT-IR and solid-state NMR spectroscopies. It was observed that samples containing increasing amounts of the anhydride bridges resulted in higher adsorption capacities for methane and carbon dioxide at 30 °C and 10 bar of the respective gas. Partial

reversibility of the anhydride bridges was also observed when the samples were in contact with water vapour.

Redox processes have also been observed to occur postsynthetically in a single-crystal to single-crystal (SCSC) manner in UiO-68-(OH)<sub>2</sub>, which contains 2',5'-dihydroxy-*p*-terphenyl-4,4''-dicarboxylate ligands.<sup>160</sup> The ligands within the MOF could be oxidised in the solid phase from the diol to the quinone form, resulting in altered spectroscopic properties (Figure 1.26). The transformation was fully reversible, and it was observed that the transformation occurs on the outmost surface of the crystals and gradually diffuses inwards. Interestingly, the MOF could not be directly synthesised with the quinone based ligand while incorporating these organic-based molecular switches into the solid phase may prove useful for applications such as memory storage or redox-based electronic devices.



**Figure 1.26.** Schematic illustration of the redox switching behaviour of UiO-68-(OH)<sub>2</sub> to the quinone form, which was unable to be synthesised directly (scale bar = 50 μm). Reproduced (modified) with permission from Ref.<sup>160</sup> Copyright (2015) American Chemical Society.

There has clearly been a significant drive to study the postsynthetic modification of pendant functionalities within Zr MOFs in a similar manner to earlier efforts focusing on the modification of other transition metal containing MOFs. The enhanced chemical and mechanical stabilities of Zr MOFs are advantageous, as the MOFs are tolerant of a wealth of harsh chemical conditions, meaning that facile access to the specialised modified materials facilitates their utilisation into desired applications.

### 1.5.2 Integral Postsynthetic Modification of Zr MOFs

There are considerably fewer examples of postsynthetic modification of MOFs at integral linker sites rather than on pendant functional groups, likely as a consequence of the generally low reactivity of the largely structural components. The chemical stability of Zr MOFs means they can tolerate harsh reaction conditions, facilitating reactions directly on unfunctionalised aromatic rings. Bradshaw *et al.* showed that UiO-66 was stable in the presence of hydroxyl radicals in water to selectively form UiO-66-OH by PSM with no loss of crystallinity.<sup>161</sup> The  $\cdot\text{OH}$  radicals can be generated by UV-A irradiation of the superparamagnetic photocatalytic composite material  $\gamma\text{-Fe}_2\text{O}_3@\text{SiO}_2@\text{TiO}_2$  or UV-C irradiation of aqueous  $\text{H}_2\text{O}_2$  solutions, with the former method resulting in a higher hydroxylation yield (77% vs 41% conversion, Figure 1.27). Introduction of free hydroxyl units to MOFs by PSM is valuable as they routinely disrupt direct synthesis by coordinating to the metals.

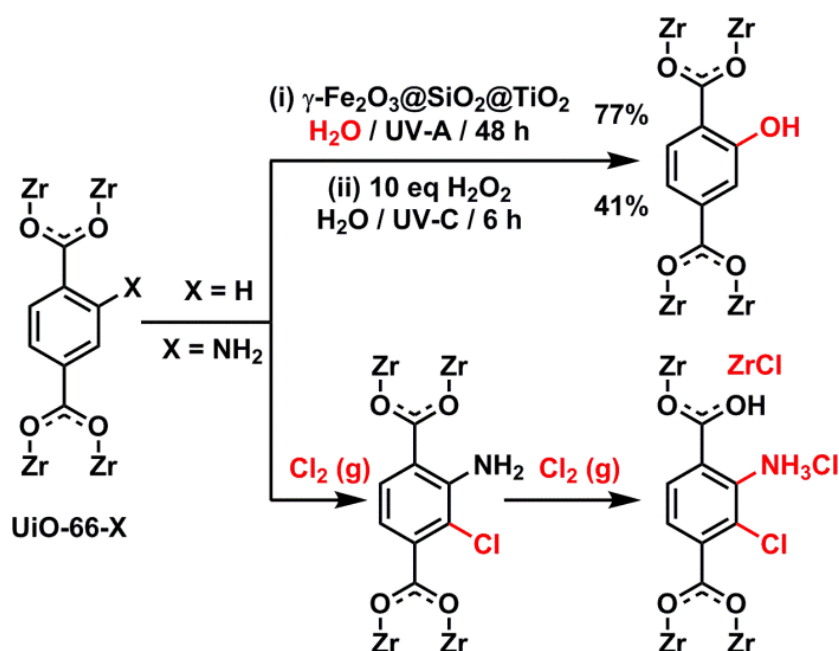


**Figure 1.27.** Conditions for postsynthetic hydroxylation and chlorination directly on the aromatic rings of UiO-66 and UiO-66-NH<sub>2</sub> respectively. Exposure of UiO-66-NH<sub>2</sub> to excess chlorine gas eventually results in its decomposition.

Similar chemical stability of UiO-66 in the presence of Cl<sub>2</sub> gas was demonstrated by DeCoste and Peterson, who showed that UiO-66-NH<sub>2</sub> underwent electrophilic aromatic substitution in the presence of chlorine to form UiO-66-NH<sub>2</sub>-Cl.<sup>162</sup> Further exposure to Cl<sub>2</sub> resulted in eventual degradation of the MOF and pore collapse (Figure 1.27), but UiO-66-NH<sub>2</sub> exhibits a Cl<sub>2</sub> storage capacity of 124% w/w, and is a candidate material for air purification.

It is also possible to carry out reactions at heteroatoms in ligand ring systems. Chen and Qian prepared the MOF known both as UiO-67(bipy) and MOF-867 – [Zr<sub>6</sub>O<sub>4</sub>(OH)<sub>4</sub>(bpydc)<sub>6</sub>]<sub>n</sub> where bpydc = 2,2'-bipyridine-5,5'-dicarboxylate – and methylated the nitrogen atoms of the bpydc linker with methyl triflate in 70% yield. The generation of cationic pyridinium sites (the charges are balanced by nitrate counterions introduced during washing) means the material is highly efficient for the removal of pollutant dichromate anions (Cr<sub>2</sub>O<sub>7</sub><sup>2-</sup>) from aqueous solution.<sup>163</sup>

There are considerably fewer reports of integral postsynthetic modifications of Zr MOFs compared with the large number of covalent transformations that have been investigated on pendant functionality. Zr MOFs can be viewed as ideal platforms for investigating the

reactivity of integral sites due to their high mechanical<sup>95</sup> and chemical stabilities.<sup>136</sup> As an alternative approach to incorporate integral reactive sites, we have designed a series of carboxylate based ligands bearing either alkene, alkyne or butadiyne units. The unsaturated integral sites offer opportunities for further reactivity, with bromination, bromohydration and iodination investigated and the transformations are characterised in detail in Chapter 3.

## 1.6 References

- (1) Férey, G. *Chem. Soc. Rev.* **2008**, 37, 191.
- (2) Long, J. R.; Yaghi, O. M. *Chem. Soc. Rev.* **2009**, 38, 1213.
- (3) Zhou, H.-C.; Long, J. R.; Yaghi, O. M. *Chem. Rev.* **2012**, 112, 673.
- (4) Kondo, M.; Yoshitomi, T.; Matsuzaka, H.; Kitagawa, S.; Seki, K. *Angew. Chem. Int. Ed.* **1997**, 36, 1725.
- (5) Yaghi, O. M.; Li, H. *J. Am. Chem. Soc.* **1995**, 117, 10401.
- (6) Kitagawa, S.; Kitaura, R.; Noro, S.-i. *Angew. Chem. Int. Ed.* **2004**, 43, 2334.
- (7) Kesanli, B.; Lin, W. *Coord. Chem. Rev.* **2003**, 246, 305.
- (8) Lin, X.; Telepeni, I.; Blake, A. J.; Dailly, A.; Brown, C. M.; Simmons, J. M.; Zoppi, M.; Walker, G. S.; Thomas, K. M.; Mays, T. J.; Hubberstey, P.; Champness, N. R.; Schröder, M. *J. Am. Chem. Soc.* **2009**, 131, 2159.
- (9) Serre, C.; Millange, F.; Thouvenot, C.; Noguès, M.; Marsolier, G.; Louër, D.; Férey, G. *J. Am. Chem. Soc.* **2002**, 124, 13519.
- (10) Cavka, J. H.; Jakobsen, S.; Olsbye, U.; Guillou, N.; Lamberti, C.; Bordiga, S.; Lillerud, K. P. *J. Am. Chem. Soc.* **2008**, 130, 13850.
- (11) Batten, S. R.; Champness, N. R.; Chen, X.-M.; Garcia-Martinez, J.; Kitagawa, S.; Ohrstrom, L.; O'Keeffe, M.; Suh, M. P.; Reedijk, J. *CrystEngComm* **2012**, 14, 3001.
- (12) Li, H.; Eddaoudi, M.; O'Keeffe, M.; Yaghi, O. M. *Nature* **1999**, 402, 276.
- (13) Yaghi, O. M.; O'Keeffe, M.; Ockwig, N. W.; Chae, H. K.; Eddaoudi, M.; Kim, J. *Nature* **2003**, 423, 705.
- (14) Thomas, K. M. *Dalton Trans.* **2009**, 1487.
- (15) Rowsell, J. L. C.; Yaghi, O. M. *J. Am. Chem. Soc.* **2006**, 128, 1304.
- (16) Jiang, H.-L.; Makal, T. A.; Zhou, H.-C. *Coord. Chem. Rev.* **2013**, 257, 2232.
- (17) Yang, S.; Lin, X.; Lewis, W.; Suyetin, M.; Bichoutskaia, E.; Parker, J. E.; Tang, C. C.; Allan, D. R.; Rizkallah, P. J.; Hubberstey, P.; Champness, N. R.; Mark Thomas, K.; Blake, A. J.; Schröder, M. *Nat. Mater.* **2012**, 11, 710.
- (18) Eddaoudi, M.; Kim, J.; Rosi, N.; Vodak, D.; Wachter, J.; O'Keeffe, M.; Yaghi, O. M. *Science* **2002**, 295, 469.
- (19) Ma, S.; Sun, D.; Ambrogio, M.; Fillinger, J. A.; Parkin, S.; Zhou, H.-C. *J. Am. Chem. Soc.* **2007**, 129, 1858.

- (20) Ferguson, A.; Liu, L.; Tapperwijn, S. J.; Perl, D.; Coudert, F.-X.; Van Cleuvenbergen, S.; Verbiest, T.; van der Veen, M. A.; Telfer, S. G. *Nat. Chem.* **2016**, *8*, 250.
- (21) Go, Y. B.; Wang, X.; Jacobson, A. J. *Inorg. Chem.* **2007**, *46*, 6594.
- (22) Farha, O. K.; Malliakas, C. D.; Kanatzidis, M. G.; Hupp, J. T. *J. Am. Chem. Soc.* **2010**, *132*, 950.
- (23) Yao, Q.; Su, J.; Cheung, O.; Liu, Q.; Hedin, N.; Zou, X. *J. Mater. Chem.* **2012**, *22*, 10345.
- (24) Liu, J.; Thallapally, P. K.; McGrail, B. P.; Brown, D. R.; Liu, J. *Chem. Soc. Rev.* **2012**, *41*, 2308.
- (25) Chui, S. S.-Y.; Lo, S. M.-F.; Charmant, J. P. H.; Orpen, A. G.; Williams, I. D. *Science* **1999**, *283*, 1148.
- (26) Yakovenko, A. A.; Reibenspies, J. H.; Bhuvanesh, N.; Zhou, H.-C. *J. Appl. Crystallogr.* **2013**, *46*, 346.
- (27) Gadzikwa, T.; Farha, O. K.; Mulfort, K. L.; Hupp, J. T.; Nguyen, S. T. *Chem. Commun.* **2009**, 3720.
- (28) Maniam, P.; Stock, N. *Inorg. Chem.* **2011**, *50*, 5085.
- (29) Dybtsev, D. N.; Chun, H.; Kim, K. *Angew. Chem. Int. Ed.* **2004**, *43*, 5033.
- (30) Henke, S.; Schneemann, A.; Wütscher, A.; Fischer, R. A. *J. Am. Chem. Soc.* **2012**, *134*, 9464.
- (31) Dau, P. V.; Kim, M.; Garibay, S. J.; Münch, F. H. L.; Moore, C. E.; Cohen, S. M. *Inorg. Chem.* **2012**, *51*, 5671.
- (32) Deng, H.; Doonan, C. J.; Furukawa, H.; Ferreira, R. B.; Towne, J.; Knobler, C. B.; Wang, B.; Yaghi, O. M. *Science* **2010**, *327*, 846.
- (33) Karagiari, O.; Bury, W.; Mondloch, J. E.; Hupp, J. T.; Farha, O. K. *Angew. Chem. Int. Ed.* **2014**, *53*, 4530.
- (34) Kim, M.; Cahill, J. F.; Fei, H.; Prather, K. A.; Cohen, S. M. *J. Am. Chem. Soc.* **2012**, *134*, 18082.
- (35) Liu, L.; Telfer, S. G. *J. Am. Chem. Soc.* **2015**, *137*, 3901.
- (36) Mondloch, J. E.; Karagiari, O.; Farha, O. K.; Hupp, J. T. *CrystEngComm* **2013**, *15*, 9258.
- (37) Morris, R. E.; Wheatley, P. S. *Angew. Chem. Int. Ed.* **2008**, *47*, 4966.
- (38) Murray, L. J.; Dinca, M.; Long, J. R. *Chem. Soc. Rev.* **2009**, *38*, 1294.
- (39) Sumida, K.; Rogow, D. L.; Mason, J. A.; McDonald, T. M.; Bloch, E. D.; Herm, Z. R.; Bae, T.-H.; Long, J. R. *Chem. Rev.* **2012**, *112*, 724.

- (40) Li, J.-R.; Kuppler, R. J.; Zhou, H.-C. *Chem. Soc. Rev.* **2009**, 38, 1477.
- (41) Lee, J.; Farha, O. K.; Roberts, J.; Scheidt, K. A.; Nguyen, S. T.; Hupp, J. T. *Chem. Soc. Rev.* **2009**, 38, 1450.
- (42) Farrusseng, D.; Aguado, S.; Pinel, C. *Angew. Chem. Int. Ed.* **2009**, 48, 7502.
- (43) Ma, L.; Abney, C.; Lin, W. *Chem. Soc. Rev.* **2009**, 38, 1248.
- (44) Gascon, J.; Corma, A.; Kapteijn, F.; Llabrés i Xamena, F. X. *ACS Catal.* **2014**, 4, 361.
- (45) Horcajada, P.; Chalati, T.; Serre, C.; Gillet, B.; Sebrie, C.; Baati, T.; Eubank, J. F.; Heurtaux, D.; Clayette, P.; Kreuz, C.; Chang, J.-S.; Hwang, Y. K.; Marsaud, V.; Bories, P.-N.; Cynober, L.; Gil, S.; Férey, G.; Couvreur, P.; Gref, R. *Nat. Mater.* **2010**, 9, 172.
- (46) Huxford, R. C.; Della Rocca, J.; Lin, W. *Curr. Opin. Chem. Biol.* **2010**, 14, 262.
- (47) McKinlay, A. C.; Morris, R. E.; Horcajada, P.; Férey, G.; Gref, R.; Couvreur, P.; Serre, C. *Angew. Chem. Int. Ed.* **2010**, 49, 6260.
- (48) Walton, K. S.; Snurr, R. Q. *J. Am. Chem. Soc.* **2007**, 129, 8552.
- (49) Suh, M. P.; Park, H. J.; Prasad, T. K.; Lim, D.-W. *Chem. Rev.* **2012**, 112, 782.
- (50) He, Y.; Zhou, W.; Qian, G.; Chen, B. *Chem. Soc. Rev.* **2014**, 43, 5657.
- (51) Britt, D.; Furukawa, H.; Wang, B.; Glover, T. G.; Yaghi, O. M. *Proc. Natl. Acad. Sci. USA* **2009**, 106, 20637.
- (52) Kong, X.; Scott, E.; Ding, W.; Mason, J. A.; Long, J. R.; Reimer, J. A. *J. Am. Chem. Soc.* **2012**, 134, 14341.
- (53) Dietzel, P. D. C.; Johnsen, R. E.; Blom, R.; Fjellvåg, H. *Chem. Eur. J.* **2008**, 14, 2389.
- (54) Kapelewski, M. T.; Geier, S. J.; Hudson, M. R.; Stück, D.; Mason, J. A.; Nelson, J. N.; Xiao, D. J.; Hulvey, Z.; Gilmour, E.; FitzGerald, S. A.; Head-Gordon, M.; Brown, C. M.; Long, J. R. *J. Am. Chem. Soc.* **2014**, 136, 12119.
- (55) Ma, L.; Lin, W. In *Functional Metal-Organic Frameworks: Gas Storage, Separation and Catalysis*; Schröder, M., Ed.; Springer Berlin Heidelberg: Berlin, Heidelberg, 2010, p 175.
- (56) Liu, J.; Chen, L.; Cui, H.; Zhang, J.; Zhang, L.; Su, C.-Y. *Chem. Soc. Rev.* **2014**, 43, 6011.
- (57) Chughtai, A. H.; Ahmad, N.; Younus, H. A.; Laypkov, A.; Verpoort, F. *Chem. Soc. Rev.* **2015**, 44, 6804.
- (58) Fujita, M.; Kwon, Y. J.; Washizu, S.; Ogura, K. *J. Am. Chem. Soc.* **1994**, 116, 1151.



- (59) Hasegawa, S.; Horike, S.; Matsuda, R.; Furukawa, S.; Mochizuki, K.; Kinoshita, Y.; Kitagawa, S. *J. Am. Chem. Soc.* **2007**, *129*, 2607.
- (60) Yoon, M.; Srirambalaji, R.; Kim, K. *Chem. Rev.* **2012**, *112*, 1196.
- (61) Bradshaw, D.; Prior, T. J.; Cussen, E. J.; Claridge, J. B.; Rosseinsky, M. J. *J. Am. Chem. Soc.* **2004**, *126*, 6106.
- (62) Lin, Z.; Slawin, A. M. Z.; Morris, R. E. *J. Am. Chem. Soc.* **2007**, *129*, 4880.
- (63) Seo, J. S.; Whang, D.; Lee, H.; Jun, S. I.; Oh, J.; Jeon, Y. J.; Kim, K. *Nature* **2000**, *404*, 982.
- (64) Wu, C.-D.; Hu, A.; Zhang, L.; Lin, W. *J. Am. Chem. Soc.* **2005**, *127*, 8940.
- (65) Tamames-Tabar, C.; Cunha, D.; Imbuluzqueta, E.; Ragon, F.; Serre, C.; Blanco-Prieto, M. J.; Horcajada, P. *J. Mater. Chem. B* **2014**, *2*, 262.
- (66) Low, J. J.; Benin, A. I.; Jakubczak, P.; Abrahamian, J. F.; Faheem, S. A.; Willis, R. R. *J. Am. Chem. Soc.* **2009**, *131*, 15834.
- (67) Horcajada, P.; Serre, C.; Vallet-Regí, M.; Sebban, M.; Taulelle, F.; Férey, G. *Angew. Chem. Int. Ed.* **2006**, *45*, 5974.
- (68) Horcajada, P.; Serre, C.; Maurin, G.; Ramsahye, N. A.; Balas, F.; Vallet-Regí, M.; Sebban, M.; Taulelle, F.; Férey, G. *J. Am. Chem. Soc.* **2008**, *130*, 6774.
- (69) Taylor-Pashow, K. M. L.; Rocca, J. D.; Xie, Z.; Tran, S.; Lin, W. *J. Am. Chem. Soc.* **2009**, *131*, 14261.
- (70) Bai, Y.; Dou, Y.; Xie, L.-H.; Rutledge, W.; Li, J.-R.; Zhou, H.-C. *Chem. Soc. Rev.* **2016**, *45*, 2327.
- (71) Hobday, C. L.; Marshall, R. J.; Murphie, C. F.; Sotelo, J.; Richards, T.; Allan, D. R.; Düren, T.; Coudert, F.-X.; Forgan, R. S.; Morrison, C. A.; Moggach, S. A.; Bennett, T. D. *Angew. Chem. Int. Ed.* **2016**, *55*, 2401.
- (72) Hu, Z.; Zhao, D. *Dalton Trans.* **2015**, *44*, 19018.
- (73) Guillerm, V.; Ragon, F.; Dan-Hardi, M.; Devic, T.; Vishnuvarthan, M.; Campo, B.; Vimont, A.; Clet, G.; Yang, Q.; Maurin, G.; Férey, G.; Vittadini, A.; Gross, S.; Serre, C. *Angew. Chem. Int. Ed.* **2012**, *51*, 9267.
- (74) Schaate, A.; Roy, P.; Preuße, T.; Lohmeier, S. J.; Godt, A.; Behrens, P. *Chem. Eur. J.* **2011**, *17*, 9320.
- (75) Chen, D.; Xing, H.; Wang, C.; Su, Z. *J. Mater. Chem. A* **2016**, *4*, 2657.
- (76) Doan, T. L. H.; Nguyen, H. L.; Pham, H. Q.; Pham-Tran, N.-N.; Le, T. N.; Cordova, K. E. *Chem. Asian J.* **2015**, *10*, 2660.

- (77) Babarao, R.; Rubio-Martinez, M.; Hill, M. R.; Thornton, A. W. *J. Phys. Chem. C* **2016**, *120*, 13013.
- (78) Marshall, R. J.; Griffin, S. L.; Wilson, C.; Forgan, R. S. *Chem. Eur. J.* **2016**, *22*, 4870.
- (79) Lippke, J.; Brosent, B.; von Zons, T.; Virmani, E.; Lilienthal, S.; Preuße, T.; Hülsmann, M.; Schneider, A. M.; Wuttke, S.; Behrens, P.; Godt, A. *Inorg. Chem.* **2016**.
- (80) Ma, J.; Wong-Foy, A. G.; Matzger, A. J. *Inorg. Chem.* **2015**, *54*, 4591.
- (81) Wang, R.; Wang, Z.; Xu, Y.; Dai, F.; Zhang, L.; Sun, D. *Inorg. Chem.* **2014**, *53*, 7086.
- (82) Furukawa, H.; Gándara, F.; Zhang, Y.-B.; Jiang, J.; Queen, W. L.; Hudson, M. R.; Yaghi, O. M. *J. Am. Chem. Soc.* **2014**, *136*, 4369.
- (83) Liang, W.; Chevreau, H.; Ragon, F.; Southon, P. D.; Peterson, V. K.; D'Alessandro, D. M. *CrystEngComm* **2014**, *16*, 6530.
- (84) Feng, D.; Gu, Z.-Y.; Li, J.-R.; Jiang, H.-L.; Wei, Z.; Zhou, H.-C. *Angew. Chem. Int. Ed.* **2012**, *51*, 10307.
- (85) Morris, W.; Voloskiy, B.; Demir, S.; Gándara, F.; McGrier, P. L.; Furukawa, H.; Cascio, D.; Stoddart, J. F.; Yaghi, O. M. *Inorg. Chem.* **2012**, *51*, 6443.
- (86) Feng, D.; Jiang, H.-L.; Chen, Y.-P.; Gu, Z.-Y.; Wei, Z.; Zhou, H.-C. *Inorg. Chem.* **2013**, *52*, 12661.
- (87) Mondloch, J. E.; Bury, W.; Fairen-Jimenez, D.; Kwon, S.; DeMarco, E. J.; Weston, M. H.; Sarjeant, A. A.; Nguyen, S. T.; Stair, P. C.; Snurr, R. Q.; Farha, O. K.; Hupp, J. T. *J. Am. Chem. Soc.* **2013**, *135*, 10294.
- (88) Deria, P.; Mondloch, J. E.; Tylianakis, E.; Ghosh, P.; Bury, W.; Snurr, R. Q.; Hupp, J. T.; Farha, O. K. *J. Am. Chem. Soc.* **2013**, *135*, 16801.
- (89) Deria, P.; Chung, Y. G.; Snurr, R. Q.; Hupp, J. T.; Farha, O. K. *Chem. Sci.* **2015**, *6*, 5172.
- (90) Li, Z.; Schweitzer, N. M.; League, A. B.; Bernales, V.; Peters, A. W.; Getsoian, A. B.; Wang, T. C.; Miller, J. T.; Vjunov, A.; Fulton, J. L.; Lercher, J. A.; Cramer, C. J.; Gagliardi, L.; Hupp, J. T.; Farha, O. K. *J. Am. Chem. Soc.* **2016**, *138*, 1977.
- (91) Zhang, Q.; Su, J.; Feng, D.; Wei, Z.; Zou, X.; Zhou, H.-C. *J. Am. Chem. Soc.* **2015**, *137*, 10064.
- (92) Mouchaham, G.; Cooper, L.; Guillou, N.; Martineau, C.; Elkaïm, E.; Bourrelly, S.; Llewellyn, P. L.; Allain, C.; Clavier, G.; Serre, C.; Devic, T. *Angew. Chem. Int. Ed.* **2015**, *54*, 13297.

- (93) Gao, C.; Ai, J.; Tian, H.-R.; Wu, D.; Sun, Z.-M. *Chem. Commun.* **2016**.
- (94) Shearer, G. C.; Chavan, S.; Ethiraj, J.; Vitillo, J. G.; Svelle, S.; Olsbye, U.; Lamberti, C.; Bordiga, S.; Lillerud, K. P. *Chem. Mater.* **2014**, 26, 4068.
- (95) Wu, H.; Yildirim, T.; Zhou, W. *J. Phys. Chem. Lett.* **2013**, 4, 925.
- (96) Yot, P. G.; Yang, K.; Ragon, F.; Dmitriev, V.; Devic, T.; Horcajada, P.; Serre, C.; Maurin, G. *Dalton Trans.* **2016**, 45, 4283.
- (97) Rogge, S. M. J.; Wieme, J.; Vanduyfhuys, L.; Vandenbrande, S.; Maurin, G.; Verstraelen, T.; Waroquier, M.; Van Speybroeck, V. *Chem. Mater.* **2016**, 28, 5721.
- (98) deKrafft, K. E.; Boyle, W. S.; Burk, L. M.; Zhou, O. Z.; Lin, W. *J. Mater. Chem.* **2012**, 22, 18139.
- (99) Jakobsen, S.; Gianolio, D.; Wragg, D. S.; Nilsen, M. H.; Emerich, H.; Bordiga, S.; Lamberti, C.; Olsbye, U.; Tilset, M.; Lillerud, K. P. *Phys. Rev. B* **2012**, 86, 125429.
- (100) Falaise, C.; Charles, J.-S.; Volkringer, C.; Loiseau, T. *Inorg. Chem.* **2015**, 54, 2235.
- (101) Falaise, C.; Volkringer, C.; Vigier, J.-F.; Henry, N.; Beaurain, A.; Loiseau, T. *Chem. Eur. J.* **2013**, 19, 5324.
- (102) Lammert, M.; Wharmby, M. T.; Smolders, S.; Bueken, B.; Lieb, A.; Lomachenko, K. A.; Vos, D. D.; Stock, N. *Chem. Commun.* **2015**, 51, 12578.
- (103) Xue, D.-X.; Belmabkhout, Y.; Shekhah, O.; Jiang, H.; Adil, K.; Cairns, A. J.; Eddaoudi, M. *J. Am. Chem. Soc.* **2015**, 137, 5034.
- (104) Zheng, J.; Wu, M.; Jiang, F.; Su, W.; Hong, M. *Chem. Sci.* **2015**, 6, 3466.
- (105) Hermes, S.; Witte, T.; Hikov, T.; Zacher, D.; Bahnmüller, S.; Langstein, G.; Huber, K.; Fischer, R. A. *J. Am. Chem. Soc.* **2007**, 129, 5324.
- (106) Cho, W.; Lee, H. J.; Oh, M. *J. Am. Chem. Soc.* **2008**, 130, 16943.
- (107) Tsuruoka, T.; Furukawa, S.; Takashima, Y.; Yoshida, K.; Isoda, S.; Kitagawa, S. *Angew. Chem. Int. Ed.* **2009**, 48, 4739.
- (108) McGuire, C. V.; Forgan, R. S. *Chem. Commun.* **2015**, 51, 5199.
- (109) Schaate, A.; Roy, P.; Godt, A.; Lippke, J.; Waltz, F.; Wiebcke, M.; Behrens, P. *Chem. Eur. J.* **2011**, 17, 6643.
- (110) Zahn, G.; Zerner, P.; Lippke, J.; Kempf, F. L.; Lilienthal, S.; Schroder, C. A.; Schneider, A. M.; Behrens, P. *CrystEngComm* **2014**, 16, 9198.
- (111) Guillermin, V.; Gross, S.; Serre, C.; Devic, T.; Bauer, M.; Ferey, G. *Chem. Commun.* **2010**, 46, 767.
- (112) Øien, S.; Wragg, D.; Reinsch, H.; Svelle, S.; Bordiga, S.; Lamberti, C.; Lillerud, K. P. *Cryst. Growth Des.* **2014**, 14, 5370.

- (113) Wißmann, G.; Schaate, A.; Lilienthal, S.; Bremer, I.; Schneider, A. M.; Behrens, P. *Micropor. Mesopor. Mater.* **2012**, *152*, 64.
- (114) Schaate, A.; Dühnen, S.; Platz, G.; Lilienthal, S.; Schneider, A. M.; Behrens, P. *Eur. J. Inorg. Chem.* **2012**, *2012*, 790.
- (115) Katz, M. J.; Brown, Z. J.; Colon, Y. J.; Siu, P. W.; Scheidt, K. A.; Snurr, R. Q.; Hupp, J. T.; Farha, O. K. *Chem. Commun.* **2013**, *49*, 9449.
- (116) Trickett, C. A.; Gagnon, K. J.; Lee, S.; Gándara, F.; Bürgi, H.-B.; Yaghi, O. M. *Angew. Chem. Int. Ed.* **2015**, *54*, 11162.
- (117) Han, Y.; Liu, M.; Li, K.; Zuo, Y.; Wei, Y.; Xu, S.; Zhang, G.; Song, C.; Zhang, Z.; Guo, X. *CrystEngComm* **2015**, *17*, 6434.
- (118) Vermoortele, F.; Bueken, B.; Le Bars, G.; Van de Voorde, B.; Vandichel, M.; Houthoofd, K.; Vimont, A.; Daturi, M.; Waroquier, M.; Van Speybroeck, V.; Kirschhock, C.; De Vos, D. E. *J. Am. Chem. Soc.* **2013**, *135*, 11465.
- (119) Marshall, R. J.; Hobday, C. L.; Murphie, C. F.; Griffin, S. L.; Morrison, C. A.; Moggach, S. A.; Forgan, R. S. *J. Mater. Chem. A* **2016**, *4*, 6955.
- (120) Gutov, O. V.; Molina, S.; Escudero-Adán, E. C.; Shafir, A. *Chem. Eur. J.* **2016**, *22*, 13582.
- (121) Gutov, O. V.; Hevia, M. G.; Escudero-Adán, E. C.; Shafir, A. *Inorg. Chem.* **2015**, *54*, 8396.
- (122) Fang, Z.; Bueken, B.; De Vos, D. E.; Fischer, R. A. *Angew. Chem. Int. Ed.* **2015**, *54*, 7234.
- (123) Wu, H.; Chua, Y. S.; Krungleviciute, V.; Tyagi, M.; Chen, P.; Yildirim, T.; Zhou, W. *J. Am. Chem. Soc.* **2013**, *135*, 10525.
- (124) Shearer, G. C.; Chavan, S.; Bordiga, S.; Svelle, S.; Olsbye, U.; Lillerud, K. P. *Chem. Mater.* **2016**, *28*, 3749.
- (125) Van de Voorde, B.; Stassen, I.; Bueken, B.; Vermoortele, F.; De Vos, D.; Ameloot, R.; Tan, J.-C.; Bennett, T. D. *J. Mater. Chem. A* **2015**, *3*, 1737.
- (126) Stock, N.; Biswas, S. *Chem. Rev.* **2012**, *112*, 933.
- (127) Wang, Z.; Cohen, S. M. *Chem. Soc. Rev.* **2009**, *38*, 1315.
- (128) Cohen, S. M. *Chem. Sci.* **2010**, *1*, 32.
- (129) Tanabe, K. K.; Cohen, S. M. *Chem. Soc. Rev.* **2011**, *40*, 498.
- (130) Deria, P.; Mondloch, J. E.; Karagiari, O.; Bury, W.; Hupp, J. T.; Farha, O. K. *Chem. Soc. Rev.* **2014**, *43*, 5896.
- (131) Brozek, C. K.; Dinca, M. *Chem. Soc. Rev.* **2014**, *43*, 5456.

- (132) Evans, J. D.; Sumbly, C. J.; Doonan, C. J. *Chem. Soc. Rev.* **2014**, 43, 5933.
- (133) Cohen, S. M. *Chem. Rev.* **2012**, 112, 970.
- (134) Kandiah, M.; Nilsen, M. H.; Usseglio, S.; Jakobsen, S.; Olsbye, U.; Tilset, M.; Larabi, C.; Quadrelli, E. A.; Bonino, F.; Lillerud, K. P. *Chem. Mater.* **2010**, 22, 6632.
- (135) Garibay, S. J.; Cohen, S. M. *Chem. Commun.* **2010**, 46, 7700.
- (136) DeCoste, J. B.; Peterson, G. W.; Jasuja, H.; Glover, T. G.; Huang, Y.-G.; Walton, K. S. *J. Mater. Chem. A* **2013**, 1, 5642.
- (137) Mondloch, J. E.; Katz, M. J.; Planas, N.; Semrouni, D.; Gagliardi, L.; Hupp, J. T.; Farha, O. K. *Chem. Commun.* **2014**, 50, 8944.
- (138) Yang, L.-M.; Ganz, E.; Svelle, S.; Tilset, M. *J. Mater. Chem. C* **2014**, 2, 7111.
- (139) Yuan, S.; Lu, W.; Chen, Y.-P.; Zhang, Q.; Liu, T.-F.; Feng, D.; Wang, X.; Qin, J.; Zhou, H.-C. *J. Am. Chem. Soc.* **2015**, 137, 3177.
- (140) Marshall, R. J.; Forgan, R. S. *Eur. J. Inorg. Chem.* **2016**, 2016, 4310.
- (141) Servalli, M.; Ranocchiari, M.; Van Bokhoven, J. A. *Chem. Commun.* **2012**, 48, 1904.
- (142) Hintz, H.; Wuttke, S. *Chem. Mater.* **2014**, 26, 6722.
- (143) Morris, W.; Doonan, C. J.; Yaghi, O. M. *Inorg. Chem.* **2011**, 50, 6853.
- (144) Luan, Y.; Qi, Y.; Gao, H.; Andriamitantsoa, R. S.; Zheng, N.; Wang, G. *J. Mater. Chem. A* **2015**, 3, 17320.
- (145) Bonnefoy, J.; Legrand, A.; Quadrelli, E. A.; Canivet, J.; Farrusseng, D. *J. Am. Chem. Soc.* **2015**, 137, 9409.
- (146) Zhang, Y.; Feng, X.; Li, H.; Chen, Y.; Zhao, J.; Wang, S.; Wang, L.; Wang, B. *Angew. Chem. Int. Ed.* **2015**, 54, 4259.
- (147) Kim, M.; Garibay, S. J.; Cohen, S. M. *Inorg. Chem.* **2011**, 50, 729.
- (148) Roy, P.; Schaate, A.; Behrens, P.; Godt, A. *Chem. Eur. J.* **2012**, 18, 6979.
- (149) Li, B.; Gui, B.; Hu, G.; Yuan, D.; Wang, C. *Inorg. Chem.* **2015**, 54, 5139.
- (150) Jiang, H.-L.; Feng, D.; Liu, T.-F.; Li, J.-R.; Zhou, H.-C. *J. Am. Chem. Soc.* **2012**, 134, 14690.
- (151) Ishiwata, T.; Furukawa, Y.; Sugikawa, K.; Kokado, K.; Sada, K. *J. Am. Chem. Soc.* **2013**, 135, 5427.
- (152) Yi, X.-C.; Xi, F.-G.; Qi, Y.; Gao, E.-Q. *RSC Adv.* **2015**, 5, 893.
- (153) Gui, B.; Hu, G.; Zhou, T.; Wang, C. *J. Solid State Chem.* **2015**, 223, 79.
- (154) Hindelang, K.; Kronast, A.; Vagin, S. I.; Rieger, B. *Chem. Eur. J.* **2013**, 19, 8244.
- (155) Yang, Q.; Wiersum, A. D.; Llewellyn, P. L.; Guillerm, V.; Serre, C.; Maurin, G. *Chem. Commun.* **2011**, 47, 9603.

- (156) Torrisi, A.; Mellot-Draznieks, C.; Bell, R. G. *J. Chem. Phys.* **2010**, *132*, 044705.
- (157) Shigematsu, A.; Yamada, T.; Kitagawa, H. *J. Am. Chem. Soc.* **2011**, *133*, 2034.
- (158) Phang, W. J.; Jo, H.; Lee, W. R.; Song, J. H.; Yoo, K.; Kim, B.; Hong, C. S. *Angew. Chem. Int. Ed.* **2015**, *54*, 5142.
- (159) Ragon, F.; Campo, B.; Yang, Q.; Martineau, C.; Wiersum, A. D.; Lago, A.; Guillermin, V.; Hemsley, C.; Eubank, J. F.; Vishnuvarthan, M.; Taulelle, F.; Horcajada, P.; Vimont, A.; Llewellyn, P. L.; Daturi, M.; Devautour-Vinot, S.; Maurin, G.; Serre, C.; Devic, T.; Clet, G. *J. Mater. Chem. A* **2015**, *3*, 3294.
- (160) Gui, B.; Meng, X.; Chen, Y.; Tian, J.; Liu, G.; Shen, C.; Zeller, M.; Yuan, D.; Wang, C. *Chem. Mater.* **2015**, *27*, 6426.
- (161) Aguilera-Sigalat, J.; Fox-Charles, A.; Bradshaw, D. *Chem. Commun.* **2014**, *50*, 15453.
- (162) DeCoste, J. B.; Browe, M. A.; Wagner, G. W.; Rossin, J. A.; Peterson, G. W. *Chem. Commun.* **2015**, *51*, 12474.
- (163) Zhang, Q.; Yu, J.; Cai, J.; Zhang, L.; Cui, Y.; Yang, Y.; Chen, B.; Qian, G. *Chem. Commun.* **2015**, *51*, 14732.

## Chapter 2

# Amino Acid Modulation of Zr and Hf Metal-Organic Frameworks

**This Chapter is based upon the following publication:**

Amino Acids as Highly Efficient Modulators for Single Crystals of Zirconium and Hafnium Metal-Organic Frameworks

*J. Mater. Chem. A.*, **2016**, 4, 6955–6963.

**R. J. Marshall**, C. L. Hobday, C. F. Murphie, S. L. Griffin, C. A. Morrison, S. A. Moggach and R. S. Forgan

## Contents

<b>Chapter 2 .....</b>	<b>52</b>
<b>2.1 Introduction.....</b>	<b>54</b>
<b>2.2 Aims.....</b>	<b>56</b>
<b>2.3 Amino Acid Modulation .....</b>	<b>58</b>
<b>2.4 Bulk Synthesis of Zr and Hf MOFs Containing L5-L8.....</b>	<b>67</b>
<b>2.5 Microwave Assisted Synthesis of Zr-L6.....</b>	<b>72</b>
<b>2.6 Single Crystal Synthesis of Zr and Hf MOFs Containing L5-L8 .....</b>	<b>74</b>
<b>2.7 Design and Synthesis of Extended Ligands .....</b>	<b>77</b>
<b>2.8. Synthesis of Zr and Hf MOFs Containing L9-L11 .....</b>	<b>79</b>
<b>2.9 Conclusions and Future Work.....</b>	<b>85</b>
<b>2.10 Experimental .....</b>	<b>87</b>
2.10.1 General Experimental Remarks .....	87
2.10.2 Amino Acid Modulation of Zr MOFs Containing L1-L8 .....	88
2.10.3 Amino Acid Modulation of Hf MOFs Containing L1-L8.....	89
2.10.4 Zr-L6 and Hf-L6 L-Proline/HCl Modulator Comparison .....	89
2.10.5 Zr-L6 L-Proline Concentration Investigation .....	90
2.10.6 Bulk Synthesis of Zr and Hf MOFs Containing L5-L8 .....	90
2.10.7 Microwave Assisted Synthesis of Zr-L6.....	91
2.10.8 Single Crystal Synthesis of Zr-L6, Zr-L7, Zr-L8, Hf-L6 and Hf-L7 .....	91
2.10.9 Extended Ligand Synthesis.....	94
2.10.10 Bulk Synthesis Zr and Hf MOFs Containing L9-L11 .....	99
2.10.11 Single Crystal Synthesis of Zr and Hf MOFs Containing L9-L11 .....	100
<b>2.11 References .....</b>	<b>104</b>



## 2.1 Introduction

Increased interest in zirconium MOFs<sup>1-3</sup> in recent years is mostly attributable to their excellent chemical<sup>4-6</sup> and mechanical stabilities.<sup>7-9</sup> Their superior stabilities relative to other families of MOFs<sup>10</sup> has resulted in great efforts towards the synthesis of Zr MOFs containing specific functionality,<sup>11-13</sup> usually tailored towards certain technologies or applications.<sup>2,14</sup> The quest to advance Zr MOFs has resulted in materials containing diverse structural topologies<sup>15-21</sup> as well as a range of properties, however significant research has focused on understanding fundamental aspects of Zr MOFs, such as their synthesis which is often troublesome.<sup>22,23</sup>

The synthesis of phase pure, highly crystalline and defect free<sup>24</sup> Zr MOFs is routinely difficult, and this has been postulated to be due to fast crystallisation kinetics resulting from limited reversibility during synthesis. This is believed to be the result of strong interactions between the hard  $\text{Zr}^{4+}$  cations and the hard carboxylate oxygen atoms of the ligands. In 2011, Behrens *et al.* discovered that coordination modulation,<sup>25,26</sup> a term used to describe the deliberate addition of a known amount of a synthetic modulator to MOF synthetic mixtures, is able to drastically improve the crystallisation of Zr MOFs.<sup>27</sup> During the initial report, an excess of benzoic acid was used as the modulating agent and the potential of this technique was realised as it resulted in the first crystal structure of a Zr MOF (from single crystal X-ray diffraction), allowing greater structural resolution to be obtained.

Coordination modulation revolutionised Zr MOFs, such that synthetic modulators are now accepted to be a key component during synthesis. Unfortunately, it has been realised that benzoic acid is not a universal modulator, as it is able to enhance the crystallinity of some MOFs but not others, which to date cannot be predicted logically and is very much based upon trial and error. However, the scope of modulators has been extended and often other small monodentate organic molecules containing carboxylic acids, such as formic-,<sup>28</sup> acetic-<sup>29</sup> and trifluoroacetic acid<sup>30</sup> when added in large excesses (typically no less than 30 equivalents) to the synthetic mixture, are able to improve the crystallinity of Zr MOFs. It has also been found that hydrochloric acid<sup>23</sup> is able to modulate Zr MOFs, although this has been linked to the creation of defects.<sup>31-33</sup> Defects are thought to result from missing ligands or clusters,

creating materials with altered properties, and they may be advantageous depending on whether they are beneficial for the application being considered.<sup>34,35</sup>

## 2.2 Aims

The successful synthesis of Zr and Hf MOFs often relies on the addition of synthetic modulators, which often improve the materials physical properties and synthetic reproducibility. To expand the scope of synthetic modulators, seven amino acids are investigated as modulators for eight different Zr MOFs with ligands of varying length and chemical functionality (Figure 2.1). The modulating ability of the amino acids is evaluated by comparison with products obtained in the absence of a synthetic modulator. The analogous Hf MOFs are also investigated, as although they are less common than Zr MOFs they have been receiving increasing interest recently due to their very close similarities, in terms of both structures and properties, to Zr MOFs.<sup>36,37</sup>

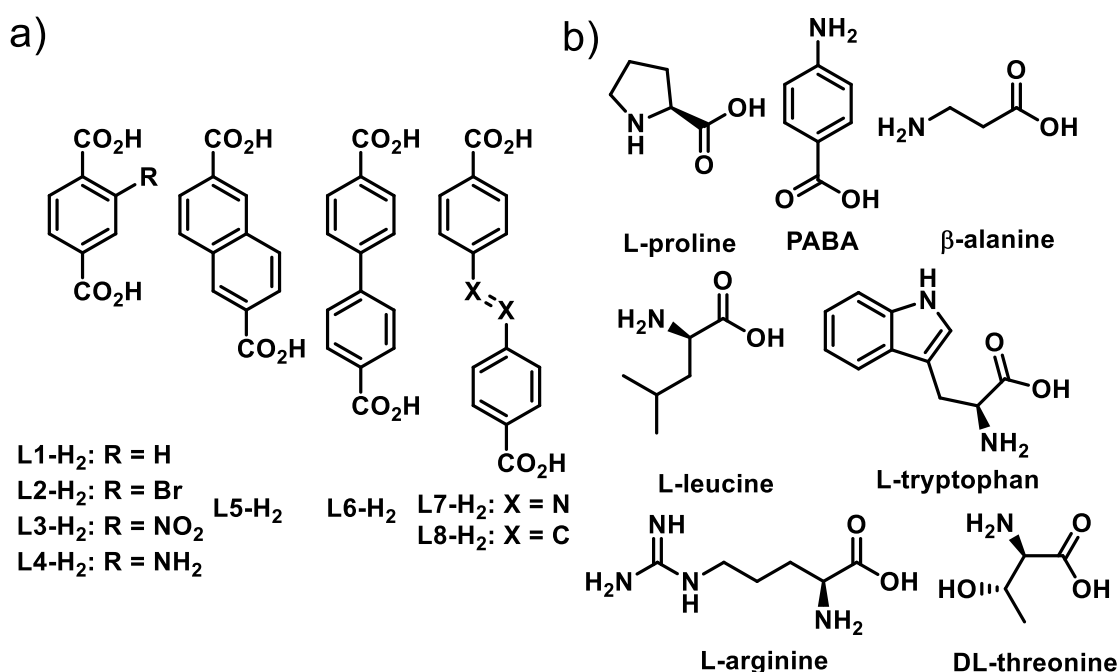


**Figure 2.1.** Schematic representation of a) the ligands and b) the amino acids used throughout the amino acid modulation studies (4-aminobenzoic acid is abbreviated to PABA).

The Zr and Hf MOFs investigated throughout this modulation study contain ligands that are commercially available (Figure 2.1a), allowing numerous reactions to be performed and for scale-up to be attempted without ligand quantities being problematic. Prior to this study, Zr MOFs containing L1-L7 had been reported as bulk microcrystalline powders only. A Zr MOF containing L8, which contains an integral *trans*-stilbene unit, should be feasible as it is

structurally very similar to L7 which contains an integral azo unit. The bidentate nature of the ligands results in Zr and Hf MOFs of the well-known UiO-66 (UiO stands for the University of Oslo) topology, containing 12-connected  $Zr_6$  or  $Hf_6$  clusters that form 3-dimensional porous frameworks with **fcu** topology and overall formula  $[M_6O_4(OH)_4L_6]_n$ . The ligands were chosen based on their ability to produce MOFs containing different chemical functionality and with different pore dimensions, to enable the true potential of amino acid modulation to be realised.

Likewise a broad range of amino acids were selected, and as they contain carboxylic acids they can be considered as potential modulating agents. Amino acids have been chosen as potential modulators because they are cheap, readily available biomolecules that contain a diverse range of pre-installed chemical functionality. The diverse side-chain functionality of amino acids results in a variety of physical properties, for instance L-proline is non-polar while DL-threonine is polar, and it was postulated that these differences would affect their modulation abilities.

## 2.3 Amino Acid Modulation

A standard synthetic protocol was adopted for all the Zr and Hf MOF modulation experiments, enabling direct comparability. This ensured that any variation in crystallinity or properties of the resulting MOFs was due to the modulators. There are a vast number of amino acids available; however we selected seven (Figure 2.1b) prototypical examples that display a range of physical properties. It was anticipated that differences in hydrophobicity/hydrophilicity, basicity and chemical functionality would provide different modulating abilities. In a typical modulation experiment one equivalent each of  $\text{MCl}_4$  and the chosen ligand were dissolved separately in reagent grade *N,N*-dimethylformamide (DMF), with five equivalents of the amino acid and one equivalent of HCl added to the metal solution. The solutions were combined (the final concentrations of metal and ligand being 45 mM), sonicated and heated for 24 hours at 120 °C. The resultant precipitates were collected by centrifugation, washing thoroughly with DMF and methanol, and vacuum dried. Powder X-ray diffraction (PXRD) analysis was used to determine the extent of formation and crystallinity of the MOFs in comparison to control samples with no amino acid added. The results obtained for the Zr and Hf MOFs are very similar, which is not surprising since they are expected to be isostructural, and so they will be discussed together.

During the study, an obvious starting point was to modulate MOFs containing L1 and work through the ligands in order. The Zr MOF containing L1 (**Zr-L1**), also known as UiO-66, was one of the first Zr MOFs reported and subsequently it is one of the easiest Zr MOFs to reproducibly synthesise. Crystalline **Zr-L1** can be synthesised in the presence of HCl alone, and it was found that the addition of amino acids to the synthetic mixture did not provide a beneficial effect (Figure 2.2.a). L-proline and PABA were the only amino acids that did not disrupt the formation of **Zr-L1**, however they did not provide any beneficial effect compared to HCl alone. Zr MOF syntheses containing  $\beta$ -alanine resulted in an unknown impurity, which was observed in the PXRD patterns and hence this modulator was excluded from the Hf modulation experiments. The synthesis of **Hf-L1** has been less well studied and in the case of the HCl-only synthesis (Figure 2.2.b) crystalline material is obtained, but the improvement is not to the same extent as observed for **Zr-L1**. However, the addition of L-proline or PABA also results in crystalline **Hf-L1**. In the case of **Hf-L1**, PABA is the most beneficial modulator, although the benefit of amino acids as modulators was not initially

obvious and so Zr and Hf MOFs containing functionalised terephthalate (L2-L4) and longer ligands (L5-L8) were examined.

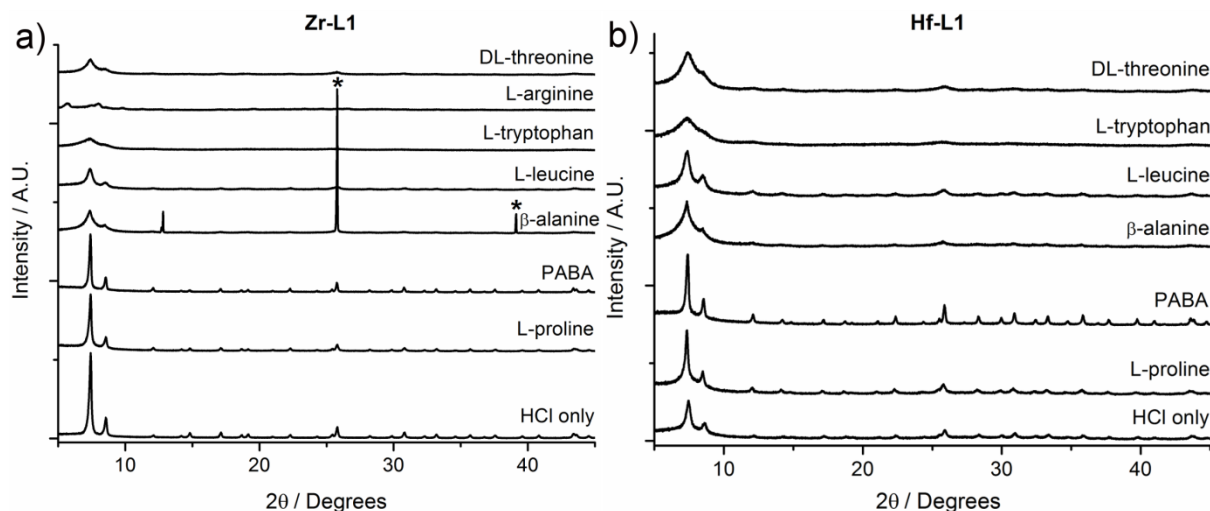


**Figure 2.2.** Stacked PXRD patterns of the materials obtained during amino acid modulation of a) **Zr-L1** and b) **Hf-L1**. An unknown impurity in the  $\beta$ -alanine sample (a only) is marked with an asterisk.

Unfortunately, the results described above for **Zr-L1** and **Hf-L1**, which contain terephthalate ligands, are representative of the results obtained for both the Zr and Hf MOFs containing functionalised terephthalate ligands (L2, L3 and L4). In most cases crystalline phase pure material can be synthesised in the presence of HCl alone, however the combined addition of HCl and PABA also results in crystalline samples in all six cases (see the stacked PXRD patterns in the Appendix, Chapter 6 Figures 6.1-6.4 and Figures 6.9-6.12). There was no obvious benefit upon the addition of amino acid modulators to the syntheses of Zr and Hf MOFs to this point and so it could reasonably be assumed that amino acids were not going to act as effective modulators, although they contain the necessary prerequisites.

The true benefit of amino acid modulation was discovered upon proceeding to the modulation of Zr and Hf MOFs containing longer ligands. Unlike the terephthalate based Zr and Hf MOFs, the addition of HCl alone to the synthesis of the MOFs containing the longer ligands no longer appears to result in crystalline material. Stacked PXRD patterns of amino acid modulated **Zr-L5** and **Hf-L5** are shown overleaf and are typical of the results obtained for the longer ligands (Figure 2.3).

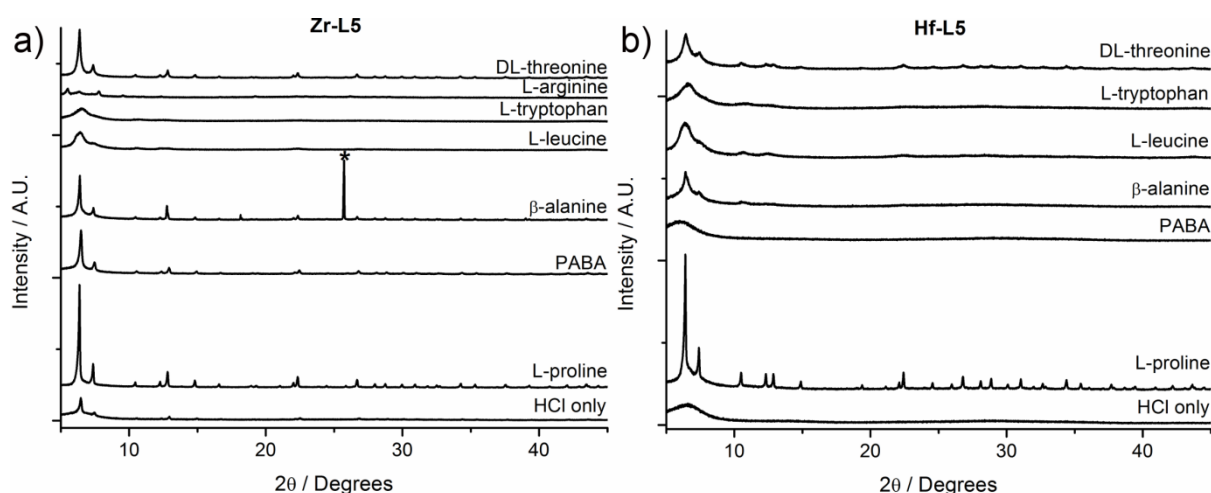


**Figure 2.3.** Stacked PXRD patterns of the materials obtained during amino acid modulation of a) **Zr-L5** and b) **Hf-L5**. An unknown impurity in the  $\beta$ -alanine sample (a only) is marked with an asterisk.

In the case of **Zr-L5** (Figure 2.3.a) there is an obvious improvement in crystallinity observed when a number of the amino acids are used, most notably L-proline, PABA,  $\beta$ -alanine and DL-threonine. An unknown impurity was again observed in the PXRD pattern of the  $\beta$ -alanine modulated sample. The most pronounced improvement in crystallinity is observed in the case of L-proline, and this is also true of **Hf-L5** where only the material synthesised in the presence of L-proline is crystalline. The results obtained during the modulation of Zr and Hf MOFs containing L5 were encouraging, and this was the first example where the amino acids provided an obvious improvement in crystallinity.

Similar beneficial results were found during the amino acid modulation of Zr MOFs containing L6-L8. The amino acid modulation results of the Zr MOFs are summarised in Table 2.1 (stacked PXRD patterns of the modulation experiments are provided in the Appendix, Chapter 6 Figures 6.1-6.8), revealing that there is no clear advantage of using amino acids during the synthesis of terephthalate based Zr MOFs (L1-L4), however for L5-L8 clear improvements in crystallinity are observed.

**Table 2.1.** Summary of amino acid modulation of Zr MOFs containing L1-L8.

<b>Modulator</b>							
	L-proline	PABA	$\beta$ -alanine	L-leucine	L-tryptophan	L-arginine	DL-threonine
<b>L1</b>	•	•	—	—	—	—	—
<b>L2</b>	—	•	—	—	—	—	—
<b>L3</b>	—	•	—	—	—	—	—
<b>L4</b>	—	•	—	—	—	—	—
<b>L5</b>	+	+	+	—	—	—	+
<b>L6</b>	+	•	+	+	+	—	+
<b>L7</b>	+	•	+	+	•	•	+
<b>L8</b>	+	•	•	+	+	•	•
<b>Key:</b> + represents enhanced crystallinity, — represents a decline in crystallinity, and • represents very little effect on crystallinity compared with the HCl only sample.							

The amino acids were able to modulate the Zr MOFs to different abilities and although  $\beta$ -alanine is able to improve the crystallinity of Zr MOFs containing L5-L7, the presence of impurities in their PXRD patterns suggests that it is not the most suitable modulator. The most pronounced improvement in crystallinity is observed when L-proline (in concert with HCl) is used to modulate Zr MOFs containing L5-L8. The only modulator that was unable to modulate any MOF was L-arginine, which presumably decomposed during synthesis as thick gum-like materials were obtained rather than fine powders. For this reason L-arginine was not examined for the modulation of the Hf MOFs and these results are summarised in Table 2.2 (stacked PXRD patterns of the modulation experiments are provided in the Appendix, Chapter 6 Figures 6.9-6.16).



**Table 2.2.** Summary of amino acid modulation of Hf MOFs containing L1-L8.

<b>Modulator</b>						
	L-proline	PABA	$\beta$ -alanine	L-leucine	L-tryptophan	DL-threonine
<b>L1</b>	+	+	—	—	—	—
<b>L2</b>	—	+	—	—	—	—
<b>L3</b>	+	+	—	•	—	—
<b>L4</b>	—	+	—	—	—	—
<b>L5</b>	+	•	+	•	•	+
<b>L6</b>	+	+	+	+	•	+
<b>L7</b>	+	•	+	+	•	+
<b>L8</b>	+	•	•	+	+	+
<b>Key:</b> + represents enhanced crystallinity, — represents a decline in crystallinity, and • represents very little effect on crystallinity compared with the HCl only sample.						

The results of the Hf modulation experiments are similar to those obtained for Zr however this is unsurprising due to the structural and chemical similarities of the two series of MOFs. In the case of Hf MOFs containing L1-L4, PABA improved the crystallinity of all four MOFs to some extent, while for Hf MOFs containing L5-L8 L-proline and DL-threonine provide the greatest enhancement. As L-proline is hydrophobic and DL-threonine is hydrophilic the mechanism of modulation remains unclear. The modulation effect could be provided by competitive attachment of the amino acids to the  $\text{Hf}_6$  clusters as they form through coordination of the carboxylate group, while it has also been postulated that degradation of the amino acids may regulate the pH during the course of the synthesis.

The modulation experiments revealed that L-proline demonstrates the greatest modulating potential, resulting in pronounced improvements in crystallinity of Zr and Hf MOFs containing L5-L8. Stacked PXRD patterns highlighting the increase in crystallinity of the MOFs containing L6-L8 are shown in Figure 2.4.

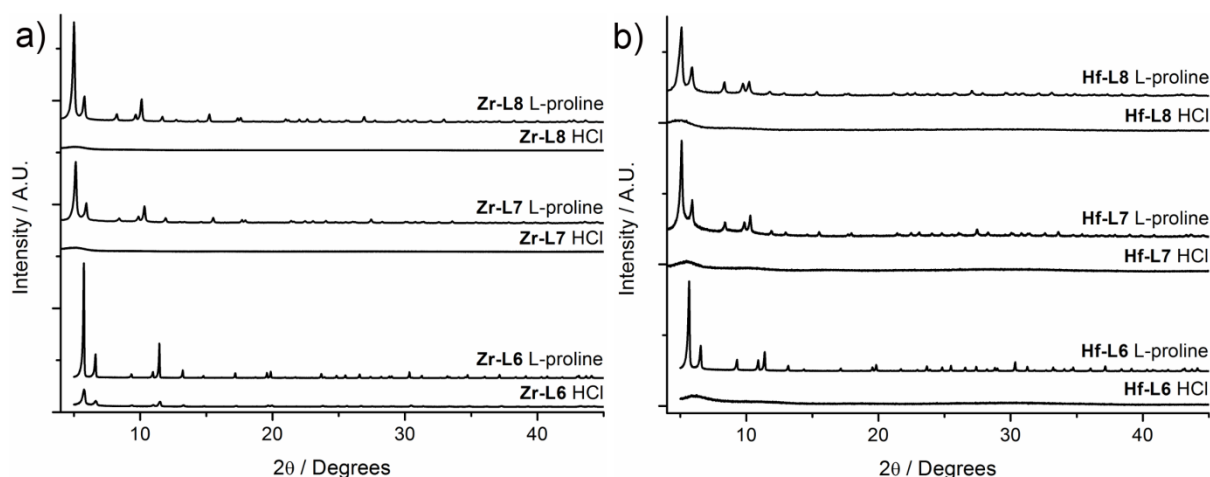


**Figure 2.4.** Stacked PXRD patterns comparing HCl and L-proline modulation of a) Zr MOFs and b) Hf MOFs containing L6, L7 and L8.

PXRD analysis reveals that HCl alone is unable to produce crystalline Zr and Hf MOFs containing L6-L8, however with the addition of small quantities of L-proline (5 equivalents) significant improvements in crystallinity are observed.

Optical microscopy was used to analyse the materials obtained to try and discern any differences in crystallinity, however the small crystallite size meant that no differences in the materials could be observed. Scanning electron microscopy (SEM) revealed that small octahedral crystals were obtained when a combination of HCl and L-proline were used, compared with small aggregated particles obtained when HCl was used alone. SEM images of **Zr-L6** and **Hf-L6** are shown overleaf as representative examples (Figure 2.5).

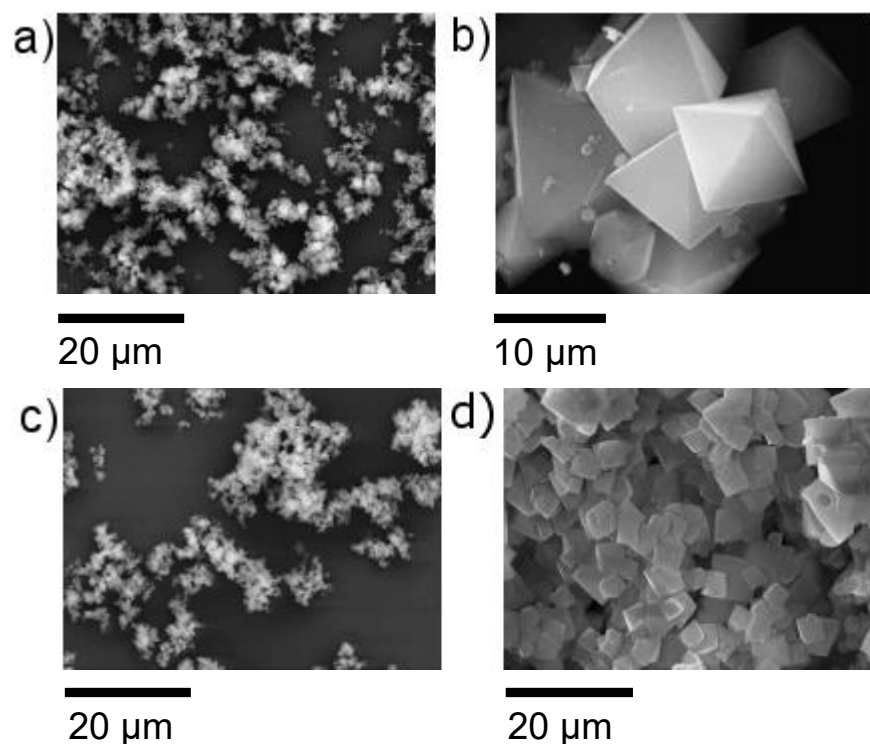


**Figure 2.5.** SEM images of **Zr-L6** synthesised with a) HCl only, b) HCl and L-proline and **Hf-L6** synthesised with c) HCl only and d) HCl and L-proline.

The SEM images of **Zr-L6** and **Hf-L6** are representative of the MOFs containing the longer ligands, highlighting the beneficial effect of HCl and L-proline, as discrete small octahedral crystals ( $\sim 10\ \mu\text{m}$  for **Zr-L6** and  $\sim 5\ \mu\text{m}$  for **Hf-L6**) are obtained when both modulators are used. Based on the observed increase in crystallinity through both PXRD and SEM analysis when L-proline and HCl are used in concert it was necessary to determine the ability of L-proline to act as a modulator in the absence of HCl. Experiments were performed to compare the effect of no modulator, HCl only, L-proline only and both HCl and L-proline on the products obtained during the synthesis of **Zr-L6** and **Hf-L6** (Figure 2.6).

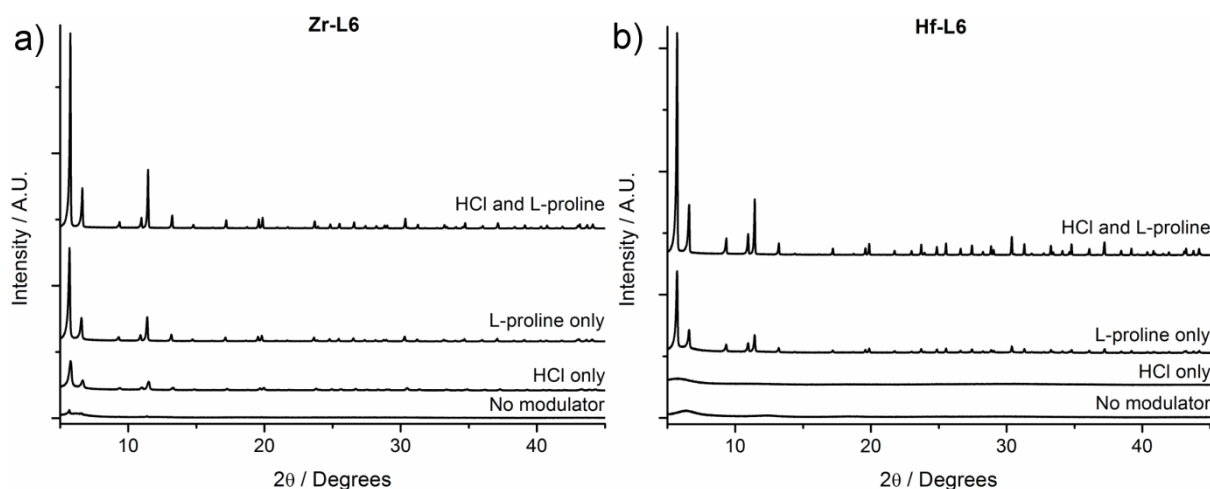


**Figure 2.6.** Stacked PXRD patterns of a) **Zr-L6** and b) **Hf-L6** synthesised with no modulator, HCl only, L-proline only and HCl and L-proline.

Using **Zr-L6** and **Hf-L6** as representative examples, it is evident that in both cases the combined effect of HCl and L-proline (as used during amino acid modulation experiments) provides the greatest enhancement in crystallinity of the products. Interestingly, the addition of one equivalent of HCl to the synthesis of **Zr-L6** is able to improve the crystallinity of the products; however the same effect is not observed for **Hf-L6**. The addition of five equivalents of L-proline improves the crystallinity of both **Zr-L6** and **Hf-L6** although the most pronounced effect is observed when HCl (one equivalent) and L-proline (five equivalents) are used together.

The synthetic protocol was further optimised by varying the number of equivalents of L-proline (maintaining one equivalent of HCl) added to the synthesis of **Zr-L6**. The effect on the crystallinity of the products was determined by PXRD analysis and SEM imaging (Figure 2.7).

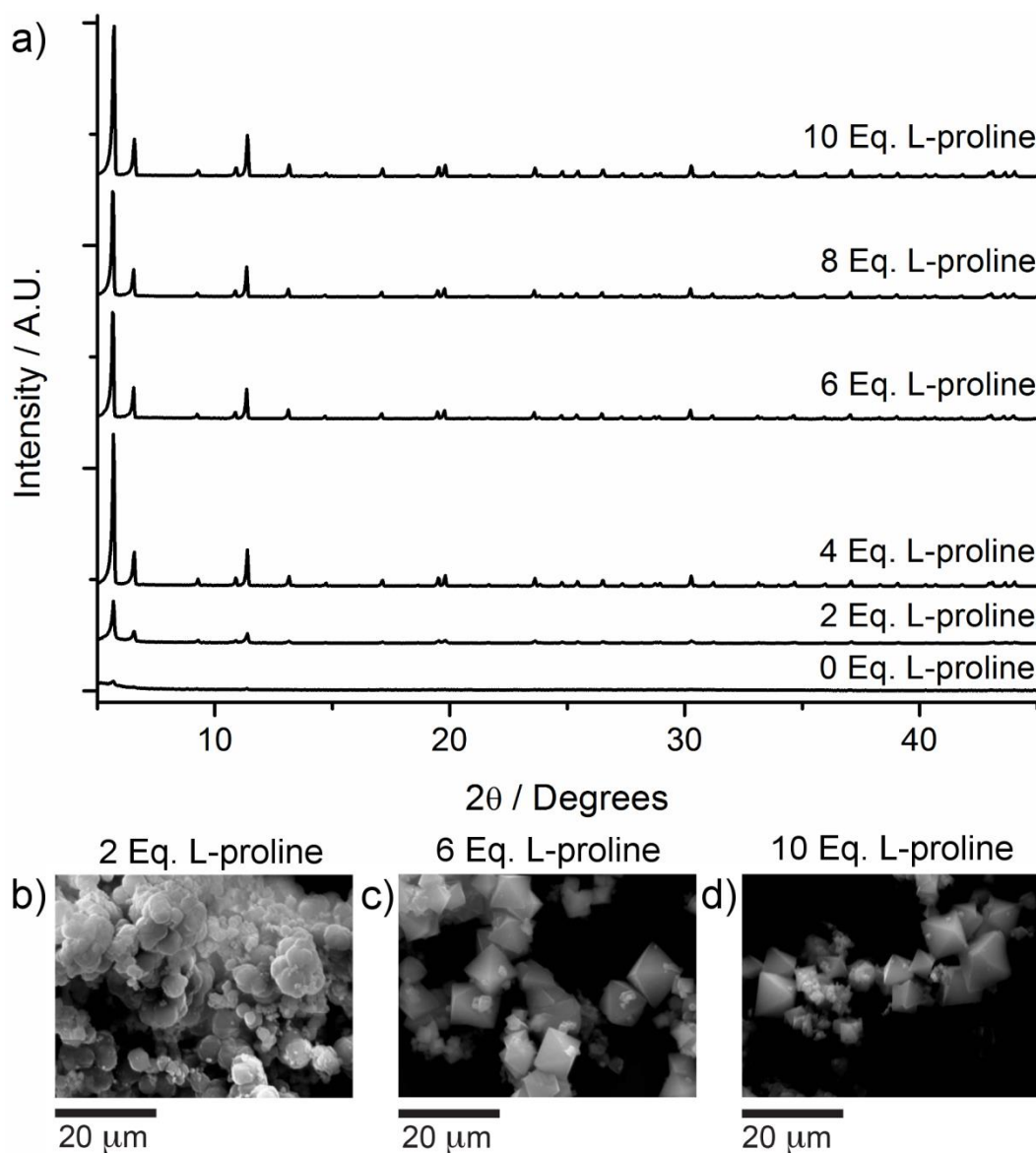


**Figure 2.7.** a) Stacked PXRD patterns and b) SEM images of **Zr-L6** synthesised with different equivalents of L-proline (maintaining one equivalent of HCl).

PXRD analysis of the L-proline equivalency scans of **Zr-L6** revealed that the addition of as little as 2 equivalents of L-proline is enough to improve crystallinity, although the improvement is only marginal compared with the enhancement observed in the presence of 4-10 equivalents. This is further backed up by SEM images showing that **Zr-L6** synthesised with 2 equivalents of L-proline (Figure 2.7.b) is ill-defined with a globular morphology, however the addition of between 6 and 10 equivalents of L-proline results in discrete octahedral single crystals ~10 μm in size. Overall, the L-proline equivalency results revealed that the addition of between 4 and 10 equivalents of L-proline combined with 1 equivalent of HCl greatly enhances the crystallinity of **Zr-L6**. This highlights the superior modulating

ability of L-proline with only 4 equivalents required for effective modulation, while using conventional modulators large excesses are typically required.<sup>38</sup>

The amino acid modulation experiments pointed towards the superior modulating ability of L-proline for the syntheses of Zr and Hf MOFs containing L5-L8. Further optimisation of the synthetic protocol was investigated by performing L-proline equivalency studies during the synthesis of **Zr-L6** as a representative example (Figure 2.7). With optimised conditions in hand, bulk scale syntheses of Zr and Hf MOFs containing L5-L8 were carried out to allow full characterisation of their properties, enabling comparisons with literature reported materials synthesised using conventional modulators.

## 2.4 Bulk Synthesis of Zr and Hf MOFs Containing L5-L8

A general synthetic procedure was used for the synthesis of bulk MOF samples, with the addition of one equivalent of HCl and five equivalents of L-proline used in all cases to allow direct comparison between the different MOF samples. For activation, the bulk MOF samples were immersed in THF and heated at 50 °C overnight. The THF was replaced daily for four consecutive days then the MOFs were dried under vacuum. The activated MOFs were analysed by PXRD, <sup>1</sup>H nuclear magnetic resonance spectroscopy (NMR), thermogravimetric analysis (TGA) and N<sub>2</sub> uptake experiments to assess their phase purity, level of modulator incorporation, thermal stability and porosity respectively.

The influence of the combined addition of L-proline (5 equivalents) and HCl (1 equivalent) on the crystallinity of Zr and Hf MOFs containing L5 and L6-L8 is shown in Figures 2.3 and 2.4 respectively. With highly crystalline materials in hand, <sup>1</sup>H NMR spectroscopy of acid digested MOF samples (DMSO-*d*<sub>6</sub>/D<sub>2</sub>SO<sub>4</sub>) was used to investigate the incorporation of L-proline within the MOFs, whether it be coordinated at defects<sup>28,32</sup> or trapped within the pores. The NMR results (see Appendix, Chapter 6 Figures 6.17-6.24) revealed that, with the exception of **Zr-L5** and **Hf-L5**, the MOFs do not contain significant amounts of L-proline, suggesting that the activation/washing conditions were successful. Interestingly, there still remained some residual L-proline in **Zr-L5** and **Hf-L5** although the same activation conditions were used for all MOFs. This suggests that L-proline is physically trapped within

the frameworks otherwise it would have been washed out from the samples during activation (Figure 2.8).

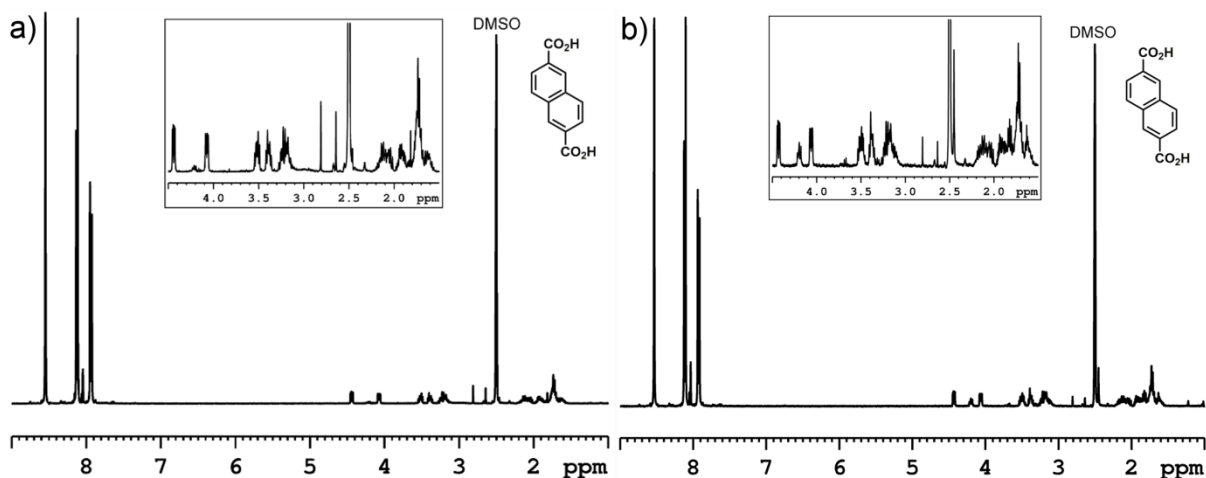


**Figure 2.8.**  $^1\text{H}$  NMR spectra of  $\text{DMSO-}d_6/\text{D}_2\text{SO}_4$  digests of a) **Zr-L5** and b) **Hf-L5**. The insets are expanded regions containing signals that correspond to residual L-proline.

The drawback of liquid NMR analysis of acid digested MOF samples ( $\text{DMSO-}d_6/\text{D}_2\text{SO}_4$ ) is that it does not help with determining the location of L-proline within the structure. Using integral ratios of the ligand to the L-proline signals (multiple signals are observed between  $\delta = 1.5$  and  $\delta = 4.5$  ppm, see Figure 2.8 insets) the L-proline content of the L5 MOFs is calculated to be as high as one molecule of L-proline per four molecules of L5. Considering that only MOFs containing L5 contain appreciable quantities of L-proline, this suggests that trapping of L-proline within the framework is a size based effect. Expansion of the pore windows in the MOFs containing the longer ligands (L6-L8) appears to be sufficient to allow the L-proline to be removed during activation.

TGA experiments were conducted from room temperature to  $1000\text{ }^\circ\text{C}$  under a nitrogen atmosphere to compare the thermal stabilities of the MOFs. Zr MOFs are well-known for their high thermal stabilities<sup>31</sup> and all of the L-proline modulated samples display thermal stabilities in excess of  $500\text{ }^\circ\text{C}$  (Figure 2.9).

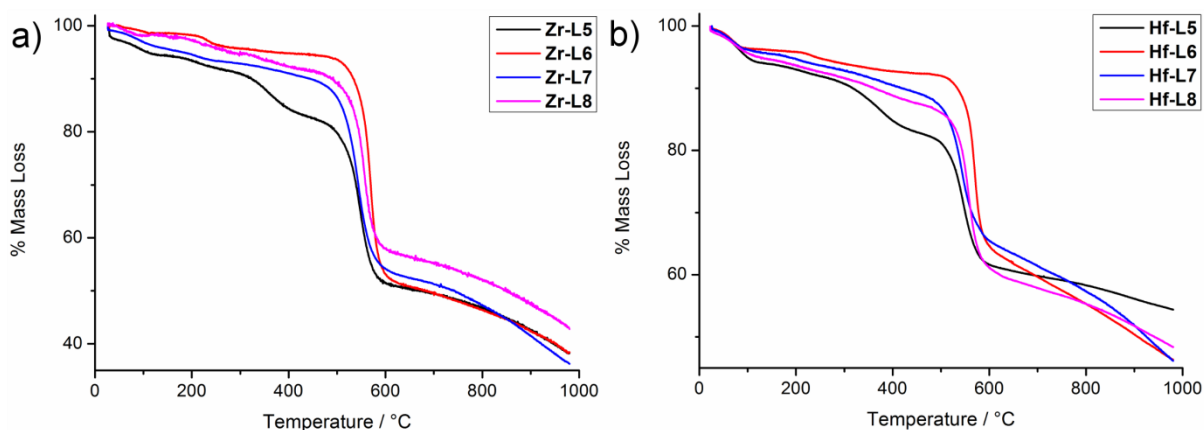


**Figure 2.9.** TGA profiles of a) Zr MOFs and b) Hf MOFs containing L5-L8.

Comparing the thermal stabilities of Zr and Hf MOFs containing L5-L8, it is clear that the choice of bridging ligand imparts only slight differences on thermal stability. In both cases, **Zr-L5** and **Hf-L5** demonstrate the lowest thermal stabilities, with significant mass losses at ~300 °C observed, prior to framework collapse. The same mass loss is not observed for the other MOFs, and the removal of residual solvent is usually observed around 200 °C. Therefore, the stepwise mass loss of **Zr-L5** and **Hf-L5** is expected to be due to the removal of trapped L-proline, which was also observed by  $^1\text{H}$  NMR spectroscopy (Figure 2.8). Removal of L-proline from the L5 MOFs may explain why they display the lowest thermal stabilities. In both cases, the L6 containing MOFs are the most thermally stable. There has been a lot of interest in Zr MOFs regarding their superior thermal stabilities compared with late transition metal containing MOFs, while the TGA profiles of the Hf MOFs proves that they are also thermally very stable.

$\text{N}_2$  adsorption/desorption isotherms were collected at 77 K (Figure 2.10) to allow BET surface areas of the MOFs to be calculated. Samples were thermally activated by heating at 120 °C for 20 hours under vacuum prior to the measurements to remove residual solvent, however on several occasions lower than expected surface areas were obtained. As an alternative, the materials with lower than expected surface areas were activated by immersion in chloroform rather than THF (full details are given in Section 2.10.6). Changing the solvent used for activation resulted in satisfactory surface areas. This suggests that the expected MOF structures are obtained using L-proline modulation and that they were only partially activated or they were collapsing during THF activation.



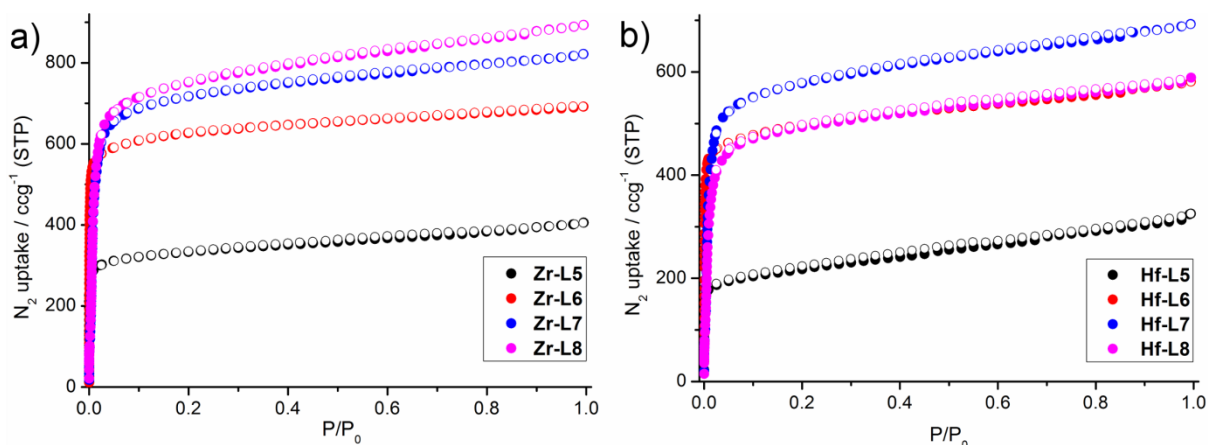


**Figure 2.10.** N<sub>2</sub> adsorption (closed circles) and desorption (open circles) isotherms collected at 77 K of a) Zr and b) Hf MOFs containing L5-L8. The N<sub>2</sub> uptakes of **Hf-L6** and **Hf-L8** are very similar and hence they are superimposed.

The N<sub>2</sub> adsorption/desorption isotherms of the Zr MOFs are as expected, with the volume of N<sub>2</sub> adsorbed increasing as the length of the bridging ligand increases. The BET surface area of **Zr-L5** was found to be 1300 m<sup>2</sup>g<sup>-1</sup> which is slightly lower than the previously published value of 1400 m<sup>2</sup>g<sup>-1</sup> and this decrease in BET surface area is expected to be due to residual L-proline trapped within the framework.<sup>38</sup> The calculated BET surface areas for each of the eight MOFs are shown below in Table 2.3. The gravimetric N<sub>2</sub> uptake capacities of the Hf MOFs are lower than that of the Zr MOFs due to the increased mass of Hf relative to Zr. The slight increase in uptake of **Zr-L8** relative to **Zr-L7** may be due to slight differences arising from activation or due to the slightly larger unit cell of **Zr-L8** (see Section 2.10.8).

**Table 2.3.** Measured BET surface areas of Zr and Hf MOFs containing L5-L8.

	<b>L5</b>	<b>L6</b>	<b>L7</b>	<b>L8</b>
<b>Zr</b>	1300 m <sup>2</sup> g <sup>-1</sup>	2465 m <sup>2</sup> g <sup>-1</sup>	2830 m <sup>2</sup> g <sup>-1</sup>	2950 m <sup>2</sup> g <sup>-1</sup>
<b>Hf</b>	810 m <sup>2</sup> g <sup>-1</sup>	1390 m <sup>2</sup> g <sup>-1</sup>	2270 m <sup>2</sup> g <sup>-1</sup>	2020 m <sup>2</sup> g <sup>-1</sup>

The N<sub>2</sub> uptake and subsequently the BET surface area of **Hf-L5** is significantly lower than expected and the increase in mass of Hf relative to Zr cannot fully account for the decrease relative to **Zr-L5**. Similar to **Zr-L5**, it is clear that trapped L-proline will occupy pore space and as a result reduce the N<sub>2</sub> uptake; however incomplete activation may also be responsible. The uptake of **Hf-L8** is lower than expected with a very similar uptake to **Hf-L6** and as a

result their isotherms are superimposed in the comparison (Figure 2.10). **Hf-L8** is expected to be more porous than **Hf-L6** due to the increased length of the ligand however, multiple isotherms were collected on different batches of **Hf-L8** and lower than expected N<sub>2</sub> uptakes were repeatedly obtained. SEM images of bulk samples of L-proline modulated **Hf-L8** were collected to try and account for the lower than expected N<sub>2</sub> uptake (Figure 2.11).

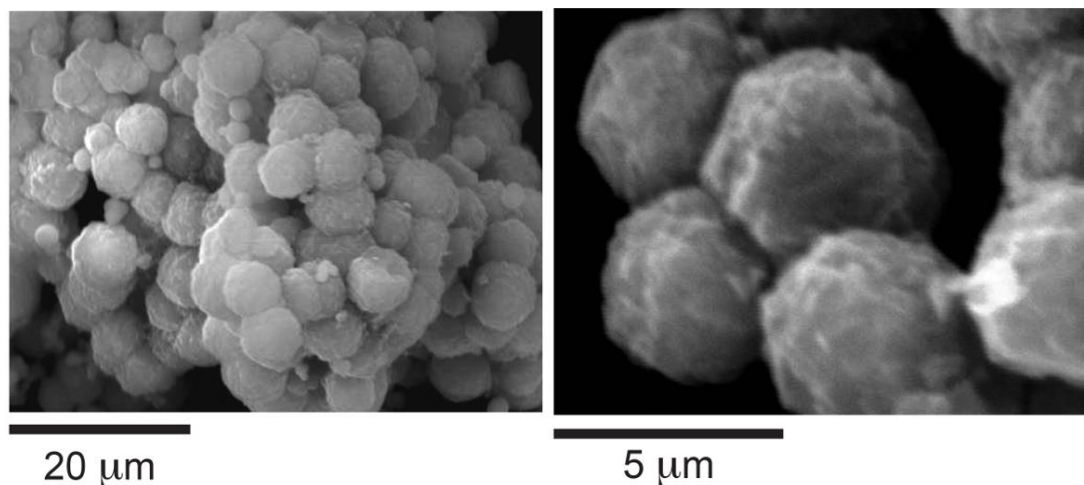


**Figure 2.11.** SEM images at different zoom levels of bulk samples of **Hf-L8** synthesised using L-proline modulation, highlighting the spherical aggregates around 5 μm that form.

The SEM images of **Zr-L6** and **Hf-L6** (Figure 2.5) synthesised using L-proline modulation contain well shaped discrete octahedral crystals, while the SEM images of **Hf-L8** (Figure 2.11) reveal that spherical aggregates are formed. Within the spherical aggregates there appear to be distinct edges and shape, however individual crystals are not obtained and this may reduce the porosity and hence explain the low N<sub>2</sub> uptake.

Where individual N<sub>2</sub> uptakes or BET surface areas have not been discussed then the experimental value obtained (Table 2.3) matches with the literature reported value.<sup>23,38,39</sup> This was the case for most of the samples, confirming that they are of high quality. Pore-size distributions (PSDs) were calculated (QSDFT, slit/cylindrical pore, N<sub>2</sub> on carbon at 77 K) from the experimental N<sub>2</sub> isotherms to try and elucidate the lower than expected N<sub>2</sub> uptakes observed for **Hf-L5** and **Hf-L8** (Figure 2.12).

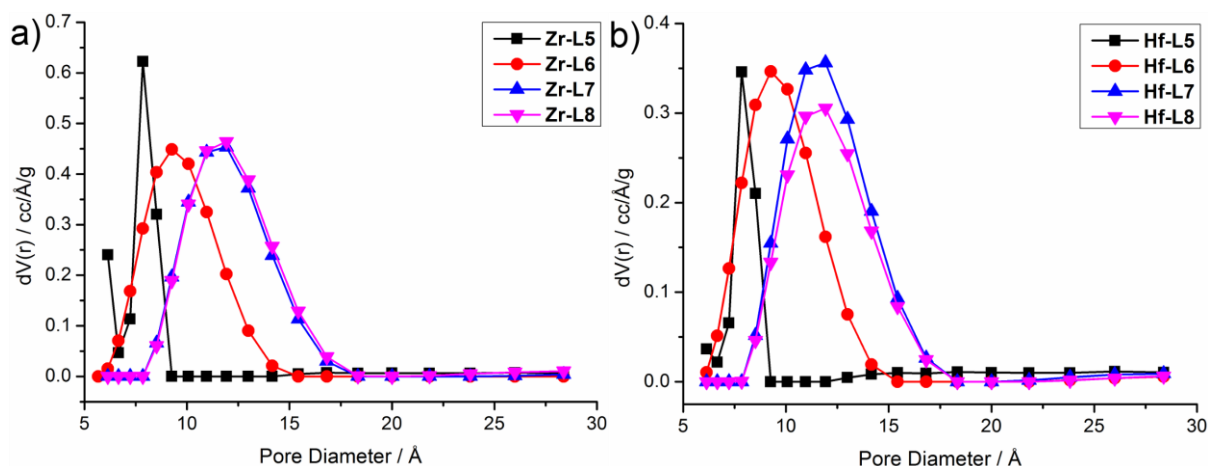


**Figure 2.12.** Pore size distributions of a) Zr and b) Hf MOFs of L5-L8 calculated from the  $N_2$  adsorption isotherms.

Comparing the PSDs of the Zr and Hf MOFs it is clear that in both cases pore diameter increases as the length of the bridging ligand increases. There is very close agreement between the pore diameter of Zr and Hf MOFs containing the same ligand proving the two series of MOFs to be isostructural. However, for both **Hf-L5** and **Hf-L8** relative to their Zr counterparts there is a greater than expected reduction in cumulative pore volume, suggesting that the lower than expected surface areas obtained are the result of inaccessible pore space rather than structural collapse.

The analysis carried out on the bulk MOF samples synthesised using L-proline modulation confirms that bulk phase-pure highly crystalline materials are obtained. L-proline is an effective modulator in small quantities and is able to dramatically improve the crystallinity of Zr and Hf MOFs containing the longer ligands. Considering the increase in crystallinity and the superior modulation ability of L-proline during solvothermal syntheses, the microwave assisted synthesis of **Zr-L6** was attempted to determine the efficacy of L-proline modulation.

## 2.5 Microwave Assisted Synthesis of Zr-L6

Microwave assisted synthesis of MOFs has been investigated,<sup>40</sup> mainly because of the reduced timescales compared with conventional solvothermal synthesis. The ability of L-proline to effectively modulate the microwave assisted synthesis of **Zr-L6** was examined.

Very similar conditions to those used throughout the amino acid modulation experiments were employed, with one equivalent of HCl and five equivalents of L-proline added to the synthesis. **Zr-L6** was synthesised at 100 °C for 1 hour using a laboratory microwave and the product was treated in a similar manner to the oven-synthesised samples. Phase purity, BET surface area and particle morphology were used to assess the quality of the MOF obtained using the reduced timescale microwave assisted method (Figure 2.13).

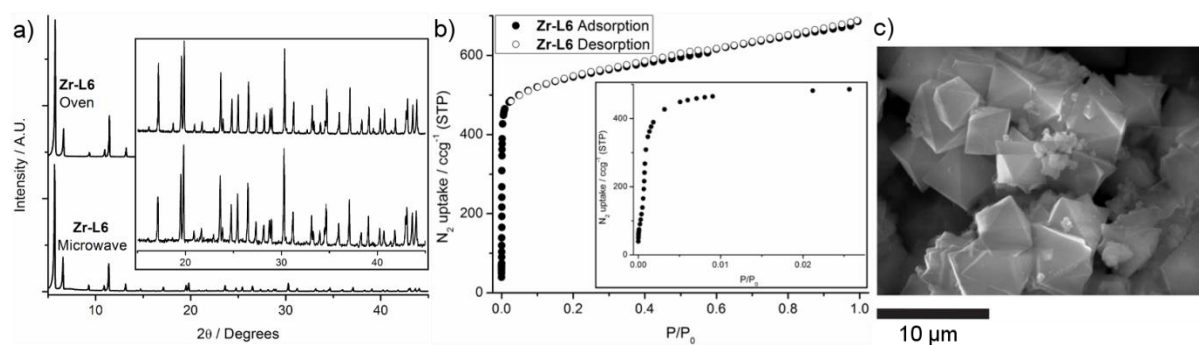


**Figure 2.13.** Characterisation of **Zr-L6** synthesised using a microwave assisted method by a) PXRD, b) N<sub>2</sub> adsorption/desorption isotherms and c) SEM imaging.

Excellent agreement between the PXRD patterns of solvothermally and microwave synthesised **Zr-L6** confirms that the microwave synthesised **Zr-L6** is phase pure, highly crystalline and defect free. The BET surface area, calculated from the N<sub>2</sub> adsorption data is 2100 m<sup>2</sup>g<sup>-1</sup> which is slightly lower than the theoretical surface area, however this has been known to vary widely from sample to sample.<sup>23</sup> The SEM image shows that aggregated octahedral crystals ~5-10 µm in size are obtained.

The combination of analysis performed on the microwave synthesised **Zr-L6** suggests that high quality material of a comparable standard to the solvothermally prepared material was obtained. These results highlight the very efficient modulation ability of L-proline, as highly crystalline material can be obtained in as little as one hour, which is a vast improvement compared with the 24 hours typically required during solvothermal synthesis, while it is possible that the synthesis time could be further reduced.

With L-proline proving to be an effective modulator, in small quantities and under different synthetic conditions (solvothermal and microwave assisted syntheses), efforts were directed

towards the synthesis of single crystals to allow accurate structural models of the materials to be obtained.

## 2.6 Single Crystal Synthesis of Zr and Hf MOFs Containing L5-L8

The synthesis of single crystals of Zr and Hf MOFs is routinely very difficult, although it is becoming more common with the aid of modulation. Systematically varying the synthetic conditions, octahedral single crystals of **Zr-L6**, **Zr-L7**, **Zr-L8**, **Hf-L6** and **Hf-L7** around 60–100  $\mu\text{m}$  in size were obtained using L-proline modulation. When the crystals were obtained, only the single crystal structure of **Zr-L5** had been reported<sup>38</sup> and so full data collections were obtained for each of the MOFs. Single crystal data collections were successful using laboratory X-ray sources, allowing the solid state structures of the MOFs to be observed for the first time (Figure 2.14).

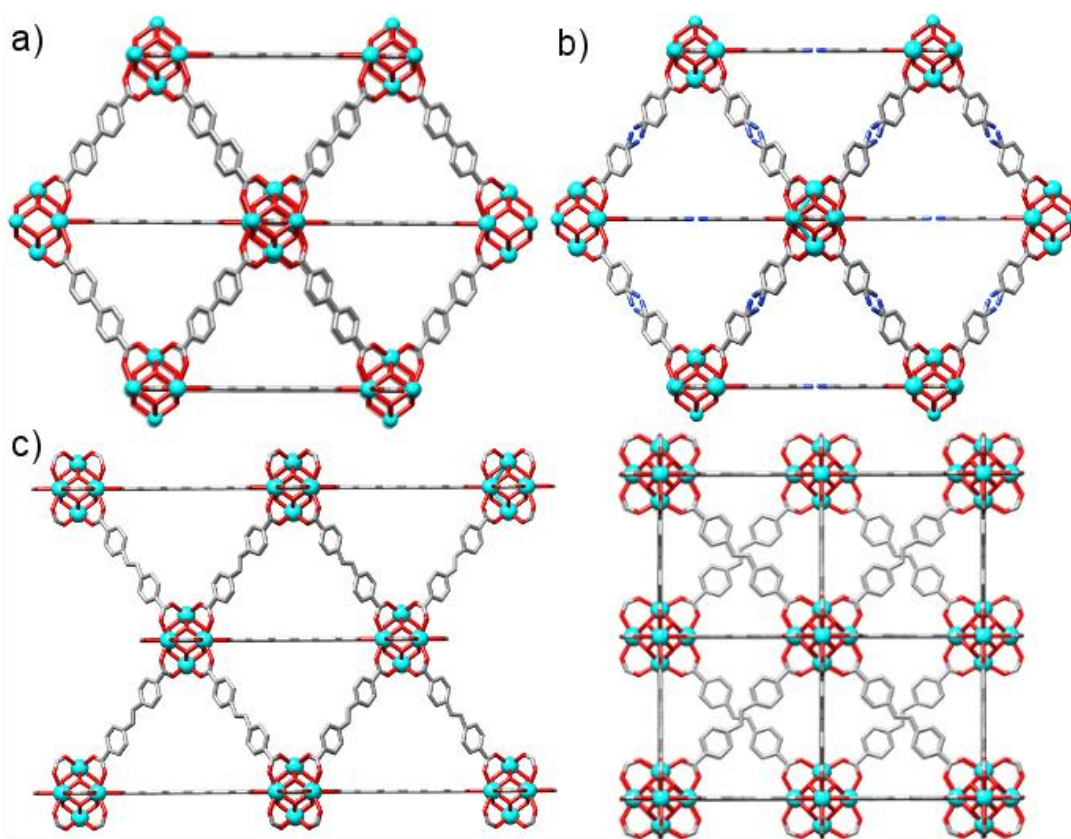


**Figure 2.14.** Portion of the solid state packing structure of a) **Zr-L6**, b) **Zr-L7** and c) **Zr-L8** in two alternative orientations with disorder deleted around the integral alkene. Atom colour scheme: Zr, cyan; C, grey; O, red; N, blue. Hydrogen atoms are omitted for clarity.

During our studies other groups reported the single crystal X-ray structure of **Zr-L6**,<sup>24,41,42</sup> however L-proline is an effective modulator and single crystals of five Zr and Hf MOFs were grown in total. L6 is linear and as such fulfils the symmetry requirements of the cubic  $Fm-3m$  space group of UiO-66 type MOFs, adopting a linear bridging position between adjacent  $Zr_6$  clusters (Figure 2.14.a). However, the bent geometry of L7 and L8 theoretically breaks the symmetry as a result of their non-linearity. This caused confusion during an earlier report on **Zr-L7**,<sup>39</sup> where the authors describe that an ordering of the ligands would reduce the overall symmetry from  $Fm-3m$  to  $I4/m$ . Although single crystals of **Zr-L7** were obtained during the previous study they were of insufficient quality to allow precise structural information to be obtained. Single-crystal X-ray diffraction (SCXRD) was used to analyse the L-proline modulated crystals and from the data it is possible to discern that **Zr-L7**, **Hf-L7** and **Zr-L8** are in fact able to adopt UiO-66 type structures with cubic  $Fm-3m$  symmetry. The MOFs are therefore part of an isorecticular series as they share the same common structure and topology with expansion in their unit cells observed as the length of the bridging ligand increases. In Figure 2.14.b, disorder around the central azobenzene unit is observed and this is due to the different orientations adopted by the ligand within the MOF, however the geometrical average of the disordered arrangements satisfies the symmetry constraints. The structure of **Zr-L8** is very similar to that of **Zr-L7** and the two MOFs are essentially isostructural due to the close structural similarities of L7 and L8. In the solid state structure of **Zr-L8** (Figure 2.14.c) disorder of the stilbene unit has been omitted to facilitate visualisation of the *trans*-stilbene unit. The structures of **Hf-L6** and **Hf-L7** have not been shown due to their very close structural similarities with their Zr counterparts. Full synthetic details and crystal data are reported in Section 2.10.8.

The structural similarities of the Zr and Hf MOFs are realised upon comparison of their PXRD patterns, which are in excellent agreement. Comparing the experimental PXRD patterns of the Zr and Hf MOFs with the patterns calculated from their single crystal models confirms their bulk phase purity (Figure 2.15).

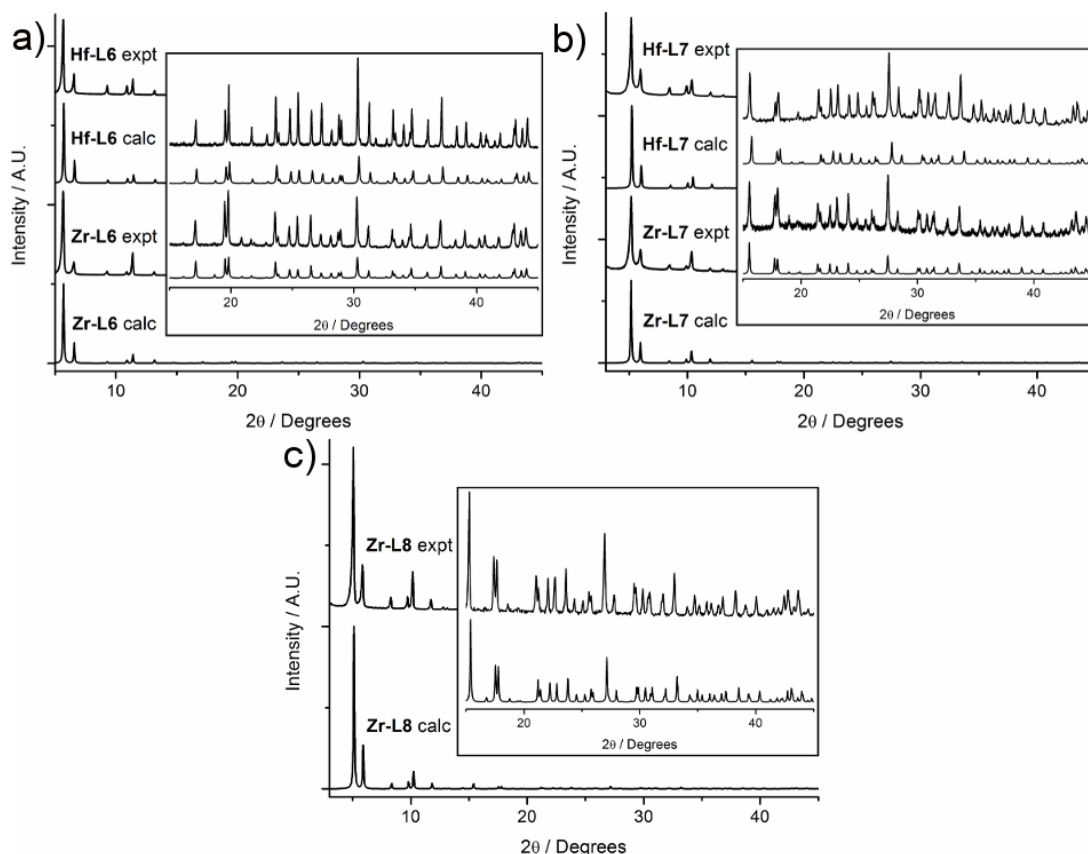


**Figure 2.15.** Comparisons of the calculated and experimental PXRD patterns of Zr and Hf MOFs containing a) L6 and b) L7. c) Calculated and experimental PXRD patterns of **Zr-L8** only as single crystals of **Hf-L8** were not obtained. The insets are expanded regions of the high angle data.

The PXRD patterns of the Zr and Hf MOFs containing either L6 or L7 are in good agreement with one another, confirming that the two series of MOFs are isostructural. By comparing the calculated (from SCXRD data) and experimental PXRD patterns it is clear that the single crystal X-ray structures are representative of the bulk microcrystalline powders. This again highlights the superior and very efficient modulation ability of L-proline during the synthesis of Zr and Hf MOFs with longer ligands, as it provides access to phase-pure microcrystalline powders or single crystals depending on requirements by subtle alterations to the reaction conditions. It should be noted that L-proline fails to produce single crystals of **Hf-L8** although bulk crystalline powders can be obtained. SEM images revealed that spherical aggregates were obtained rather than discrete octahedral single crystals (Figure 2.11).



With the crystal structures of the MOFs in hand (Figure 2.14), we performed an extensive study investigating the mechanical properties of Zr MOFs with collaborators from the Universities of Edinburgh and Cambridge.<sup>9</sup> High pressure single crystal X-ray diffraction and single crystal nanoindentation were used to probe the mechanical properties of the MOFs and the study was only made possible by L-proline modulation providing access to diffraction quality single crystals. **Zr-L6** and **Zr-L7** were investigated during the study and it was found that subtle changes to the linearity of the bridging ligand results in large differences in their elasticity, highlighting future directions for fine-tuning the mechanical properties of these highly porous materials.

Considering the success of L-proline modulation in the syntheses Zr and Hf MOFs containing the longer ligands of the series, the newly developed synthetic procedure was investigated for the modulation Zr and Hf MOFs containing even longer ligands. A series of three extended ligands, namely L9-L11, containing integral unsaturated alkyne and butadiyne units were designed and synthesised.

## 2.7 Design and Synthesis of Extended Ligands

Methyl 4-(2-(trimethylsilyl)ethynyl)benzoate, L9-Me<sub>2</sub> and L11-Me<sub>2</sub> (Figure 2.16) are synthesised by Sonogashira coupling, a very famous reaction which results in the formation of new carbon-carbon bonds by coupling terminal alkynes with either aryl or vinyl halides. Typically the reactions are performed in the presence of both palladium and copper catalysts. The judicious choice of starting materials has enabled us to achieve a series of ligands that demonstrate a variety of lengths, interesting for their incorporation within Zr and Hf MOFs, as they permit control over pore volume, surface area and the size of the pore windows.

An alternative synthetic route was used for the homo-coupling of methyl 4-ethynylbenzoate, resulting in L10-Me<sub>2</sub> which contains a butadiyne functional unit. Initial attempts to synthesise L10-Me<sub>2</sub> via Glaser coupling resulted in issues regarding recovery of the product from the DMSO reaction mixture, with unsatisfactory low yields obtained. As an alternative, an Eglinton reaction, which is very similar to the Glaser coupling but is performed in the



presence of a  $\text{Cu}^{\text{II}}$  catalyst rather than a  $\text{Cu}^{\text{I}}$  catalyst, was used to successfully synthesise L10- $\text{Me}_2$ .

Deprotection of the esters was necessary to generate the free acids required for MOF syntheses and this was successfully carried out under typical conditions using potassium hydroxide, followed by acidification with an aqueous hydrochloric acid solution. The deprotections were generally carried out in the presence of 10 equivalents of potassium hydroxide, with the exception of the synthesis of L10- $\text{H}_2$  as unwanted side-products were obtained, most likely due to cleavage of the butadiyne unit. The quantity of base added to the reaction mixture was scaled back to 2.5 equivalents, enabling the efficient synthesis of L10- $\text{H}_2$ .

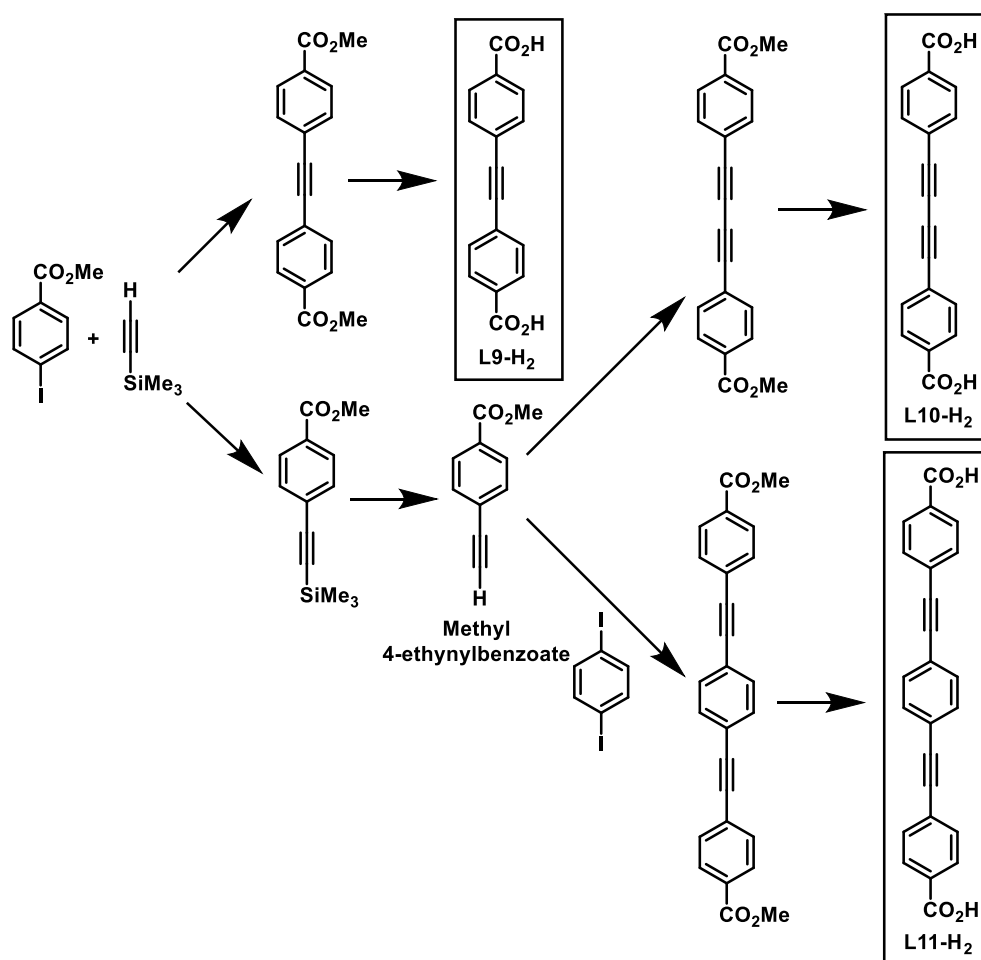


**Figure 2.16.** Schematic representation of the divergent synthetic route to L9- $\text{H}_2$ , L10- $\text{H}_2$  and L11- $\text{H}_2$ .

Once optimised, syntheses of the ligands were straightforward and they could be scaled up to allow multiple grams of product to be obtained. Based on the previous success of L-proline modulation for Zr and Hf MOFs containing L5-L8, it was reasonable to assume that the same synthetic procedures would be transferrable to Zr and Hf MOFs containing L9-L11.

## 2.8. Synthesis of Zr and Hf MOFs Containing L9-L11

Initial efforts focused on the synthesis of bulk microcrystalline samples of Zr and Hf MOFs containing L9-L11. Highly crystalline and defect free bulk samples of **Zr-L9**, **Hf-L9**, **Zr-L11** and **Hf-L11** were obtained using L-proline modulation, although difficulties were observed during the synthesis of **Zr-L10**. It is not obvious why L-proline modulation is ineffective for the synthesis of **Zr-L10** however, the obtained samples were dark in colour and diffracted weakly. The L-proline modulated **Zr-L10** samples demonstrated low N<sub>2</sub> uptakes and as an alternative synthetic route benzoic acid modulation was investigated.<sup>15</sup> Benzoic acid modulated samples of **Zr-L10** were a light yellow colour and characterisation by PXRD revealed that improvements in crystallinity were evident compared with L-proline modulated samples. **Zr-L10** is the most porous UiO-66 type framework reported<sup>43</sup> and as L-proline effectively modulates Zr MOFs containing the longer ligand, L11, it is not clear why it fails to produce high quality samples of **Zr-L10**. The anomalies observed for **Zr-L10** were also observed for **Hf-L10**, with L-proline again failing to reliably synthesise crystalline material. In a similar manner, benzoic acid modulation was investigated as an alternative modulator although this was found not to be straightforward. Light coloured powders of **Hf-L10** were obtained using benzoic acid modulation although issues were encountered regarding crystallinity and stability. Considering the very similar structures and properties of Zr and Hf MOFs containing the same ligand, it was decided not to pursue the synthesis of **Hf-L10**. Using optimised bulk synthetic conditions, large scale syntheses of each of the MOFs was carried out and the materials were fully characterised. PXRD was used to initially assess the crystallinity of the extended Zr and Hf MOFs (Figure 2.17).

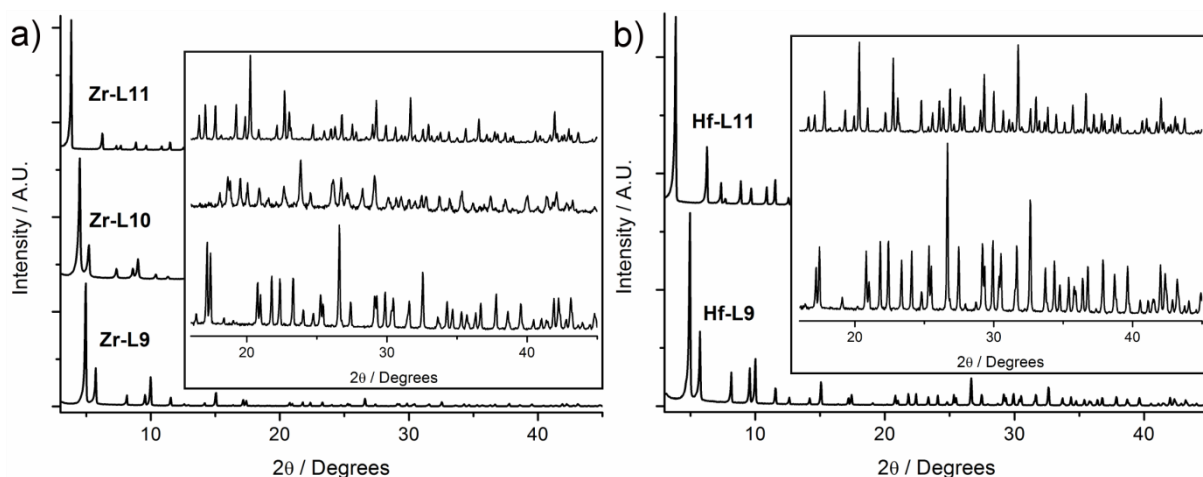


**Figure 2.17.** PXRD patterns of a) Zr MOFs containing L9-L11 and b) Hf MOFs containing L9 and L11 only. The insets are expanded regions of the high angle data.

PXRD analysis reveals that the bulk samples of the Zr and Hf MOFs containing the extended ligands are all highly crystalline, with the insets showing that this is true even to high angles of  $2\theta$ . It is obvious from the PXRD comparisons that when longer ligands are incorporated the low angle diffraction peaks move to lower angles of  $2\theta$ , suggesting an expected increase in unit cell dimensions. Fine-tuning of reaction conditions resulted in the isolation of single crystals suitable for single crystal X-ray diffraction. Single crystal data was collected either in-house or at the UK National Crystallography Service and the solid state structures provide accurate structural representations, allowing the increase in unit cell suggested from PXRD to be quantified (Figure 2.18).

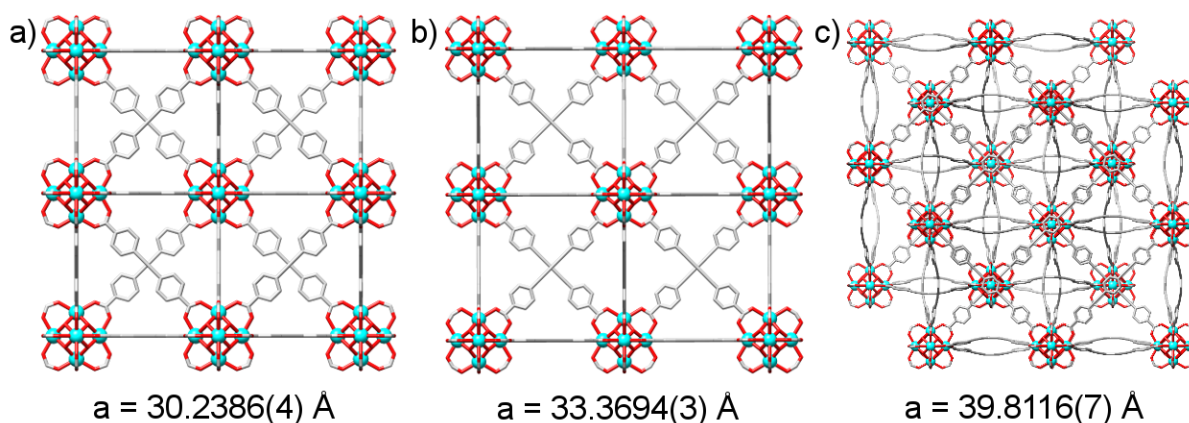


**Figure 2.18.** Portions of the solid state structures of a) **Zr-L9**, b) **Zr-L10** and c) **Zr-L11** alongside their unit cell edge dimensions. Atom colour scheme: Zr, cyan; C, grey; O, red. Hydrogen atoms are omitted for clarity.

The unit cell edges increase in line with the increase in ligand length across the series of Zr MOFs and the unit cell volume increases from 27649.4 Å<sup>3</sup> to 37157.4 Å<sup>3</sup> for **Zr-L9** and **Zr-L10** respectively. **Zr-L11** and **Hf-L11** are 2-fold interpenetrated due to the increased length of L11 relative to the other ligands. This means that the MOFs containing L11 are sufficiently porous that a second framework can grow within the pore space of the first framework, and likely the interpenetrated structure is obtained for stability reasons. Interpenetration in the MOFs containing L11 results in a slight reduction of their symmetry and they crystallise in the *Fd-3m* space group rather than the *Fm-3m* space group typical of non-interpenetrated UiO-66 type materials. The single crystal structures of the corresponding Hf MOFs are not shown due to their close structural similarities with the Zr derivatives however single crystal data for all five MOFs is reported in Section 2.10.11. The calculated (from single crystal models) and experimental PXRD patterns of the extended MOFs are compared, confirming the structural similarities of the Zr and Hf MOFs (Figure 2.19).

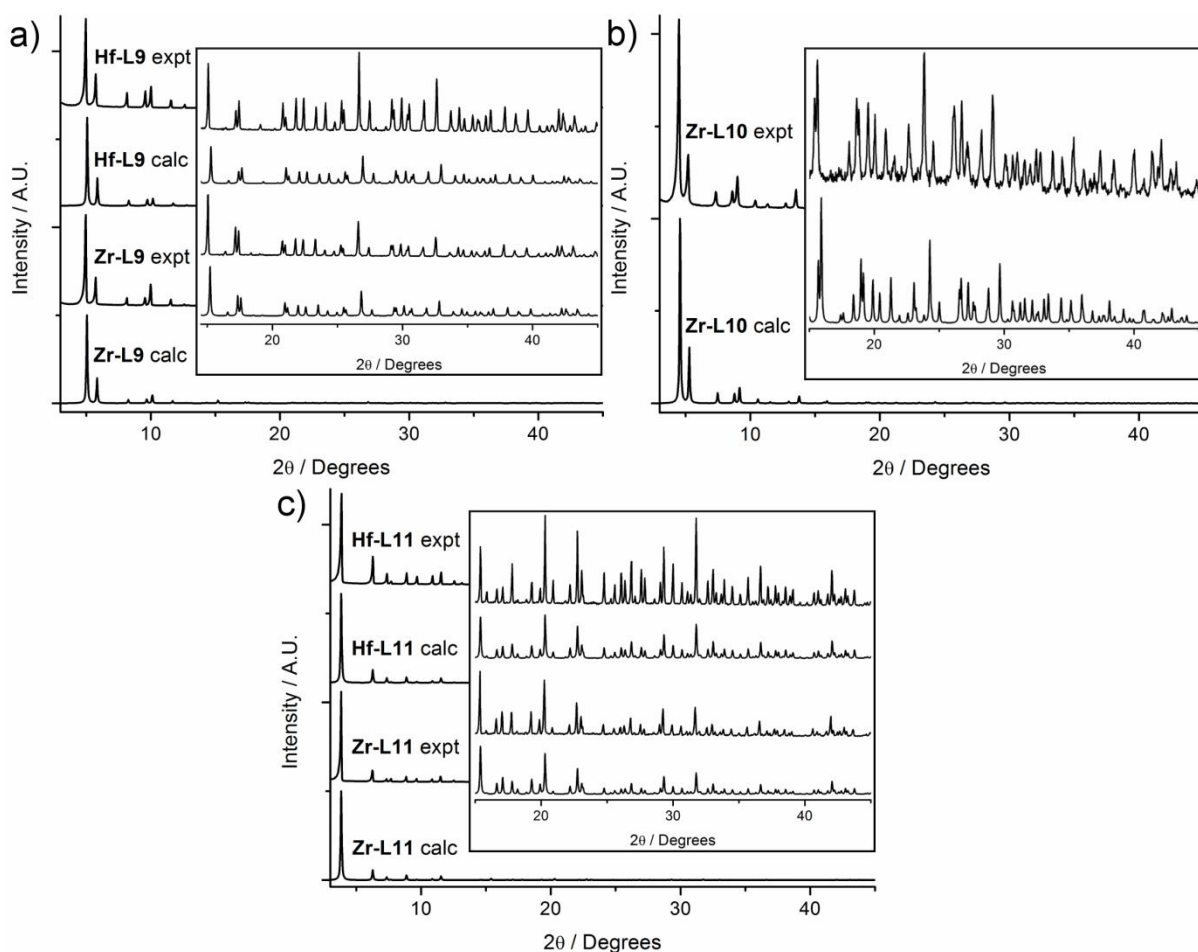


**Figure 2.19.** Comparisons of the calculated and experimental PXRD patterns of a) **Zr-L9** and **Hf-L9**, b) **Zr L10** and c) **Zr-L11** and **Hf-L11**.

The very close agreement between the PXRD patterns calculated from the single crystal X-ray structures and the experimental patterns for each MOF provides evidence that bulk-phase pure materials are obtained and that the single crystal models are accurate. The similarity of the PXRD patterns of the Zr and Hf MOFs containing each ligand confirms that both sets of MOFs are structurally very similar, irrespective of the metal contained within the cluster.

The effect of the increased ligand length on the thermal stability of the MOFs was investigated by TGA experiments (Figure 2.20).

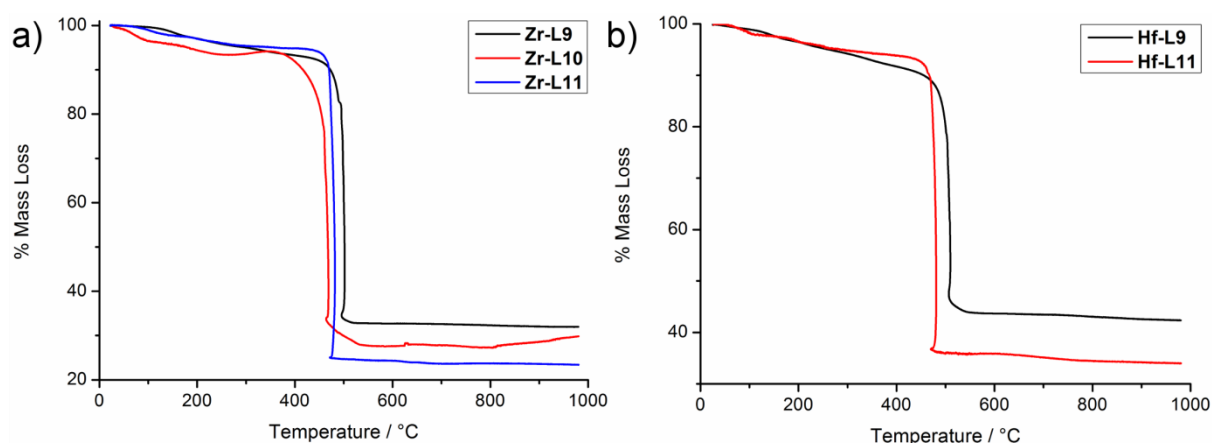


**Figure 2.20.** TGA profiles of a) Zr MOFs containing L9-L11 and b) Hf MOFs containing L9 and L11 only.

Zr and Hf MOFs containing the extended ligands are thermally stable to ~450-500 °C, with the MOFs containing L9 found to be the most thermally stable. In the case of the Zr MOFs, **Zr-L10** is less thermally stable than **Zr-L11** which may not be expected based on considerations of ligand length, although it can be understood that framework interpenetration, observed in **Zr-L11**, results in an enhanced thermal stability. The 2-fold interpenetration observed in **Zr-L11** (and **Hf-L11**) may improve the thermal stability of the material through inter-framework interactions. Both the inclusion of extended ligands and framework interpenetration in the Zr and Hf MOFs prompted analysis of their porosity by N<sub>2</sub> uptake experiments (Figure 2.21).

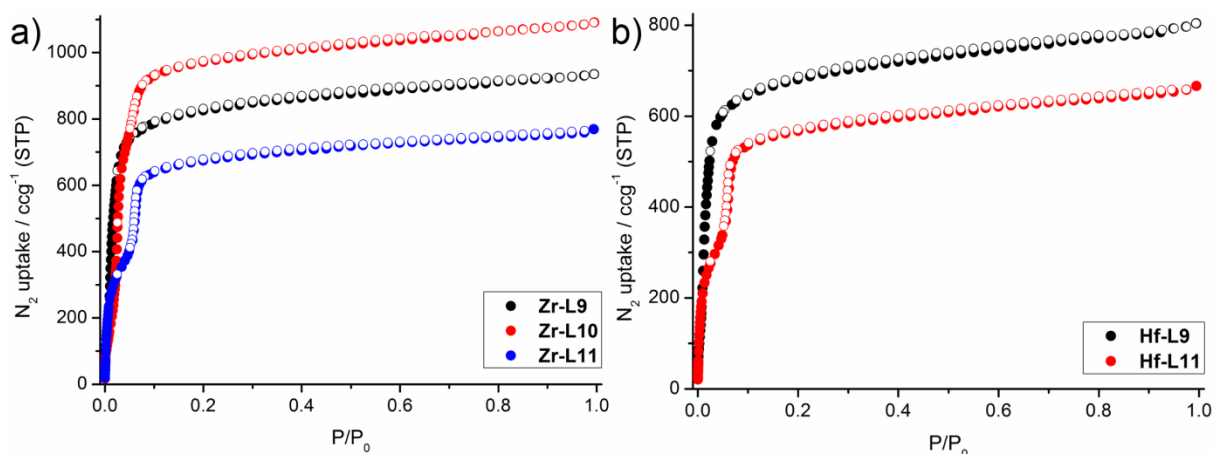


**Figure 2.21.**  $N_2$  adsorption (closed circles) and desorption (open circles) isotherms collected at 77 K of a) Zr MOFs containing L9-L11 and b) Hf MOFs containing L9 and L11 only.

The  $N_2$  uptake experiments reveal the high porosity of the materials, while the observed steps in the isotherms in the low  $P/P_0$  range are characteristic of the filling of the two different types of pores within the structures.<sup>15</sup> For the UiO-66 topology MOFs (**Zr-L9**, **Hf-L9**, **Zr-L10**) the steps are due to preferential filling of the smaller tetrahedral pores prior to filling of the larger octahedral pores, while for the interpenetrated derivatives (**Zr-L11** and **Hf-L11**) it is the result of filling of the smaller tetrahedral pores before the larger tetrahedral pores. In the interpenetrated MOFs the  $Zr_6/Hf_6$  clusters of the second framework occupy the octahedral pores of the first framework, reducing the octahedral pore into smaller tetrahedral pores. The calculated BET surface areas further prove the high permanent porosity of the frameworks containing the extended ligands (Table 2.4).

**Table 2.4.** Calculated BET surface areas of the extended Zr and Hf MOFs.

	<b>L9</b>	<b>L10</b>	<b>L11</b>
<b>Zr</b>	3280 m <sup>2</sup> g <sup>-1</sup>	3850 m <sup>2</sup> g <sup>-1</sup>	2680 m <sup>2</sup> g <sup>-1</sup>
<b>Hf</b>	2730 m <sup>2</sup> g <sup>-1</sup>	n/a	2080 m <sup>2</sup> g <sup>-1</sup>

Incorporation of longer ligands results in more porous frameworks which correlates with the increase in BET surface area of **Zr-L10** compared with **Zr-L9**. Despite framework interpenetration, **Zr-L11** and **Hf-L11** maintain their high porosity and although the pores are reduced in size they are still accessible to  $N_2$ . The porosity of the MOFs correlates well with the inclusion of longer ligands and this is also evidenced by an increase in the unit cell

dimensions, revealed by shifting of peaks to lower values of  $2\theta$  in the PXRD patterns and is also evident in the single crystal X-ray structures.

Access to bulk phase-pure microcrystalline and single crystal samples of the MOFs containing extended ligands has enabled in-depth studies into their mechanical properties to be conducted. This is an extension of an earlier study investigating differences in the mechanical properties of Zr MOFs containing either flexible or rigid ligands.<sup>9</sup> The presence of integral unsaturated functional units presents reactive sites within the MOFs for integral postsynthetic modification (PSM). Comprehensive integral PSM studies were performed on the Zr and Hf MOFs and these are discussed in detail in Chapter 3.

## 2.9 Conclusions and Future Work

To conclude, it has been shown that amino acids, in particular L-proline, when used in concert with HCl are able to effectively modulate the syntheses of Zr and Hf MOFs. The L-proline modulation protocol is ineffective for terephthalate based Zr and Hf MOFs, but when longer ligands are used (e.g. 2,6-naphthalenedicarboxylic acid – L5) obvious improvements in crystallinity are revealed by PXRD analysis. Using a comprehensive range of ligands with different functionality and of varying lengths a wide range of high quality materials were obtained. The developed modulation conditions require as little as 4-5 equivalents of L-proline which is a major reduction compared with the quantities typically required during conventional modulation procedures. The reaction conditions were successfully integrated to microwave assisted synthetic methods, allowing highly crystalline materials to be obtained in short timescales.

Fine-tuning of reaction conditions in many cases resulted in the isolation of single crystals suitable for single crystal X-ray diffraction. Accessing single crystals enabled highly specialised techniques, namely single crystal nanoindentation and high pressure X-ray diffraction, to be used to develop a greater understanding of the mechanical properties of Zr MOFs and how they are influenced by the choice of bridging organic ligand. It was observed that flexible organic ligands greatly alter the mechanical properties of the MOFs and as such a series of extended ligands were designed and conveniently synthesised by Sonagashira cross coupling reactions. The extended ligands were successfully incorporated into Zr and Hf MOFs, and in the case of the longest ligand, L11, interpenetrated materials were obtained.

The presence of alkene, alkyne and butadiyne units within L8-L11 presents sites for integral PSM when they are contained within Zr and Hf MOFs. Postsynthetic halogenation of the unsaturated sites was investigated and is discussed in detail in Chapter 3.

Amino acid modulation of Zr and Hf MOFs has been limited to UiO-66 type MOFs or interpenetrated derivatives in the case of MOFs containing L11. As the interest in Zr and Hf MOFs has increased alternative topologies have been discovered when ligands with different geometries are incorporated. Zr and Hf MOFs containing trigonal and tetrahedral ligands are known and similar to UiO-66 type materials synthetic modulators are required during their



syntheses. Amino acid modulation could be extended to these alternative structure types and if effective it may provide access to new frameworks with interesting properties not obtainable at present using conventional modulators. Moreover, amino acid modulation could be extended to the synthesis of MOFs containing metals other than Zr or Hf. For instance, it is reasonable to assume that amino acids may be beneficial for the synthesis of Ti MOFs. Ti MOFs are reported infrequently due to their difficult syntheses, however the few known structures are interesting and have been investigated for photocatalytic applications.<sup>44,45</sup>

It has been demonstrated that amino acids are effective modulators for the synthesis of a wide variety of Zr and Hf MOFs, although we are relatively unaware of the modulation mechanism. There are a number of plausible reasons for the effective modulation of Zr and Hf MOFs by L-proline, such as competitive coordination with the bridging organic ligand to the metal clusters as they form in solution or a pH buffering effect. A greater understanding of the modulation mechanism would be beneficial to direct future MOF synthesis attempts. In-situ techniques are required to determine the mechanism of modulation. Useful techniques include in-situ PXRD,<sup>46</sup> mass spectrometry, which can be used at set time-intervals to determine mononuclear/cluster species formed in solution, and finally turbidity measurements which would be useful for determining the rate of MOF formation.<sup>47</sup> A better understanding of the mechanism of modulation is required to allow access to more interesting MOF structures, and this information is likely to be obtained from in-situ characterisation techniques.

## 2.10 Experimental

### 2.10.1 General Experimental Remarks

All ligands, modulators, chemicals and solvents were purchased from Alfa Aesar, Acros Organics, Fisher Scientific, Fluorochem, Sigma-Aldrich, and Tokyo Chemical Industry and used without further purification.

**Powder X-ray diffraction (PXRD):** PXRD measurements were carried out at 298 K using a PANalytical X'Pert PRO diffractometer ( $\lambda$  (CuK $\alpha$ ) = 1.5405 Å) on a mounted bracket sample stage. Data were collected over the range  $2\theta = 3\text{--}45^\circ$  or  $5\text{--}45^\circ$ . PXRD patterns were predicted from single crystal data using Mercury 3.7.<sup>48</sup> (University of Glasgow)

**Microwave synthesis:** Microwave reactions were performed in 35 ml pressure vials using a CEM Discover SP microwave equipped with an Explorer 12 Hybrid autosampler. The power was allowed to fluctuate to maintain a constant temperature of 100 °C throughout the reaction. (University of Glasgow)

**Single crystal X-ray diffraction (SCXRD):** Single crystals were mounted onto MiTiGen Microloops<sup>TM</sup> for data collection. Data for **Zr-L6**, **Zr-L7**, **Hf-L7** and **Zr-L8** were collected on a Bruker Smart Apex II diffractometer with graphite monochromated MoK $\alpha$  radiation ( $\lambda = 0.71073$  Å). Data for **Hf-L6** were collected on Agilent Technologies SuperNova diffractometer using CuK $\alpha$  radiation ( $\lambda = 1.5418$  Å). (University of Edinburgh)

Data for **Zr-L9**, **Hf-L9**, **Zr-L10** and **Zr-L11** were collected using a Rigaku AFC12 goniometer equipped with an enhanced sensitivity (HG) Saturn724+ detector mounted at the window of an FR-E+ SuperBright molybdenum rotating anode generator ( $\lambda = 0.71073$  Å) with VHF Varimax optics (70  $\mu\text{m}$  focus) equipped with an Oxford Cryosystems cryostream device. (EPSRC UK National Crystallography Service)

Data for **Hf-L11** were collected using a Bruker ApexII CCD kappa goniometer with a Mo sealed tube source ( $\lambda = 0.71073$  Å) and equipped with an Oxford Cryosystems n-Helix device. (University of Glasgow)

**Scanning electron microscopy (SEM):** Powder samples were deposited onto conductive carbon tabs mounted on an aluminium stub and coated with Pd for 150 seconds using a Polaron SC7640 sputter coater. The prepared samples were transferred to and imaged using a Philips XL30 ESEM tungsten filament electron microscope, operating at an acceleration voltage of 20 kV. (University of Glasgow)

**Gas uptake:** N<sub>2</sub> adsorption/desorption isotherms were collected at 77 K on a Quantachrome Autosorb iQ gas sorption analyser. Samples were degassed under vacuum at 120 °C for 20 hours using the internal turbo pump. BET surface areas were calculated from the isotherms using the Micropore BET Assistant and pore-size distribution analysis was carried out using QSDFT (N<sub>2</sub> on carbon at 77 K, slit/cylindrical pore model) both in the Quantachrome ASiQwin operating software. (University of Glasgow)

**Thermogravimetric analysis (TGA):** Measurements were carried out using a TA Instruments Q500 thermogravimetric analyser. Measurements were collected from room temperature to 1000 °C with a heating rate of 10 °C/min. The measurements were performed under an N<sub>2</sub> atmosphere for Zr/Hf MOFs containing L1-L8, whilst an air atmosphere was used for Zr/Hf MOFs containing L9-L11. (University of Glasgow)

**Nuclear magnetic resonance (NMR):** Spectra were recorded on either a Bruker AVIII 400 MHz spectrometer or a Bruker AVI 500 MHz spectrometer at room temperature (unless stated otherwise) and referenced to residual solvent peaks. (University of Glasgow)

### 2.10.2 Amino Acid Modulation of Zr MOFs Containing L1-L8

The effect of amino acid modulation was examined using a general synthetic procedure for Zr MOFs containing L1-L8. Tables 6.1-6.8 contain full synthetic parameters for the Zr modulation experiments and are provided in the Appendix, Chapter 6.

The amino acid (2.25 mmol, 5 eq) was added directly to a 50 ml Pyrex screw top jar followed by addition of ZrCl<sub>4</sub> (0.105 g, 0.45 mmol, 1 eq) as a 5 ml *N,N*-dimethylformamide (DMF, reagent grade) solution containing concentrated HCl (0.04 ml). The resulting mixture was sonicated for 5 minutes. The ligand (0.45 mmol, 1 eq) was subsequently added to the reaction

flask as a DMF solution (5 ml). The reaction mixture was subject to sonication for a further 5 minutes to aid solvation of the reactants. The glass jar was placed in the oven at 120 °C for a period of 24 hours before being removed and allowed to cool to room temperature. The products were added to centrifuge tubes and collected by centrifugation, washing once with fresh DMF (30 ml) and twice with MeOH (2 x 30 ml). It was subsequently found that **Zr-L8** was sensitive to MeOH, and so in these cases MeOH was replaced by acetone. The products were dried in a desiccator under vacuum where they remained until analysed by PXRD.

### 2.10.3 Amino Acid Modulation of Hf MOFs Containing L1-L8

The effect of amino acid modulation was examined using a general synthetic procedure for the Hf MOFs containing L1-L8. Tables 6.9-6.16 contain full synthetic parameters for the Zr modulation experiments and are provided in the Appendix, Chapter 6.

The amino acid (2.25 mmol, 5 eq) was added directly to a 50 ml Pyrex screw top jar followed by addition of HfCl<sub>4</sub> (0.144 g, 0.45 mmol, 1 eq) as a 5 ml DMF solution containing concentrated HCl (0.04 ml). The resulting mixture was sonicated for 5 minutes. The ligand (0.45 mmol, 1 eq) was subsequently added to the reaction flask as a DMF solution (5 ml). The reaction mixture was subject to sonication for a further 5 minutes to aid solvation of the reactants. The glass jar was placed in the oven at 120 °C for a period of 24 hours before being removed and allowed to cool to room temperature. The products were added to centrifuge tubes and collected by centrifugation, washing once with fresh DMF (30 ml) and twice with MeOH (2 x 30 ml). It was subsequently found that **Hf-L8** was sensitive to MeOH, and so in these cases MeOH was replaced by acetone. The products were dried in a desiccator under vacuum where they remained until analysed by PXRD.

### 2.10.4 Zr-L6 and Hf-L6 L-Proline/HCl Modulator Comparison

The ability of L-proline and HCl to independently modulate the syntheses of **Zr-L6** and **Hf-L6** was systematically investigated. Syntheses were performed under the same conditions as those described in Sections 2.10.2 and 2.10.3 respectively, either in the presence of no modulator, one of the two modulators or both modulators. PXRD was used to assess the effect of the modulators on the MOFs' crystallinity.

### 2.10.5 Zr-L6 L-Proline Concentration Investigation

The effect of L-proline modulator concentration on the synthesis of **Zr-L6** was examined by carrying out syntheses under the same conditions as described in Section 2.10.2, but with varying amounts of L-proline modulator added to the solvothermal reactions (Table 2.5). Samples were washed with acetone rather than methanol after synthesis.

**Table 2.5.** Synthetic parameters for L-proline modulated syntheses of **Zr-L6**.

<b>L6-H<sub>2</sub></b>		<b>ZrCl<sub>4</sub></b>		<b>HCl</b>	<b>L-Proline</b>		
<b>Moles (mmol)</b>	<b>Mass (g)</b>	<b>Moles (mmol)</b>	<b>Mass (g)</b>	<b>Volume (ml)</b>	<b>Equivalents</b>	<b>Moles (mmol)</b>	<b>Mass (g)</b>
0.45	0.1090	0.45	0.1049	0.04	0	0	0
0.45	0.1090	0.45	0.1049	0.04	2	0.90	0.1036
0.45	0.1090	0.45	0.1049	0.04	4	1.80	0.2072
0.45	0.1090	0.45	0.1049	0.04	6	2.70	0.3109
0.45	0.1090	0.45	0.1049	0.04	8	3.60	0.4145
0.45	0.1090	0.45	0.1049	0.04	10	4.50	0.5181

### 2.10.6 Bulk Synthesis of Zr and Hf MOFs Containing L5-L8

Zr and Hf MOFs containing L5-L8 were synthesised in bulk quantities using the general synthetic procedures (Sections 2.10.2 and 2.10.3 for Zr and Hf respectively), with five equivalents of L-proline used in all cases due to its superior modulating properties. For activation, the MOFs were placed in 50 ml reagent bottles and immersed in 25 ml THF, dispersed by stirring and placed in the oven at 50 °C. The THF was replenished and the process repeated consecutively over four days. After this period the THF was removed and the MOFs were placed in a vacuum desiccator. The THF activated samples were used for the remainder of the analysis, however in some cases lower than expected surface areas were obtained. This was the case for **Zr-L7**, **Hf-L5**, **Hf-L7** and **Hf-L8** and alternative activation conditions were used on samples to be analysed by N<sub>2</sub> uptake experiments. The activation conditions were similar to those detailed above involving THF but instead CHCl<sub>3</sub> was used and the MOFs were left to settle at room temperature rather than at 50 °C.

### 2.10.7 Microwave Assisted Synthesis of Zr-L6

L-proline (0.259 g, 2.25 mmol 5 eq), L6-H<sub>2</sub> (0.109 g, 0.45 mmol, 1 eq) and ZrCl<sub>4</sub> (0.105 g, 0.45 mmol, 1 eq) were added to a 35 ml microwave vial. DMF (10 ml) was added, followed by concentrated HCl (0.04 ml) and the vial was sealed. The reaction vessel was then subject to an automated microwave programme consisting of 5 minutes of stirring at 30 °C to homogenously distribute the reagents, followed by heating at 100 °C for 1 hour without stirring. The bulk material was collected from the vial upon completion, centrifuged once with fresh DMF (30 ml) and twice with acetone (2 x 30 ml), before being placed in a desiccator under vacuum for drying. For activation, **Zr-L6** was added to a 50 ml Pyrex reagent bottle and stirred in CHCl<sub>3</sub>, then left to settle. The CHCl<sub>3</sub> was exchanged for fresh CHCl<sub>3</sub> a further 2 times over 48 hours, before being collected by centrifugation and placed in a desiccator under vacuum for drying.

### 2.10.8 Single Crystal Synthesis of Zr-L6, Zr-L7, Zr-L8, Hf-L6 and Hf-L7

#### Zr-L6

ZrCl<sub>4</sub> (0.210 g, 0.90 mmol, 1 eq), L6-H<sub>2</sub> (0.218 g, 0.90 mmol, 1 eq) and L-proline (0.500 g, 4.50 mmol, 5 eq) were added to a 50 ml screw top Pyrex jar. 20 ml of DMF was added, followed by concentrated HCl (0.08 ml, 1 eq). The reaction mixture was sonicated for several minutes until a homogeneous white suspension remained. The white suspension was transferred to an acid digestion vessel and sealed before being placed in the oven at 120 °C for 24 hours. The reaction vessel was removed from the oven and allowed to cool to room temperature. The contents of the acid digestion vessel were removed by pipette and added to a 50 ml centrifuge tube. The reaction DMF was exchanged for fresh DMF several times. The crystals were retained in DMF before being analysed by SCXRD.

**Crystal data for Zr-L6.** Zr<sub>6</sub>O<sub>4</sub>(OH)<sub>4</sub>(C<sub>14</sub>H<sub>8</sub>O<sub>4</sub>)<sub>6</sub>,  $M_r = 2116.61$ , crystal dimensions 0.05 x 0.05 x 0.02 mm, Cubic,  $a = 26.8564 (5) \text{ \AA}$ ,  $V = 19370.6 (11) \text{ \AA}^3$ ,  $T = 120 \text{ K}$ , space group *Fm-3m* (no. 225),  $Z = 4$ , 31465 reflections measured, 568 unique ( $R_{\text{int}} = 0.138$ ), which were used in all calculations. The final  $R_I = 0.034$  for 447 observed data [ $F^2 > 2\sigma(F^2)$ ] and  $wR_2(F^2) = 0.087$  (all data). Using the SQUEEZE algorithm within PLATON<sup>49</sup> the pore volume and electron density within the voids were calculated and found to be  $13769 \text{ \AA}^3$  and 1696

electrons per unit cell (the equivalent of ~42 molecules of DMF) respectively. Crystal structure data for **Zr-L6** is available from the CCDC, deposition number 1441659.

### Zr-L7

ZrCl<sub>4</sub> (0.052 g, 0.225 mmol, 1 eq), L7-H<sub>2</sub> (0.061 g, 0.225 mmol, 1 eq) and L-proline (0.104 g, 0.900 mmol, 4 eq) were added to a 50 ml screw top Pyrex jar. 10 ml of DMF was added and the mixture was sonicated for 5 minutes. Concentrated HCl (0.02 ml, 1 eq) was added to the resulting suspension and the jar was placed in the sonicator for 5 minutes. The glass jar was placed in the oven at 100 °C for 48 hours, and allowed to cool to room temperature after it was removed. The reaction solvent was exchanged for fresh DMF several times. The crystals were retained in DMF before being analysed by SCXRD.

**Crystal data for Zr-L7.** Zr<sub>6</sub>O<sub>4</sub>(OH)<sub>4</sub>(C<sub>14</sub>H<sub>8</sub>N<sub>2</sub>O<sub>4</sub>)<sub>6</sub>,  $M_r = 2368.73$ , crystal dimensions 0.20 x 0.20 x 0.10 mm, Cubic, 29.3248 (8) Å,  $V = 25217.7 (12) \text{ Å}^3$ ,  $T = 100 \text{ K}$ , space group *Fm-3m* (no. 225),  $Z = 4$ , 35050 reflections measured, 772 unique ( $R_{\text{int}} = 0.083$ ), which were used in all calculations. The final  $R_I = 0.083$  for 532 observed data [ $F^2 > 2\sigma(F^2)$ ] and  $wR_2(F^2) = 0.096$  (all data). Using the SQUEEZE algorithm within PLATON<sup>49</sup> the pore volume and electron density within the voids were calculated and found to be 17672 Å<sup>3</sup> and contain 5439 electrons per unit cell (the equivalent of ~136 molecules of DMF) respectively. Crystal structure data for **Zr-L7** is available from the CCDC, deposition number 1441660.

### Zr-L8

ZrCl<sub>4</sub> (0.052 g, 0.225 mmol, 1 eq), L8-H<sub>2</sub> (0.060 g, 0.225 mmol, 1 eq) and L-proline (0.104 g, 0.900 mmol, 4 eq) were added to a 50 ml screw top Pyrex jar. 10 ml of DMF was added and the mixture was sonicated for 5 minutes. Concentrated HCl (0.02 ml, 1 eq) was added to the resulting suspension and the jar was placed in the sonicator for 5 minutes. The glass jar was placed in the oven at 100 °C for 48 hours, and allowed to cool to room temperature after it was removed. The reaction DMF was exchanged for fresh DMF several times. The crystals were retained in DMF before being analysed by SCXRD.

**Crystal data for Zr-L8.** Zr<sub>6</sub>O<sub>4</sub>(OH)<sub>4</sub>(C<sub>16</sub>H<sub>10</sub>O<sub>4</sub>)<sub>6</sub>,  $M_r = 3235.71$ , crystal dimensions 0.07 x 0.07 x 0.07 mm, Cubic,  $a = 29.8884 (3) \text{ Å}$ ,  $V = 26699.9 (8) \text{ Å}^3$ ,  $T = 100 \text{ K}$ , space group *Fm-3m* (no. 225),  $Z = 4$ , 95174 reflections measured, 1235 unique ( $R_{\text{int}} = 0.068$ ), which were used

in all calculations. The final  $R_I = 0.0761$  for 951 observed data [ $F > 2\sigma(F)$ ] and  $wR_2(F) = 0.0871$  (all data). Using the SQUEEZE algorithm within PLATON<sup>49</sup> the pore volume and electron density within the voids were calculated and found to be 17550 Å<sup>3</sup> and 5529 electrons per unit cell (the equivalent of ~138 molecules of DMF) respectively. Crystal structure data for **Zr-L8** is available from the CCDC, deposition number 1418959.

### Hf-L6

HfCl<sub>4</sub> (0.144 g, 0.45 mmol, 1 eq) and L-proline (0.259 g, 2.25 mmol, 5 eq) were added to a 50 ml screw top Pyrex jar. 10 ml of DMF was added and the jar was placed in the sonicator for 5 minutes. L6-H<sub>2</sub> (0.109 g, 0.45 mmol, 1 eq) and concentrated HCl (0.04 ml) were added to the resulting suspension and the jar was placed in the sonicator for 5 minutes. The glass jar was placed in the oven at 120 °C for 24 hours. The glass jar was removed from the oven and allowed to cool to room temperature. The reaction DMF was exchanged for fresh DMF several times. The crystals were retained in DMF before being analysed by SCXRD.

**Crystal data for Hf-L6.** Hf<sub>6</sub>O<sub>4</sub>(OH)<sub>4</sub>(C<sub>14</sub>H<sub>8</sub>O<sub>4</sub>)<sub>6</sub>,  $M_r = 2644.26$ , crystal dimensions 0.05 x 0.05 x 0.05 mm, Cubic,  $a = 26.762(3)$  Å,  $V = 19167(6)$  Å<sup>3</sup>,  $T = 120$  K, space group *Fm-3m* (no. 225),  $Z = 4$ , 44943 reflections measured, 1059 unique ( $R_{\text{int}} = 0.083$ ), which were used in all calculations. The final  $R_I = 0.0373$  for 1013 observed data [ $F^2 > 2\sigma(F^2)$ ] and  $wR_2(F^2) = 0.1001$  (all data). Using the SQUEEZE algorithm within PLATON<sup>49</sup> the pore volume and electron density within the voids were calculated and found to be 11923 Å<sup>3</sup> and contain 6115 electrons per unit cell (the equivalent of ~153 molecules of DMF) respectively. Crystal structure data for **Hf-L6** is available from the CCDC, deposition number 1442842.

### Hf-L7

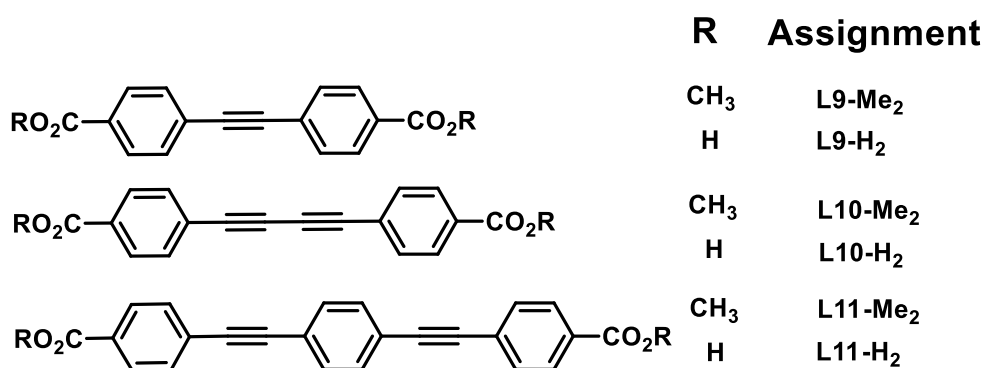
HfCl<sub>4</sub> (0.144 g, 0.45 mmol, 1 eq) and L-proline (0.155 g, 1.35 mmol, 3 eq) were added to a 50 ml screw top Pyrex jar. 10 ml of DMF was added and the jar was placed in the sonicator for 5 minutes. L7-H<sub>2</sub> (0.122 g, 0.45 mmol, 1 eq) and concentrated HCl (0.04 ml) were added to the resulting suspension and the jar was placed in the sonicator for 5 minutes. The glass jar was placed in the oven at 120 °C for 24 hours. The glass jar was removed from the oven and allowed to cool to room temperature. The reaction DMF was exchanged for fresh DMF several times. The crystals were retained in DMF before being analysed by SCXRD.



**Crystal data for Hf-L7.**  $\text{Hf}_6\text{O}_4(\text{OH})_4(\text{C}_{14}\text{H}_8\text{N}_2\text{O}_4)_6$ ,  $M_r = 2896.38$ , crystal dimensions 0.20 x 0.20 x 0.10 mm, Cubic,  $a = 29.3248(8) \text{ \AA}$ ,  $V = 25218(2) \text{ \AA}^3$ ,  $T = 150 \text{ K}$ , space group  $Fm-3m$  (no. 225),  $Z = 4$ , 10347 reflections measured, 954 unique ( $R_{\text{int}} = 0.073$ ), which were used in all calculations. The final  $R_1 = 0.0739$  for 750 observed data [ $F^2 > 2\sigma(F^2)$ ] and  $wR_2(F^2) = 0.1634$  (all data). Using the SQUEEZE algorithm within PLATON<sup>49</sup> the pore volume and electron density within the voids were calculated and found to be  $17151 \text{ \AA}^3$  and 4188 electrons per unit cell (the equivalent of ~105 molecules of DMF) respectively. Crystal structure data for **Hf-L7** is available from the CCDC, deposition number 1442841.

### 2.10.9 Extended Ligand Synthesis

Following the success of L-proline modulation of Zr and Hf MOFs containing longer ligands (**L5-L8**) the following extended ligands were designed and synthesised (Scheme 2.1).



**Scheme 2.1.** Schematic representation of the extended ligands synthesised for incorporation into Zr and Hf MOFs.

The compound dimethyl 4,4'-ethynylenedibenzoate (**L9-Me<sub>2</sub>**) was synthesised according to modified literature procedures with subsequent saponification resulting in 4,4'-ethynylenedibenzoic acid (**L9-H<sub>2</sub>**).<sup>50</sup>

#### **L9-Me<sub>2</sub>**

Methyl-4-iodobenzoate (5.241 g, 20.00 mmol, 2 eq), bis(triphenylphosphine) palladium(II) dichloride (0.140 g, 0.20 mmol) and copper(I) iodide (0.120 g, 0.63 mmol) were added to a 250 ml round bottom flask under an  $\text{N}_2$  atmosphere. 1,8-Diazabicyclo[5.4.0]undec-7-ene (40 ml) and TEA (20 ml) were added and the mixture was stirred. Trimethylsilylacetylene (1.40

ml, 10.00 mmol, 1 eq) and H<sub>2</sub>O (0.14 ml) were added and the reaction was left to stir for 2 hours under an N<sub>2</sub> atmosphere. The reaction was stopped by the addition of H<sub>2</sub>O, with addition continued until no further precipitation of the product was observed. The red solid that remained was collected by vacuum filtration. The product was purified by recrystallisation in EtOAc to yield a light coloured solid (2.460 g, 8.37 mmol, 84%). <sup>1</sup>H NMR (CDCl<sub>3</sub>): δ/ppm 3.93 (s, 6H), 7.60 (d, 4H, *J* = 8.6 Hz), 8.04 (d, 4H, *J* = 8.6 Hz); <sup>13</sup>C NMR (CDCl<sub>3</sub>): δ/ppm 52.4 (CH<sub>3</sub>), 91.5 (C), 127.5 (C), 129.7 (CH), 130.1 (C), 131.8 (CH), 166.6 (C); HRMS (ESI) calculated for C<sub>18</sub>H<sub>15</sub>O<sub>4</sub> (M+H)<sup>+</sup> 295.0970, found *m/z* 295.0973.

### L9-H<sub>2</sub>

L9-Me<sub>2</sub> (2.421 g, 8.23 mmol, 1 eq) was dissolved in EtOH in a round bottom flask (240 ml) with stirring. Potassium hydroxide (4.618 g, 82.30 mmol, 10 eq) was dissolved separately in H<sub>2</sub>O (240 ml), then added to the EtOH solution containing the diester. The mixture was left to stir under reflux at 85 °C overnight. The transparent solution was then removed from the heat and allowed to cool to room temperature, before the product was precipitated by addition of 1 M HCl (aq). The white solid was collected by vacuum filtration and washed with copious amounts of water until the washings were pH neutral. The product was dried under vacuum (2.060 g, 7.74 mmol, 94%). <sup>1</sup>H NMR (DMSO-*d*<sub>6</sub>): δ/ppm 7.71 (d, 4H, *J* = 8.5 Hz), 7.99 (d, 4H, *J* = 8.5 Hz), 13.21 (br s, 2H); <sup>13</sup>C NMR (DMSO-*d*<sub>6</sub>): δ/ppm 91.0 (C), 126.0 (C), 129.6 (CH), 131.0 (C), 131.7 (CH), 166.6 (C); HRMS (ESI) calculated for C<sub>16</sub>H<sub>9</sub>O<sub>4</sub> (M-H)<sup>-</sup> 265.0501, found *m/z* 265.0497.

The precursor methyl 4-ethynylbenzoate, required for the synthesis of L10-Me<sub>2</sub> and L11-Me<sub>2</sub>, was obtained via deprotection of methyl 4-(2-(trimethylsilyl)ethynyl)benzoate.<sup>51</sup>

### Methyl 4-(2-(trimethylsilyl)ethynyl)benzoate

Methyl 4-iodobenzoate (11.400 g, 43.50 mmol, 1 eq) and trimethylsilylacetylene (6.80 ml, 47.77 mmol, 1.1 eq) were added to a stirring solution of THF (80 ml) and TEA (20 ml). The solution was degassed for 10 minutes before bis(triphenylphosphine)palladium(II) dichloride (0.914 g, 1.30 mmol) and copper(I) iodide (0.496 g, 2.60 mmol) were added under an N<sub>2</sub> atmosphere. The reaction mixture was subject to reflux at 80 °C for 4 hours under an N<sub>2</sub> atmosphere. After cooling to room temperature, the resulting mixture was filtered over celite and washed with diethyl ether until washings were colourless. The organic phase was washed with saturated NH<sub>4</sub>Cl (aq) (2 x 100 ml), brine (1 x 100 ml), dried over MgSO<sub>4</sub> and the filtrate

collected. The solvent was removed under reduced pressure to yield a dark solid. The product was purified by flash chromatography eluting hexane:DCM (2:1), yielding the product as a light coloured solid (8.508 g, 36.60 mmol, 84%).  $^1\text{H}$  NMR ( $\text{CDCl}_3$ ):  $\delta/\text{ppm}$  0.26 (s, 9H), 3.91 (s, 3H), 7.52 (d, 2H,  $J = 8.6$  Hz), 7.97 (d, 2H,  $J = 8.6$  Hz);  $^{13}\text{C}$  NMR ( $\text{CDCl}_3$ ):  $\delta/\text{ppm}$  0.0 ( $\text{CH}_3$ ), 52.4 ( $\text{CH}_3$ ), 97.9 (C), 104.2 (C), 128.0 (C), 129.5 (CH), 129.9 (C), 132.0 (CH), 166.7 (C); HRMS (CI) calculated for  $\text{C}_{13}\text{H}_{17}\text{O}_2\text{Si}$  ( $\text{M}+\text{H}$ ) $^+$  232.0998, found  $m/z$  232.0995.

### Methyl 4-ethynylbenzoate

Methyl 4-(2-(trimethylsilyl)ethynyl)benzoate (8.508 g, 36.62 mmol, 1 eq) was dissolved in a solution of DCM (200 ml) and MeOH (20 ml) by stirring. Potassium carbonate (10.117 g, 73.20 mmol, 2 eq) was added and the mixture was stirred at room temperature for 3 hours. A colourless filtrate was collected by eluting through a silica plug with MeOH. The solvent was removed under reduced pressure to yield an off white solid. The solid was re-dissolved in  $\text{CHCl}_3$  and filtered to remove any residual silica. The solvent was removed under reduced pressure to yield the final product as a light coloured solid (5.237 g, 32.69 mmol, 89%).  $^1\text{H}$  NMR ( $\text{CDCl}_3$ ):  $\delta/\text{ppm}$  3.23 (s, 1H), 3.92 (s, 3H), 7.55 (d, 2H,  $J = 8.7$  Hz), 8.00 (d, 2H,  $J = 8.7$  Hz);  $^{13}\text{C}$  NMR ( $\text{CDCl}_3$ ):  $\delta/\text{ppm}$  52.4 ( $\text{CH}_3$ ), 80.2 (CH), 82.9 (C), 126.9 (C), 129.6 (CH), 130.3 (C), 132.2 (CH), 166.6 (C); HRMS (CI) calculated for  $\text{C}_{10}\text{H}_8\text{O}_2$  ( $\text{M}$ ) $^+$  160.0524, found  $m/z$  160.0522.

The compound dimethyl 4,4'-(buta-1,3-diyne-1,4-diyl)dibenzoate (L10-Me<sub>2</sub>) was synthesised according to modified literature procedures<sup>52</sup> with subsequent saponification resulting in 4,4'-(buta-1,3-diyne-1,4-diyl)dibenzoic acid (L10-H<sub>2</sub>).<sup>50</sup>

### L10-Me<sub>2</sub>

Methyl 4-ethynylbenzoate (0.641 g, 4.00 mmol, 1 eq), tetramethylethylenediamine (0.60 ml, 4.01 mmol, 1 eq) and DMF (20 ml) were added to a round bottom flask under an  $\text{N}_2$  atmosphere. Copper(II) chloride (0.268 g, 1.99 mmol, 0.5 eq) was added and the reaction mixture was left to stir at 40 °C under an  $\text{N}_2$  atmosphere. After 2 hours, the reaction was quenched by addition of EtOAc. The solvent was removed under reduced pressure, yielding a light green solid. The product was dissolved in  $\text{CHCl}_3$  and washed several times with an aqueous solution of ethylenediaminetetraacetic acid disodium salt dihydrate until a light yellow solution remained. The organic phase was washed with brine (2 x 40 ml), dried over  $\text{MgSO}_4$  and filtered. The filtrate was collected and the solvent removed under reduced

pressure to yield a light yellow solid (0.498 g, 1.56 mmol, 78%).  $^1\text{H}$  NMR ( $\text{CDCl}_3$ ):  $\delta$ /ppm 3.93 (s, 6H), 7.59 (d, 4H,  $J = 8.7$  Hz), 8.02 (d, 4H,  $J = 8.7$  Hz);  $^{13}\text{C}$  NMR ( $\text{CDCl}_3$ ):  $\delta$ /ppm 52.4 ( $\text{CH}_3$ ), 76.3 (C), 81.8 (C), 126.1 (C), 129.6 (CH), 130.6 (C), 132.5 (CH), 166.3 (C); HRMS (CI) calculated for  $\text{C}_{20}\text{H}_{14}\text{O}_4$  ( $\text{M}$ ) $^+$  318.0892, found  $m/z$  318.0895.

### L10-H<sub>2</sub>

L10-Me<sub>2</sub> (0.650 g, 2.04 mmol, 1 eq) was suspended in EtOH (40 ml) with stirring. Potassium hydroxide (0.286 g, 5.10 mmol, 2.5 eq) was dissolved separately in H<sub>2</sub>O (40 ml) then added to the flask containing the diester and subject to reflux overnight. The transparent solution was then removed from the heat and allowed to cool to room temperature, before the product was precipitated by addition of 6 M HCl (aq). The product was collected by centrifugation multiple times with H<sub>2</sub>O (40 ml) until the washings were pH neutral. The light coloured product was dried under vacuum (0.469 g, 1.62 mmol, 79%).  $^1\text{H}$  NMR ( $\text{DMSO}-d_6$ ):  $\delta$ /ppm 7.75 (d, 4H,  $J = 8.6$  Hz), 7.98 (d, 4H,  $J = 8.6$  Hz); HRMS (ESI) calculated for  $\text{C}_{18}\text{H}_9\text{O}_4$  ( $\text{M}-\text{H}$ ) $^-$  289.0506, found  $m/z$  289.0510.

The compound dimethyl 4,4'-[1,4-phenylenebis(ethyne-2,1-diyl)]-dibenzoate (L11-Me<sub>2</sub>) was synthesised according to modified literature procedures<sup>53</sup> with subsequent saponification resulting in 4,4'-[1,4-phenylenebis(ethyne-2,1-diyl)]-dibenzoic acid (L11-H<sub>2</sub>).<sup>54</sup>

### L11-Me<sub>2</sub>

Methyl 4-ethynylbenzoate (2.497 g, 15.59 mmol, 2.5 eq) was dissolved in TEA (160 ml) by stirring. The solution was degassed for 10 minutes, before 1,4-diiodobenzene (2.059 g, 6.24 mmol, 1 eq), bis(triphenylphosphine)palladium(II) dichloride (0.295 g, 0.42 mmol) and copper(I) iodide (0.072 g, 0.38 mmol) were added. The reaction mixture was left to stir at 50 °C overnight under an N<sub>2</sub> atmosphere. The mixture was removed from the heat and once cooled to room temperature the product was collected by vacuum filtration and washed with hexane until washings were colourless. The product was stirred overnight in H<sub>2</sub>O (300 ml), then collected by vacuum filtration. The product was stirred in a minimal volume of DCM, collected by vacuum filtration and dried under vacuum (2.445 g, 6.20 mmol, 99%).  $^1\text{H}$  NMR ( $\text{CDCl}_3$ ):  $\delta$ /ppm 3.94 (s, 6H), 7.54 (s, 4H), 7.60 (d, 4H,  $J = 8.6$  Hz), 8.04 (d, 4H,  $J = 8.6$  Hz); HRMS (ESI) calculated for  $\text{C}_{26}\text{H}_{18}\text{NaO}_4$  ( $\text{M}+\text{Na}$ ) $^+$  417.1103, found  $m/z$  417.1052.

Single crystals of L11-Me<sub>2</sub> were isolated from an NMR solution upon slow evaporation of CDCl<sub>3</sub> (Figure 2.22).

Crystal data for L11-Me<sub>2</sub>. C<sub>26</sub>H<sub>18</sub>O<sub>4</sub>,  $M_r$  = 394.40, crystal dimensions 0.32 x 0.1 x 0.03 mm, Orthorhombic,  $a$  = 7.186 (2) Å,  $b$  = 5.9324 (19) Å,  $c$  = 45.765 (14) Å,  $V$  = 1950.8 (11) Å<sup>3</sup>,  $T$  = 100 K, space group *Pbca* (no. 61),  $Z$  = 4, 9927 measured reflections, 1709 unique ( $R_{\text{int}}$  = 0.196), which were used in all calculations. The final  $R_I$  = 0.108 for 939 observed data [ $R[F^2 > 2\sigma(F^2)]$  and  $wR(F^2) = 0.238$  (all data)]. Crystal structure data for L11-Me<sub>2</sub> is available from the CCDC, deposition number 1516206.

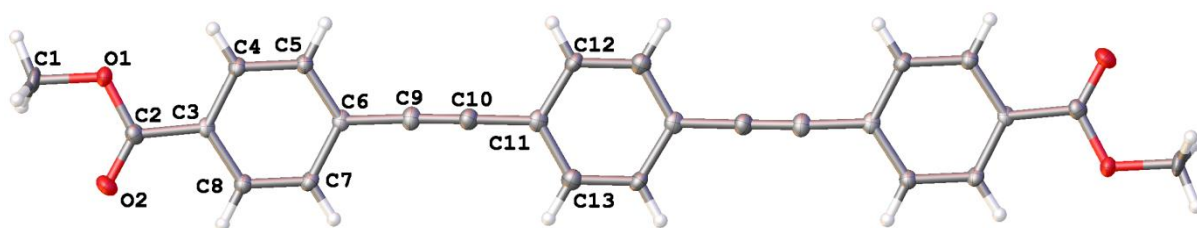


**Figure 2.22.** Portion of the solid state structure and atom labelling scheme (labels for asymmetric unit only) of L11-Me<sub>2</sub>. Displacement ellipsoids are drawn at 50% probability level.

### L11-H<sub>2</sub>

L11-Me<sub>2</sub> (1.892 g, 4.80 mmol, 1 eq) was dissolved in 1:1 MeOH/THF (350 ml). Potassium hydroxide (2.693 g, 48.00 mmol, 10 eq) was dissolved separately in H<sub>2</sub>O by stirring and added to the solution containing the diester. The resulting solution was allowed to reflux overnight at 85 °C. The transparent solution was then removed from the heat and allowed to cool to room temperature, before the product was precipitated by addition of 6 M HCl (aq). The product was collected by vacuum filtration and washed with copious amounts of water until the washings were pH neutral. The light coloured solid was dried under vacuum (0.931 g, 2.54 mmol, 53%). <sup>1</sup>H NMR (DMSO-*d*<sub>6</sub>): δ/ppm 7.67 (s, 4H), 7.70 (d, 4H,  $J$  = 8.6 Hz), 8.0 (d, 4H,  $J$  = 8.6 Hz); <sup>13</sup>C NMR (DMSO-*d*<sub>6</sub>): δ/ppm 90.6 (C), 91.2 (C), 122.3 (C), 126.1 (C), 129.3 (CH), 130.8 (C), 131.4 (CH), 131.7 (CH), 166.4 (C); HRMS (ESI) calculated for C<sub>24</sub>H<sub>12</sub>O<sub>4</sub>Na (M-2H+Na)<sup>+</sup> 387.0639, found  $m/z$  387.0620.

### 2.10.10 Bulk Synthesis Zr and Hf MOFs Containing L9-L11

It was not possible to reliably synthesise bulk samples of **Hf-L10** with the materials obtained often displaying poor crystallinity and stability issues. This MOF was therefore not studied further during our investigations.

#### Zr-L9

L-proline (0.259 g, 2.25 mmol, 5 eq), L9-H<sub>2</sub> (0.120 g, 0.45 mmol, 1 eq) and ZrCl<sub>4</sub> (0.105 g, 0.45 mmol, 1 eq) were added to a 35 ml microwave vial. To the vial 10 ml of DMF was added, followed by concentrated HCl (0.04 ml) and the vial was sealed. The reaction vessel was then subject to an automated microwave programme consisting of 10 minutes of stirring at 30 °C to homogenously distribute the reagents, followed by heating at 100 °C for 4 hours without stirring. The bulk material was collected from the vial upon completion, centrifuged once with fresh DMF (30 ml) and twice with acetone (2 x 30 ml), before being dried under vacuum ([Zr<sub>6</sub>O<sub>4</sub>(OH)<sub>4</sub>(L9)<sub>6</sub>]<sub>n</sub>, 0.154 g, 0.068 mmol, 91%).

#### Hf-L9

L-proline (0.259 g, 2.25 mmol, 5 eq), L9-H<sub>2</sub> (0.120 g, 0.45 mmol, 1 eq) and HfCl<sub>4</sub> (0.144 g, 0.45 mmol, 1 eq) were added to a 50 ml Pyrex reagent bottle. To the bottle, 10 ml DMF was added, the mixture was sonicated and, following addition of concentrated HCl (0.04 ml), the bottle was sealed. The reaction vessel was then subject to sonication to aid homogenous distribution of the reagents, followed by heating at 120 °C for 24 hours in the oven. The bulk material was collected from the bottle upon completion, centrifuged once with fresh DMF (30 ml) and twice with acetone (2 x 30 ml), before being dried under vacuum ([Hf<sub>6</sub>O<sub>4</sub>(OH)<sub>4</sub>(L9)<sub>6</sub>]<sub>n</sub>, 0.197 g, 0.071 mmol, 95%).

#### Zr-L10

Benzoic acid (1.649 g, 13.50 mmol, 30 eq), ZrCl<sub>4</sub> (0.105 g, 0.45 mmol, 1 eq) and DMF (20 ml) were added to a 50 ml Pyrex reagent bottle and sonicated for 10 minutes. L10-H<sub>2</sub> (0.131 g, 0.45 mmol, 1 eq) and concentrated HCl (0.04 ml) were added and the suspension was sonicated for a further 10 minutes, before being placed in the oven at 120 °C for 72 hours. The bulk material was collected from the bottle upon completion, centrifuged once with fresh DMF (30 ml) and twice with acetone (2 x 30 ml), before being dried under vacuum ([Zr<sub>6</sub>O<sub>4</sub>(OH)<sub>4</sub>(L10)<sub>6</sub>]<sub>n</sub>, 0.102 g, 0.04 mmol, 53%).

**Zr-L11**

L-proline (0.130 g, 1.13 mmol, 5 eq),  $\text{ZrCl}_4$  (0.052 g, 0.22 mmol, 1 eq) and DMF (10 ml) were added to a 50 ml Pyrex reagent bottle and sonicated for 10 minutes. L11-H<sub>2</sub> (0.082 g, 0.22 mmol, 1 eq) and concentrated HCl (0.02 ml) were added and the suspension was sonicated for a further 10 minutes before being placed in the oven at 120 °C for 60 hours. The bulk material was collected from the bottle upon completion, centrifuged once with fresh DMF (30 ml) and twice with acetone (2 x 30 ml), before being dried under vacuum ( $[\text{Zr}_6\text{O}_4(\text{OH})_4(\text{L11})_6]_n$ , 0.099 g, 0.035 mmol, 95%).

**Hf-L11**

L-proline (0.130 g, 1.13 mmol, 5 eq),  $\text{HfCl}_4$  (0.072 g, 0.22 mmol, 1 eq) and DMF (10 ml) were added to a 50 ml Pyrex reagent bottle and sonicated for 10 minutes. L11-H<sub>2</sub> (0.082 g, 0.22 mmol, 1 eq) and concentrated HCl (0.02 ml) were added and the suspension was sonicated for a further 10 minutes before being placed in the oven at 120 °C for 60 hours. The bulk material was collected from the bottle upon completion, centrifuged once with fresh DMF (30 ml) and twice with acetone (2 x 30 ml), before being dried under vacuum ( $[\text{Hf}_6\text{O}_4(\text{OH})_4(\text{L11})_6]_n$ , 0.120 g, 0.035 mmol, 95%).

**Activation:** Powder samples were added to 50 ml Pyrex reagent bottles and left to stand in  $\text{CHCl}_3$ . The  $\text{CHCl}_3$  was exchanged for fresh  $\text{CHCl}_3$  a further 4 times over 4 days, before being collected by centrifugation and dried under vacuum.

**2.10.11 Single Crystal Synthesis of Zr and Hf MOFs Containing L9-L11**

Similar to bulk syntheses, it was not possible to grow single crystals of **Hf-L10**. After multiple failed attempts to crystallise **Hf-L10** it was decided not to pursue this material any further.

**Zr-L9**

L-proline (0.104 g, 0.90 mmol, 4 eq), L9-H<sub>2</sub> (0.060 g, 0.23 mmol, 1 eq) and  $\text{ZrCl}_4$  (0.052 g, 0.23 mmol, 1 eq) were added to a 50 ml Pyrex reagent bottle. To the bottle 10 ml DMF was added, the mixture was sonicated and following addition of concentrated HCl (0.02 ml) the bottle was sealed. The reaction vessel was then subject to sonication to aid homogenous

distribution of the reagents, followed by heating at 100 °C for 48 hours in the oven. The bottle was removed from the oven after this period, and allowed to cool to room temperature. The crystals were left to stand in their mother solution.

**Crystal data for Zr-L9.**  $\text{Zr}_6\text{O}_4(\text{OH})_4(\text{C}_{16}\text{H}_8\text{O}_4)_6$ ,  $M_r = 2264.69$ , crystal dimensions 0.04 x 0.04 x 0.03 mm, Cubic,  $a = 30.2386$  (4) Å,  $V = 27649.3$  (11) Å<sup>3</sup>,  $T = 100$  K, space group *Fm-3m* (no. 225),  $Z = 4$ , 77174 reflections measured, 1264 unique ( $R_{\text{int}} = 0.102$ ), which were used in all calculations. The final  $R_I = 0.069$  for 1171 observed data [ $F^2 > 2\sigma(F^2)$ ] and  $wR(F^2) = 0.187$  (all data). Over 70% of the cell volume is not occupied by the framework and contains diffuse and disordered solvent molecules. This electron density was accounted for using SQUEEZE within PLATON<sup>49</sup> which calculated a solvent accessible volume of 21365 Å<sup>3</sup> containing 1308 electrons (the equivalent of ~32 molecules of DMF). Crystal structure data for **Zr-L9** is available from the CCDC, deposition number 1062508.

### Hf-L9

L-proline (0.104 g, 0.90 mmol, 4 eq), L9-H<sub>2</sub> (0.060 g, 0.23 mmol, 1 eq) and HfCl<sub>4</sub> (0.072 g, 0.23 mmol, 1 eq) were added to a 50 ml Pyrex reagent bottle. To the bottle 10 ml DMF was added, the mixture was sonicated and following addition of concentrated HCl (0.02 ml) the bottle was sealed. The reaction vessel was then subject to sonication to aid homogenous distribution of the reagents, followed by heating at 100 °C for 48 hours in the oven. The bottle was removed from the oven after this period, and allowed to cool to room temperature. The crystals were left to stand in their mother solution.

**Crystal data for Hf-L9.**  $\text{Hf}_6\text{O}_4(\text{OH})_4(\text{C}_{16}\text{H}_8\text{O}_4)_6$ ,  $M_r = 2788.31$ , crystal dimensions 0.03 x 0.02 x 0.02 mm, Cubic,  $a = 30.1107$  (12) Å,  $V = 27300$  (3) Å<sup>3</sup>,  $T = 100$  K, space group *Fm-3m* (no. 225),  $Z = 4$ , 23032 reflections measured, 1601 unique ( $R_{\text{int}} = 0.034$ ), which were used in all calculations. The final  $R_I = 0.046$  for 1495 observed data [ $F^2 > 2\sigma(F^2)$ ] and  $wR(F^2) = 0.131$  (all data). Over 70% of the cell volume is not occupied by the framework and contains diffuse and disordered solvent molecules. This electron density was accounted for using SQUEEZE within PLATON<sup>49</sup> which calculated a solvent accessible volume of 20364 Å<sup>3</sup> containing 3439 electrons (the equivalent of ~86 molecules of DMF). Crystal structure data for **Hf-L9** is available from the CCDC, deposition number 1062509.



**Zr-L10**

Benzoic acid (0.824 g, 6.75 mmol, 30 eq),  $\text{ZrCl}_4$  (0.052 g, 0.22 mmol, 1 eq) and 13 ml DMF were added to a 50 ml Pyrex reagent bottle and sonicated. L10- $\text{H}_2$  (0.065 g, 0.22 mmol, 1 eq) and concentrated HCl (0.02 ml) were added and the suspension was sonicated, followed by heating at 120 °C for 24 hours in the oven. The bottle was removed from the oven after this period, and allowed to cool to room temperature. The crystals were left to stand in their mother solution.

**Crystal data for Zr-L10.**  $\text{C}_{108}\text{H}_{52}\text{O}_{32}\text{Zr}_6$ ,  $M_r = 2408.81$ , crystal dimensions 0.13 x 0.13 x 0.13 mm, Cubic,  $a = 33.3694$  (3) Å,  $V = 37157.4$  (10) Å<sup>3</sup>,  $T = 100$  K, space group  $Fm-3m$  (no. 225),  $Z = 4$ , 49850 measured reflections, 1676 unique ( $R_{\text{int}} = 0.058$ ), which were used in all calculations. The final  $R_I = 0.219$  for 1424 observed data  $R[F^2 > 2\sigma(F^2)]$  and  $wR(F^2) = 0.605$  (all data). Almost 80% of the cell volume is not occupied by the framework and contains diffuse and disordered solvent molecules. This electron density was accounted for using SQUEEZE within PLATON<sup>49</sup> which calculated a solvent accessible volume of 30003 Å<sup>3</sup> containing 3394 electrons (the equivalent of ~85 molecules of DMF). The high final R-factors are thought to be a consequence of the high level of disorder in the material. Crystal structure data for **Zr-L10** is available from the CCDC, deposition number 1443195.

**Zr-L11**

Benzoic acid (0.824 g, 6.75 mmol, 30 eq),  $\text{ZrCl}_4$  (0.052 g, 0.22 mmol, 1 eq) and DMF (13 ml) were added to a 50 ml Pyrex reagent bottle and sonicated for 10 minutes. L11- $\text{H}_2$  (0.082 g, 0.22 mmol, 1 eq) and concentrated HCl (0.02 ml) were added and the suspension was sonicated for a further 10 minutes before being placed in the oven at 120 °C for 24 hours. The bottles were removed from the oven after this period, and allowed to cool to room temperature. The crystals were left to stand in their mother solution.

**Crystal data for Zr-L11.**  $\text{C}_{144}\text{H}_{76}\text{O}_{32}\text{Zr}_6$ ,  $M_r = 2865.36$ , crystal dimensions 0.08 x 0.08 x 0.08 mm, Cubic,  $a = 39.8116$  (7) Å,  $V = 63100$  (3) Å<sup>3</sup>,  $T = 100$  K, space group  $Fd-3m$  (no. 227),  $Z = 8$ , 85487 measured reflections, 3407 unique ( $R_{\text{int}} = 0.040$ ), which were used in all calculations. The final  $R_I = 0.082$  for 3404 observed data  $R[F^2 > 2\sigma(F^2)]$  and  $wR(F^2) = 0.211$  (all data). Approximately 63% of the cell volume is not occupied by the framework and contains diffuse and disordered solvent molecules. This electron density was accounted for

using SQUEEZE within PLATON<sup>49</sup> which calculated a solvent accessible volume of 40049 Å<sup>3</sup> containing 7636 electrons (the equivalent of ~190 molecules of DMF). Crystal structure data for **Zr-L11** is available from the CCDC, deposition number 1443196.

### **Hf-L11**

Benzoic acid (0.824 g, 6.75 mmol, 30 eq), HfCl<sub>4</sub> (0.072 g, 0.22 mmol, 1 eq) and DMF (13 ml) were added to a 50 ml Pyrex reagent bottle and sonicated for 10 minutes. L11-H<sub>2</sub> (0.082 g, 0.22 mmol, 1 eq) and concentrated HCl (0.02 ml) were added and the suspension was sonicated for a further 10 minutes before being placed in the oven at 120 °C for 24 hours. The bottles were removed from the oven after this period, and allowed to cool to room temperature. The crystals were left to stand in their mother solution.

**Crystal data for Hf-L11.** C<sub>144</sub>H<sub>76</sub>Hf<sub>6</sub>O<sub>32</sub>,  $M_r = 3388.98$ , crystal dimensions 0.11 x 0.10 x 0.10 mm, Cubic,  $a = 39.806$  (5) Å,  $V = 63074$  (25) Å<sup>3</sup>,  $T = 100$  K, space group  $Fd-3m$  (no. 227),  $Z = 8$ , 30725 measured reflections, 2646 unique ( $R_{\text{int}} = 0.225$ ), which were used in all calculations. The final  $R_I = 0.109$  for 1830 observed data  $R[F^2 > 2\sigma(F^2)]$  and  $wR(F^2) = 0.199$  (all data). Approximately 63% of the cell volume is not occupied by the framework and contains diffuse and disordered solvent molecules. This electron density was accounted for using SQUEEZE within PLATON<sup>49</sup> which calculated a solvent accessible volume of 40068 Å<sup>3</sup> containing 19296 electrons (the equivalent of ~482 molecules of DMF). Crystal structure data for **Hf-L11** is available from the CCDC, deposition number 1443197.

## 2.11 References

- (1) Cavka, J. H.; Jakobsen, S.; Olsbye, U.; Guillou, N.; Lamberti, C.; Bordiga, S.; Lillerud, K. P. *J. Am. Chem. Soc.* **2008**, *130*, 13850.
- (2) Bai, Y.; Dou, Y.; Xie, L.-H.; Rutledge, W.; Li, J.-R.; Zhou, H.-C. *Chem. Soc. Rev.* **2016**, *45*, 2327.
- (3) Hu, Z.; Zhao, D. *Dalton Trans.* **2015**, *44*, 19018.
- (4) Kandiah, M.; Nilsen, M. H.; Usseglio, S.; Jakobsen, S.; Olsbye, U.; Tilset, M.; Larabi, C.; Quadrelli, E. A.; Bonino, F.; Lillerud, K. P. *Chem. Mater.* **2010**, *22*, 6632.
- (5) DeCoste, J. B.; Peterson, G. W.; Jasuja, H.; Glover, T. G.; Huang, Y.-G.; Walton, K. S. *J. Mater. Chem. A* **2013**, *1*, 5642.
- (6) Mondloch, J. E.; Katz, M. J.; Planas, N.; Semrouni, D.; Gagliardi, L.; Hupp, J. T.; Farha, O. K. *Chem. Commun.* **2014**, *50*, 8944.
- (7) Wu, H.; Yildirim, T.; Zhou, W. *J. Phys. Chem. Lett.* **2013**, *4*, 925.
- (8) Van de Voorde, B.; Stassen, I.; Bueken, B.; Vermoortele, F.; De Vos, D.; Ameloot, R.; Tan, J.-C.; Bennett, T. D. *J. Mater. Chem. A* **2015**, *3*, 1737.
- (9) Hobday, C. L.; Marshall, R. J.; Murphie, C. F.; Sotelo, J.; Richards, T.; Allan, D. R.; Düren, T.; Coudert, F.-X.; Forgan, R. S.; Morrison, C. A.; Moggach, S. A.; Bennett, T. D. *Angew. Chem. Int. Ed.* **2016**, *55*, 2401.
- (10) Li, H.; Eddaoudi, M.; O'Keeffe, M.; Yaghi, O. M. *Nature* **1999**, *402*, 276.
- (11) Furukawa, H.; Gándara, F.; Zhang, Y.-B.; Jiang, J.; Queen, W. L.; Hudson, M. R.; Yaghi, O. M. *J. Am. Chem. Soc.* **2014**, *136*, 4369.
- (12) Mondloch, J. E.; Bury, W.; Fairen-Jimenez, D.; Kwon, S.; DeMarco, E. J.; Weston, M. H.; Sarjeant, A. A.; Nguyen, S. T.; Stair, P. C.; Snurr, R. Q.; Farha, O. K.; Hupp, J. T. *J. Am. Chem. Soc.* **2013**, *135*, 10294.
- (13) Garibay, S. J.; Cohen, S. M. *Chem. Commun.* **2010**, *46*, 7700.
- (14) Marshall, R. J.; Forgan, R. S. *Eur. J. Inorg. Chem.* **2016**, *2016*, 4310.
- (15) Schaate, A.; Roy, P.; Preuße, T.; Lohmeier, S. J.; Godt, A.; Behrens, P. *Chem. Eur. J.* **2011**, *17*, 9320.
- (16) Guillermin, V.; Ragon, F.; Dan-Hardi, M.; Devic, T.; Vishnuvarthan, M.; Campo, B.; Vimont, A.; Clet, G.; Yang, Q.; Maurin, G.; Férey, G.; Vittadini, A.; Gross, S.; Serre, C. *Angew. Chem. Int. Ed.* **2012**, *51*, 9267.
- (17) Ma, J.; Wong-Foy, A. G.; Matzger, A. J. *Inorg. Chem.* **2015**, *54*, 4591.

- (18) Wang, R.; Wang, Z.; Xu, Y.; Dai, F.; Zhang, L.; Sun, D. *Inorg. Chem.* **2014**, *53*, 7086.
- (19) Morris, W.; Voloskiy, B.; Demir, S.; Gándara, F.; McGrier, P. L.; Furukawa, H.; Cascio, D.; Stoddart, J. F.; Yaghi, O. M. *Inorg. Chem.* **2012**, *51*, 6443.
- (20) Zhang, Q.; Su, J.; Feng, D.; Wei, Z.; Zou, X.; Zhou, H.-C. *J. Am. Chem. Soc.* **2015**, *137*, 10064.
- (21) Mouchaham, G.; Cooper, L.; Guillou, N.; Martineau, C.; Elkaïm, E.; Bourrelly, S.; Llewellyn, P. L.; Allain, C.; Clavier, G.; Serre, C.; Devic, T. *Angew. Chem. Int. Ed.* **2015**, *54*, 13297.
- (22) Zahn, G.; Zerner, P.; Lippke, J.; Kempf, F. L.; Lilienthal, S.; Schroder, C. A.; Schneider, A. M.; Behrens, P. *CrystEngComm* **2014**, *16*, 9198.
- (23) Katz, M. J.; Brown, Z. J.; Colon, Y. J.; Siu, P. W.; Scheidt, K. A.; Snurr, R. Q.; Hupp, J. T.; Farha, O. K. *Chem. Commun.* **2013**, *49*, 9449.
- (24) Gutov, O. V.; Hevia, M. G.; Escudero-Adán, E. C.; Shafir, A. *Inorg. Chem.* **2015**, *54*, 8396.
- (25) Tsuruoka, T.; Furukawa, S.; Takashima, Y.; Yoshida, K.; Isoda, S.; Kitagawa, S. *Angew. Chem. Int. Ed.* **2009**, *48*, 4739.
- (26) McGuire, C. V.; Forgan, R. S. *Chem. Commun.* **2015**, *51*, 5199.
- (27) Schaate, A.; Roy, P.; Godt, A.; Lippke, J.; Waltz, F.; Wiebcke, M.; Behrens, P. *Chem. Eur. J.* **2011**, *17*, 6643.
- (28) Trickett, C. A.; Gagnon, K. J.; Lee, S.; Gándara, F.; Bürgi, H.-B.; Yaghi, O. M. *Angew. Chem. Int. Ed.* **2015**, *54*, 11162.
- (29) Wu, H.; Chua, Y. S.; Krungleviciute, V.; Tyagi, M.; Chen, P.; Yildirim, T.; Zhou, W. *J. Am. Chem. Soc.* **2013**, *135*, 10525.
- (30) Vermoortele, F.; Bueken, B.; Le Bars, G.; Van de Voorde, B.; Vandichel, M.; Houthoofd, K.; Vimont, A.; Daturi, M.; Waroquier, M.; Van Speybroeck, V.; Kirschhock, C.; De Vos, D. E. *J. Am. Chem. Soc.* **2013**, *135*, 11465.
- (31) Shearer, G. C.; Chavan, S.; Ethiraj, J.; Vitillo, J. G.; Svelle, S.; Olsbye, U.; Lamberti, C.; Bordiga, S.; Lillerud, K. P. *Chem. Mater.* **2014**, *26*, 4068.
- (32) Fang, Z.; Bueken, B.; De Vos, D. E.; Fischer, R. A. *Angew. Chem. Int. Ed.* **2015**, *54*, 7234.
- (33) Shearer, G. C.; Chavan, S.; Bordiga, S.; Svelle, S.; Olsbye, U.; Lillerud, K. P. *Chem. Mater.* **2016**, *28*, 3749.
- (34) Sholl, D. S.; Lively, R. P. *J. Phys. Chem. Lett.* **2015**, *6*, 3437.

- (35) Stassen, I.; Bueken, B.; Reinsch, H.; Oudenhoven, J. F. M.; Wouters, D.; Hajek, J.; Van Speybroeck, V.; Stock, N.; Vereecken, P. M.; Van Schaijk, R.; De Vos, D.; Ameloot, R. *Chem. Sci.* **2016**, *7*, 5827.
- (36) Beyzavi, M. H.; Klet, R. C.; Tussupbayev, S.; Borycz, J.; Vermeulen, N. A.; Cramer, C. J.; Stoddart, J. F.; Hupp, J. T.; Farha, O. K. *J. Am. Chem. Soc.* **2014**, *136*, 15861.
- (37) Cliffe, M. J.; Wan, W.; Zou, X.; Chater, P. A.; Kleppe, A. K.; Tucker, M. G.; Wilhelm, H.; Funnell, N. P.; Coudert, F.-X.; Goodwin, A. L. *Nat. Commun.* **2014**, *5*, 4176.
- (38) Bon, V.; Senkovska, I.; Weiss, M. S.; Kaskel, S. *CrystEngComm* **2013**, *15*, 9572.
- (39) Schaate, A.; Dühnen, S.; Platz, G.; Lilienthal, S.; Schneider, A. M.; Behrens, P. *Eur. J. Inorg. Chem.* **2012**, *2012*, 790.
- (40) Li, Y.; Liu, Y.; Gao, W.; Zhang, L.; Liu, W.; Lu, J.; Wang, Z.; Deng, Y.-J. *CrystEngComm* **2014**, *16*, 7037.
- (41) Øien, S.; Wragg, D.; Reinsch, H.; Svelle, S.; Bordiga, S.; Lamberti, C.; Lillerud, K. P. *Cryst. Growth Des.* **2014**, *14*, 5370.
- (42) Ko, N.; Hong, J.; Sung, S.; Cordova, K. E.; Park, H. J.; Yang, J. K.; Kim, J. *Dalton Trans.* **2015**, *44*, 2047.
- (43) Marshall, R. J.; Griffin, S. L.; Wilson, C.; Forgan, R. S. *Chem. Eur. J.* **2016**, *22*, 4870.
- (44) Hendon, C. H.; Tiana, D.; Fontecave, M.; Sanchez, C.; D'arras, L.; Sassoie, C.; Rozes, L.; Mellot-Draznieks, C.; Walsh, A. *J. Am. Chem. Soc.* **2013**, *135*, 10942.
- (45) Zou, L.; Feng, D.; Liu, T.-F.; Chen, Y.-P.; Yuan, S.; Wang, K.; Wang, X.; Fordham, S.; Zhou, H.-C. *Chem. Sci.* **2016**, *7*, 1063.
- (46) Millange, F.; Medina, M. I.; Guillou, N.; Férey, G.; Golden, K. M.; Walton, R. I. *Angew. Chem. Int. Ed.* **2010**, *49*, 763.
- (47) Smith, B. J.; Dichtel, W. R. *J. Am. Chem. Soc.* **2014**, *136*, 8783.
- (48) Macrae, C. F.; Bruno, I. J.; Chisholm, J. A.; Edgington, P. R.; McCabe, P.; Pidcock, E.; Rodriguez-Monge, L.; Taylor, R.; van de Streek, J.; Wood, P. A. *J. Appl. Crystallogr.* **2008**, *41*, 466.
- (49) Spek, A. *Acta Crystallogr. Sect. C* **2015**, *71*, 9.
- (50) Gadzikwa, T.; Zeng, B.-S.; Hupp, J. T.; Nguyen, S. T. *Chem. Commun.* **2008**, 3672.
- (51) Vivas, M. G.; Silva, D. L.; De Boni, L.; Bretonniere, Y.; Andraud, C.; Laibe-Darbour, F.; Mulatier, J. C.; Zalesny, R.; Bartkowiak, W.; Canuto, S.; Mendonca, C. R. *J. Phys. Chem. B* **2012**, *116*, 14677.

- (52) Zhang, G.; Yi, H.; Zhang, G.; Deng, Y.; Bai, R.; Zhang, H.; Miller, J. T.; Kropf, A. J.; Bunel, E. E.; Lei, A. *J. Am. Chem. Soc.* **2014**, *136*, 924.
- (53) Ballesteros, L. M.; Martín, S.; Cortés, J.; Marqués-González, S.; Higgins, S. J.; Nichols, R. J.; Low, P. J.; Cea, P. *Chem. Eur. J.* **2013**, *19*, 5352.
- (54) Frahm, D.; Hoffmann, F.; Fröba, M. *Cryst. Growth Des.* **2014**, *14*, 1719.

## Chapter 3

# Stereoselective Halogenation of Integral Unsaturated C-C Bonds in Chemically and Mechanically Robust Zr and Hf MOFs

This chapter is based upon the following publications:

Single-Crystal to Single-Crystal Mechanical Contraction of Metal-Organic Frameworks through Stereoselective Postsynthetic Bromination

*J. Am. Chem. Soc.*, **2015**, 137, 9527–9530.

**R. J. Marshall**, S. L. Griffin, C. Wilson and R. S. Forgan

Postsynthetic Bromination of UiO-66 Analogues: Altering Linker Flexibility and Mechanical Compliance

*Dalton Trans.*, **2016**, 45, 4132–4135.

**R. J. Marshall**, T. Richards, C. L. Hobday, C. F. Murphie, C. Wilson, S. Moggach, T. D. Bennett and R. S. Forgan

*This article is part of a themed collection on “Flexibility and Disorder in Metal-Organic Frameworks”.*

Stereoselective Halogenation of Integral Unsaturated C-C Bonds in Chemically and Mechanically Robust Zr and Hf MOFs

*Chem. Eur. J.*, **2016**, 22, 4870–4877.

**R. J. Marshall**, S. L. Griffin, C. Wilson and R. S. Forgan

*Selected as a Hot Paper.*

## Contents

<b>Chapter 3 .....</b>	<b>108</b>
<b>3.1 Introduction .....</b>	<b>110</b>
<b>3.2 Aims.....</b>	<b>112</b>
<b>3.3 Bulk Postsynthetic Bromination of Zr-L8 .....</b>	<b>114</b>
<b>3.4 Alternative Bulk Postsynthetic Bromination of Zr-L8.....</b>	<b>117</b>
<b>3.5 Single-Crystal Postsynthetic Bromination of Zr-L8 .....</b>	<b>120</b>
<b>3.6 Attempted Synthesis of a Zr MOF Containing etdb.....</b>	<b>122</b>
<b>3.7 Bulk Postsynthetic Bromination of Zr-L9 and Hf-L9 .....</b>	<b>123</b>
<b>3.8 Single Crystal Postsynthetic Bromination of Zr-L9 and Hf-L9 .....</b>	<b>129</b>
<b>3.9 Solution Phase Bromination of L9-Me<sub>2</sub>, L10-Me<sub>2</sub> and L11-Me<sub>2</sub> .....</b>	<b>132</b>
<b>3.10 Postsynthetic Bromination of Zr-L10 .....</b>	<b>136</b>
<b>3.11 Bulk Postsynthetic Bromination of Zr-L11 and Hf-L11 .....</b>	<b>140</b>
<b>3.12 Single Crystal Postsynthetic Bromination of Zr-L11 and Hf-L11 .....</b>	<b>145</b>
<b>3.13 Postsynthetic Iodination of Zr-L8, Zr-L9, Zr-L10 and Zr-L11.....</b>	<b>147</b>
<b>3.14 Conclusions and Future Work.....</b>	<b>150</b>
<b>3.15 Experimental .....</b>	<b>152</b>
3.15.1 General Experimental Remarks .....	152
3.15.2 Ligand Synthesis .....	153
3.15.3 Ligand Brominations.....	155
3.15.4 Bulk MOF Synthesis.....	157
3.15.5 Bulk Postsynthetic Bromination of Zr-L8, Zr-L9, Hf-L9, Zr-L10, Zr-L11 and Hf-L11 .....	158
3.15.6 Single Crystal Postsynthetic Bromination of Zr-L8, Zr-L9, Hf-L9, Zr-L10, Zr-L11 and Hf-L11 .....	160
3.15.7 Iodine Uptake Experiments of Zr-L8, Zr-L9, Zr-L10 and Zr-L11.....	162
<b>3.16 References .....</b>	<b>166</b>



### 3.1 Introduction

Functionalisation of MOFs is an attractive route to specialised materials tailored to specific applications.<sup>1</sup> An early concept in the quest for functionalised MOFs was materials containing more than one bridging ligand, known as multivariate MOFs,<sup>2,3</sup> allowing the introduction of multiple functionalities. The most well-known routes to functionalised MOFs are via direct synthesis with ligands containing the desired functionality<sup>4</sup> or by postsynthetic modification (PSM).<sup>5-9</sup> Postsynthetic modification – chemical transformations on pre-synthesised MOFs – has been highlighted as an attractive alternative route due to the vast number of potential modifications possible. Moreover, Zr MOFs are attractive candidates for PSM<sup>10</sup> due to their high chemical<sup>11-13</sup> and mechanical stabilities,<sup>14-17</sup> enabling them to tolerate a wide variety of reaction conditions, opening up new possibilities for functional group incorporation. PSM of Zr MOFs has mainly been limited to covalent modification of pendant functional groups,<sup>18-20</sup> cluster modifications,<sup>21-23</sup> linker metallation<sup>24-27</sup> or ligand/metal ion exchange (Figure 3.1).<sup>8,28-30</sup>

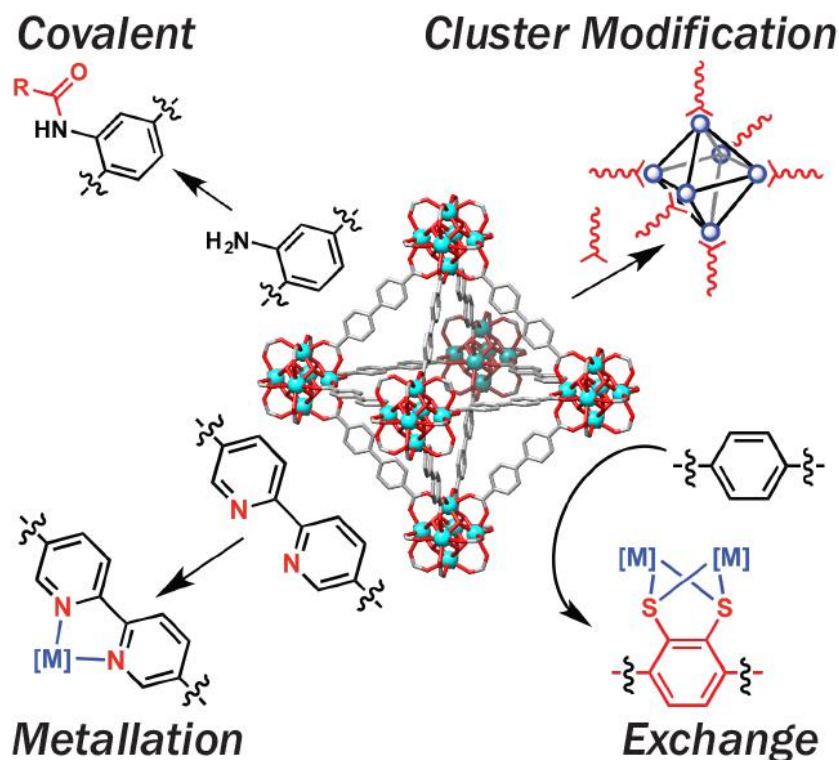


**Figure 3.1.** Overview of the most common PSM methods used for the functionalisation of Zr MOFs.

Integral PSM of MOFs – performing reactions on the ligand scaffold itself rather than pendant reactive handles – has been reported infrequently and with limited success. Insertion of functionality onto the aromatic backbone of Zr MOFs has been attempted, with hydroxy<sup>31</sup> and chloride<sup>32</sup> handles successfully grafted onto the ligands. Zr-bipy, that is the Zr MOF containing 2,2'-bipyridine-5,5'-dicarboxylate ligands, is routinely postsynthetically metallated and subsequently investigated for catalytic activity<sup>10</sup> however, it has also been demonstrated that the nitrogen atoms can be methylated, changing the framework from neutral to cationic leading to applications in anion sequestration.<sup>33</sup>

Introduction of ligands containing integral unsaturated functionality within MOFs presents sites for potential transformation. Postsynthetic bromination of a Zn-stilbene MOF has been reported,<sup>34</sup> and although the stilbene units could be postsynthetically brominated, the harsh chemical conditions and mechanical constraints of the transformation resulted in framework collapse upon quantitative conversion. Interestingly, it was found that the topological constraints of the MOF resulted in a stereoselective transformation, resulting exclusively in the *meso*-dibromoalkane product. The limited success seems to have hindered further attempts to postsynthetically transform integral reactive sites, with only one account briefly describing the postsynthetic bromination of integral alkyne units within a copper MOF.<sup>35</sup>

### 3.2 Aims

In Chapter 2, the syntheses of extended ligands containing unsaturated functionality are described and it is shown that they are able to be incorporated into highly porous Zr and Hf MOFs (Figure 3.2). The ligands contain either alkene (L8), alkyne (L9 and L11) or butadiyne (L10) functionality that can be viewed as attractive sites for potential transformation. The versatile addition of halogens across unsaturated functional units prompted us to investigate the MOFs' abilities to undergo integral postsynthetic halogenation (Figure 3.2d). The previously described postsynthetic bromination of a Zn-stilbene MOF provides evidence that the transformation is feasible.<sup>34</sup>

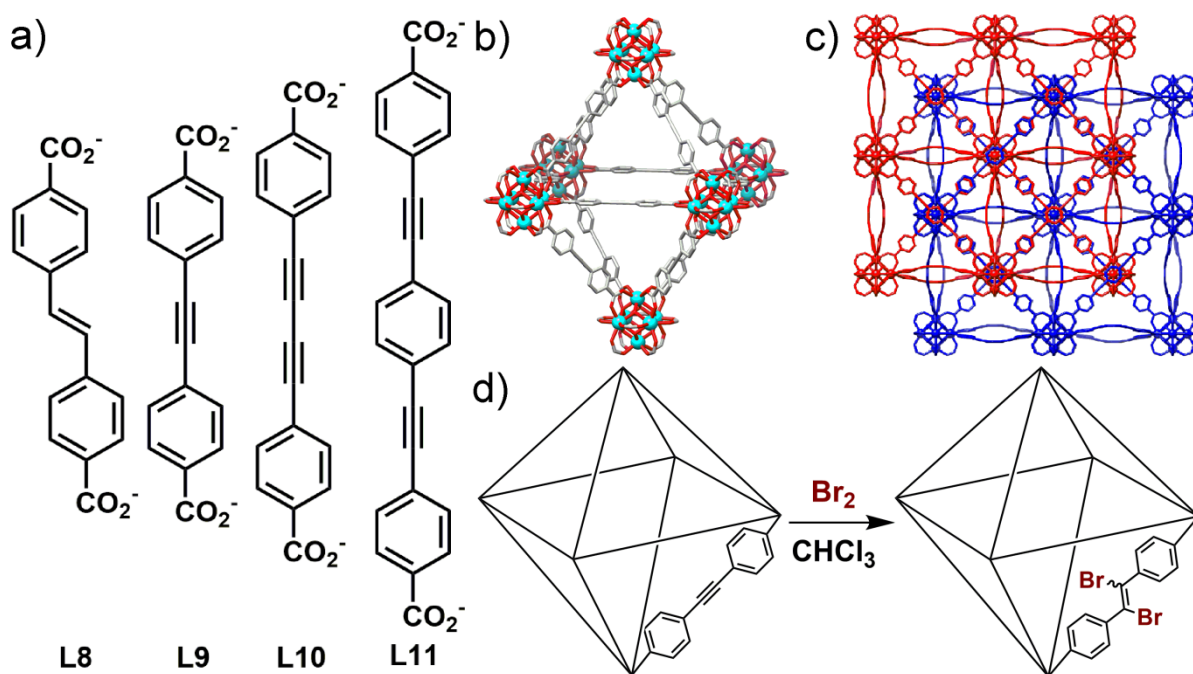


**Figure 3.2.** a) Schematic representation of L8-L11 which contain unsaturated functionality. Portions of the solid state structures of b) **Zr-L9** and c) **Zr-L11**. The two independent nets of **Zr-L11** have been coloured red and blue for clarity. d) Proposed postsynthetic bromination of integral alkyne units within **M-L9** to form **M-L9-Br<sub>2</sub>** (**M** = **Zr** or **Hf**). Atom colour scheme: Zr, cyan; C, grey; O, red. Hydrogen atoms are omitted for clarity.

Zr and Hf MOFs have been chosen as platforms for investigating integral postsynthetic halogenation (Figure 3.2d) due to their high chemical and mechanical stabilities. The MOFs investigated contain a variety of unsaturated functional units for postsynthetic halogenation, allowing differences in their reactivity to be evaluated.

Bulk postsynthetic bromination will initially be investigated and the products will be extensively characterised using a wide range of experimental techniques, to determine not only structural modifications of the MOFs but also the stereoselectivity of the transformations. Both neat Br<sub>2</sub> and *N*-bromosuccinimide will be investigated as brominating agents, while postsynthetic bromination will be extended to single crystals to enable accurate structural descriptions of the materials and subsequently the transformations to be obtained.

Postsynthetic halogenation will be extended to investigate the vapour phase iodine uptake capabilities of the Zr MOFs. Sequestration of radioactive iodine released during nuclear disasters is an important real-world application, and it is expected that the high intrinsic porosity of the Zr MOFs as well as their integral reactive sites will result in high uptake capacities.

### 3.3 Bulk Postsynthetic Bromination of Zr-L8

In Chapter 2 (Section 2.10.6) the synthesis of **Zr-L8** is described using a solvothermal L-proline modulation protocol however, bulk quantities of **Zr-L8** for postsynthetic bromination were synthesised using a slightly modified microwave assisted synthetic method.  $\text{CHCl}_3$  was used to activate bulk samples of **Zr-L8**, to enable direct comparisons with the brominated product **Zr-L8-Br<sub>2</sub>** as postsynthetic bromination is performed in  $\text{CHCl}_3$ . Bulk samples of **Zr-L8** were postsynthetically brominated by immersing microcrystalline samples in a  $\text{CHCl}_3$  solution containing neat bromine (5 eq) for 48 hours then collecting the modified product by centrifugation with fresh  $\text{CHCl}_3$  (Figure 3.3).

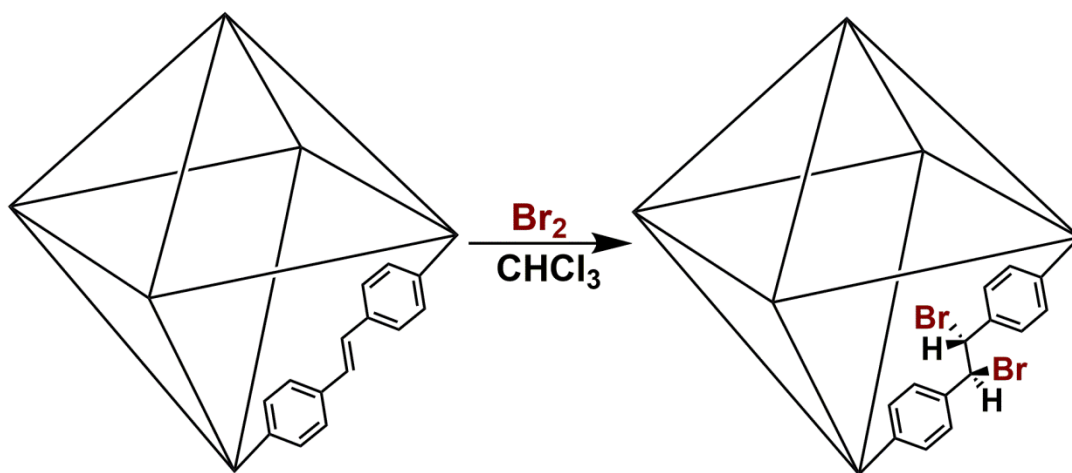


**Figure 3.3.** Schematic representation of bulk postsynthetic bromination of **Zr-L8**, which is expected to result exclusively in *meso*-**Zr-L8-Br<sub>2</sub>** based on previous stilbene containing MOF bromination attempts.<sup>34</sup>

Bromine analysis was initially used to determine the extent of bromination with bulk samples of **Zr-L8-Br<sub>2</sub>** displaying a slightly lower than expected bromine content (29.6% calculated, 27.7% found).  $^1\text{H}$  NMR spectra of acid digests of the products ( $\text{DMSO-}d_6/\text{D}_2\text{SO}_4$ ) were used to further quantify the extent of bromination (Figure 3.4).

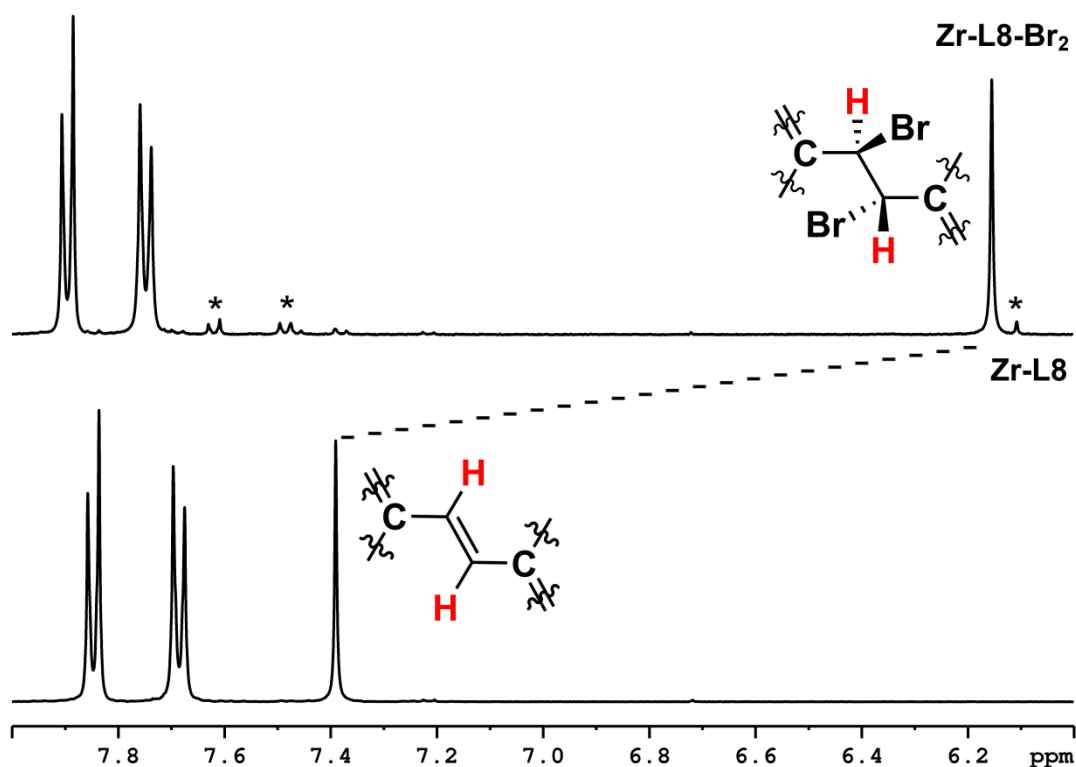


**Figure 3.4.** Stacked partial  $^1\text{H}$  NMR spectra ( $\text{DMSO-}d_6/\text{D}_2\text{SO}_4$ ) of **Zr-L8** and its brominated product **Zr-L8-Br<sub>2</sub>**.

Comparing the  $^1\text{H}$  NMR spectra of **Zr-L8** and **Zr-L8-Br<sub>2</sub>** it is clear that quantitative conversion of the alkene units to dibromoalkane units has been achieved with complete disappearance of the peaks corresponding to the starting material. The most obvious difference between the spectra is the characteristic up-field shift of the integral bridging protons on bromination (Figure 3.4). There are additional signals in the  $^1\text{H}$  NMR spectrum of **Zr-L8-Br<sub>2</sub>** (marked by asterisk) which are assumed to be *racemic* bromination products.

With **Zr-L8-Br<sub>2</sub>** in hand, further characterisation methods were required to fully analyse the transformation. Thermogravimetric analysis (TGA) was used to determine the extent of bromination, as the increased molecular weight of **Zr-L8-Br<sub>2</sub>** relative to **Zr-L8** was expected to result in an increase in mass loss (Figure 3.5).

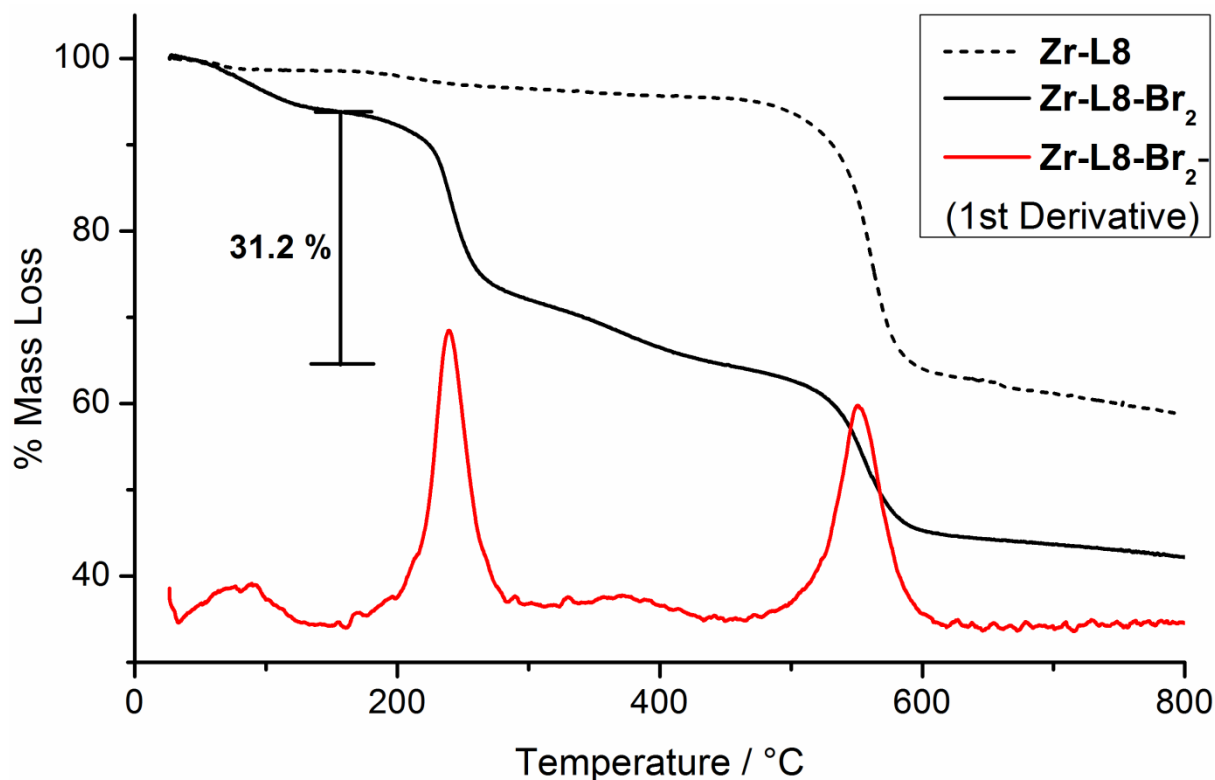


**Figure 3.5.** TGA profiles of **Zr-L8** and **Zr-L8-Br<sub>2</sub>**, with **Zr-L8-Br<sub>2</sub>** also shown in first derivative format to allow the mass loss events to be easily visualised.

TGA experiments were conducted under a nitrogen atmosphere from room temperature to 800 °C. As expected, comparing the percentage mass loss of the parent and brominated products it is clear that the increased molecular weight of **Zr-L8-Br<sub>2</sub>** results in a larger mass loss. However, it was interesting to see an extra mass loss event for **Zr-L8-Br<sub>2</sub>** prior to framework collapse and this is presumably due to debromination of the framework. If the mass loss of **Zr-L8-Br<sub>2</sub>** below 160 °C is assumed to result in completely desolvated material then the mass loss between 160 °C and 450 °C accounts for 31.2% of the total mass, while the theoretical bromine content is calculated as 29.6%. This very close correlation suggests quantitative bromination, and although debromination begins around 160 °C, the underlying thermal stability appears to be unaltered.

Experimental N<sub>2</sub> uptake experiments were performed at 77 K for **Zr-L8** and **Zr-L8-Br<sub>2</sub>** to determine the effect of bromination on their surface areas (Figure 3.6a). The N<sub>2</sub> uptake of **Zr-L8-Br<sub>2</sub>** is lower than that of **Zr-L8**, while the low pressure adsorption data suggests different pore textures in the two materials. The combined effect of bromine atoms lining the pores and an increased molecular weight results in a decrease of BET surface area from 2900 m<sup>2</sup>g<sup>-1</sup>

for **Zr-L8** to  $1580 \text{ m}^2\text{g}^{-1}$  for **Zr-L8-Br<sub>2</sub>**. Pore size distributions were subsequently calculated to visualise the effect of bromination on the pore diameter (Figure 3.6b).

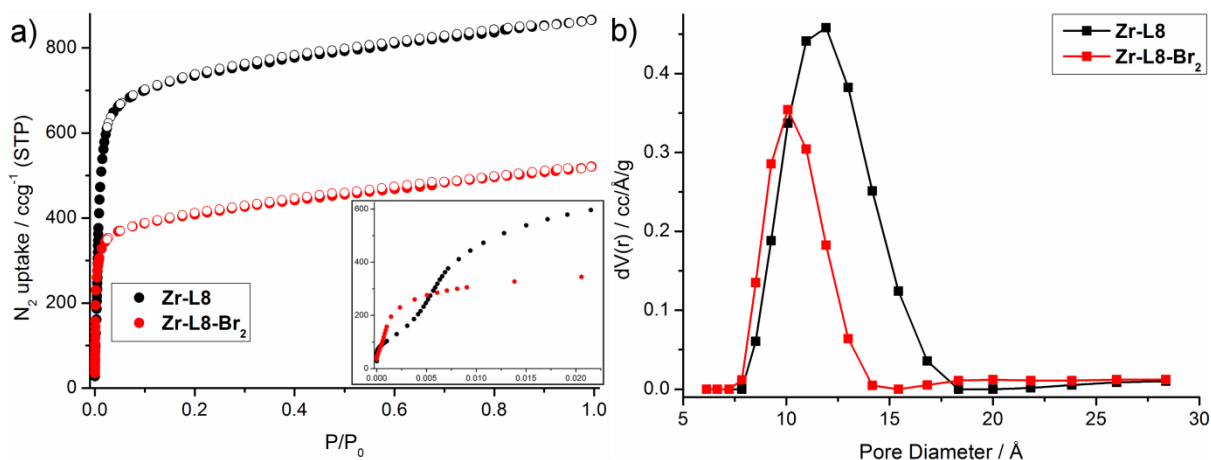


**Figure 3.6.** a)  $\text{N}_2$  adsorption (closed circles) and desorption (open circles) isotherms of **Zr-L8** and **Zr-L8-Br<sub>2</sub>**. The inset is an expansion of the low  $P/P_0$  adsorption data, highlighting the change in adsorption behaviour upon bromination. b) Calculated pore size distributions (QSDFT,  $\text{N}_2$  at 77 K on carbon) of **Zr-L8** and **Zr-L8-Br<sub>2</sub>**.

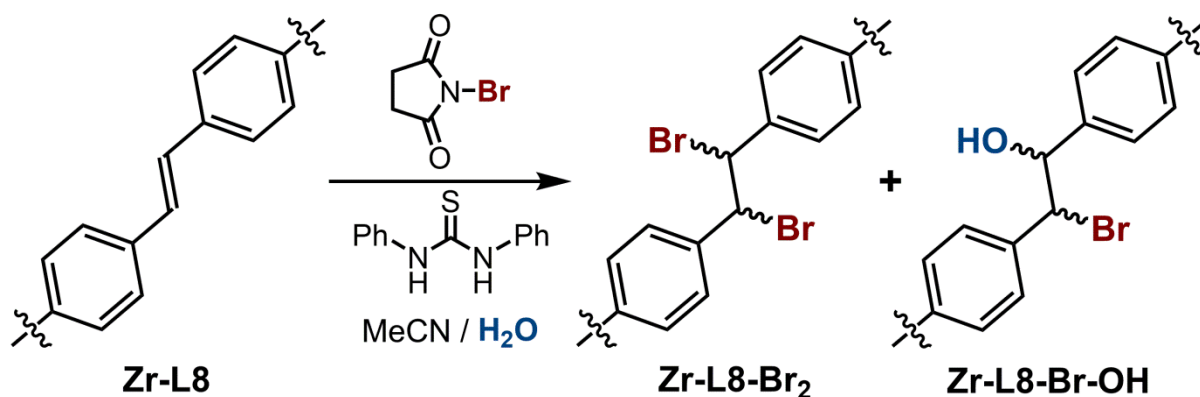
Pore size distributions reveal a reduction of the main pore diameter in **Zr-L8** from  $\sim 11.9 \text{ \AA}$  to  $\sim 10.1 \text{ \AA}$  in **Zr-L8-Br<sub>2</sub>**. The reduction in pore diameter suggests that the framework has contracted upon bromination, likely as a result of a change in hybridisation of the integral ligand carbon atoms from  $\text{sp}^2$  to  $\text{sp}^3$ , resulting in changes to both bond lengths and angles.

The postsynthetic bromination conditions employed are relatively harsh (neat  $\text{Br}_2$ ) and so milder bromination conditions were investigated, as although bulk samples of **Zr-L8** can withstand the harsh conditions it was thought that single crystals might have been more susceptible to damage by highly corrosive  $\text{Br}_2$ .

### 3.4 Alternative Bulk Postsynthetic Bromination of Zr-L8

Postsynthetic bromination was attempted using *N*-bromosuccinimide (NBS) in the presence of *N,N'*-diphenylthiourea (DPT) as a milder, alternative brominating agent. The use of NBS in the presence of  $\text{H}_2\text{O}$  is known to result in bromohydrination and so this was also explored as a potential route for the functionalisation of **Zr-L8** (Scheme 3.1).





**Scheme 3.1.** Reaction scheme for the PSM of **Zr-L8** using NBS highlighting potential products.

Reaction conditions were systematically altered and the product distributions were determined by  $^1\text{H}$  NMR spectroscopy of acid digests ( $\text{DMSO-}d_6/\text{D}_2\text{SO}_4$ ) of the products (Table 3.1).

**Table 3.1.** Summary of the reaction conditions investigated for PSM of **Zr-L8** using NBS alongside their respective product distributions.

Entry	mmol alkene in Zr-L8	NBS eq.	DPT eq.	Solvent Mixture (ml)		Product Distribution (%)		
				MeCN	H <sub>2</sub> O	Zr-L8	Zr-L8-Br <sub>2</sub>	Zr-L8-Br-OH
1	0.053	5	0	5	0	45	55	0
2	0.053	15	0	5	0	0	100	0
3	0.053	5	0.1	5	0	38	50	12
4	0.053	15	0.1	5	0	21	62	17
5	0.053	5	0	3	2	29	29	42
6	0.053	5	0.1	3	2	0	51	49
7	0.053	5	0.1	3	3	0	33	67
8	0.053	5	0.1	3	4	0	35	65
9	0.053	3	0.1	3	3	0	34	66
10	0.053	2	0.1	3	3	0	37	63
11	0.264	5	0.1	15	10	0	43	57

Addition of 15 equivalents of NBS (Entry 2) was necessary to quantitatively brominate **Zr-L8**. Addition of DPT, which is known to promote bromohydrination, resulted in small

amounts of the bromohydrated product **Zr-L8-Br-OH** when no water was added to the reaction (Entry 3), presumably resulting from residual water. Increased amounts of NBS (Entry 4) gave slightly better conversion but still a low yield of **Zr-L8-Br-OH**. Addition of water (Entry 5) gave significantly more bromohydrated product, while the presence of water and DPT resulted in full conversion and up to 67% bromohydration (Entries 6-8). Similar yields of **Zr-L8-Br<sub>2</sub>** and **Zr-L8-Br-OH** were obtained with as little as two equivalents of NBS (Entries 9-10), and the reaction could also be scaled up with a similar product distribution (Entry 11). Overall, attempts to selectively form **Zr-L8-Br-OH** were unsuccessful as **Zr-L8-Br<sub>2</sub>** was always present. <sup>1</sup>H NMR spectroscopy revealed that in a similar manner to postsynthetic bromination, bromohydration proceeds stereoselectively, resulting exclusively in the enantiomeric (*R,S/S,R*) bromohydrated products. The stereoselectivity of the transformation suggests a solid-phase reaction, however PXRD analysis was used to determine the crystallinity of the products (Figure 3.7).

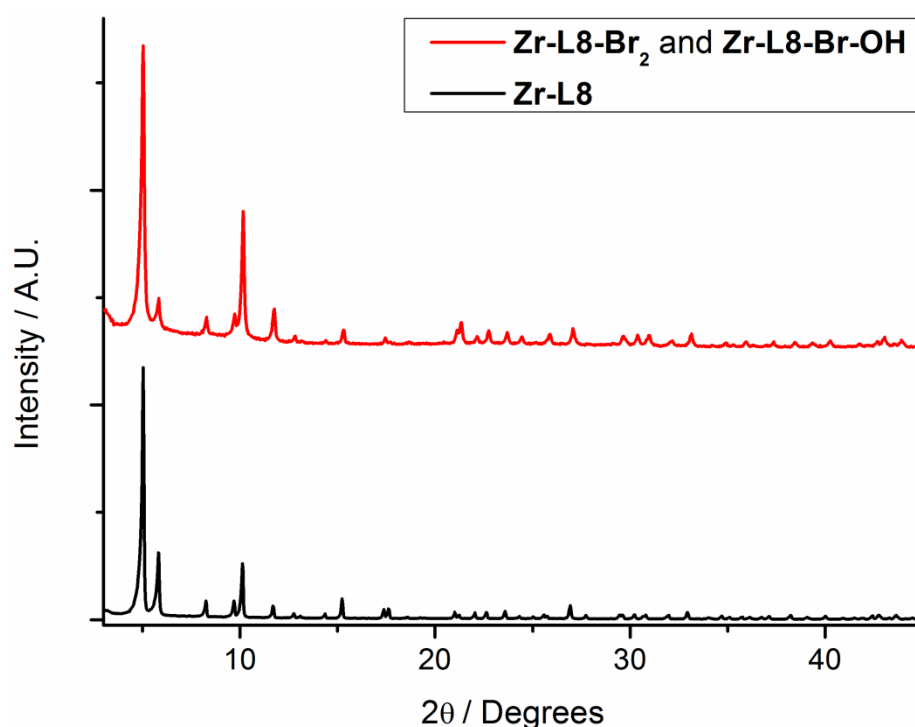


**Figure 3.7.** Comparison of the PXRD patterns of **Zr-L8** and the products resulting from bromohydration (Entry 11), **Zr-L8-Br<sub>2</sub>** and **Zr-L8-Br-OH**.

Retention of crystallinity proves that the modification occurs postsynthetically. The ability of **Zr-L8** to remain crystalline during PSM with NBS confirms its high mechanical (change in hybridisation of integral carbon atoms) and chemical (ability to tolerate H<sub>2</sub>O, which typically

hydrolyses other MOF families) stabilities. Considering multiple products were obtained when NBS was used as a bromine source, neat bromine was used in all further brominations.

### 3.5 Single-Crystal Postsynthetic Bromination of **Zr-L8**

Previous reports on postsynthetic bromination of integral unsaturated functionality<sup>34,35</sup> within MOFs describe the reactivity of bulk microcrystalline samples. Single-crystal to single-crystal (SCSC) transformations of MOFs are relatively rare and considering the facile addition of bromine across the integral alkene units in bulk samples of **Zr-L8**, postsynthetic bromination of single crystals was attempted. A small quantity of single crystals of **Zr-L8** were immersed in a  $\text{CHCl}_3$  solution containing  $\text{Br}_2$  and allowed to react for 48 hours, then the solvent was exchanged for fresh solvent and the crystals left to stand. The brominated crystals were of the same quality as their parent samples and they were analysed by single crystal X-ray diffraction (SCXRD). The single crystal structure confirms postsynthetic addition of bromine atoms across the integral stilbene unit and this is a rare example of a SCSC transformation (Figure 3.8a). **Zr-L8-Br<sub>2</sub>** solves in the cubic  $Fm-3m$  space group, the same as **Zr-L8** with the unit cell edge decreasing from 29.8884(3) Å to 29.784(4) Å upon bromination. The decrease in unit cell edge is due to the hybridisation of the central carbon atoms changing from  $\text{sp}^2$  to  $\text{sp}^3$ , resulting in a mechanical contraction and although small this is consistent with the decrease in pore diameter revealed by pore size distributions (Figure 3.6b). The PXRD pattern of **Zr-L8-Br<sub>2</sub>** was calculated from the single crystal model and compared with the experimental pattern to confirm bulk phase purity. It was also necessary to compare the experimental and calculated PXRD patterns of **Zr-L8**, to confirm that bulk samples prepared by microwave assisted techniques were phase pure (Figure 3.8b).

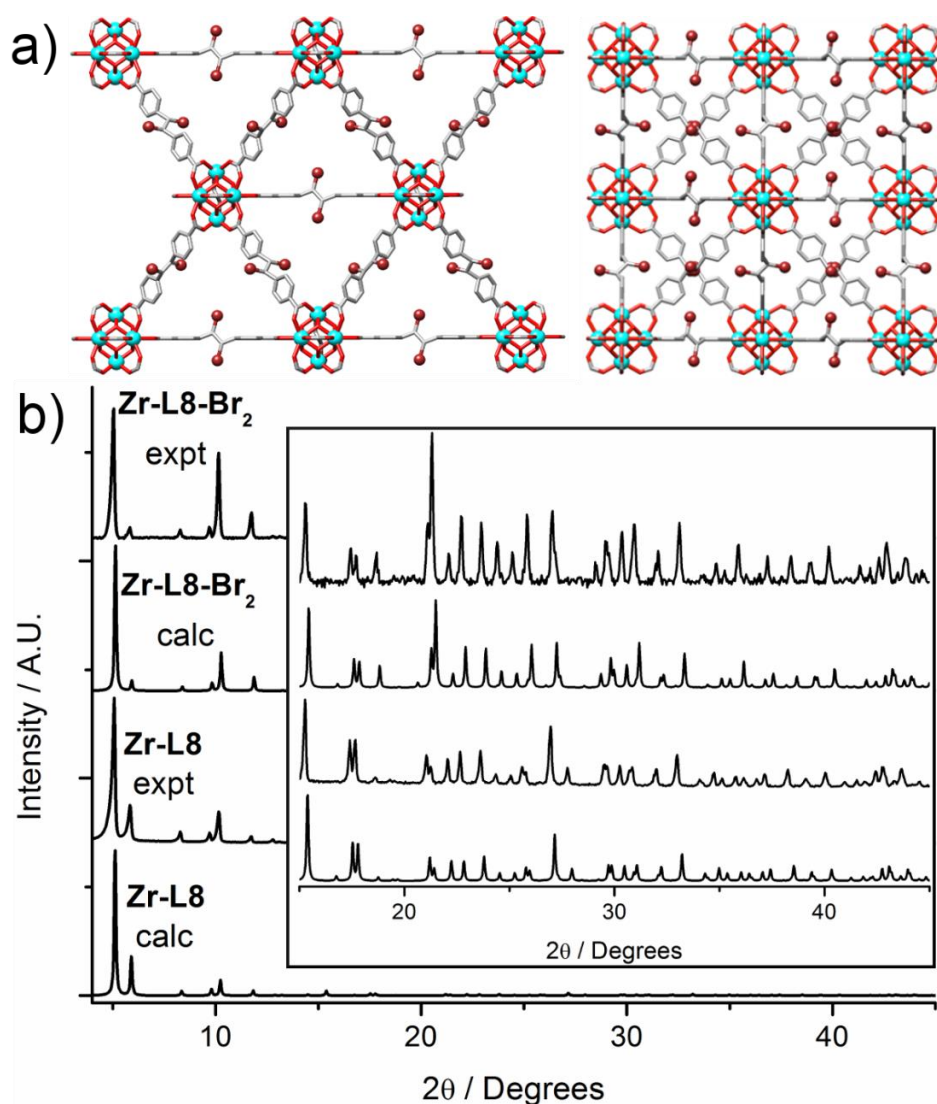


**Figure 3.8.** a) Portion of the solid state structure of **Zr-L8-Br<sub>2</sub>** in two different orientations, clearly showing the dibromoalkane core of the ligand, confirming bromination of the *trans*-stilbene ligands (disorder of the dibromoethane unit has been omitted for clarity). b) Comparison of calculated (from the single crystal structure) and experimental PXRD patterns of **Zr-L8** and **Zr-L8-Br<sub>2</sub>**. The inset is an expanded view of the high angle data. Atom colour scheme: Zr, cyan; C, grey; O, red; Br, brown. Hydrogen atoms are omitted for clarity.

There is excellent agreement between the predicted and experimental PXRD patterns of both **Zr-L8** and **Zr-L8-Br<sub>2</sub>**. Comparing the calculated PXRD patterns of **Zr-L8** and **Zr-L8-Br<sub>2</sub>** it is clear that there are some differences expected upon bromination and this is consistent with the experimental patterns, where peak positions, shapes and relative intensities change. Postsynthetic bromination has introduced a highly flexible ligand containing a dibromoalkane core into an extremely robust and rigid MOF topology whilst remaining crystalline.

### 3.6 Attempted Synthesis of a Zr MOF Containing etdb

A highly flexible ligand with similar topology and flexibility to **L8-Br<sub>2</sub>** was designed and synthesised. 4,4'-Ethane-1,2-diylidibenzoic acid, which is abbreviated to etdb-H<sub>2</sub>, was synthesised as it contains a bridging alkane core, closely resembling L8-Br<sub>2</sub>. Initially the synthesis of L8-Br<sub>2</sub>-H<sub>2</sub> was attempted although difficulties were encountered during saponification of the dimethyl ester L8-Br<sub>2</sub>-Me<sub>2</sub>. The bromine atoms were partially eliminated during saponification, resulting in the mono-brominated alkene ligand. The close match in terms of length, topology and flexibility between etdb and L8-Br<sub>2</sub> (the solid state structure of etdb-Me<sub>2</sub> is shown in Figure 3.9a and full crystallographic data is available in Section 3.15.2) prompted us to attempt direct Zr-MOF synthesis with etdb-H<sub>2</sub>. A variety of reaction conditions were investigated for Zr MOF syntheses, including both oven and microwave methods and the modulator was also varied. PXRD was used to determine the success of Zr MOF formation with the highly flexible etdb ligand (Figure 3.9b).

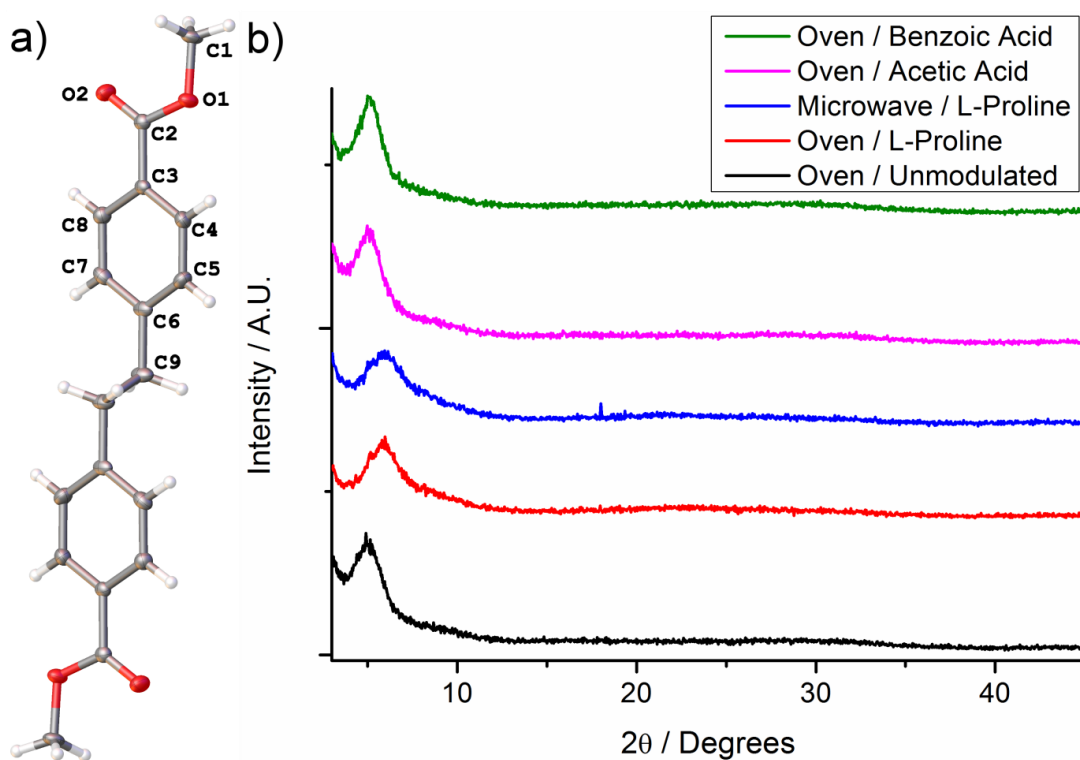


**Figure 3.9.** a) Solid state structure and atom labelling scheme of etdb-Me<sub>2</sub> (asymmetric unit only). Displacement ellipsoids are drawn at 50% probability level. b) Stacked PXRD patterns of the material obtained upon attempted Zr MOF syntheses containing etdb under a variety of conditions.

PXRD analysis of the materials resulting from the synthetic attempts at a Zr MOF containing etdb revealed that amorphous powder was obtained. This confirms that under the conditions investigated, which are known to reliably produce Zr MOFs, a Zr MOF containing etdb could not be successfully synthesised. The unsuccessful incorporation of etdb into a UiO-66 type MOF is likely due to the very high flexibility of the ligand, suggesting that postsynthetic bromination of **Zr-L8** provides access to a highly flexible MOF that under typical synthetic conditions cannot be obtained, proving the potential of PSM as an alternative synthetic route. Having successfully postsynthetically brominated **Zr-L8**, both as bulk microcrystalline powders and as single crystals, the potential of Zr and Hf MOFs containing integral alkyne units (L9) to undergo postsynthetic bromination was considered.

### 3.7 Bulk Postsynthetic Bromination of Zr-L9 and Hf-L9

Postsynthetic bromination of MOFs containing L9 requires the addition of bromine across integral alkyne units, resulting in dibromoalkene units (Figure 3.2d) and considering the topological induced stereoselective bromination of **Zr-L8** it was expected that only the *trans*-dibromoalkene product would be obtained. Bulk microcrystalline powders of **Zr-L9** and **Hf-L9** were brominated by immersion in a CHCl<sub>3</sub> solution containing Br<sub>2</sub> (30 equivalents per alkyne) and left to stand in the dark for either 48 (**Zr-L9**) or 72 hours (**Hf-L9**). The brominated products were collected by centrifugation with fresh CHCl<sub>3</sub> and analysed by PXRD (Figure 3.10).

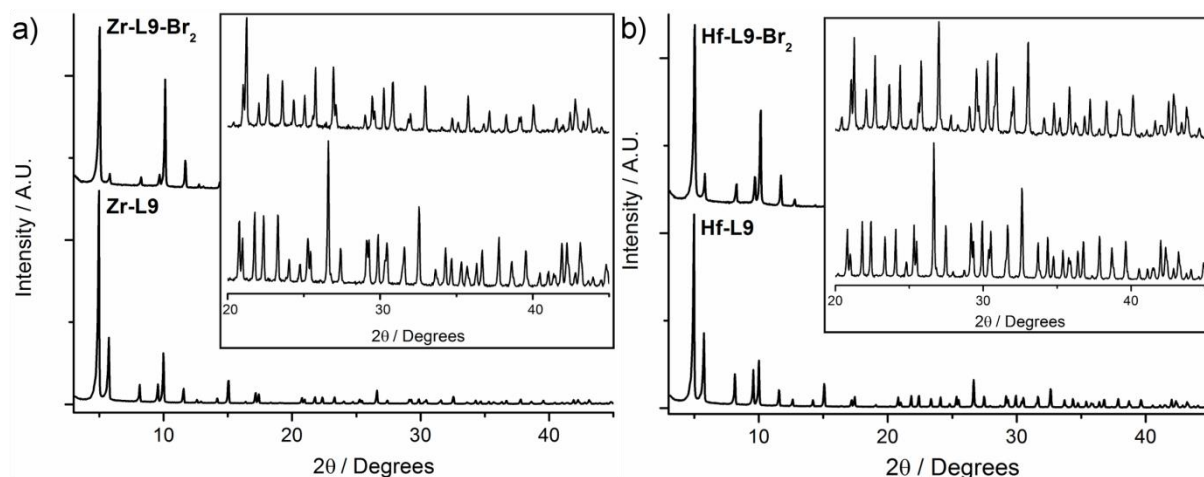


**Figure 3.10.** Stacked PXRD patterns of a) **Zr-L9** and its brominated product **Zr-L9-Br<sub>2</sub>** and b) **Hf-L9** and its brominated product **Hf-L9-Br<sub>2</sub>**. The insets are expanded views of the high angle data.

PXRD analysis confirms that both brominated MOFs are highly crystalline, even to high angles of  $2\theta$ . Comparing the PXRD patterns of the parent and brominated MOFs, subtle changes in peak positions and their relative intensities are observed. On bromination, the integral sp alkyne carbon atoms are transformed to sp<sup>2</sup> dibromoalkene carbon atoms, changing the geometry of the ligand from linear to stepped. This change in hybridisation results in a contraction of the MOF, which is evidenced by the diffraction peaks in the brominated samples moving to higher angles of  $2\theta$  to reflect the decrease in the unit cell edge.

Bromine analysis of **Zr-L9**, **Hf-L9** and their brominated products were obtained to determine the percentage bromination (Table 3.2).

**Table 3.2.** Summary of the theoretical and experimental bromine contents of bulk samples of **Zr-L9**, **Zr-L9-Br<sub>2</sub>**, **Hf-L9** and **Hf-L9-Br<sub>2</sub>**.

	Theoretical Br Content (%)	Experimental Br Content (%)
<b>Zr-L9</b>	0	0.1
<b>Zr-L9-Br<sub>2</sub></b>	29.8	26.2
<b>Hf-L9</b>	0	0.3
<b>Hf-L9-Br<sub>2</sub></b>	25.6	23.2

The experimentally measured bromine content is slightly low for both **Zr-L9-Br<sub>2</sub>** and **Hf-L9-Br<sub>2</sub>**, however the MOFs likely contain residual solvent in their pores, increasing their molecular weight and hence lowering their actual Br content. The bromine analysis results suggest quantitative bromination and so alternative techniques were used to characterise the transformation.

Thermogravimetric analysis was performed from room temperature to 800 °C under an N<sub>2</sub> atmosphere and used to determine the effect of bromination on the MOFs thermal stabilities. The presence of a thermally induced debromination step can be used to quantify the percentage bromination (Figure 3.11).

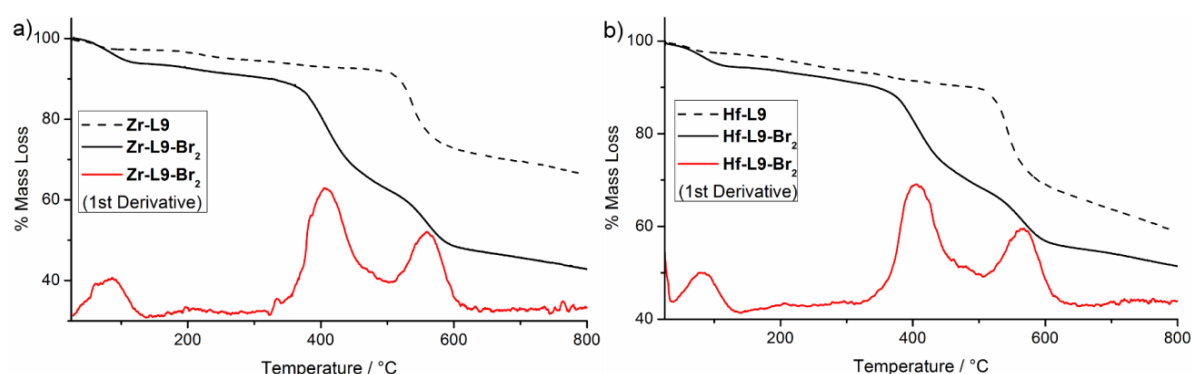


**Figure 3.11.** Comparison of the TGA profiles of a) **Zr-L9** and **Zr-L9-Br<sub>2</sub>** and b) **Hf-L9** and **Hf-L9-Br<sub>2</sub>**.

The TGA profiles are similar for the Zr and Hf MOFs, with one major weight loss observed for the parent materials while two distinct mass loss events are observed for the brominated products. **Zr-L9** and **Hf-L9** are thermally stable to around 500 °C and ignoring debromination it is clear that the brominated MOFs share the same high thermal stabilities of their parent materials. For the brominated MOFs, the first mass loss occurs between 350-500 °C for **Zr-L9-Br<sub>2</sub>** and between 330-500 °C for **Hf-L9-Br<sub>2</sub>**. Assuming the material prior to this mass loss in each case corresponds to completely evacuated MOF then the mass loss in these temperature regions correlates closely to the bromine content of fully brominated MOFs; 29.6% for **Zr-L9-Br<sub>2</sub>** (29.8% calculated) and 24.2% for **Hf-L9-Br<sub>2</sub>** (25.6% calculated). **Zr-L9-Br<sub>2</sub>** and **Hf-L9-Br<sub>2</sub>** lose ~10% mass prior to debromination and this is attributed to dehydroxylation of the M<sub>6</sub> clusters<sup>36</sup> and also removal of occluded solvent molecules from the pores. The presence of residual solvent in the brominated MOFs is in agreement with the lower than expected Br analysis, while both TGA and Br analysis



together confirm quantitative bromination of **Zr-L9** and **Hf-L9** as bulk microcrystalline powders.

Raman spectroscopy was used to analyse small quantities of microcrystalline MOF powders placed on a glass slide and irradiated with a green laser ( $\lambda = 532$  nm, 100 mW) (Figure 3.12).

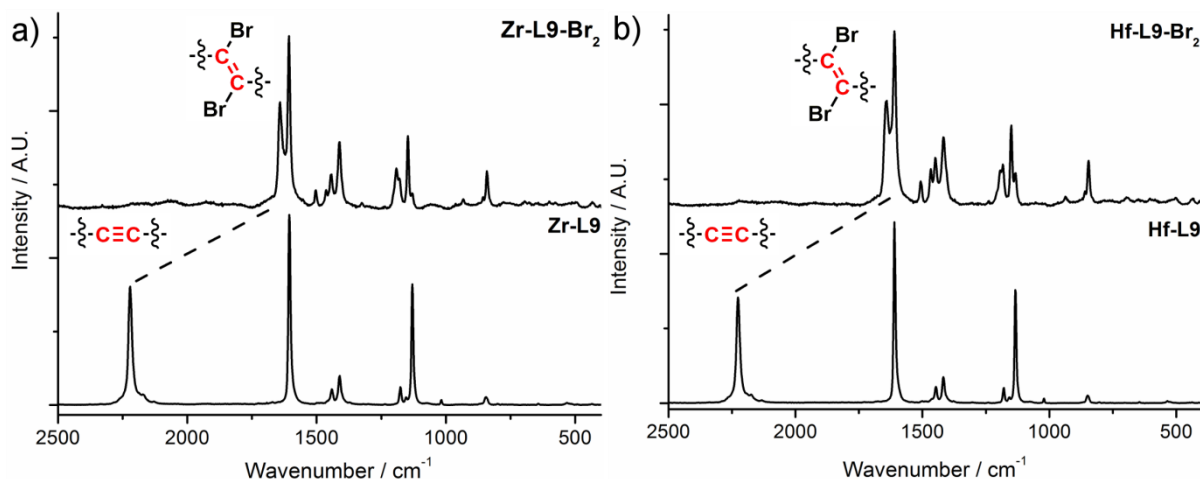


**Figure 3.12.** Comparison of the Raman spectra of a) **Zr-L9** and **Zr-L9-Br<sub>2</sub>** and b) **Hf-L9** and **Hf-L9-Br<sub>2</sub>**.

The Raman spectra of **Zr-L9** and **Hf-L9** are in close agreement, as are those of **Zr-L9-Br<sub>2</sub>** and **Hf-L9-Br<sub>2</sub>** confirming that the same brominated products are formed. There are noticeable differences between the parent and brominated MOFs in terms of peak positions and their relative intensities, however the most distinct observation is the disappearance of the peak corresponding to the alkyne unit ( $\sim 2225$   $\text{cm}^{-1}$ ) which suggests quantitative conversion. This is consistent with the appearance of a peak at  $\sim 1640$   $\text{cm}^{-1}$  corresponding to the newly formed dibromoalkene unit.<sup>35</sup>

$^1\text{H}$  NMR spectroscopy of acid digested MOF samples ( $\text{DMSO-}d_6/\text{D}_2\text{SO}_4$ ) was used to assess the extent of bromination. Very little information is available from the  $^1\text{H}$  NMR spectra of the digested MOF samples due to the symmetry of the ligands (Figure 3.2a) with only two doublets obtained for the aromatic protons in both the parent and brominated materials. However, the distance between the two doublets increases upon bromination (the splitting increases from  $\sim 0.28$  ppm to  $\sim 0.38$  ppm) and as no other signals are present in the  $^1\text{H}$  NMR spectra this indicates stereoselective and quantitative conversion to a single symmetrical product (see Appendix, Chapter 6 Figures 6.25-6.26). The  $^{13}\text{C}$  NMR spectra of digested

samples of **Zr-L9-Br<sub>2</sub>** and **Hf-L9-Br<sub>2</sub>** are very similar with both showing only six resonances, indicating the formation of a single isomer upon bromination of the parent MOFs. A comparison of the <sup>13</sup>C NMR spectra of **Zr-L9** and **Zr-L9-Br<sub>2</sub>** is shown below (Figure 3.13) while the analogous comparison of the Hf MOFs is available in the Appendix (Chapter 6, Figure 6.27).

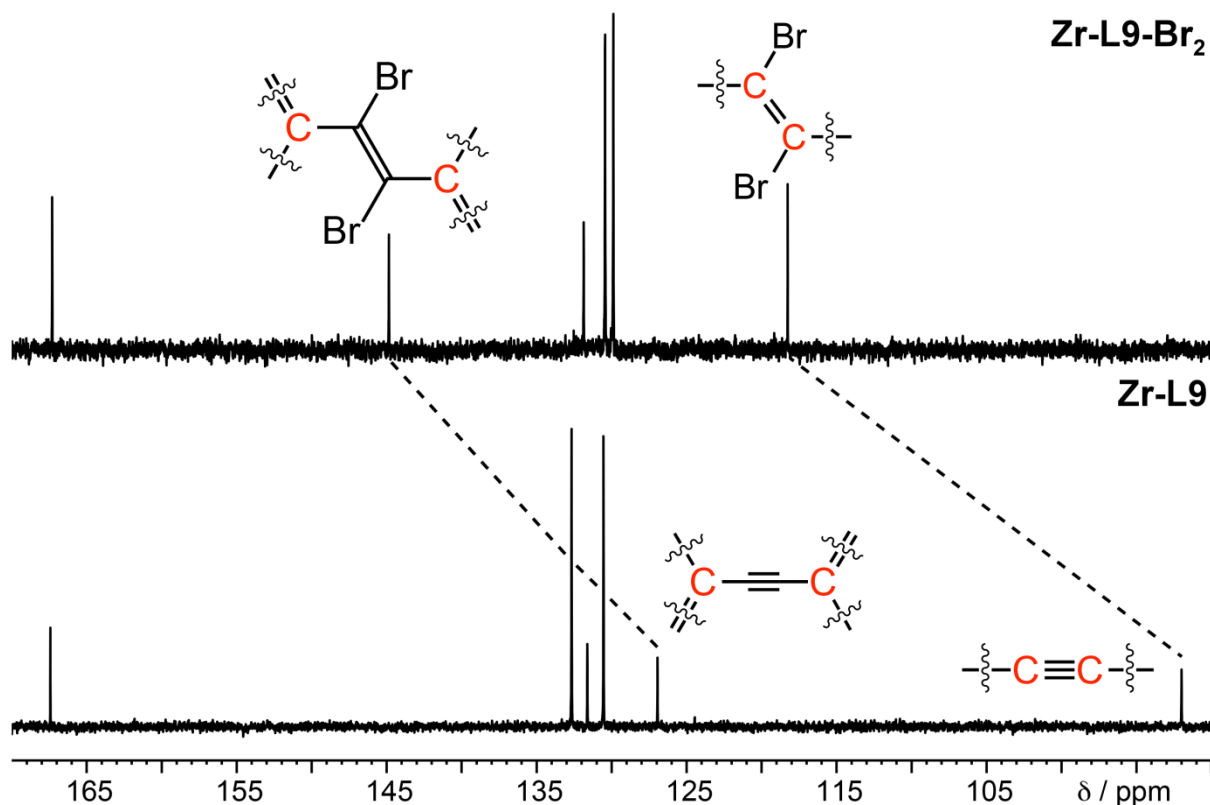


**Figure 3.13.** Stacked partial <sup>13</sup>C NMR spectra of digested samples (DMSO-*d*<sub>6</sub>/D<sub>2</sub>SO<sub>4</sub>) of **Zr-L9** and **Zr-L9-Br<sub>2</sub>** highlighting the characteristic downfield shift of deterministic carbon atoms upon bromination.

The resonances assigned to the alkyne (sp) carbon atoms, found at  $\delta = 92.0$  ppm for **Zr-L9** and  $\delta = 91.9$  ppm for **Hf-L9**, are significantly shifted downfield upon bromination to dibromoalkene (sp<sup>2</sup>) carbon atoms, occurring at  $\delta = 118.2$  ppm for **Zr-L9-Br<sub>2</sub>** and  $\delta = 118.5$  ppm for **Hf-L9-Br<sub>2</sub>**. The presence of only one resonance for the dibromoalkene carbon atoms confirms the stereoselectivity of the transformation, with *trans*-L9-Br<sub>2</sub>-H<sub>2</sub> formed exclusively due to the steric restraints imposed on L9 whilst bound within the MOF. There are conflicting reports detailing the <sup>13</sup>C NMR spectroscopic characterisation of dibromostilbene units in the literature,<sup>37-39</sup> while the stereoselective bromination of L9 within **Zr-L9** and **Hf-L9**

unambiguously shows that signals observed around  $\delta = 118$  ppm correspond to the *trans* isomer, while those around  $\delta = 124$  ppm correspond to the *cis* isomer.

The parent and brominated MOFs were subject to  $N_2$  uptake experiments at 77 K and upon comparing the isotherms it is clear that bromination results in a substantial decrease in  $N_2$  uptake (Figure 3.14). The insertion of Br atoms within the MOF pores results in a different pore texture, evidenced by a change in shape of the isotherms in the low  $P/P_0$  region.

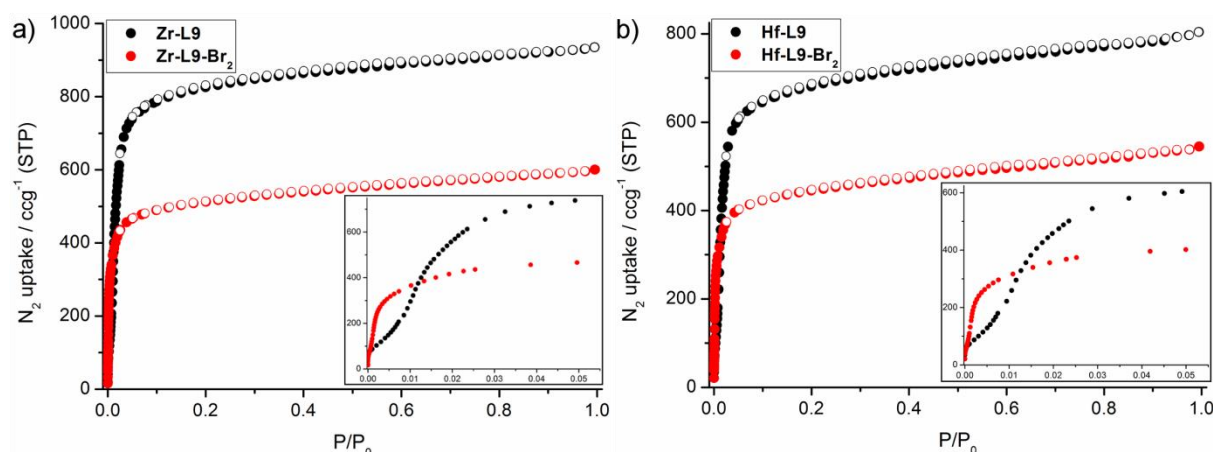


**Figure 3.14.**  $N_2$  adsorption (closed circles) and desorption (open circles) isotherms of a) **Zr-L9** and **Zr-L9-Br<sub>2</sub>** and b) **Hf-L9** and **Hf-L9-Br<sub>2</sub>**. The insets are expanded views of the low  $P/P_0$  adsorption data, highlighting the change in adsorption behaviour upon bromination.

The  $N_2$  uptakes and corresponding BET surface areas of the MOFs are expected to decrease upon bromination due to the increase in molecular weight. BET surface areas were calculated for the four MOFs and are summarised in Table 3.3.

**Table 3.3.** BET surface areas of **Zr-L9**, **Zr-L9-Br<sub>2</sub>**, **Hf-L9** and **Hf-L9-Br<sub>2</sub>** alongside the observed and theoretical decrease in surface area upon bromination.

	<b>Zr-L9</b>	<b>Zr-L9-Br<sub>2</sub></b>	<b>Hf-L9</b>	<b>Hf-L9-Br<sub>2</sub></b>
<b>BET surface area (m<sup>2</sup>g<sup>-1</sup>)</b>	3280	2000	2730	1730
<b>Observed Decrease (%)</b>	40		36	
<b>Theoretical Decrease (%)</b>	29		25	

The observed decrease in gravimetric surface areas cannot be fully accounted for by considering the increase in molecular weight upon bromination. The lower than expected  $N_2$  uptakes and surface areas of the brominated MOFs are consequences of the mechanical contractions that bromination induces. Pore size distributions (PSDs) were calculated for both pairs of MOFs to confirm the induced mechanical contraction (Figure 3.15).

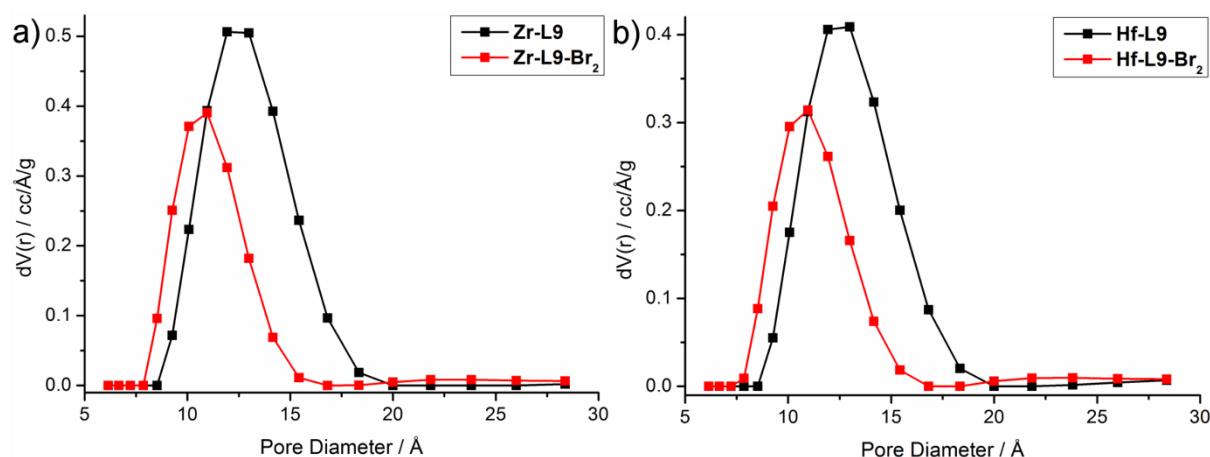


**Figure 3.15.** Comparison of the calculated PSDs (QSDFT,  $N_2$  at 77 K on carbon) of a) **Zr-L9** and **Zr-L9-Br<sub>2</sub>** and b) **Hf-L9** and **Hf-L9-Br<sub>2</sub>**.

The calculated pore size distributions show in both cases a contraction of the main pore diameter from  $\sim 12.5$  Å to  $\sim 11.0$  Å on bromination. The ability of **Zr-L9** and **Hf-L9** to withstand the mechanical contraction imposed during bromination exemplifies their high mechanical stabilities as they remain crystalline and porous as they are transformed to **Zr-L9-Br<sub>2</sub>** and **Hf-L9-Br<sub>2</sub>** respectively.

Single crystals of **Zr-L9** and **Hf-L9** were grown by fine-tuning the L-proline modulation conditions. With single crystals of **Zr-L9** and **Hf-L9** in hand bromination was attempted in a SCSC manner to obtain greater structural information and to confirm the stereoselective formation of the *trans* brominated product.

### 3.8 Single Crystal Postsynthetic Bromination of Zr-L9 and Hf-L9

Single crystals of **Zr-L9** and **Hf-L9** were immersed in a  $CHCl_3$  solution containing  $Br_2$  and left to react at room temperature for 96 hours. After this time the crystals were resolvated in

fresh  $\text{CHCl}_3$  and finally to DMF. The crystals' appearance did not change during bromination, highlighting their high chemical stability as they are able to withstand contact with highly corrosive  $\text{Br}_2$  for prolonged periods of time. The crystals were subject to single crystal X-ray diffraction and although there is disorder of the integral dibromoalkene units the *trans* stereoselectivity of the transformation is evident (Figure 3.16).

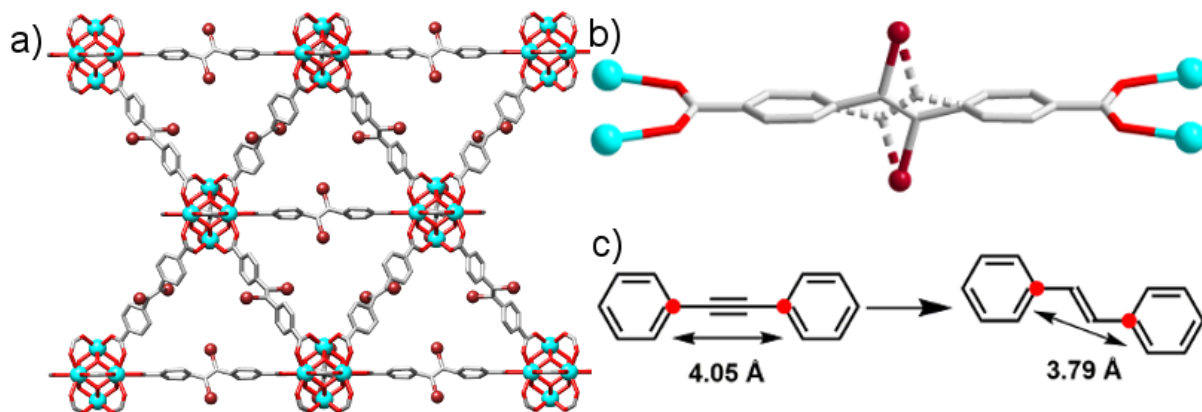


**Figure 3.16.** a) Portion of the solid state structure of **Zr-L9-Br<sub>2</sub>** with disorder omitted for clarity. b) View of *trans*-L9-Br<sub>2</sub> within **Zr-L9-Br<sub>2</sub>** highlighting the disordered dibromoalkene orientations. c) Schematic representation of the ligand-based contraction expected upon bromination, calculated using standard crystallographic bond lengths.<sup>40</sup> Atom colour scheme: Zr, cyan; C, grey; O, red; Br, brown. Hydrogen atoms are omitted for clarity.

The structures of **Zr-L9-Br<sub>2</sub>** and **Hf-L9-Br<sub>2</sub>** are very similar with both MOFs adopting the cubic  $Fm-3m$  space group of their parent structures and in both cases it is clear that *trans*-L9-Br<sub>2</sub> is formed exclusively. The transformation is stereoselective due to the topological constraints of the ligands within the MOFs, reducing their conformational freedom, and this prevents *cis*-L9-Br<sub>2</sub> from being formed. In the solid state structure of the brominated MOFs there is end-to-end disorder of the ligands and as such two conformations of the dibromoalkene are observed (Figure 3.16b). **Zr-L9** and **Hf-L9** undergo a mechanical contraction during postsynthetic bromination, although this is expected as the hybridisation of the integral carbons atoms changes from  $sp$  to  $sp^2$ , resulting in changes to both bond lengths and angles (Figure 3.16c). Pertinent crystallographic and surface area values of **Zr-L9** and **Hf-L9** and their brominated products are summarised in Table 3.4.

**Table 3.4.** Summary of selected crystallographic parameters from the solid state structures of **Zr-L9** and **Hf-L9** as well as their brominated products.

	<i>a</i> (Å)	<i>V</i> (Å <sup>3</sup> )	Linker Length (Å)	M-OOC (Å)	<sup>a</sup> SAV (Å <sup>3</sup> )	<sup>b</sup> BET SA (m <sup>2</sup> g <sup>-1</sup> )
<b>Zr-L9</b>	30.2386(4)	27649(1)	12.52	2.224(4)	21365	3280
<b>Hf-L9</b>	30.111(1)	27300(5)	12.61	2.172(6)	20364	2730
<b>Zr-L9-Br<sub>2</sub></b>	29.861(2)	26626(5)	12.30	2.200(5)	16938	2000
<b>Hf-L9-Br<sub>2</sub></b>	29.825(2)	26530(5)	12.30	2.196(5)	16961	1730

<sup>a</sup>Solvent accessible volume (SAV) calculated using the SQUEEZE module in PLATON.<sup>41</sup><sup>b</sup>Calculated from N<sub>2</sub> adsorption isotherms collected at 77 K.

The ligands contract by 0.22 Å and 0.31 Å upon bromination of **Zr-L9** and **Hf-L9** respectively, and these values are in line with the calculated ligand based contraction of 0.26 Å (Figure 3.16c). The unit cell edge *a* decreases by ~0.38 Å upon bromination of **Zr-L9** with the unit cell volume reducing by 3.7%. A similar mechanical contraction is observed during bromination of **Hf-L9**, with *a* decreasing by ~0.29 Å and the unit cell volume reducing by 2.8%. The decrease in SAVs and BET surface areas are further evidence of the mechanical contractions, with the ability of the MOFs to withstand them highlighting their high mechanical stabilities.

The experimental PXRD patterns of the brominated MOFs, **Zr-L9-Br<sub>2</sub>** and **Hf-L9-Br<sub>2</sub>**, were compared with the patterns calculated from the solid state structures (Figure 3.17).

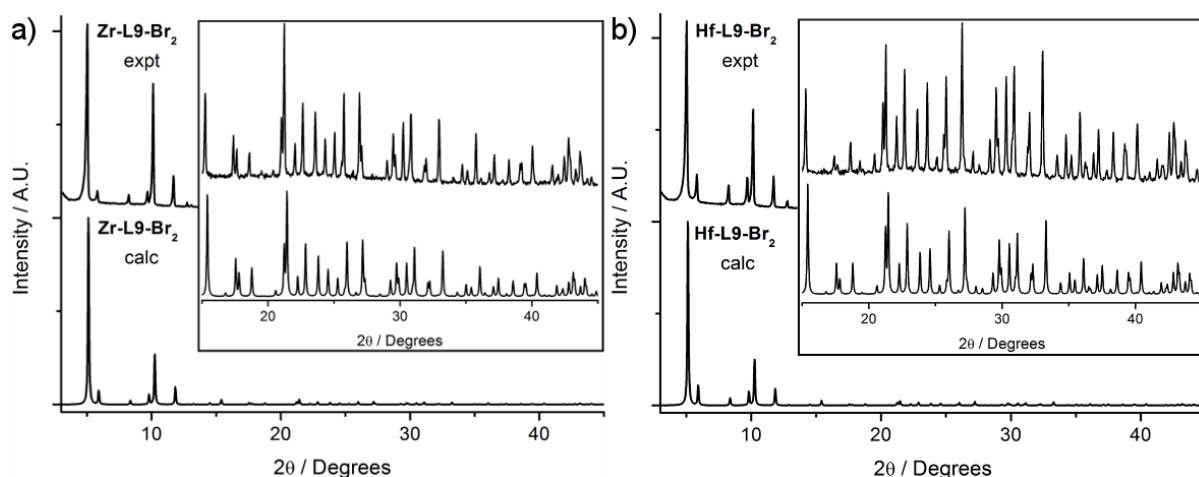


**Figure 3.17.** Comparison of the calculated (from the single crystal structure) and experimental PXRD patterns of a) **Zr-L9-Br<sub>2</sub>** and b) **Hf-L9-Br<sub>2</sub>**. The insets are expanded views of the high angle data.

The excellent agreement between the calculated and experimental PXRD patterns of **Zr-L9-Br<sub>2</sub>** and **Hf-L9-Br<sub>2</sub>** confirms their bulk phase purity. This again highlights the high mechanical and chemical stabilities of the MOFs as they are able to withstand harsh chemical conditions and a considerable mechanical contraction. Inspired by the quantitative and stereoselective formation of *trans*-L9-Br<sub>2</sub> when **Zr-L9** and **Hf-L9** are postsynthetically brominated, liquid phase bromination of L9-Me<sub>2</sub> was attempted to compare the stereoselectivity of the transformation.

### 3.9 Solution Phase Bromination of L9-Me<sub>2</sub>, L10-Me<sub>2</sub> and L11-Me<sub>2</sub>

Solution phase bromination of the integral alkyne units of L9-Me<sub>2</sub> to dibromoalkene units was attempted, with the dimethyl ester of the ligand chosen due to its increased solubility in CHCl<sub>3</sub>. After bromination the products were analysed by <sup>1</sup>H (Figure 3.18) and <sup>13</sup>C NMR spectroscopies (see Appendix, Chapter 6 Figure 6.28) which confirmed the presence of a mixture of two products that have been assigned as *cis*-L9-Br<sub>2</sub>-Me<sub>2</sub> and *trans*-L9-Br<sub>2</sub>-Me<sub>2</sub>.

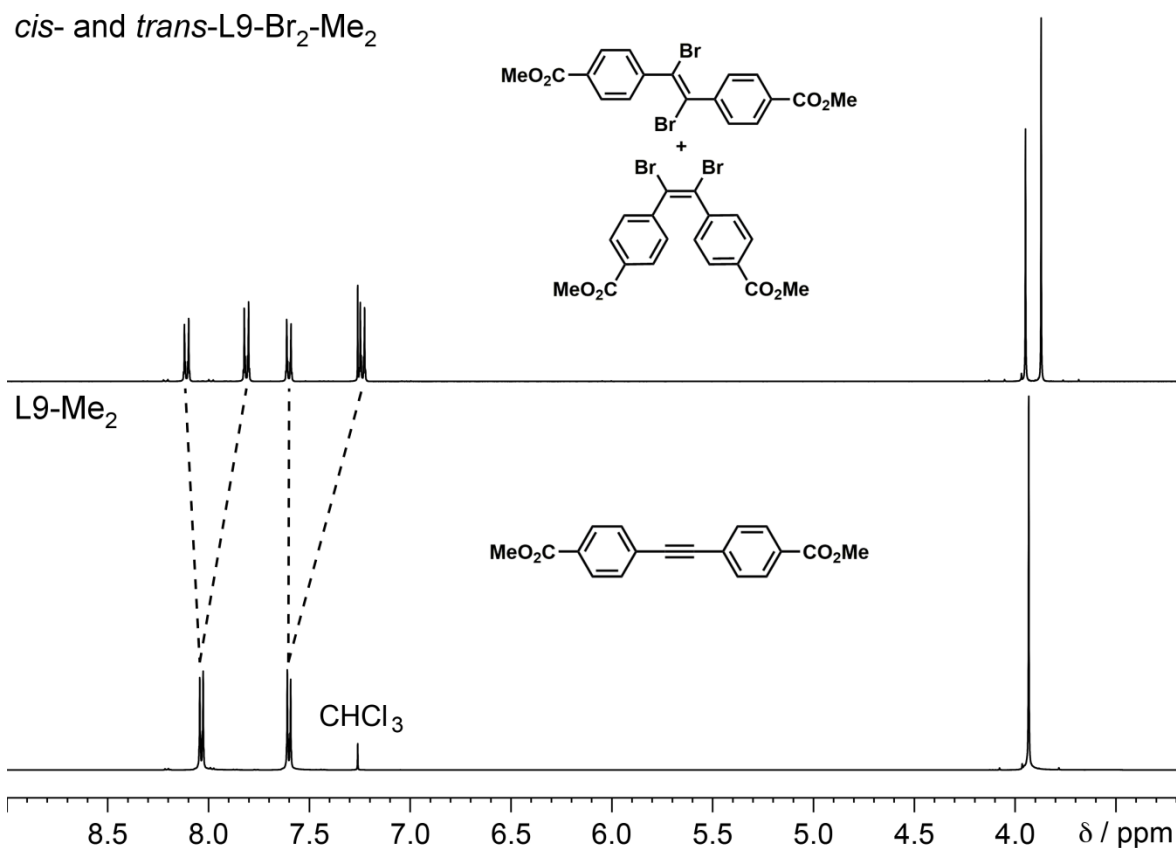


**Figure 3.18.** Stacked partial <sup>1</sup>H NMR spectra (CDCl<sub>3</sub>) of L9-Me<sub>2</sub> and its brominated products which have been assigned as *cis*- and *trans*-L9-Br<sub>2</sub>-Me<sub>2</sub>.

<sup>1</sup>H NMR integral ratios confirm that the products are present in an approximate 40:60 ratio. Complete disappearance of the peaks corresponding to L9-Me<sub>2</sub> confirms quantitative bromination and mass spectrometry of the product mixture found a peak at  $m/z = 476.9147$ , corresponding to the molecular ion [Na(L9-Br<sub>2</sub>-Me<sub>2</sub>)]<sup>+</sup>, which has a calculated  $m/z = 476.9136$ . The absence of peaks of higher mass confirms that the products are *cis*- and *trans*-L9-Br<sub>2</sub>-Me<sub>2</sub> and that higher order brominated products have not been formed even in the presence of an excess of Br<sub>2</sub>. Single crystal X-ray diffraction was performed on single crystals obtained upon slow evaporation of the NMR solution of L9-Br<sub>2</sub>-Me<sub>2</sub>. Data was collected for two crystals with different morphologies, revealing two *trans*-L9-Br<sub>2</sub>-Me<sub>2</sub> polymorphs (Figure 3.19).



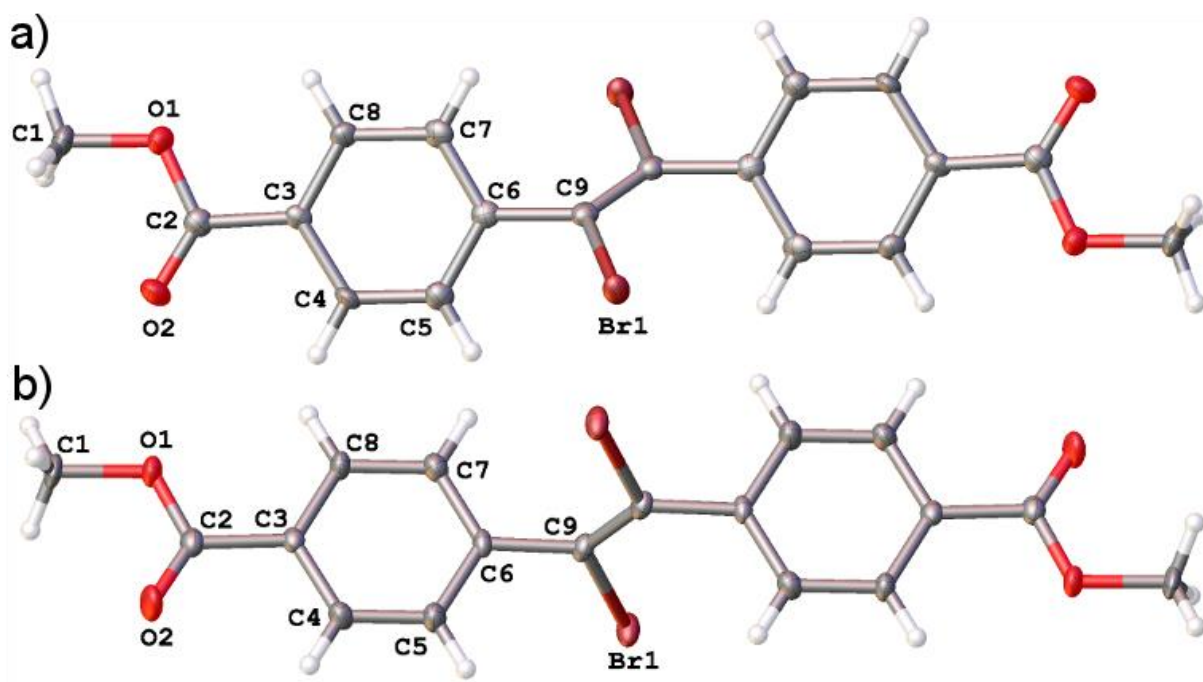


**Figure 3.19.** Solid state structure and atom labelling scheme (asymmetric unit only) of a) *trans*-L9-Br<sub>2</sub>-Me<sub>2</sub>-I and b) *trans*-L9-Br<sub>2</sub>-Me<sub>2</sub>-II. Displacement ellipsoids are drawn at 50% probability level.

The major difference between the solid-state structures of the two polymorphs is the orientation of the benzene rings with respect to the *trans*-dibromoalkene unit, illustrated by torsion angles C5-C6-C9-Br1 = -51.4(10)° for I and C5-C6-C9-Br1 = 71.2(5)° for II.

The mixture of *cis*- and *trans*-L9-Br<sub>2</sub>-Me<sub>2</sub> resulting from the solution phase bromination of L9-Me<sub>2</sub> is in stark contrast to the stereoselective formation of *trans*-L9-Br<sub>2</sub> when **Zr-L9** and **Hf-L9** are postsynthetically brominated. The enhanced stereoselectivity results from the topological constraints of the ligands when contained within the MOFs. This enhanced stereoselectivity prompted the solution phase bromination of L10-Me<sub>2</sub> and L11-Me<sub>2</sub> to compare with their transformation when locked within MOFs.

L10-Me<sub>2</sub> contains an integral butadiyne unit and there is very little literature on halogenation of butadiyne moieties<sup>42</sup> however, the solution phase bromination of L10-Me<sub>2</sub> was attempted. Mass spectrometry indicated that a tetrabromodialkene species had been synthesised, with no evidence of partially brominated products. <sup>1</sup>H (Figure 3.20) and <sup>13</sup>C NMR spectroscopies were used to characterise the products, revealing that a mixture of products were obtained.

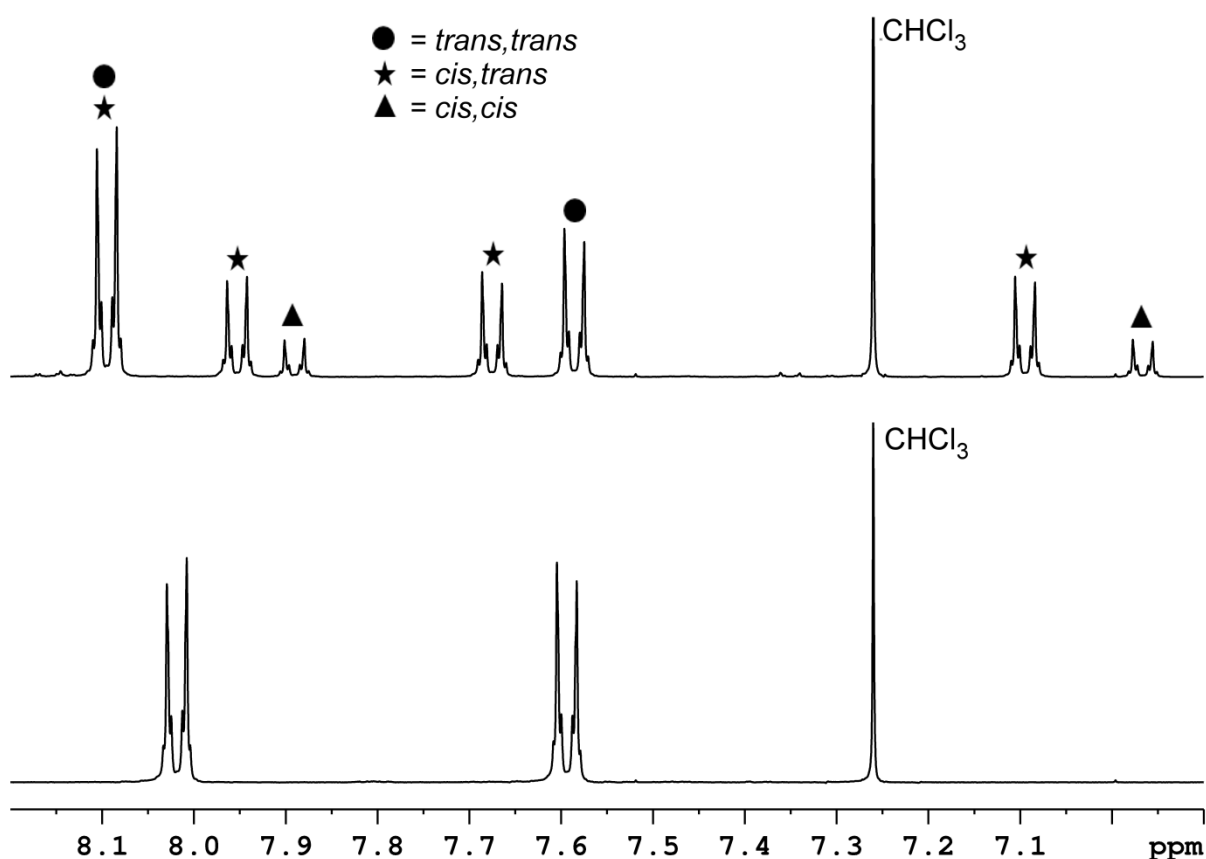


**Figure 3.20.** Stacked partial  $^1\text{H}$  NMR spectra ( $\text{CDCl}_3$ ) of  $\text{L10-Me}_2$  (bottom) and its brominated products (top), the isomers of  $\text{L10-Br}_4\text{-Me}_2$ .

The products have been assigned as *trans,trans*-, *cis,trans*- and *cis,cis*- $\text{L10-Br}_4\text{-Me}_2$  and using  $^1\text{H}$  NMR integral ratios the relative product distribution is calculated as 50:40:10 (*trans,trans*:*cis,trans*:*cis,cis*). The signals corresponding to the *cis,trans* isomer were confidently assigned due to the lower symmetry of the ligand while the *trans,trans* and *cis,cis* isomers have been assigned based on steric interactions, assuming that formation of the less sterically hindered *trans,trans* product is favoured. The  $^{13}\text{C}$  NMR spectrum was complicated by the presence of multiple geometrical isomers and their close chemical shifts prevented their confident assignment, but the  $^1\text{H}$  and  $^{13}\text{C}$  NMR spectra unambiguously show that solution phase bromination of  $\text{L10-Me}_2$  is non-stereoselective.

Similarly, the solution phase bromination of  $\text{L11-Me}_2$  resulted in a mixture of all three possible geometric isomers of  $\text{L11-Br}_4\text{-Me}_2$ .  $^1\text{H}$  NMR spectroscopy (see Appendix, Chapter 6 Figure 6.29) revealed that the three geometric isomers, namely *trans,trans*-, *cis,trans*- and *cis,cis*- $\text{L10-Br}_4\text{-Me}_2$  were present in a 60:35:5 ratio, assuming that formation of the

*trans,trans* isomer is preferred over the sterically more hindered *cis,cis* isomer. The limited solubility of L11-Br<sub>4</sub>-Me<sub>2</sub> in routine NMR solvents prevented <sup>13</sup>C NMR spectroscopic data from being collected. Nevertheless, solution phase brominations of L10-Me<sub>2</sub> and L11-Me<sub>2</sub> have been shown to be non-stereoselective with a mixture of all three geometric isomers obtained. Postsynthetic bromination of the corresponding MOFs was attempted to determine whether improved stereoselectivities could be obtained by placing the ligands under the topological constraints of the MOFs.

### 3.10 Postsynthetic Bromination of Zr-L10

**Zr-L10** contains integral butadiyne units and although there exists very little literature on the halogenation of butadiyne units,<sup>42</sup> postsynthetic bromination of **Zr-L10** was attempted, to compare with the solution phase bromination of L10-Me<sub>2</sub> where a mixture of all three geometric isomers were obtained. Transformation of integral butadiyne units to tetrabromodialkene units is expected to result in a considerable mechanical contraction of the MOF. PXRD was used to assess the crystallinity of the brominated product, **Zr-L10-Br<sub>4</sub>** (Figure 3.21).

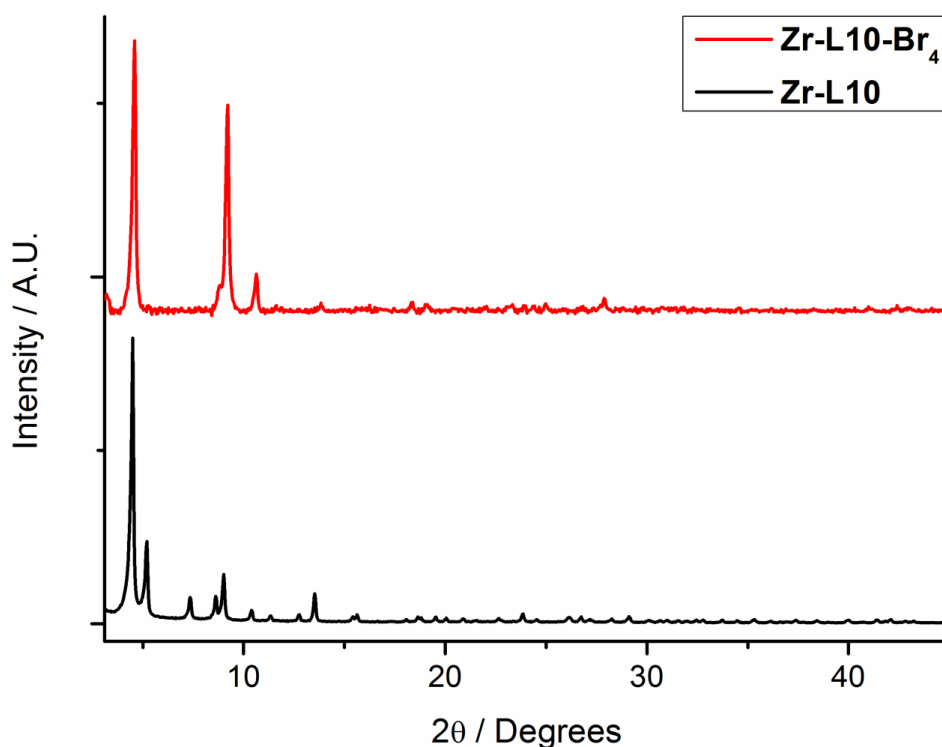


**Figure 3.21.** Stacked PXRD patterns of **Zr-L10** and its brominated product **Zr-L10-Br<sub>4</sub>**.

Comparing the PXRD patterns of **Zr-L10** and **Zr-L10-Br<sub>4</sub>** there are obvious changes in peak positions and their relative intensities, suggesting chemical transformation of the butadiyne units.

<sup>1</sup>H NMR spectroscopy of acid digested MOF (DMSO-*d*<sub>6</sub>/D<sub>2</sub>SO<sub>4</sub>) samples was used to determine the percentage bromination (Figure 3.22). Complete disappearance of peaks corresponding to L10-H<sub>2</sub> combined with the presence of two aromatic doublets with increased splitting confirms quantitative conversion to either *cis,cis*- or *trans,trans*-L10-Br<sub>4</sub>-H<sub>2</sub> (due to the lower symmetry of *cis,trans*-L10-Br<sub>4</sub>-H<sub>2</sub> four signals would be expected for the aromatic protons). Peaks corresponding to residual benzoic acid remaining from the modulated synthesis of **Zr-L10** are highlighted with an asterisk. Based on the significant steric clash between bulky bromine atoms of the tetrabromodialkene unit and the constraints of the UiO-66 MOF topology the product is expected to be *trans,trans*-L10-Br<sub>4</sub>-H<sub>2</sub>.

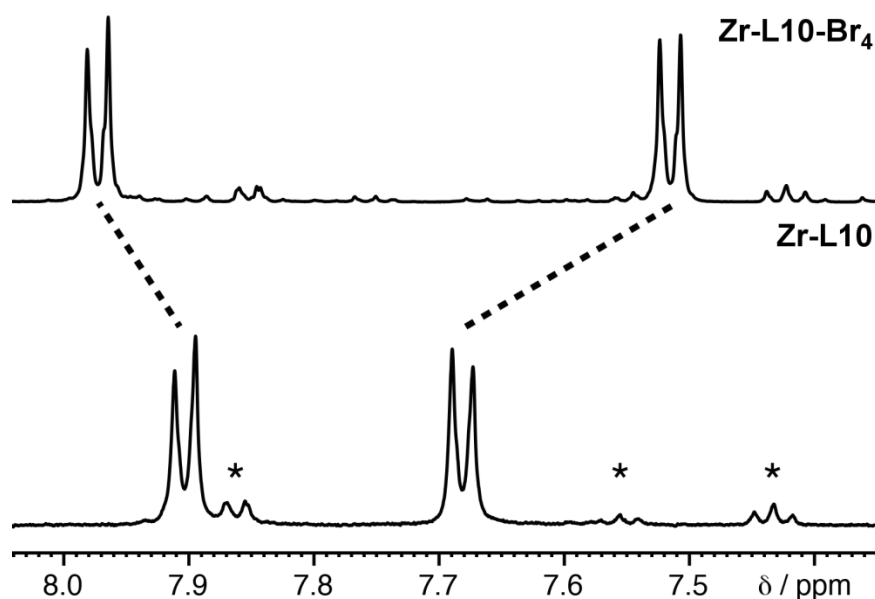


**Figure 3.22.** Stacked partial  $^1\text{H}$  NMR spectra of digested samples ( $\text{DMSO-}d_6/\text{D}_2\text{SO}_4$ ) of **Zr-L10** and **Zr-L10-Br<sub>4</sub>**. The asterisks represent peaks corresponding to residual benzoic acid.

The limited solubility of L10- $\text{H}_2$  in routine NMR solvents prevents  $^{13}\text{C}$  NMR spectroscopy of digested samples of **Zr-L10** from being obtained. Only seven resonances corresponding to the brominated product are observed in the  $^{13}\text{C}$  NMR spectrum of **Zr-L10-Br<sub>4</sub>**, providing further evidence of conversion to a single product. The very similar values for the chemical shifts of the *trans*-dibromoalkene carbon atoms in **Zr-L10-Br<sub>4</sub>** and **Zr-L9-Br<sub>2</sub>** ( $\delta = 117.6$  ppm vs.  $\delta = 118.2$  ppm, respectively) suggests that the single species is *trans,trans*-L10-Br<sub>4</sub>- $\text{H}_2$  (see Appendix, Chapter 6 Figure 6.30).

Small amounts of bulk microcrystalline powders of **Zr-L10** and **Zr-L10-Br<sub>4</sub>** were analysed by Raman spectroscopy, although **Zr-L10-Br<sub>4</sub>** appeared to be sensitive to laser irradiation and this is reflected in the increased background noise in the spectrum (Figure 3.23a). However, decreasing the laser power and narrowing the hole size allowed spectra to be successfully collected, and comparing the two materials it is clear that **Zr-L10** has been quantitatively brominated. There is complete disappearance of the alkyne peak at  $2230\text{ cm}^{-1}$  and, combined with the emergence of a distinct shoulder on the alkene peak at  $1600\text{ cm}^{-1}$ , this is representative of the butadiyne unit being brominated to become a tetrabromodialkene.<sup>35</sup>

Comparing the TGA profiles of **Zr-L10** and **Zr-L10-Br<sub>4</sub>** it is evident that a two-step profile is obtained for the brominated material (excluding solvent loss), with the first step

representing debromination while the resulting material also appears to be thermally stable to higher temperatures (Figure 3.23b).

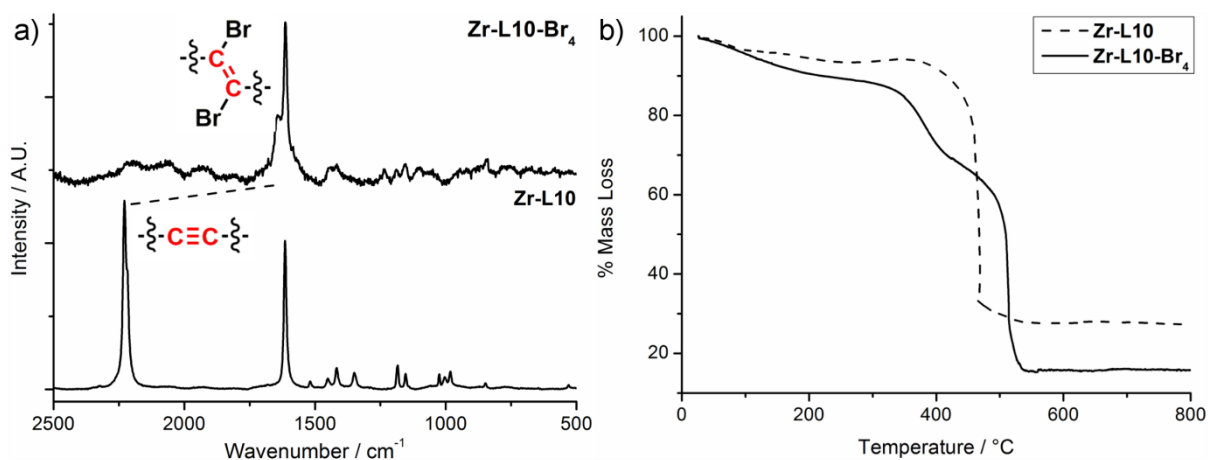


**Figure 3.23.** Comparison of a) the Raman spectra and b) the TGA profiles of **Zr-L10** and its brominated product **Zr-L10-Br<sub>4</sub>**.

The mass loss during the first step of **Zr-L10-Br<sub>4</sub>** (~200-450 °C) corresponds to a mass loss of ~26.4%, whilst the expected bromine content is 44.3%. This observation is inconsistent with the very close correlation found from bromine analysis (44.3% calculated; 43.1% found) and spectroscopic evidence which suggest quantitative bromination. The total mass loss between 200-550 °C is ~82.9% which matches exactly with the theoretical mass loss expected upon decomposition of **Zr-L10-Br<sub>4</sub>** to ZrO<sub>2</sub>. Therefore it is likely that during thermal decomposition of **Zr-L10-Br<sub>4</sub>** there is a temperature range in which both debromination and framework collapse occur simultaneously.

Single crystals of **Zr-L10** were brominated in a SCSC manner and <sup>1</sup>H NMR spectroscopy of a small amount of digested crystals (DMSO-*d*<sub>6</sub>/D<sub>2</sub>SO<sub>4</sub>) confirmed quantitative bromination. The appearance of the crystals did not alter during the transformation, however despite multiple data collection attempts the data were insufficient to allow a single crystal model to be obtained. **Zr-L10-Br<sub>4</sub>** retains the cubic *Fm-3m* space group of its parent material with the unit cell edge *a* decreasing from 33.3694(3) Å to 32.7864(7) Å during bromination. The tetrabromodialkene unit of **Zr-L10-Br<sub>4</sub>** exhibits significant disorder, being geometrically frustrated both vertically and horizontally, and this is likely the reason for weak single crystal data. The ability to stereoselectively brominate butadiyne units within a Zr MOF, which is able to remain crystalline even in the presence of an extreme mechanical contraction (~0.58

Å) prompted attempts to postsynthetically brominate **Zr-L11** and **Hf-L11**. Similar to **Zr-L10**, **Zr-L11** and **Hf-L11** contain two integral alkyne units, although they are separated by a phenylene moiety. The presence of the phenylene spacer will remove part of the disorder observed in **Zr-L10-Br<sub>4</sub>** which resulted in unsatisfactory single crystal data collections.

### 3.11 Bulk Postsynthetic Bromination of Zr-L11 and Hf-L11

The structures of **Zr-L11** and **Hf-L11** are different to the other MOFs investigated for postsynthetic bromination as they exhibit two-fold interpenetration (Figure 3.2c). Despite framework interpenetration, **Zr-L11** and **Hf-L11** are still highly porous with surface areas of 2680 m<sup>2</sup>g<sup>-1</sup> and 2080 m<sup>2</sup>g<sup>-1</sup> respectively. Therefore, it was postulated that the considerable intrinsic porosity of the interpenetrated MOFs should permit Br<sub>2</sub> to react with the integral alkyne moieties provided inter-framework interactions do not disrupt the transformation. Bulk samples of **Zr-L11** and **Hf-L11** were brominated in the usual manner and the products were first analysed by PXRD (Figure 3.24).

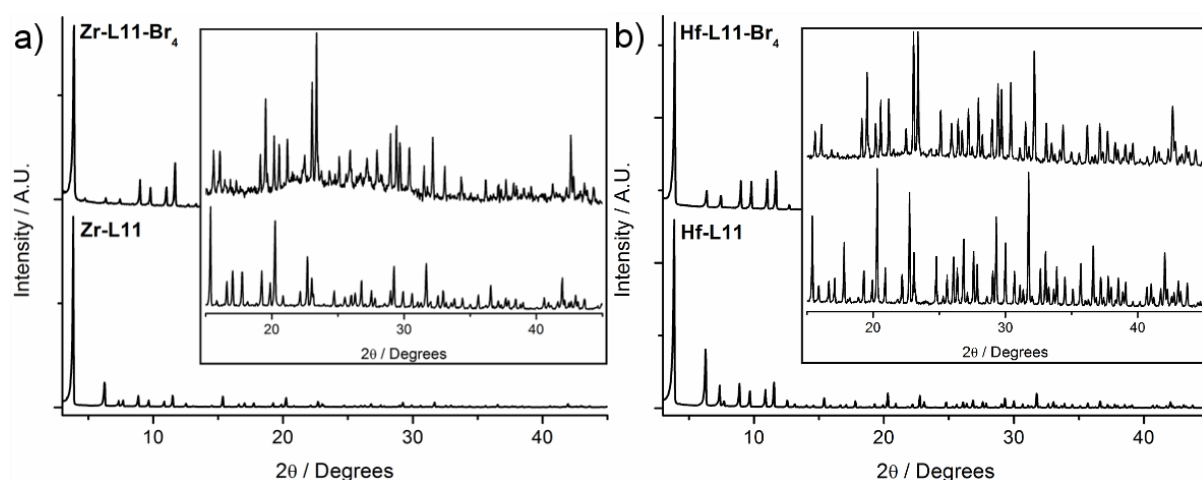


**Figure 3.24.** Stacked PXRD patterns of a) **Zr-L11** and **Zr-L11-Br<sub>4</sub>** and b) **Hf-L11** and **Hf-L11-Br<sub>4</sub>**. The insets are expanded views of the high angle data.

PXRD analysis confirms that both brominated MOFs are highly crystalline, even to high angles of  $2\theta$ . There are differences between the parent and brominated MOFs in terms of peak positions (the peaks of the brominated MOFs move to higher angles of  $2\theta$ ) and also their relative intensities, although this is in line with the mechanical contraction expected

upon transformation of alkyne units to dibromoalkene units. In **Zr-L9** postsynthetic bromination of the alkyne units resulted in a mechanical contraction of  $\sim 0.38$  Å and, as there are twice as many alkyne units in **L11** compared with **L9**, a larger mechanical contraction is expected. The ability of **Zr-L11** and **Hf-L11** to withstand this large mechanical contraction highlights their high mechanical stabilities.

$^1\text{H}$  NMR spectroscopy of acid digests ( $\text{DMSO-}d_6/\text{D}_2\text{SO}_4$ ) of the MOFs were used to assess the extent of bromination and to reveal the stereoselectivity of the transformation (Figure 3.25). Based on the stereoselective postsynthetic bromination of **Zr-L9** and **Hf-L9** it is expected that *trans,trans*-**L11-Br<sub>4</sub>** will be formed exclusively, compared with the liquid phase bromination of **L11-Me<sub>2</sub>** which results in a mixture of all three possible geometric isomers.

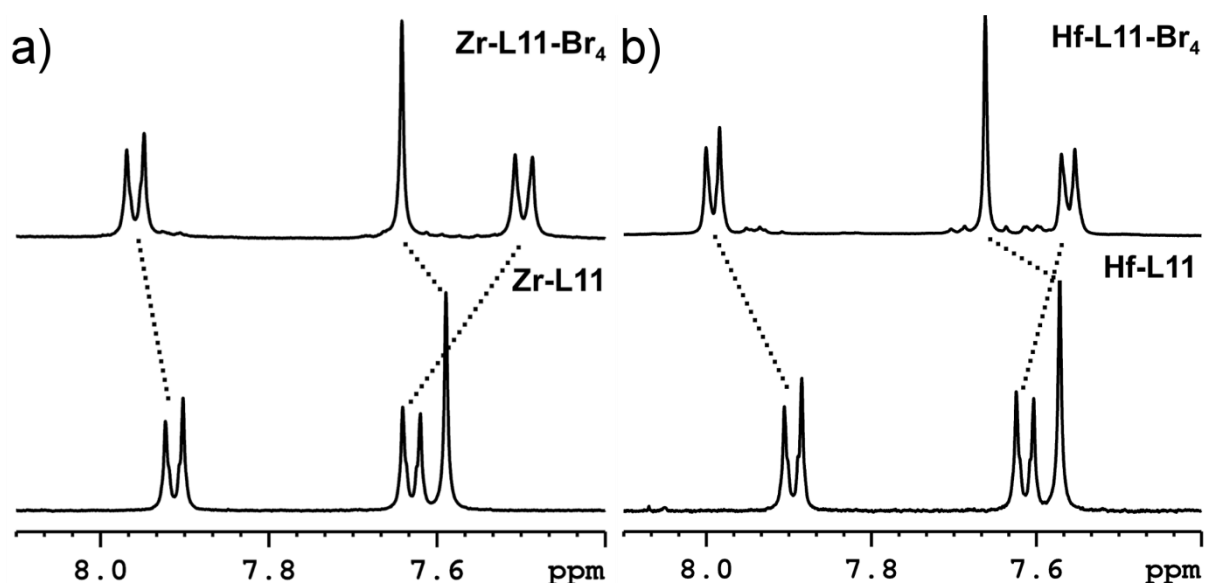


**Figure 3.25.** Stacked partial  $^1\text{H}$  NMR spectra of acid digests ( $\text{DMSO-}d_6/\text{D}_2\text{SO}_4$ ) of a) **Zr-L11** and **Zr-L11-Br<sub>4</sub>** and b) **Hf-L11** and **Hf-L11-Br<sub>4</sub>**.

There are obvious changes in the spectra of the digested MOF samples before and after bromination with complete disappearance of peaks corresponding to **L11-H<sub>2</sub>** confirming near-quantitative bromination. It is not possible to identify the single brominated species from the  $^1\text{H}$  NMR spectra, however it is possible to determine that either *cis,cis*- or *trans,trans*-**L11-Br<sub>4</sub>** is formed exclusively based on their symmetry. Due to symmetry constraints within the MOFs the single brominated species is believed to be *trans,trans*-**L11-Br<sub>4</sub>**.



Raman spectra of the MOFs are further evidence of quantitative postsynthetic bromination, revealing that interpenetration does not hinder the transformation (Figure 3.26).

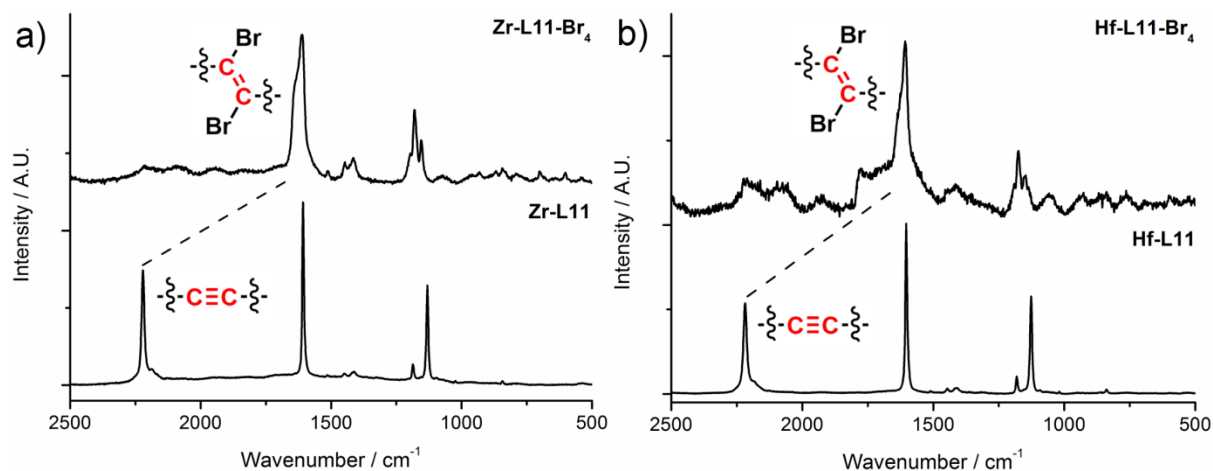


**Figure 3.26.** Comparison of the Raman spectra of a) **Zr-L11** and **Zr-L11-Br<sub>4</sub>** and b) **Hf-L11** and **Hf-L11-Br<sub>4</sub>**. The brominated materials were sensitive to laser irradiation, resulting in spectra of lower resolution and with increased background noise.

Postsynthetic bromination of alkyne to dibromoalkene units in **Zr-L11** and **Hf-L11** is evident from their Raman spectra with disappearance of the characteristic alkyne peak at ~2220 cm<sup>-1</sup> coupled with broadening of the alkene peak at ~1600 cm<sup>-1</sup>.<sup>35</sup> There are also distinct changes in terms of peak positions and their relative intensities observed on postsynthetic bromination. Spectroscopic analysis reveals the quantitative and stereoselective postsynthetic bromination of **Zr-L11** and **Hf-L11** and so TGA was used to determine the thermal stabilities of the brominated products (Figure 3.27).

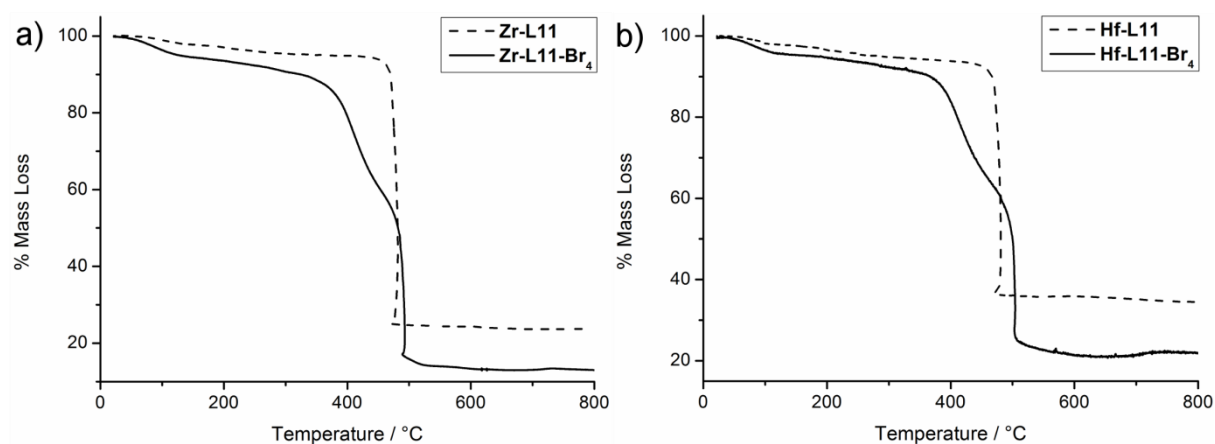


**Figure 3.27.** Comparison of the TGA profiles of a) **Zr-L11** and **Zr-L11-Br<sub>4</sub>** and b) **Hf-L11** and **Hf-L11-Br<sub>4</sub>**.

All four MOFs decompose at temperatures close to 500 °C, proving their high thermal stabilities, while the brominated materials, **Zr-L11-Br<sub>4</sub>** and **Hf-L11-Br<sub>4</sub>**, demonstrate two-step profiles. The first step represents debromination and assuming the material prior to the first mass loss to be fully evacuated MOF then the weight % of bromine can be calculated and these values are in close agreement with the values obtained from Br elemental analysis (Table 3.5). The thermal stabilities of **Zr-L11** and **Hf-L11** following debromination correlate well with the observed thermal properties of the parent materials.

**Table 3.5.** Comparison of the theoretical and experimental bromine content (from TGA and elemental Br analysis) of **Zr-L11-Br<sub>4</sub>** and **Hf-L11-Br<sub>4</sub>**.

	Theoretical Br content (%)	TGA (%)	Elemental Br analysis (%)
<b>Zr-L11-Br<sub>4</sub></b>	40.1	39.1	41.9
<b>Hf-L11-Br<sub>4</sub></b>	36.1	34.9	33.3

Close agreement between the theoretical and experimentally measured Br contents of **Zr-L11-Br<sub>4</sub>** and **Hf-L11-Br<sub>4</sub>** confirms that quantitative postsynthetic bromination was achieved. The presence of bulky Br atoms lining the MOF pores, their increased molecular weight and the mechanically induced contraction prompted N<sub>2</sub> uptake analysis (77 K) to determine the effect of bromination on the MOFs porosity (Figure 3.28).

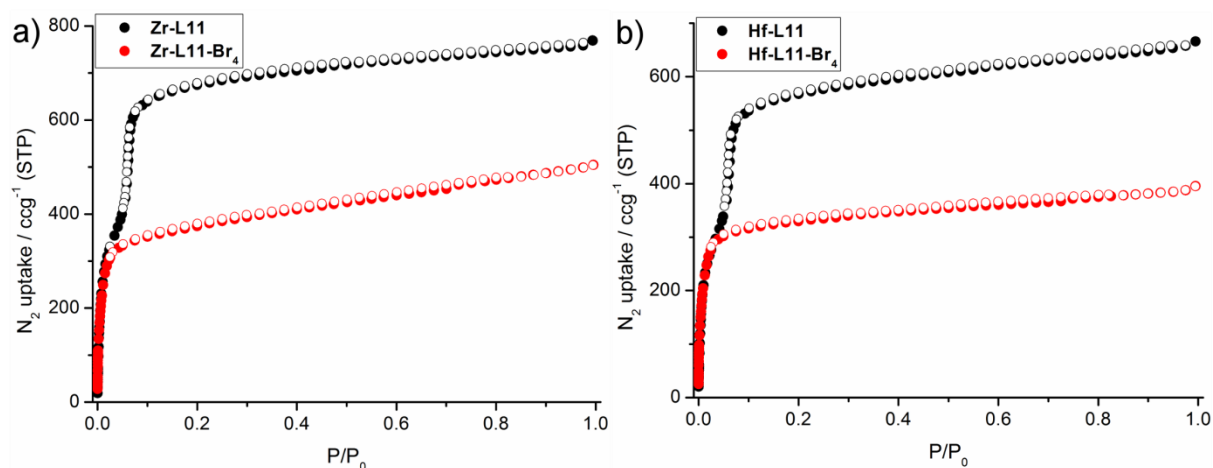


**Figure 3.28.** N<sub>2</sub> adsorption (closed circles) and desorption (open circles) isotherms of a) **Zr-L11** and **Zr-L11-Br<sub>4</sub>** and b) **Hf-L11** and **Hf-L11-Br<sub>4</sub>**.

It is clear that the N<sub>2</sub> adsorption isotherms of the parent and brominated materials are significantly different, with the brominated MOFs taking up considerably less N<sub>2</sub>. Upon bromination stepwise adsorption is lost, suggesting different pore filling mechanisms, as in the parent materials the smaller tetrahedral pores fill prior to the larger tetrahedral pores. The BET surface areas of the four MOFs were calculated and are summarised in Table 3.6.

**Table 3.6.** BET surface areas of **Zr-L11**, **Zr-L11-Br<sub>4</sub>**, **Hf-L11** and **Hf-L11-Br<sub>4</sub>** alongside the observed and theoretical percentage decrease in surface area upon bromination.

	<b>Zr-L11</b>	<b>Zr-L11-Br<sub>4</sub></b>	<b>Hf-L11</b>	<b>Hf-L11-Br<sub>4</sub></b>
<b>BET surface area (m<sup>2</sup>g<sup>-1</sup>)</b>	2650	1440	2250	1320
<b>Observed Decrease (%)</b>	46		41	
<b>Theoretical Decrease (%)</b>	40		36	

Comparing the gravimetric BET surface areas of the MOFs it is clear that a larger than expected reduction in porosity is observed and this is attributed to be the result of the mechanical contraction that results from bromination. Pore size distributions provide further evidence of the mechanical contraction with a reduction in the main pore diameter from 14.2 Å to 11.0 Å observed for both **Zr-L11** and **Hf-L11** upon bromination (Figure 3.29).

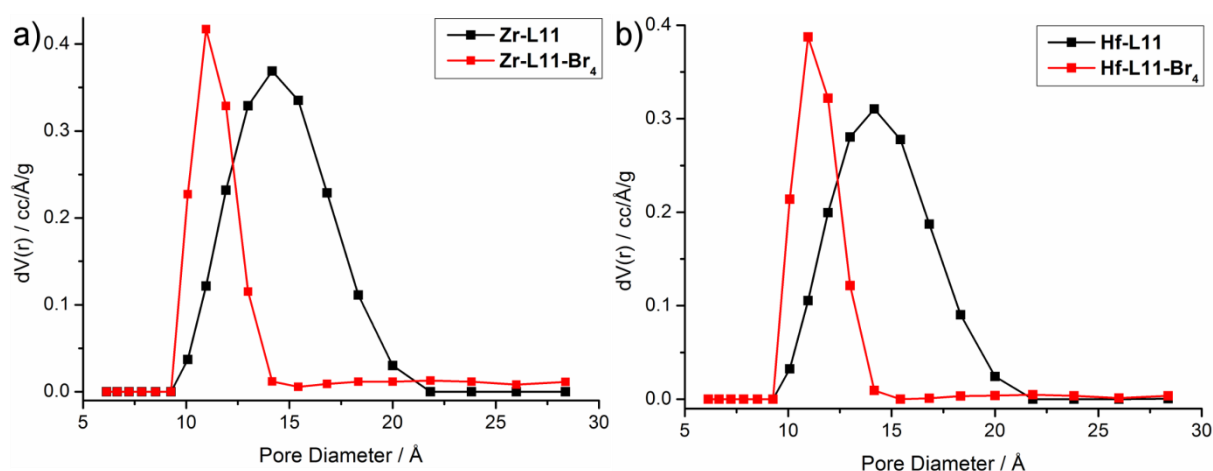


**Figure 3.29.** Comparison of the pore size distributions (QSDFT, N<sub>2</sub> at 77 K on carbon) of a) **Zr-L11** and **Zr-L11-Br<sub>2</sub>** and b) **Hf-L11** and **Hf-L11-Br<sub>4</sub>**.

The large mechanical contraction is due to the presence of two integral alkyne units per ligand. On bromination the hybridisation of the carbon atoms changes from  $sp$  to  $sp^2$  and this is accompanied by changes in bond lengths and angles.

Bulk analysis of **Zr-L11**, **Hf-L11** and their brominated products confirms that quantitative postsynthetic bromination has been achieved despite 2-fold interpenetration.  $^1\text{H}$  NMR spectroscopy confirms the stereoselectivity of the transformation while  $\text{N}_2$  uptake experiments reveal that postsynthetic bromination results in a considerable mechanical contraction. The MOFs appear to be able to withstand the demanding mechanical contraction as PXRD confirms their crystallinity and so postsynthetic bromination was attempted on single crystals to obtain accurate structural information concerning the transformation.

### 3.12 Single Crystal Postsynthetic Bromination of Zr-L11 and Hf-L11

Single crystals of **Zr-L11** and **Hf-L11** were exposed to  $\text{CHCl}_3$  solutions containing an excess of  $\text{Br}_2$  and allowed to react for 96 hours before being resolvated in fresh solvent. The crystals were sufficiently stable to withstand the harsh bromination conditions and also the induced mechanical contraction. L11 contains two integral alkynes and upon postsynthetic bromination they are transformed to flexible dibromoalkene units. The increased flexibility of the ligands is evident in the single crystal structures, with multiple ligand orientations resulting in disorder of the dibromoalkene units (Figure 3.30 shows the disorder in **Hf-L11-Br<sub>4</sub>**).

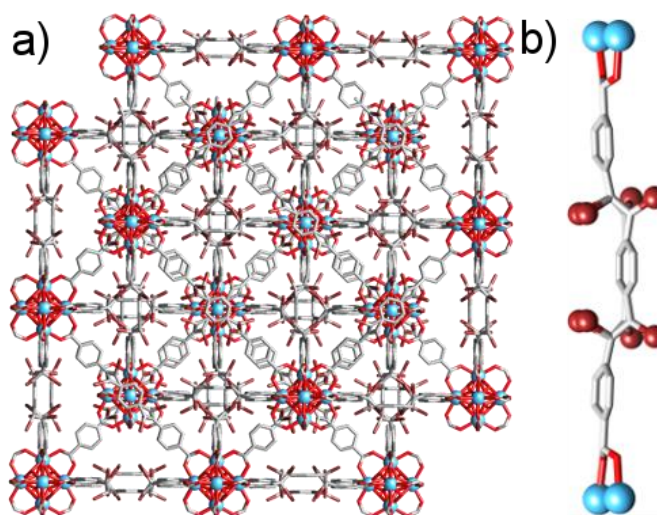


**Figure 3.30.** a) Portion of the solid state structure of **Hf-L11-Br<sub>4</sub>**. b) Structural representation of L11-Br<sub>4</sub> within **Hf-L11-Br<sub>4</sub>** highlighting the *trans,trans* configuration of the ligand despite rotation of the central phenylene core resulting in multiple bromine positions. Atom colour scheme: Hf, blue; C, grey; O, red; Br, brown. Hydrogen atoms are omitted for clarity.

SCXRD data reveal that the brominated materials retain the cubic  $Fd-3m$  space group of their parent samples. Despite the increased flexibility of the ligands and the resulting disorder, the stereoselective formation of *trans,trans*-L11-Br<sub>4</sub> is evident, in contrast to the liquid phase bromination of L11-Me<sub>2</sub> which results in a mixture of all three possible geometric isomers. Postsynthetic bromination of integral alkyne units to dibromoalkene units is accompanied by a change in hybridisation of integral carbon atoms ( $sp$  to  $sp^2$ ), resulting in alterations to the geometry and length of the ligand. This causes a considerable mechanical contraction and the observed decrease in the unit cell edges are summarised in Table 3.7.

**Table 3.7.** Unit cell edge parameters for **Zr-L11**, **Hf-L11** and their brominated products alongside the observed mechanical contraction.

	<b>Zr-L11</b>	<b>Zr-L11-Br<sub>4</sub></b>	<b>Hf-L11</b>	<b>Hf-L11-Br<sub>4</sub></b>
<b><i>a</i> (Å)</b>	39.8116(7)	39.067(7)	39.806(5)	39.0451(3)
<b>Contraction (Å)</b>	0.745		0.761	

Comparing the unit cell edges of the parent and brominated MOFs it is clear that mechanical contractions as large as  $\sim 0.75$  Å are observed. This is a considerable strain and a very demanding structural reorientation, however the high mechanical stabilities of Zr and Hf

MOFs allows them to retain their crystallinity. It is anticipated that the change in ligand geometry and the introduction of flexibility will alter the MOFs mechanical properties.

Postsynthetic bromination has been shown to proceed stereoselectively due to the topological constraints of the ligands within the MOFs, which reduces their conformational freedom. The high mechanical stabilities of Zr and Hf MOFs enables their quantitative transformation without any detrimental impact on their desirable properties. The facile addition of Br<sub>2</sub> across integral unsaturated alkene and alkyne units within Zr and Hf MOFs prompted their investigation for use as potential vapour phase iodine capture materials.

### **3.13 Postsynthetic Iodination of Zr-L8, Zr-L9, Zr-L10 and Zr-L11**

Capture and sequestration of radioactive iodine released during nuclear disasters is an important application and MOFs have previously been investigated as candidate materials.<sup>43-45</sup> The high internal pore volumes of MOFs result in large physisorption storage capacities while Zr and Hf MOFs containing integral unsaturated functionality present the opportunity for chemisorption by irreversible covalent transformation of the ligands.

A series of experiments were performed where small quantities of Zr MOFs were added to small open ended vials and placed into larger outer vials containing a known excess of I<sub>2</sub> (15 equivalents). The MOFs were then in contact with iodine vapour within the closed system and gravimetric measurements at set time intervals revealed the total iodine uptake of the MOFs (physisorption and chemisorption), while <sup>1</sup>H NMR digests (DMSO-*d*<sub>6</sub>/D<sub>2</sub>SO<sub>4</sub>) highlighted the percentage chemisorption. By using the different methods for analysing the I<sub>2</sub> uptake of the MOFs it was possible to determine both the physisorption (reversible) and chemisorption (irreversible) capacities (Figure 3.31).

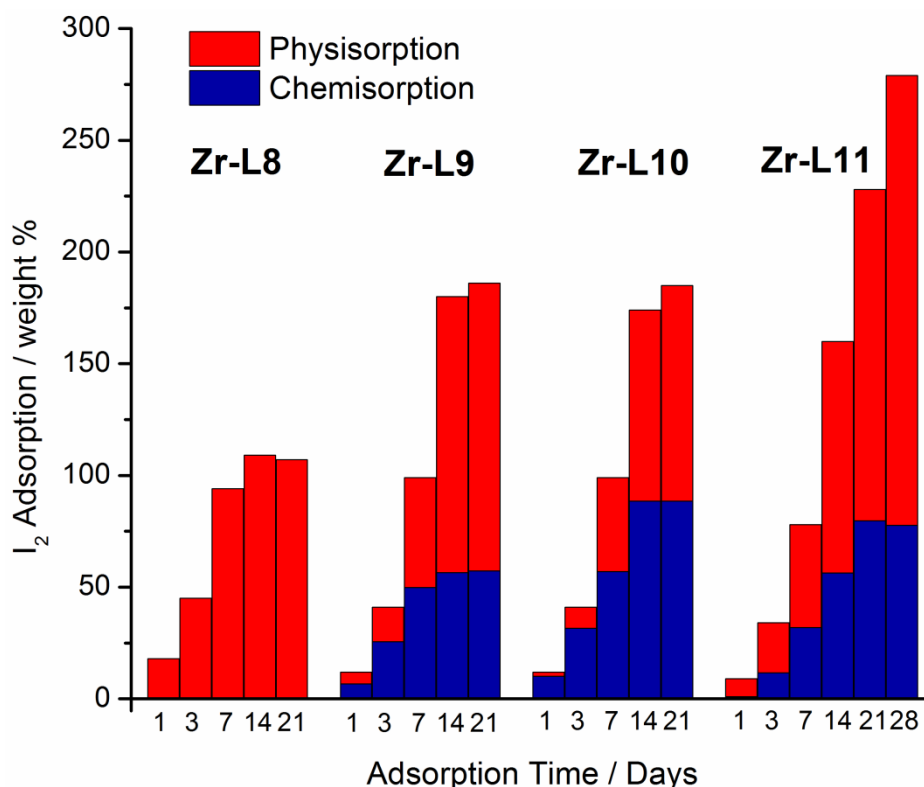


**Figure 3.31.** Summary of the physisorption and chemisorption iodine storage capacities of **Zr-L8**, **Zr-L9**, **Zr-L10** and **Zr-L11**.

It is interesting to note that **Zr-L8** is unable to chemisorb  $I_2$  across its integral alkene units, despite bromination and bromohydration occurring in a facile manner; however a maximum  $I_2$  storage capacity of 107% *w/w* was recorded. **Zr-L9** and **Zr-L10** demonstrate larger total  $I_2$  storage capacities as they can both chemisorb and physisorb  $I_2$ . The presence of twice as many alkyne units in **Zr-L10** is reflected in the chemisorption capacities, with **Zr-L9** demonstrating a maximum of 57% *w/w* irreversible trapping of  $I_2$ , compared to 88.5% *w/w* for **Zr-L10**. **Zr-L11** displays the highest storage value, with a maximum uptake of 279% *w/w*. The  $I_2$  chemisorption capacity of **Zr-L11** is slightly lower than that of **Zr-L10**, even though both materials contain similar alkyne contents; hence the superior uptake is the result of a high tendency of  $I_2$  to physisorb within the pores, possibly due to the high density of  $Zr_6$  clusters as a result of interpenetration.

Single crystals of iodinated ligands (*trans*-L9- $I_2$ -H<sub>2</sub>, *trans,trans*-L10- $I_4$ -H<sub>2</sub> and *trans,trans*-L11- $I_4$ -H<sub>2</sub>) were collected from NMR solutions of acid digested iodinated MOFs (DMSO-

$d_6/D_2SO_4$ ), confirming chemisorption of  $I_2$  by covalent attachment and also revealing the *trans* stereoselectivity (Figures 3.32).

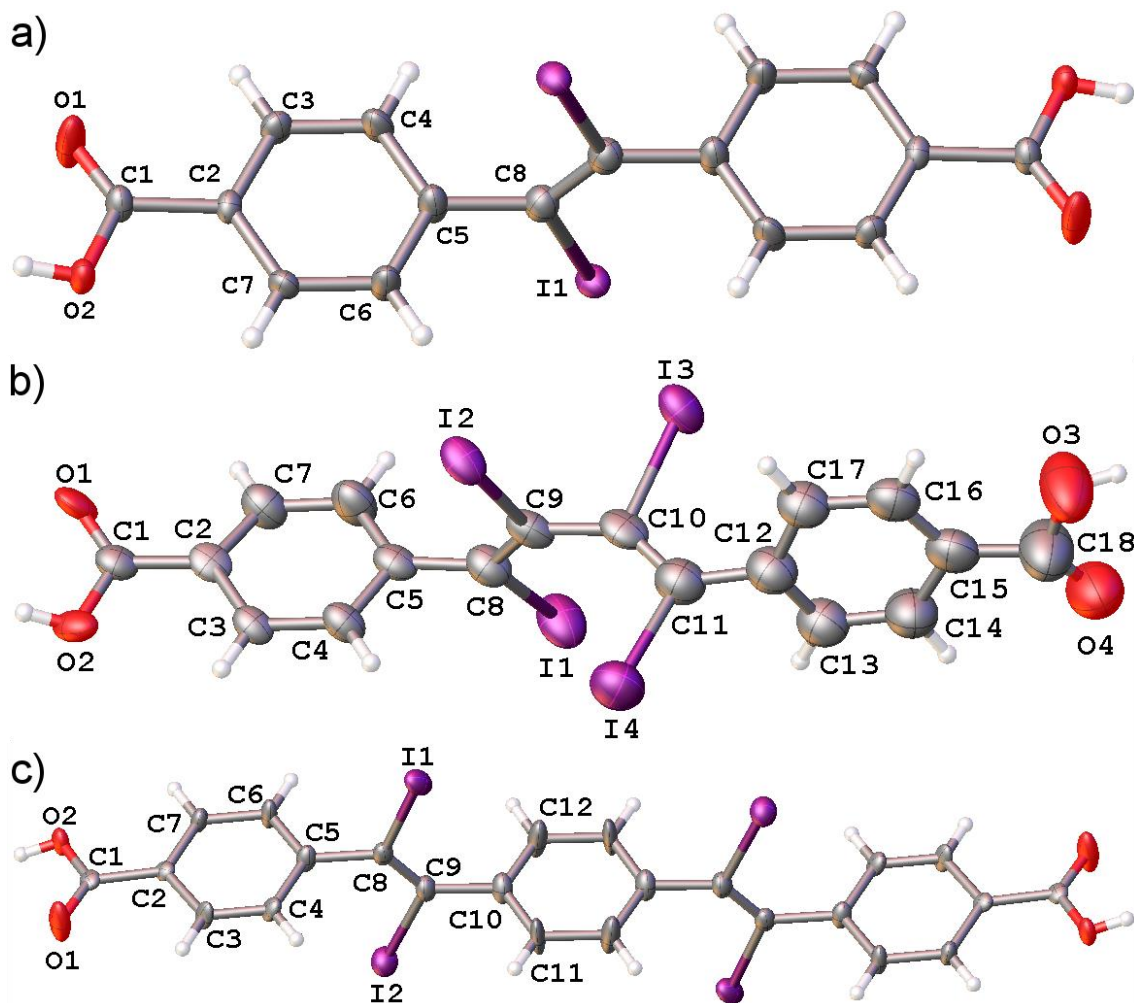


**Figure 3.32.** Solid state structures and atom labelling schemes of a) *trans*-L9- $I_2$ - $H_2$ , b) *trans,trans*-L10- $I_4$ - $H_2$  and c) *trans,trans*-L11- $I_4$ - $H_2$ . Displacement ellipsoids are drawn at 50% probability level. DMSO solvent molecules have been omitted for clarity.

The combined presence of integral unsaturated functionality and the intrinsic porosities of the Zr MOFs results in highly promising iodine uptake capacities. The combination of both physisorption and chemisorption capacities introduces aspects for both reversible and irreversible capture, while the high mechanical stabilities of Zr MOFs allows them to withstand the harsh mechanical conditions, which prevents their collapse and as a result allows encouraging storage capacities of  $I_2$  to be realised.



### 3.14 Conclusions and Future Work

In conclusion, it has been demonstrated that integral postsynthetic halogenation of unsaturated functionality within Zr and Hf MOFs is possible as a result of their high chemical and mechanical stabilities. The MOFs investigated contain integral alkene, alkyne and butadiyne units as these are attractive sites of potential reactivity.

Firstly, bulk postsynthetic bromination of **Zr-L8** was attempted as postsynthetic bromination of a Zn-stilbene MOF had previously been reported, however the harsh chemical conditions and significant mechanical strain resulted in collapse of the Zn-MOF. The increased stabilities of Zr MOFs enables **Zr-L8** (which contains integral alkene units) to be quantitatively brominated as a bulk microcrystalline powder and also as single crystals. **Zr-L8** and its postsynthetically brominated product, **Zr-L8-Br<sub>2</sub>** were characterised using a number of experimental techniques including <sup>1</sup>H and <sup>13</sup>C NMR spectroscopies, Raman spectroscopy, thermogravimetric analysis, elemental bromine analysis, powder X-ray diffraction and N<sub>2</sub> uptake measurements. Extensive characterisation definitively proved that **Zr-L8** was quantitatively brominated, resulting exclusively in the *meso* bromination product due to the decreased conformational freedom of the ligand when under the topological constraints of the MOF. Postsynthetic bromination of **Zr-L8** was also performed in a single-crystal to single-crystal (SCSC) manner providing accurate structural information regarding the transformation. While investigating milder bromination conditions, it was found that bromohydration (the dual insertion of Br and OH) of the integral stilbene units was possible. Reaction conditions were varied however it was not possible to exclusively form the bromohydration product. The high chemical stability of **Zr-L8** is evident as it remains crystalline while in contact with H<sub>2</sub>O during bromohydration, suggesting that other modifications of the integral alkene units may be possible.

Postsynthetic halogenation was extended to Zr and Hf MOFs containing integral alkyne units that upon bromination are transformed to dibromoalkene units. The transformation from alkyne to dibromoalkene is accompanied by a change in hybridisation of integral carbon atoms, transitioning from sp to sp<sup>2</sup>, resulting in changes to both bond lengths and angles causing a significant mechanical contraction. The MOFs were able to be postsynthetically brominated in a SCSC manner, providing evidence of mechanical contractions as large as

$\sim 0.75$  Å when **Zr-L11** and **Hf-L11**, which contain two alkyne units per ligand, are postsynthetically brominated. Postsynthetic bromination of integral alkyne units within Zr and Hf MOFs is stereoselective, resulting exclusively in the *trans* bromination products in contrast to solution phase bromination of the ligands which results in a mixture of the possible geometric isomers. The high chemical stability of Zr and Hf MOFs enables them to withstand contact with highly corrosive Br<sub>2</sub> solutions for prolonged periods of time while their high mechanical stabilities allows them to tolerate large mechanical contractions. Both conditions are prerequisites and allow the MOFs to undergo facile postsynthetic bromination.

Postsynthetic halogenation of Zr and Hf MOFs was extended to include vapour phase iodine capture. Interestingly, **Zr-L8** does not chemisorb vapour phase I<sub>2</sub> despite undergoing postsynthetic bromination and bromohydrination. However, the alkyne containing MOFs are able to react with vapour phase I<sub>2</sub>, resulting in irreversible chemisorption by addition of I<sub>2</sub> across integral unsaturated reactive sites. The Zr and Hf MOFs are also able to physisorb I<sub>2</sub> within their pores and **Zr-L11**, which is 2-fold interpenetrated, is able to take up considerable amounts of I<sub>2</sub> presumably due to the high density of Zr<sub>6</sub> clusters. As a result of both physisorption and chemisorption, **Zr-L11** demonstrates a very high total I<sub>2</sub> uptake of 279% w/w. The very high uptake of I<sub>2</sub> by the Zr MOFs demonstrates their potential use as adsorbents of radioactive iodine released during nuclear disasters.

It has been shown that the combined mechanical and chemical stabilities of Zr and Hf MOFs allow them to undergo facile integral stereoselective postsynthetic halogenation. It is anticipated that the range of modifications could be extended to include, for instance, thiol-ene and thiol-yne type modifications to enable the insertion of a wide range of functionality, ultimately resulting in a diverse range of functionalised MOFs suitable for different applications. The reactivity of the unsaturated units could also be extended to the capture of toxic species, such as Cl<sub>2</sub> which is highly corrosive and very dangerous to human health. Cl<sub>2</sub> gas has been used as a chemical warfare agent, and combined with its ease of production it is of great importance that efficient systems are developed for the removal of Cl<sub>2</sub> gas from airstreams. The ability of Zr MOFs containing unsaturated functionality to both physisorb and chemisorb halogens suggests they may hold great promise for Cl<sub>2</sub> capture and sequestration.

## 3.15 Experimental

### 3.15.1 General Experimental Remarks

All chemicals and solvents were purchased from Alfa Aesar, Fisher Scientific, Fluorochem, Merck Millipore, Sigma-Aldrich, Strem Chemicals and VWR and used without further purification.

**Microwave synthesis:** Microwave reactions were carried out in 35 ml pressure vials using a CEM Discover SP microwave, equipped with an Explorer 12 Hybrid auto sampler. The power was allowed to fluctuate to maintain a constant temperature of 100 °C throughout the course of the reaction. (University of Glasgow)

**Powder X-ray diffraction (PXRD):** PXRD measurements were carried out at 298 K using a PANalytical X'Pert PRO diffractometer ( $\lambda$  (CuK $\alpha$ ) = 1.5405 Å) on a mounted bracket sample stage. Data were collected over the range 3-45 °. PXRD patterns were predicted from single crystal data using Mercury 3.5.1.<sup>46</sup> (University of Glasgow)

**Single crystal X-ray diffraction (SCXRD):** Data for **Zr-L8-Br<sub>2</sub>**, **Zr-L9-Br<sub>2</sub>**, **Hf-L9-Br<sub>2</sub>**, **Zr-L10-Br<sub>4</sub>**, **Zr-L11-Br<sub>4</sub>** and **Hf-L11-Br<sub>4</sub>** were collected using a Rigaku AFC12 goniometer equipped with an enhanced sensitivity (HG) Saturn724+ detector mounted at the window of an FR-E+ SuperBright molybdenum rotating anode generator with VHF Varimax optics (70 µm focus) equipped with an Oxford Cryosystems cryostream device. (EPSRC UK National Crystallography Service)

Data for **etdb-Me<sub>2</sub>**, **trans-L9-Br<sub>2</sub>-Me<sub>2</sub>-I**, **trans-L9-Br<sub>2</sub>-Me<sub>2</sub>-II**, **trans-L9-I<sub>2</sub>-H<sub>2</sub>** and **trans,trans-L11-I<sub>4</sub>-H<sub>2</sub>** were collected using a Bruker ApexII CCD kappa goniometer with a Mo sealed tube source and equipped with an Oxford Cryosystems n-Helix device. Data for **trans,trans-L10-I<sub>4</sub>-H<sub>2</sub>** were collected using a Nonius KappaCCD with a Mo sealed tube source and equipped with an Oxford Cryosystems cryostream device. (University of Glasgow)

**Bromine analysis:** Carried out by MEDAC Ltd, analytical and chemical consultancy services. (Surrey, UK)

**Thermogravimetric analysis (TGA):** Measurements were carried out using a TA Instruments Q500 thermogravimetric analyser. Measurements were collected from room temperature to 800 °C with a heating rate of 10 °C / min. An N<sub>2</sub> atmosphere was used for L8 and L9 containing MOFs (as well as their brominated products) while an air atmosphere was used for L10 and L11 MOFs (as well as their brominated products). (University of Glasgow)

**Nuclear magnetic resonance spectroscopy (NMR):** NMR spectra were recorded on either a Bruker AVIII 400 MHz spectrometer or a Bruker AVI 500 MHz spectrometer and referenced to residual solvent peaks. (University of Glasgow)

**Raman spectroscopy:** Raman spectra were collected on a LabRAM HR system using a Ventus 532 laser ( $\lambda = 532$  nm, 100 mW), equipped with a Synapse CCD detection system. (University of Glasgow)

**Gas uptake:** N<sub>2</sub> adsorption isotherms were carried out at 77 K on a Quantachrome Autosorb iQ gas sorption analyser. Samples were degassed under vacuum at 120 °C for 20 hours using the internal turbo pump. BET surface areas were calculated from the isotherms using the Micropore BET Assistant and pore-size distribution analysis was carried out using QSDFT (N<sub>2</sub> on carbon at 77 K) both implemented in the Quantachrome ASiQwin operating software. (University of Glasgow)

### 3.15.2 Ligand Synthesis

The chemical structures of the ligands described throughout this chapter and their halogenated products, generated postsynthetically or otherwise, are shown in Scheme 3.2. Full experimental details and characterisation of the dimethyl esters and free-acids of L9, L10 and L11 are described in Chapter 2, Section 2.10.9.

	R	Abbreviaton	Isomerism
	CH <sub>3</sub>	etdb-Me <sub>2</sub>	n/a
	H	etdb-H <sub>2</sub>	
	CH <sub>3</sub>	L8-Me <sub>2</sub>	n/a
	H	L8-H <sub>2</sub>	
	CH <sub>3</sub>	L8-Br <sub>2</sub> -Me <sub>2</sub>	(R,R)/(S,S)/meso
	H	L8-Br <sub>2</sub> -H <sub>2</sub>	
	CH <sub>3</sub>	L8-Br-OH-Me <sub>2</sub>	(R,R)/(S,S)/(R,S)/(S,R)
	H	L8-Br-OH-H <sub>2</sub>	
	CH <sub>3</sub>	L9-Me <sub>2</sub>	n/a
	H	L9-H <sub>2</sub>	
	CH <sub>3</sub>	L9-X <sub>2</sub> -Me <sub>2</sub>	cis/trans
	H	L9-X <sub>2</sub> -H <sub>2</sub>	
	CH <sub>3</sub>	L10-Me <sub>2</sub>	n/a
	H	L10-H <sub>2</sub>	
	CH <sub>3</sub>	L10-X <sub>4</sub> -Me <sub>2</sub>	trans,trans/trans,cis/cis,cis
	H	L10-X <sub>4</sub> -H <sub>2</sub>	
	CH <sub>3</sub>	L11-Me <sub>2</sub>	n/a
	H	L11-H <sub>2</sub>	
	CH <sub>3</sub>	L11-X <sub>4</sub> -Me <sub>2</sub>	trans,trans/trans,cis/cis,cis
	H	L11-X <sub>4</sub> -H <sub>2</sub>	

**Scheme 3.2.** Schematic representation of the organic ligands discussed throughout this chapter alongside their abbreviations and possible isomerism. (X = Br or I)

### etdb-Me<sub>2</sub>

Dimethyl *trans*-stilbene-4,4'-dicarboxylate (0.500 g, 1.69 mmol) was dissolved in methanol (25 ml) by stirring. Palladium on carbon (10 %, 0.075 g) was added, and the solution was degassed by bubbling N<sub>2</sub> through the solution for 10 minutes. The reaction flask was purged with H<sub>2</sub>, before being left to stir at room temperature overnight under an H<sub>2</sub> atmosphere. The mixture was filtered through Celite and washed through with excess methanol. The solvent was removed under reduced pressure to yield a white solid (0.454 g, 1.52 mmol, 90%). <sup>1</sup>H NMR (DMSO-*d*<sub>6</sub>): δ/ppm 2.99 (s, 4H), 3.83 (s, 6H), 7.36 (d, 4H, *J* = 8.2 Hz), 7.86 (d, 4H, *J* =

8.2 Hz);  $^{13}\text{C}$  NMR (DMSO- $d_6$ ):  $\delta/\text{ppm}$  36.3 ( $\text{CH}_2$ ), 52.0 ( $\text{CH}_3$ ), 127.4 (C), 128.9 (CH), 129.2 (CH), 147.0 (C), 166.2 (C); HRMS (ESI) calculated for  $\text{C}_{18}\text{H}_{18}\text{O}_4$  ( $\text{M}$ ) $^+$  298.1205, found  $m/z$  298.1209.

Single crystals of etdb-Me $_2$  were isolated after slow evaporation of a methanolic solution (Figure 3.9a).

Crystal data for etdb-Me $_2$ .  $\text{C}_{18}\text{H}_{18}\text{O}_4$ ,  $M_r = 298.32$ , crystal dimensions 0.80 x 0.20 x 0.14 mm, Monoclinic,  $a = 4.7414$  (4) Å,  $b = 6.0450$  (6) Å,  $c = 25.976$  (2) Å,  $\beta = 94.197$  (4) $^\circ$ ,  $V = 742.53$  (12) Å $^3$ ,  $T = 100$  K, space group  $P2_1/n$  (no. 14),  $Z = 2$ , 10757 reflections measured, 1667 unique ( $R_{\text{int}} = 0.074$ ), which were used in all calculations. The final  $R_I = 0.059$  for 1465 observed data  $R[F^2 > 2\sigma(F^2)]$  and  $wR(F^2) = 0.160$  (all data). Crystal data for etdb-Me $_2$  is available from the CCDC, deposition number 1418960.

### etdb-H $_2$

etdb-Me $_2$  (0.383 g, 1.28 mmol, 1 eq) was dissolved in ethanol (50 ml) by stirring. Potassium hydroxide (0.372 g, 6.63 mmol, 5 eq) was dissolved separately in H $_2$ O (50 ml), then the two solutions were combined and subject to reflux overnight. The product was precipitated by addition of 1 M aqueous HCl, collected by filtration, washed with excess water until neutral and dried in a desiccator under vacuum (0.330 g, 1.22 mmol, 95%).  $^1\text{H}$  NMR (DMSO- $d_6$ ):  $\delta/\text{ppm}$  2.97 (s, 4H), 7.34 (d, 4H,  $J = 8.3$  Hz), 7.84 (d, 4H,  $J = 8.3$  Hz), 12.82 (s, 2H);  $^{13}\text{C}$  NMR (DMSO- $d_6$ ):  $\delta/\text{ppm}$  36.4 ( $\text{CH}_2$ ), 128.5 (C), 128.6 (CH), 129.3 (CH), 146.5 (C), 167.3 (C); HRMS (ESI) calculated for  $\text{C}_{16}\text{H}_{13}\text{O}_4$  ( $\text{M-H}$ ) $^-$  269.0819, found  $m/z$  269.0815.

### 3.15.3 Ligand Brominations

Solution phase brominations of L9-Me $_2$ , L10-Me $_2$  and L11-Me $_2$  were performed to compare with the stereoselectivity obtained for the corresponding heterogeneous phase reactions when the ligands are contained within Zr and Hf MOFs.  $^1\text{H}$  and  $^{13}\text{C}$  NMR spectroscopies were used to analyse the reaction products however, mixtures of geometric products were obtained and as such the spectra are discussed in Section 3.9.

**L9-Br<sub>2</sub>-Me<sub>2</sub>**

L9-Me<sub>2</sub> (0.100 g, 0.34 mmol, 1 eq) was added to a 50 ml reagent bottle followed by 10 ml CHCl<sub>3</sub>. Bromine (523 µl, 10.20 mmol, 30 eq) was added, the bottle was sealed and left to stir in the dark for 48 hours. The reaction was quenched by washing multiple times with an aqueous 1 M sodium thiosulfate solution (50 ml) until the organic phase resembled the pale starting solution. The CHCl<sub>3</sub> solution was dried over MgSO<sub>4</sub>, filtered and the solvent removed under reduced pressure to yield a pale yellow solid (0.140 g, 0.31 mmol, 91%). HRMS (ESI) calculated for C<sub>18</sub>H<sub>14</sub>Br<sub>2</sub>O<sub>4</sub>Na (M+Na)<sup>+</sup> 476.9136, found *m/z* 476.9147.

Single crystals of L9-Br<sub>2</sub>-Me<sub>2</sub> were isolated from an NMR solution upon slow evaporation of CDCl<sub>3</sub>. Single crystal X-ray diffraction identified two polymorphs of the *trans*-isomer, which have been termed *trans*-L9-Br<sub>2</sub>-Me<sub>2</sub>-I and *trans*-L9-Br<sub>2</sub>-Me<sub>2</sub>-II (Figure 3.19).

Crystal data for *trans*-L9-Br<sub>2</sub>-Me<sub>2</sub>-I. C<sub>18</sub>H<sub>14</sub>Br<sub>2</sub>O<sub>4</sub>, *M<sub>r</sub>* = 454.11, crystal dimensions 0.43 x 0.05 x 0.04 mm, Monoclinic, *a* = 12.035 (3) Å, *b* = 3.9873 (10) Å, *c* = 18.148 (5) Å, β = 109.192 (6)°, *V* = 822.5 (4) Å<sup>3</sup>, *T* = 100 K, space group *P*2<sub>1</sub>/*c* (no. 14), *Z* = 2, 8478 reflections measured, 1430 unique (*R*<sub>int</sub> = 0.100), which were used in all calculations. The final *R*<sub>I</sub> = 0.066 for 1170 observed data *R*[*F*<sup>2</sup> > 2σ(*F*<sup>2</sup>)] and *wR*(*F*<sup>2</sup>) = 0.150 (all data). Crystal data for *trans*-L9-Br<sub>2</sub>-Me<sub>2</sub>-I is available from the CCDC, deposition number 1400384.

Crystal data for *trans*-L9-Br<sub>2</sub>-Me<sub>2</sub>-II. C<sub>18</sub>H<sub>14</sub>Br<sub>2</sub>O<sub>4</sub>; *M<sub>r</sub>* = 454.11, crystal dimensions 0.54 x 0.39 x 0.3 mm, Triclinic, *a* = 7.3612 (14) Å, *b* = 7.8256 (15) Å, *c* = 8.1466 (15) Å, α = 79.735 (4)°, β = 66.523 (4)°, γ = 84.834 (5)°, *V* = 423.46 (14) Å<sup>3</sup>, *T* = 100 K, space group *P*-1 (no. 2), *Z* = 1, 6417 reflections measured, 1941 unique (*R*<sub>int</sub> = 0.075), which were used in all calculations. The final *R*<sub>I</sub> = 0.055 for 1730 observed data *R*[*F*<sup>2</sup> > 2σ(*F*<sup>2</sup>)] and *wR*(*F*<sup>2</sup>) = 0.144 (all data). Crystal data for *trans*-L9-Br<sub>2</sub>-Me<sub>2</sub>-II is available from the CCDC, deposition number 1400383.

**L10-Br<sub>4</sub>-Me<sub>2</sub>**

L10-Me<sub>2</sub> (0.060 g, 0.19 mmol, 1 eq) was added to a 50 ml reagent bottle and dissolved in 10 ml CHCl<sub>3</sub> by stirring. Bromine (292 µl, 5.70 mmol, 30 eq) was added and the jar was sealed and placed in the dark whilst stirring for 84 hours. After this time, the reaction mixture was diluted and quenched by washing with 1 M aqueous sodium thiosulfate (3 x 20 ml). The resultant yellow solution was dried over MgSO<sub>4</sub>, filtered and the solvent removed under

reduced pressure to yield a light coloured oil (0.121 g, 0.19 mmol, 100%). HRMS (ESI) calculated for  $C_{20}H_{14}Br_4NaO_4 (M+Na)^+$  656.7523, found  $m/z$  656.7518.

### **L11-Br<sub>4</sub>-Me<sub>2</sub>**

L11-Me<sub>2</sub> (0.025 g, 0.06 mmol, 1 eq) was added to a 50 ml reagent bottle and dissolved in 10 ml CHCl<sub>3</sub> by stirring. Bromine (195  $\mu$ l, 3.81 mmol, 64 eq) was added and the jar was sealed and placed in the dark whilst stirring for 48 hours. After this time, the reaction mixture was diluted and quenched by washing with 1 M aqueous sodium thiosulfate (3 x 20 ml). The reaction mixture was dried over MgSO<sub>4</sub>, filtered and the solvent removed under reduced pressure to yield a white solid (0.043 g, 0.06 mmol, 100%). HRMS (CI) calculated for  $C_{26}H_{18}Br_4O_4 (M)^+$  709.7939, found  $m/z$  709.7933.

### **3.15.4 Bulk MOF Synthesis**

Bulk microcrystalline samples of **Zr-L9**, **Hf-L9**, **Zr-L10**, **Zr-L11** and **Hf-L11** were prepared according to the synthetic conditions described in Chapter 2, Section 2.10.10. An alternative microwave assisted synthetic procedure was used to produce bulk samples of **Zr-L8** for postsynthetic bromination. All analysis reported in this chapter is of CHCl<sub>3</sub> activated materials and as postsynthetic bromination was performed in CHCl<sub>3</sub> this allows direct comparability between the parent and postsynthetically derived samples.

### **Zr-L8**

L-proline (0.518 g, 4.50 mmol 5 eq), L8-H<sub>2</sub> (0.241 g, 0.90 mmol, 1 eq) and ZrCl<sub>4</sub> (0.210 g, 0.90 mmol, 1 eq) were added to a 35 ml microwave vial. DMF (20 ml) was added, followed by concentrated HCl (0.08 ml) and the vial was sealed. The reaction vessel was then subject to an automated microwave programme consisting of 10 minutes of stirring at 30 °C to homogenously distribute the reagents, followed by heating at 100 °C for 4 hours without stirring. The bulk material was collected from the vial upon completion, centrifuged once with fresh DMF and three times with acetone, before being placed in a desiccator under vacuum for drying (0.289 g, 0.13 mmol, 87% - average yield over 4 reactions).



**Activation:** Powder samples were added to 50 ml Pyrex reagent bottles and left to stand in  $\text{CHCl}_3$ . The  $\text{CHCl}_3$  was exchanged for fresh  $\text{CHCl}_3$  a further 4 times over 4 days, before being collected by centrifugation and dried under vacuum.

Bulk Zr-MOF syntheses were attempted with etdb- $\text{H}_2$ .

### Microwave Synthesis

L-proline (0.130 g, 1.13 mmol 5 eq), etdb- $\text{H}_2$  (0.061 g, 0.23 mmol, 1 eq) and  $\text{ZrCl}_4$  (0.52 g, 0.23 mmol, 1 eq) were added to a 35 ml microwave vial. DMF (10 ml) was added, followed by concentrated HCl (0.02 ml) and the vial was sealed. The reaction vessel was then subject to an automated microwave programme consisting of 10 minutes of stirring at 30 °C to homogenously distribute the reagents, followed by heating at 100 °C for 4 hours without stirring. The powder was collected from the vial upon completion, centrifuged once with fresh DMF and two times with acetone, before being placed in a desiccator under vacuum.

### Oven Synthesis

Either L-proline (0.130 g, 1.13 mmol, 5 eq), acetic acid (0.064 ml, 1.13 mmol, 5 eq), benzoic acid (0.137 g, 1.13 mmol, 5 eq) or no modulator in the case of the unmodulated synthesis, as required, along with etdb- $\text{H}_2$  (0.061 g, 0.23 mmol, 1 eq) and  $\text{ZrCl}_4$  (0.052 g, 0.23 mmol, 1 eq) were added to a 50 ml PXREX reagent bottle. DMF (10 ml) was added, followed by concentrated HCl (0.02 ml) and the vial was sealed. The reaction vessel was then sonicated to homogenously distribute the reagents, followed by heating at 120 °C for 24 hours in the oven. The powder was collected from the bottle upon completion, centrifuged once with fresh DMF and two times with acetone, before being placed in a desiccator under vacuum.

### 3.15.5 Bulk Postsynthetic Bromination of Zr-L8, Zr-L9, Hf-L9, Zr-L10, Zr-L11 and Hf-L11

#### Zr-L8- $\text{Br}_2$

**Zr-L8** (0.150 g, 0.40 mmol double bond, 1 eq) was added to a 50 ml reagent bottle and left to stand in 15 ml  $\text{CHCl}_3$  overnight. The  $\text{CHCl}_3$  was removed and fresh  $\text{CHCl}_3$  added, followed by the addition of bromine (101  $\mu\text{l}$ , 1.98 mmol, 5 eq). The bottle was sealed and stored in the dark for a period of 48 hours. The reaction product  $[\text{Zr}_6\text{O}_4(\text{OH})_4(\text{L8-Br}_2)_6]_n$  was collected by

centrifugation and washed multiple times with fresh  $\text{CHCl}_3$ , before being placed in a desiccator under vacuum for drying. Bromine analysis: 29.6% calculated, 27.7% found.

Alternative, milder conditions were explored for the postsynthetic bromination of microcrystalline powders of **Zr-L8**. *N*-bromosuccinimide (NBS) was investigated as a milder brominating agent and reaction conditions were systematically varied to try and optimise the product distribution.

### General Procedure

**Zr-L8** (0.020 g, 0.053 mmol alkene, 1 eq) was suspended in the reaction solvent (5 ml) by stirring, then *N,N'*-diphenylthiourea (DPT) (10 mol%) was added if required, before cooling to 0 °C. NBS (0.047 g, 0.265 mmol, 5 eq) was added, the flask was sealed and the mixture was purged by passing  $\text{N}_2$  through the system. The reaction mixture was left to stir under an  $\text{N}_2$  atmosphere overnight, gradually warming to room temperature. The modified MOF was collected by centrifugation with acetonitrile (2 x 10 ml) and acetone (2 x 10 ml), before being dried under vacuum. Product distributions were calculated from  $^1\text{H}$  NMR analysis of digested ( $\text{DMSO-}d_6/\text{D}_2\text{SO}_4$ ) MOF samples.

### Zr-L9-Br<sub>2</sub>

**Zr-L9** (0.150 g, 0.40 mmol triple bond, 1 eq) was added to a 50 ml reagent bottle and left to stand in 15 ml  $\text{CHCl}_3$  overnight. The  $\text{CHCl}_3$  was removed and fresh  $\text{CHCl}_3$  added, followed by the addition of bromine (611  $\mu\text{l}$ , 11.92 mmol, 30 eq). The bottle was sealed and stored in the dark for a period of 48 hours. The reaction product  $[\text{Zr}_6\text{O}_4(\text{OH})_4(\text{L9-Br}_2)_6]_n$  was collected by centrifugation and washed multiple times with fresh  $\text{CHCl}_3$ , before being placed in a desiccator under vacuum for drying. Bromine analysis: 29.8% calculated, 26.2% found.

### Hf-L9-Br<sub>2</sub>

**Hf-L9** (0.200 g, 0.43 mmol triple bond, 1 eq) was added to a 50 ml reagent bottle and left to stand in 20 ml  $\text{CHCl}_3$  overnight. The  $\text{CHCl}_3$  was removed and fresh  $\text{CHCl}_3$  added, followed by the addition of bromine (660  $\mu\text{l}$ , 12.90 mmol, 30 eq). The bottle was sealed and stored in the dark for a period of 72 hours. The reaction product  $[\text{Hf}_6\text{O}_4(\text{OH})_4(\text{L9-Br}_2)_6]_n$  was collected by centrifugation and washed multiple times with fresh  $\text{CHCl}_3$ , before being placed in a desiccator under vacuum for drying. Bromine analysis: 25.6% calculated, 23.2% found.

**Zr-L10-Br<sub>4</sub>**

**Zr-L10** (0.100 g, 0.50 mmol triple bond, 1 eq) was added to a 50 ml reagent bottle and left to stand in 15 ml CHCl<sub>3</sub> overnight. The CHCl<sub>3</sub> was removed and fresh CHCl<sub>3</sub> added, followed by the addition of bromine (385 µl, 7.52 mmol, 15 eq). The bottle was sealed and stored in the dark for a period of 48 hours. The reaction product [Zr<sub>6</sub>O<sub>4</sub>(OH)<sub>4</sub>(L10-Br<sub>4</sub>)<sub>6</sub>]<sub>n</sub> was collected by centrifugation and washed multiple times with fresh CHCl<sub>3</sub>, before being dried under vacuum. Bromine analysis: 44.3% calculated; 43.1% found.

**Zr-L11-Br<sub>4</sub>**

**Zr-L11** (0.150 g, 0.63 mmol triple bond, 1 eq) was added to a 50 ml reagent bottle and immersed in 25 ml CHCl<sub>3</sub>. Bromine (965 µl, 18.84 mmol, 30 eq) was added and the bottle was sealed before being stored in the dark for a period of 72 hours. The reaction product [Zr<sub>6</sub>O<sub>4</sub>(OH)<sub>4</sub>(L11-Br<sub>4</sub>)<sub>6</sub>]<sub>n</sub> was collected by centrifugation and washed multiple times with fresh CHCl<sub>3</sub>, before being dried under vacuum. Bromine analysis: 40.1% calculated; 41.9% found.

**Hf-L11-Br<sub>4</sub>**

**Hf-L11** (0.065 g, 0.23 mmol triple bond, 1 eq) was added to a 50 ml reagent bottle and immersed in 15 ml CHCl<sub>3</sub>. Bromine (355 µl, 6.93 mmol, 30 eq) was added and the bottle was sealed before being stored in the dark for a period of 72 hours. The reaction product [Hf<sub>6</sub>O<sub>4</sub>(OH)<sub>4</sub>(L11-Br<sub>4</sub>)<sub>6</sub>]<sub>n</sub> was collected by centrifugation and washed multiple times with fresh CHCl<sub>3</sub>, before being dried under vacuum. Bromine analysis: 36.1% calculated; 33.3% found.

### **3.15.6 Single Crystal Postsynthetic Bromination of Zr-L8, Zr-L9, Hf-L9, Zr-L10, Zr-L11 and Hf-L11**

#### **Single Crystal Bromination – General Procedure**

Small amounts of single crystals of the MOFs, still in their mother liquor, were added by pipette to a 10 ml vial containing fresh DMF (3 ml). The DMF was exchanged for fresh DMF twice before being exchanged for CHCl<sub>3</sub> (3 ml). The CHCl<sub>3</sub> was exchanged for fresh CHCl<sub>3</sub> a further two times. Bromine (13 µl for **Zr-L8**, 50 µl for **Zr-L9**, **Hf-L9**, **Zr-L11** and **Hf-L11** and 100 µl for **Zr-L10**) was added, the vial was sealed and left to stand in the dark for 48

hours in the case of **Zr-L8** and 96 hours for the other MOFs. The  $\text{CHCl}_3$  was then replaced multiple times with fresh  $\text{CHCl}_3$ . Small portions of the crystals were added to a vial containing DMF to resolute. The DMF was exchanged for fresh DMF and the crystals left to stand.

**Crystal data for Zr-L8-Br<sub>2</sub>.**  $\text{Zr}_6\text{O}_4(\text{OH})_4(\text{C}_{16}\text{H}_{10}\text{O}_4\text{Br}_2)_6$ ,  $M_r = 3235.71$ , crystal dimensions  $0.07 \times 0.07 \times 0.07$  mm, Cubic,  $a = 29.7685$  (8) Å,  $V = 26380$  (2) Å<sup>3</sup>,  $T = 100$  K, space group *Fm-3m* (no. 225),  $Z = 4$ , 95174 reflections measured, 1211 unique ( $R_{\text{int}} = 0.088$ ), which were used in all calculations. The final  $R_I = 0.084$  for 1075 observed data  $R[F^2 > 2\sigma(F^2)]$  and  $wR_2(F^2) = 0.268$  (all data). Using the SQUEEZE algorithm within PLATON the pore volume and electron density within the voids were calculated and found to be 18145 Å<sup>3</sup> and contain 3735 electrons per unit cell (the equivalent of ~93 molecules of DMF) respectively.<sup>41</sup> Crystal data for **Zr-L8-Br<sub>2</sub>** is available from the CCDC, deposition number 1418961.

**Crystal data for Zr-L9-Br<sub>2</sub>.**  $\text{Zr}_6\text{O}_4(\text{OH})_4(\text{C}_{16}\text{H}_8\text{O}_4\text{Br}_2)_6$ ,  $M_r = 3223.61$ , crystal dimensions  $0.07 \times 0.06 \times 0.05$  mm, Cubic,  $a = 29.861$  (2) Å,  $V = 26626$  (5) Å<sup>3</sup>,  $T = 100$  K, space group *Fm-3m* (no. 225),  $Z = 4$ , Å, 22280 measured reflections, 1567 unique ( $R_{\text{int}} = 0.058$ ), which were used in all calculations. The final  $R_I = 0.078$  for 1236 observed data  $R[F^2 > 2\sigma(F^2)]$  and  $wR(F^2) = 0.231$  (all data). Using the SQUEEZE algorithm within PLATON the pore volume and electron density within the voids were calculated and found to be 16938 Å<sup>3</sup> and contain 2434 electrons per unit cell (the equivalent of ~60 molecules of DMF) respectively.<sup>41</sup> Crystal data for **Zr-L9-Br<sub>2</sub>** is available from the CCDC, deposition number 1062510.

**Crystal data for Hf-L9-Br<sub>2</sub>.**  $\text{Hf}_6\text{O}_4(\text{OH})_4(\text{C}_{16}\text{H}_8\text{Br}_2\text{O}_4)_6$ ,  $M_r = 3747.23$ , crystal dimensions  $0.04 \times 0.04 \times 0.04$  mm, Cubic,  $a = 29.825$  (2) Å,  $V = 26530$  (5) Å<sup>3</sup>,  $T = 100$  K, space group *Fm-3m* (no. 225),  $Z = 4$ , 22405 measured reflections, 1562 unique ( $R_{\text{int}} = 0.045$ ), which were used in all calculations. The final  $R_I = 0.037$  for 1367 observed data  $R[F^2 > 2\sigma(F^2)]$  and  $wR(F^2) = 0.109$  (all data). Using the SQUEEZE algorithm within PLATON the pore volume and electron density within the voids were calculated and found to be 16961 Å<sup>3</sup> and contain 2296 electrons per unit cell (the equivalent of ~57 molecules of DMF) respectively.<sup>41</sup> Crystal data for **Hf-L9-Br<sub>2</sub>** is available from the CCDC, deposition number 1062511.

**Crystal data for Zr-L10-Br<sub>4</sub>.** Unfortunately, it did not prove possible to collect anything other than unit cell parameters for **Zr-L10-Br<sub>4</sub>**, likely as a result of the significant disorder and frustration imposed by the linker.  $\text{Zr}_6\text{O}_4(\text{OH})_4(\text{C}_{18}\text{H}_8\text{Br}_4\text{O}_4)_6$ , Cubic,  $a = 32.7864(7) \text{ \AA}$ ,  $T = 100 \text{ K}$ , space group  $Fm-3m$  (no. 225).

**Crystal data for Zr-L11-Br<sub>4</sub>.**  $\text{C}_{144}\text{H}_{76}\text{Br}_{24}\text{O}_{32}\text{Zr}_6$ ,  $M_r = 4783.20$ , crystal dimensions  $0.07 \times 0.07 \times 0.07 \text{ mm}$ , Cubic,  $a = 39.067(7) \text{ \AA}$ ,  $V = 59625(32) \text{ \AA}^3$ ,  $T = 100 \text{ K}$ , space group  $Fd-3m$  (no. 227),  $Z = 8$ , 113804 measured reflections, 2511 unique ( $R_{\text{int}} = 0.095$ ), which were used in all calculations. The final  $R_I = 0.214$  for 2473 observed data  $R[F^2 > 2\sigma(F^2)]$  and  $wR(F^2) = 0.565$  (all data). Using the SQUEEZE algorithm within PLATON the pore volume and electron density within the voids were calculated and found to be  $26061 \text{ \AA}^3$  and contain 5123 electrons per unit cell (the equivalent of ~128 molecules of DMF) respectively.<sup>41</sup> Crystal data for **Zr-L11-Br<sub>4</sub>** is available from the CCDC, deposition number 1443198.

**Crystal data for Hf-L11-Br<sub>4</sub>.**  $\text{C}_{144}\text{H}_{76}\text{Br}_{24}\text{Hf}_6\text{O}_{32}$ ,  $M_r = 5306.82$ , crystal dimensions  $0.12 \times 0.10 \times 0.10 \text{ mm}$ , Cubic,  $a = 39.0451(3) \text{ \AA}$ ,  $V = 59525.0(14) \text{ \AA}^3$ ,  $T = 100 \text{ K}$ , space group  $Fd-3m$  (no. 227),  $Z = 8$ , 65301 measured reflections, 3215 unique ( $R_{\text{int}} = 0.047$ ), which were used in all calculations. The final  $R_I = 0.122$  for 4491 observed data  $R[F^2 > 2\sigma(F^2)]$  and  $wR(F^2) = 0.464$  (all data). Using the SQUEEZE algorithm within PLATON the pore volume and electron density within the voids were calculated and found to be  $29600 \text{ \AA}^3$  and contain 12699 electrons per unit cell (the equivalent of ~317 molecules of DMF) respectively.<sup>41</sup> Crystal data for **Hf-L11-Br<sub>4</sub>** is available from the CCDC, deposition number 1443199.

### 3.15.7 Iodine Uptake Experiments of Zr-L8, Zr-L9, Zr-L10 and Zr-L11

#### Iodine Chemisorption Experiments

In a typical reaction **Zr-L8**, **Zr-L9**, **Zr-L10** or **Zr-L11** was added to an open-ended 3.7 ml vial. Separately,  $\text{I}_2$  (15 eq per multiple bond) was added to a 30 ml screw top vial (Table 3.8). The small vial containing the MOF was then placed in the centre of the large vial, with the lid of the outer vial tightened to create a closed system. The experiments were allowed to stand at room temperature for the required number of days (1, 3, 7, 14 and 21 days, except for experiments containing **Zr-L11** when data was also collected at 28 days). To stop the reaction, the small vial was removed and the contents added to a 15 ml centrifuge tube. The

product was collected by centrifugation multiple times with  $\text{CHCl}_3$  (10 ml) until washings were colourless, before drying under vacuum. The percentage chemisorbed  $\text{I}_2$  was calculated from  $^1\text{H}$  NMR spectroscopic integral ratios obtained from  $\text{DMSO-}d_6/\text{D}_2\text{SO}_4$  digests of the products.

**Table 3.8.** Summary of reaction quantities for  $\text{I}_2$  chemisorption experiments.

MOF	Mass (mg)	mmol unsaturated bond	mmol $\text{I}_2$	Mass $\text{I}_2$ (mg)	Equivalents $\text{I}_2$
<b>Zr-L8</b>	10	0.026	0.40	50	15
<b>Zr-L9</b>	10	0.027	0.40	50	15
<b>Zr-L10</b>	10	0.050	0.75	95	15
<b>Zr-L11</b>	10	0.042	0.63	80	15

Single crystals of *trans*-L9- $\text{I}_2\text{-H}_2$ , *trans,trans*-L10- $\text{I}_4\text{-H}_2$ , and *trans,trans*-L11- $\text{I}_4\text{-H}_2$  were isolated from NMR solutions of the acid digested ( $\text{DMSO-}d_6/\text{D}_2\text{SO}_4$ ) iodinated MOFs over time (Figure 3.32).

Crystal data for *trans*-L9- $\text{I}_2\text{-H}_2$ .  $\text{C}_{16}\text{H}_{10}\text{I}_2\text{O}_4 \cdot 2(\text{C}_2\text{H}_6\text{OS})$ ,  $M_r = 676.29$ , crystal dimensions 0.39 x 0.34 x 0.04 mm, Triclinic,  $a = 5.8835$  (11) Å,  $b = 6.7768$  (12) Å,  $c = 16.356$ (3) Å,  $\alpha = 89.817$  (4)°,  $\beta = 83.800$  (4)°,  $\gamma = 70.889$  (4)°,  $V = 612.23$  (19) Å<sup>3</sup>,  $T = 100$  K, space group *P*-1 (no. 2),  $Z = 1$ , 13644 measured reflections, 2814 unique ( $R_{\text{int}} = 0.069$ ), which were used in all calculations. The final  $R_I = 0.035$  for 2694 observed data  $R[F^2 > 2\sigma(F^2)]$  and  $wR(F^2) = 0.094$  (all data). Crystal data for *trans*-L9- $\text{I}_2\text{-H}_2$  is available from the CCDC, deposition number 1400977.

Crystal data for *trans,trans*-L10- $\text{I}_4\text{-H}_2$ .  $\text{C}_{18}\text{H}_{10}\text{I}_4\text{O}_4 \cdot \text{C}_2\text{H}_6\text{OS}$ ,  $M_r = 875.99$ , crystal dimensions 0.30 x 0.02 x 0.02 mm, Monoclinic,  $a = 51.19$  (7) Å,  $b = 7.307$  (10) Å,  $c = 14.86$  (2) Å,  $\beta = 100.67$  (3)°,  $V = 5461$  (13) Å<sup>3</sup>,  $T = 100$  K, space group *C*2/*c* (no. 15),  $Z = 8$ , 13979 measured reflections, 4872 unique ( $R_{\text{int}} = 0.237$ ), which were used in all calculations. The final  $R_I = 0.123$  for 1564 observed data  $R[F^2 > 2\sigma(F^2)]$  and  $wR(F^2) = 0.330$  (all data). Crystal data for *trans,trans*-L10- $\text{I}_4\text{-H}_2$  is available from the CCDC, deposition number 1443200.

Crystal data for *trans,trans*-L11-I<sub>4</sub>-H<sub>2</sub>. C<sub>24</sub>H<sub>14</sub>I<sub>4</sub>O<sub>4</sub>·2(C<sub>2</sub>H<sub>6</sub>OS),  $M_r = 1030.21$ , crystal dimensions 0.31 x 0.21 x 0.03 mm, Triclinic,  $a = 5.8105$  (9) Å,  $b = 6.7307$  (10) Å,  $c = 22.342$  (4) Å,  $\alpha = 94.454$  (5)°,  $\beta = 94.741$  (5)°,  $\gamma = 108.638$  (5)°,  $V = 820.1$  (2) Å<sup>3</sup>,  $T = 100$  K, space group  $P-1$  (no. 2),  $Z = 1$ , 10741 measured reflections, 2818 unique ( $R_{\text{int}} = 0.122$ ), which were used in all calculations. The final  $R_I = 0.105$  for 2002 observed data  $R[F^2 > 2\sigma(F^2)]$  and  $wR(F^2) = 0.219$  (all data). Crystal data for *trans,trans*-L11-I<sub>4</sub>-H<sub>2</sub> is available from the CCDC, deposition number 1443201.

### Total Iodine Uptake Experiments

In a typical reaction, **Zr-L8**, **Zr-L9**, **Zr-L10** or **Zr-L11** (20 mg) was added to a pre-weighed 3.7 ml open-ended vial (Table 3.9). Separately, I<sub>2</sub> (15 eq) was added to a 30 ml screw top vial and the small vial containing the MOF was then placed in the centre of the large vial, with the lid of the outer vial tightened to create a closed system. The experiments were allowed to stand at room temperature with the small vial removed, weighed and placed back inside the large vial after 1, 3, 7, 14 and 21 days (data was also collected for the reaction containing **Zr-L11** at 28 days). The gravimetric I<sub>2</sub> uptake of the MOFs was calculated from the observed increase in mass.

**Table 3.9** Summary of reaction quantities for total I<sub>2</sub> uptake experiments.

MOF	Mass (mg)	mmol unsaturated bond	mmol I <sub>2</sub>	Mass I <sub>2</sub> (mg)	Equivalents I <sub>2</sub>
<b>Zr-L8</b>	20	0.053	0.79	100	15
<b>Zr-L9</b>	20	0.053	0.80	100	15
<b>Zr-L10</b>	20	0.100	1.49	190	15
<b>Zr-L11</b>	20	0.084	1.26	160	15

The gravimetric I<sub>2</sub> uptake of the Zr MOFs takes into account both the physi- and chemisorption capacities (Figure 3.33). Subtracting the percentage I<sub>2</sub> chemisorbed (from DMSO-*d*<sub>6</sub>/D<sub>2</sub>SO<sub>4</sub> NMR digests of the iodinated MOFs) from the total gravimetric I<sub>2</sub> uptake allows the percentage I<sub>2</sub> physisorbed to be calculated (Figure 3.31).

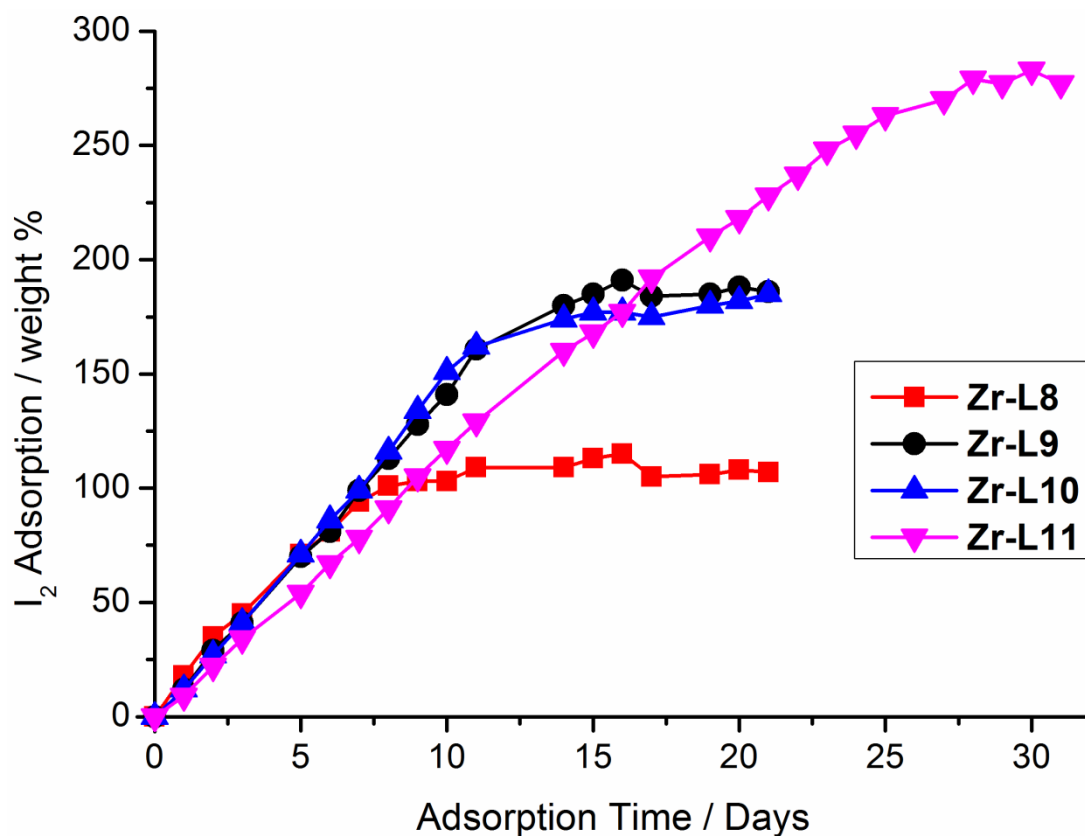


**Figure 3.33.** Comparison of the gravimetric  $I_2$  uptake capacities (physisorption and chemisorption) of the Zr MOFs.



### 3.16 References

- (1) Furukawa, H.; Cordova, K. E.; O’Keeffe, M.; Yaghi, O. M. *Science* **2013**, *341*, 974.
- (2) Deng, H.; Doonan, C. J.; Furukawa, H.; Ferreira, R. B.; Towne, J.; Knobler, C. B.; Wang, B.; Yaghi, O. M. *Science* **2010**, *327*, 846.
- (3) Sun, Y.; Sun, L.; Feng, D.; Zhou, H.-C. *Angew. Chem.* **2016**, *128*, 6581.
- (4) Stock, N.; Biswas, S. *Chem. Rev.* **2012**, *112*, 933.
- (5) Cohen, S. M. *Chem. Sci.* **2010**, *1*, 32.
- (6) Wang, Z.; Cohen, S. M. *Chem. Soc. Rev.* **2009**, *38*, 1315.
- (7) Tanabe, K. K.; Cohen, S. M. *Chem. Soc. Rev.* **2011**, *40*, 498.
- (8) Deria, P.; Mondloch, J. E.; Karagiari, O.; Bury, W.; Hupp, J. T.; Farha, O. K. *Chem. Soc. Rev.* **2014**, *43*, 5896.
- (9) Evans, J. D.; Sumbly, C. J.; Doonan, C. J. *Chem. Soc. Rev.* **2014**, *43*, 5933.
- (10) Marshall, R. J.; Forgan, R. S. *Eur. J. Inorg. Chem.* **2016**, *2016*, 4310.
- (11) DeCoste, J. B.; Peterson, G. W.; Jasuja, H.; Glover, T. G.; Huang, Y.-g.; Walton, K. S. *J. Mater. Chem. A* **2013**, *1*, 5642.
- (12) Mondloch, J. E.; Katz, M. J.; Planas, N.; Semrouni, D.; Gagliardi, L.; Hupp, J. T.; Farha, O. K. *Chem. Commun.* **2014**, *50*, 8944.
- (13) Kandiah, M.; Nilsen, M. H.; Usseglio, S.; Jakobsen, S.; Olsbye, U.; Tilset, M.; Larabi, C.; Quadrelli, E. A.; Bonino, F.; Lillerud, K. P. *Chem. Mater.* **2010**, *22*, 6632.
- (14) Wu, H.; Yildirim, T.; Zhou, W. *J. Phys. Chem. Lett.* **2013**, *4*, 925.
- (15) Marshall, R. J.; Richards, T.; Hobday, C. L.; Murphie, C. F.; Wilson, C.; Moggach, S. A.; Bennett, T. D.; Forgan, R. S. *Dalton Trans.* **2016**, *45*, 4132.
- (16) Hobday, C. L.; Marshall, R. J.; Murphie, C. F.; Sotelo, J.; Richards, T.; Allan, D. R.; Düren, T.; Coudert, F.-X.; Forgan, R. S.; Morrison, C. A.; Moggach, S. A.; Bennett, T. D. *Angew. Chem. Int. Ed.* **2016**, *55*, 2401.
- (17) Van de Voorde, B.; Stassen, I.; Bueken, B.; Vermoortele, F.; De Vos, D.; Ameloot, R.; Tan, J.-C.; Bennett, T. D. *J. Mater. Chem. A* **2015**, *3*, 1737.
- (18) Garibay, S. J.; Cohen, S. M. *Chem. Commun.* **2010**, *46*, 7700.
- (19) Jiang, H.-L.; Feng, D.; Liu, T.-F.; Li, J.-R.; Zhou, H.-C. *J. Am. Chem. Soc.* **2012**, *134*, 14690.
- (20) Morris, W.; Briley, W. E.; Auyeung, E.; Cabezas, M. D.; Mirkin, C. A. *J. Am. Chem. Soc.* **2014**, *136*, 7261.

- (21) Li, L.-J.; Liao, P.-Q.; He, C.-T.; Wei, Y.-S.; Zhou, H.-L.; Lin, J.-M.; Li, X.-Y.; Zhang, J.-P. *J. Mater. Chem. A* **2015**, *3*, 21849.
- (22) Deria, P.; Mondloch, J. E.; Tylanakis, E.; Ghosh, P.; Bury, W.; Snurr, R. Q.; Hupp, J. T.; Farha, O. K. *J. Am. Chem. Soc.* **2013**, *135*, 16801.
- (23) Yuan, S.; Chen, Y.-P.; Qin, J.; Lu, W.; Wang, X.; Zhang, Q.; Bosch, M.; Liu, T.-F.; Lian, X.; Zhou, H.-C. *Angew. Chem. Int. Ed.* **2015**, *54*, 14696.
- (24) Gonzalez, M. I.; Bloch, E. D.; Mason, J. A.; Teat, S. J.; Long, J. R. *Inorg. Chem.* **2015**, *54*, 2995.
- (25) Morris, W.; Voloskiy, B.; Demir, S.; Gándara, F.; McGrier, P. L.; Furukawa, H.; Cascio, D.; Stoddart, J. F.; Yaghi, O. M. *Inorg. Chem.* **2012**, *51*, 6443.
- (26) Fei, H.; Cohen, S. M. *J. Am. Chem. Soc.* **2015**, *137*, 2191.
- (27) Sawano, T.; Ji, P.; McIsaac, A. R.; Lin, Z.; Abney, C. W.; Lin, W. *Chem. Sci.* **2015**, *6*, 7163.
- (28) Kim, M.; Cahill, J. F.; Fei, H.; Prather, K. A.; Cohen, S. M. *J. Am. Chem. Soc.* **2012**, *134*, 18082.
- (29) Lalonde, M.; Bury, W.; Karagiari, O.; Brown, Z.; Hupp, J. T.; Farha, O. K. *J. Mater. Chem. A* **2013**, *1*, 5453.
- (30) Deria, P.; Bury, W.; Hod, I.; Kung, C.-W.; Karagiari, O.; Hupp, J. T.; Farha, O. K. *Inorg. Chem.* **2015**, *54*, 2185.
- (31) Aguilera-Sigalat, J.; Fox-Charles, A.; Bradshaw, D. *Chem. Commun.* **2014**, *50*, 15453.
- (32) DeCoste, J. B.; Browe, M. A.; Wagner, G. W.; Rossin, J. A.; Peterson, G. W. *Chem. Commun.* **2015**, *51*, 12474.
- (33) Zhang, Q.; Yu, J.; Cai, J.; Zhang, L.; Cui, Y.; Yang, Y.; Chen, B.; Qian, G. *Chem. Commun.* **2015**, *51*, 14732.
- (34) Jones, S. C.; Bauer, C. A. *J. Am. Chem. Soc.* **2009**, *131*, 12516.
- (35) Frahm, D.; Hoffmann, F.; Fröba, M. *Cryst. Growth Des.* **2014**, *14*, 1719.
- (36) Valenzano, L.; Civalleri, B.; Chavan, S.; Bordiga, S.; Nilsen, M. H.; Jakobsen, S.; Lillerud, K. P.; Lamberti, C. *Chem. Mater.* **2011**, *23*, 1700.
- (37) Schuh, K.; Glorius, F. *Synthesis* **2007**, 2007, 2297.
- (38) Schreiner, P. R.; Prall, M.; Lutz, V. *Angew. Chem. Int. Ed.* **2003**, *42*, 5757.
- (39) Bianchini, R.; Chiappe, C.; Lo Moro, G.; Lenoir, D.; Lemmen, P.; Goldberg, N. *Chem. Eur. J.* **1999**, *5*, 1570.

- (40) Allen, F. H.; Watson, D. G.; Brammer, L.; G., O. A.; Taylor, R. *International Tables for Crystallography Vol C* **2006**, Chapter 9.5, 790.
- (41) Spek, A. *Acta Crystallogr. Sect. C* **2015**, 71, 9.
- (42) Piron, F.; Vanthuyne, N.; Joulin, B.; Naubron, J.-V.; Cismaş, C.; Terec, A.; Varga, R. A.; Roussel, C.; Roncali, J.; Grosu, I. *J. Org. Chem.* **2009**, 74, 9062.
- (43) Sava, D. F.; Rodriguez, M. A.; Chapman, K. W.; Chupas, P. J.; Greathouse, J. A.; Crozier, P. S.; Nenoff, T. M. *J. Am. Chem. Soc.* **2011**, 133, 12398.
- (44) Bennett, T. D.; Saines, P. J.; Keen, D. A.; Tan, J.-C.; Cheetham, A. K. *Chem. Eur. J.* **2013**, 19, 7049.
- (45) Sava, D. F.; Chapman, K. W.; Rodriguez, M. A.; Greathouse, J. A.; Crozier, P. S.; Zhao, H.; Chupas, P. J.; Nenoff, T. M. *Chem. Mater.* **2013**, 25, 2591.
- (46) Macrae, C. F.; Bruno, I. J.; Chisholm, J. A.; Edgington, P. R.; McCabe, P.; Pidcock, E.; Rodriguez-Monge, L.; Taylor, R.; van de Streek, J.; Wood, P. A. *J. Appl. Crystallogr.* **2008**, 41, 466.

## Chapter 4

# Functionalisation of Interpenetrated Zr and Hf Metal-Organic Frameworks

**This Chapter is based upon the following publication:**

Functional Versatility of a Series of Zr Metal-Organic Frameworks Probed by Solid-State Photoluminescence Spectroscopy

*J. Am. Chem. Soc.*, **2017**, DOI: 10.1021/jacs.7b02184.

**R. J. Marshall**, Y. Kalinovsky, S. L. Griffin, C. Wilson, B. A. Blight and R. S. Forgan

## Contents

<b>Chapter 4 .....</b>	<b>169</b>
<b>4.1 Introduction .....</b>	<b>171</b>
<b>4.2 Aims.....</b>	<b>173</b>
<b>4.3 Ligand Design and Synthesis .....</b>	<b>175</b>
<b>4.4 Bulk Synthesis of Interpenetrated Zr and Hf MOFs.....</b>	<b>176</b>
<b>4.5 Single Crystal Synthesis of Interpenetrated Zr and Hf MOFs.....</b>	<b>178</b>
<b>4.6 Zr-L12 Structural Investigation .....</b>	<b>181</b>
<b>4.7 Thermal Analysis .....</b>	<b>184</b>
<b>4.8 Surface Area and Pore Size Distribution Analysis .....</b>	<b>186</b>
<b>4.9 Solid State UV-Vis Spectroscopy .....</b>	<b>190</b>
<b>4.10 Solid State Fluorescence Emission Spectroscopy .....</b>	<b>194</b>
<b>4.11 Conclusions and Future Work.....</b>	<b>200</b>
<b>4.12 Experimental .....</b>	<b>202</b>
4.12.1 General Experimental Remarks .....	202
4.12.2 Ligand Synthesis .....	204
4.12.3 Bulk Synthesis of Zr and Hf MOFs Containing L12-L17 .....	213
4.12.4 Single Crystal Synthesis of Zr and Hf MOFs Containing L12-L17 .....	217
<b>4.13 References .....</b>	<b>224</b>

## 4.1 Introduction

Zr and Hf MOFs containing linear dicarboxylate ligands generally adopt the well-documented UiO-66 topology.<sup>1</sup> Alternative topologies of Zr and Hf MOFs have been obtained, usually with non-linear carboxylate ligands,<sup>2-6</sup> while extended organic ligands have resulted in interpenetrated UiO-66 analogues (Figure 4.1).<sup>7</sup> Members of this interpenetrated series of Zr MOFs are constructed from substituted 4,4'-[1,4-phenylene-bis(ethyne-2,1-diyl)]-dibenzoate ( $\text{peb}^{2-}$ ) ligands. The family of interpenetrated MOFs has been extended to include an anthracene derivative,<sup>8</sup> and alongside other members of the series they have been investigated for catalytic applications<sup>8-10</sup> as well as  $\text{CO}_2$  separation.<sup>11</sup> Postsynthetic modification of pendant functional groups has been demonstrated, either through  $\text{Cu}^{\text{I}}$ -catalysed azide-alkyne or Diels Alder cycloadditions.<sup>12</sup> Integral PSM of MOFs is rare,<sup>13,14</sup> however the high chemical and mechanical stability of interpenetrated Zr and Hf MOFs enables stereoselective and quantitative halogenation of their integral unsaturated sites, either as bulk microcrystalline powders or single crystals (see Chapter 3).<sup>15</sup>

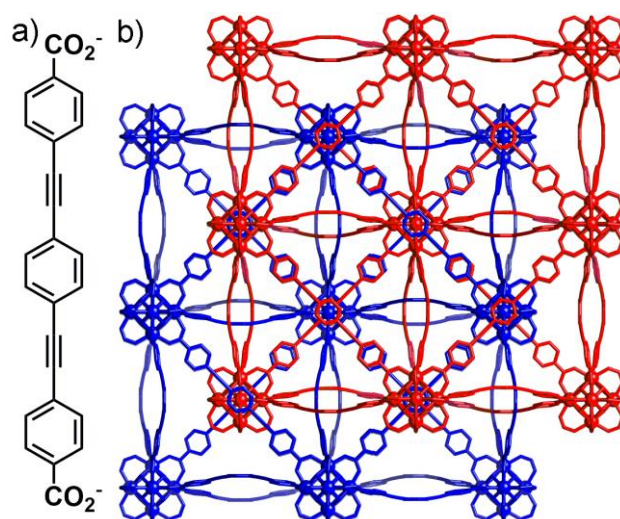


**Figure 4.1.** a) Structural representation of the extended  $\text{peb}^{2-}$  ligand that forms interpenetrated MOFs with Zr and Hf. b) Portion of the solid state structure of the interpenetrated Zr MOF containing  $\text{peb}^{2-}$  bridging ligands. The two independent nets are represented in red and blue to highlight the 2-fold interpenetration.

The dimethyl ester of the  $\pi$ -conjugated  $\text{peb}^{2-}$  ligand has been investigated for its optical properties, showing strong absorption in the UV region, while the chromophore is also highly fluorescent with a quantum yield of 0.91 ( $\lambda_{\text{abs}} = 335 \text{ nm}$ ) in dichloromethane.<sup>16</sup> The Zr MOF

containing  $\text{peb}^{2-}$  (Figure 4.1b) was investigated for photocatalytic organic dye degradation and, after optical measurements and DFT calculations, it was concluded that the optical properties of the MOF are inherited from the  $\pi$ -conjugated organic ligand.<sup>9</sup> A number of other fluorescent Zr MOFs have been reported and many of them have been used for the detection and sensing of external stimuli, such as metals,<sup>17</sup> explosives,<sup>18</sup> harmful gases/vapours<sup>19-21</sup> and antibiotics.<sup>22</sup> Alternatively, intrinsic fluorescence of Zr MOFs has been demonstrated to be useful in pH sensing<sup>23,24</sup> while rigidifying a tetraphenylethylene based ligand within a Zr MOF results in a twisting of the ligands, causing a dramatic bright blue fluorescence shift.<sup>25</sup> It has been demonstrated in two topologically different Zr-porphyrin MOFs, namely NU-902 and MOF-525, that intrinsic alterations of ligand planarity imposed by symmetry constraints results in differences in their steady state emission spectra, both in terms of band positions and intensities.<sup>26</sup>

## 4.2 Aims

Inspired by the intrinsic fluorescence of the dimethyl ester of  $\text{peb}^{2-}$  a series of functionalised  $\text{peb}^{2-}$  ligands containing a variety of chemical substituents on the central phenylene core were designed and synthesised. The ligands contain a diverse range of functionality and include methyl, fluorine, naphthalene and benzothiadiazole substituted derivatives (Figure 4.2).

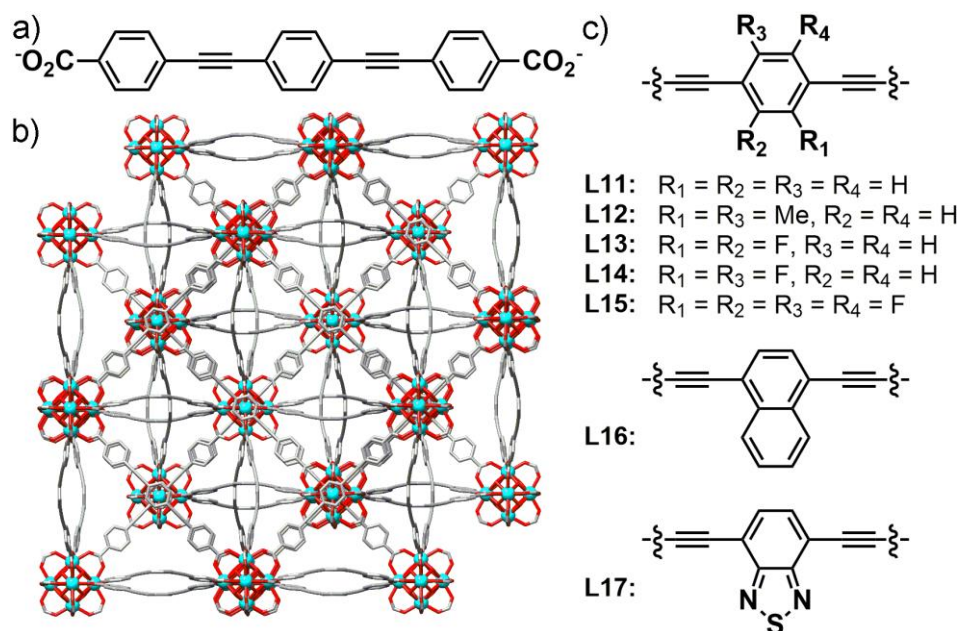


**Figure 4.2.** a) Structure of the un-functionalised  $\text{peb}^{2-}$  ligand, herein termed L11 alongside b) the solid state packing structure of the Zr MOF containing L11, **Zr-L11**. c) Schematic representation of the functionalised ligands with the numbering scheme used throughout this chapter. Atom colour scheme: Zr, cyan; C, grey; O, red. Hydrogen atoms are omitted for clarity.

Bulk microcrystalline powders and single crystals of Zr and Hf MOFs containing L11 were successfully synthesised (Chapter 2) and postsynthetically modified at integral reactive sites (Chapter 3). The very similar underlying structure of the substituted ligands suggests that they will form Zr and Hf MOFs with almost identical structures. Incorporation of well-known fluorophores, such as naphthalene and benzothiadiazole units is expected to result in MOFs with interesting optical properties and hence solid-state UV-Vis and solid state fluorescence emission spectroscopies will be used to determine their optical behaviours. Solid-state fluorescence emission spectroscopy is performed in collaboration with the Blight Group from the University of Kent. The potential of the MOFs for solid state sensing applications will be



investigated, as the high chemical stabilities of Zr and Hf MOFs enables them to tolerate a wide variety of conditions.

Alongside optical considerations, the series of interpenetrated MOFs have the potential to display interesting host-guest and host-host interactions, as it has previously been found in collaboration with researchers from the University of Edinburgh that **Hf-L11** undergoes a phase-change at 1.4 GPa in *n*-pentane, as revealed by high pressure single crystal X-ray crystallography. During the phase change the ligand core twists by  $\sim 90^\circ$  to form H-bonding interactions with the  $\text{Hf}_6$  clusters of the other independent net (Figure 4.3).

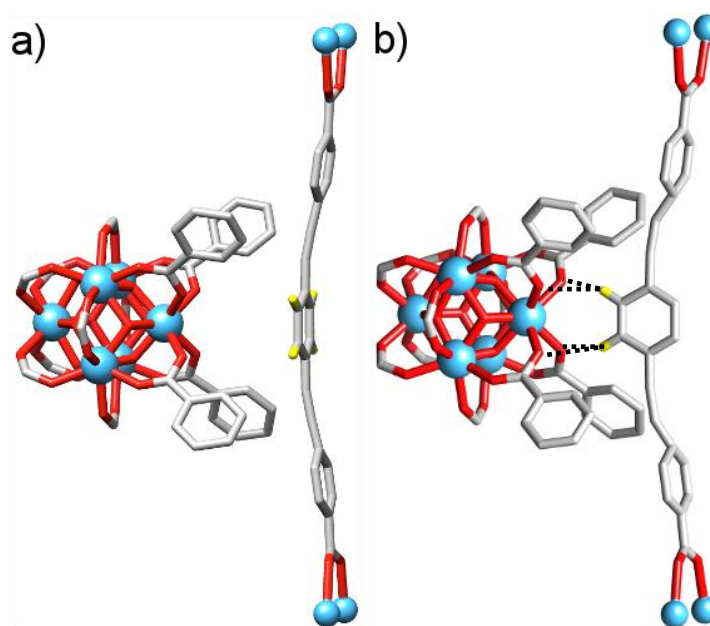


**Figure 4.3.** Portion of the solid state structure of a) **Hf-L11** at atmospheric pressure and b) **Hf-L11** in *n*-pentane at 1.4 GPa. Atom colour scheme: Hf, blue; C, grey; O, red; H, yellow. Some hydrogen atoms are omitted for clarity

By adopting a twisted conformation bifurcated hydrogen bonds form, pointing towards the carboxylate oxygens at the cluster of the other independent net. It is expected that the driving force for rotation is the formation of the hydrogen bonds which block a known binding site for water and potentially other guests.<sup>27</sup> It is expected that functionalisation of the ligand core will tune the MOFs' host-host and host-guest interactions and consequently this will modulate the material's high pressure behaviour. The ability to modulate the blocking pressure of this known binding site through ligand functionalisation opens up potential applications for storage of a range of guests and investigations are currently underway.

### 4.3 Ligand Design and Synthesis

Seven extended ligands were synthesised using similar synthetic conditions,<sup>28</sup> coupling methyl 4-ethynylbenzoate with commercial available aryl dihalides containing the desired functionality (Figure 4.4). If commercially available the diiodides were purchased, however if they were unavailable the dibromides were sourced. There did not appear to be any issues regarding the reactivity of the bromide containing aryl reagents, however the first synthetic attempts of some of the ligands were unsuccessful. If the products were not successfully isolated, changing the reaction solvent from triethylamine (TEA) to a 1:1 mixture of TEA and *N,N*-dimethylformamide (DMF) was sufficient to aid solubility of the reagents (as well as any intermediates) and allow the reactions to proceed successfully. In the reactions containing DMF the temperature was subsequently increased from 50 °C to 80 °C to reflect the higher boiling point of DMF. Saponification of the dimethyl esters resulted in the free acids required for MOF synthesis.<sup>14</sup>

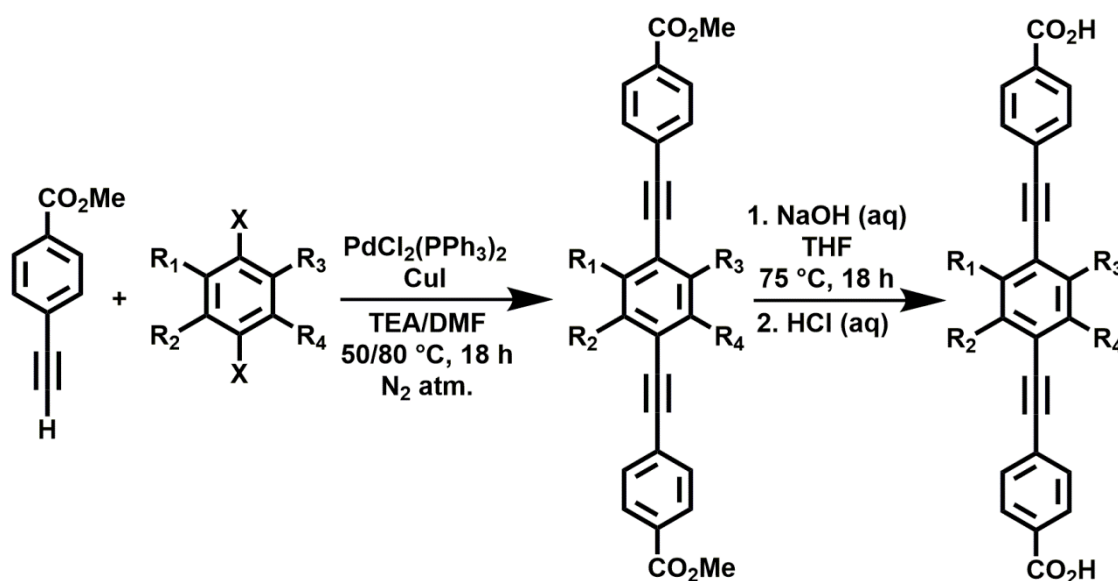


**Figure 4.4.** General procedure used to synthesise the dimethyl esters of L11-L17 and their subsequent saponification to produce the free acids.

A variety of dihalides were purchased containing diverse substituents, such as methyl, fluorine, naphthalene and benzothiadiazole functionality. Two ligands that are positional isomers (L13 and L14), in terms of the substitution pattern of pendant fluorine atoms on the central phenylene core, were intentionally synthesised. It is expected that altering the acidity of the hydrogen atoms on the central core of the ligand will result in interesting high-pressure

behaviours of the interpenetrated MOFs. Conventional fluorophores, such as naphthalene (L16) and benzothiadiazole (L17), have been incorporated onto the ligand scaffold to regulate the materials' optical properties. The very close structural similarity of the ligands, many of which had not previously used for MOF construction, both in terms of length and topology suggests they should be incorporable into isostructural interpenetrated Zr and Hf MOFs. The solid state structures of a number of the ligands confirm their structural similarity (Figures 4.26-4.30). As described in Chapter 2, Sections 2.10.10 and 2.10.11, phase pure microcrystalline and single crystal samples of **Zr-L11** and **Hf-L11** were synthesised using either L-proline<sup>29</sup> or benzoic acid<sup>7</sup> modulation. The optimised synthetic conditions for **Zr-L11** and **Hf-L11** were a useful starting point for the synthesis of Zr and Hf MOFs containing the functionalised ligands.

#### 4.4 Bulk Synthesis of Interpenetrated Zr and Hf MOFs

Solvothermal reactions containing the required ligand, ZrCl<sub>4</sub> or HfCl<sub>4</sub>, hydrochloric acid and either L-proline or benzoic acid in DMF resulted in the isolation of a series of new interpenetrated Zr and Hf MOFs. The as-prepared materials were first characterised using PXRD analysis to confirm successful MOF synthesis, and upon comparison of the PXRD patterns it is apparent that the materials are isostructural (Figure 4.5).

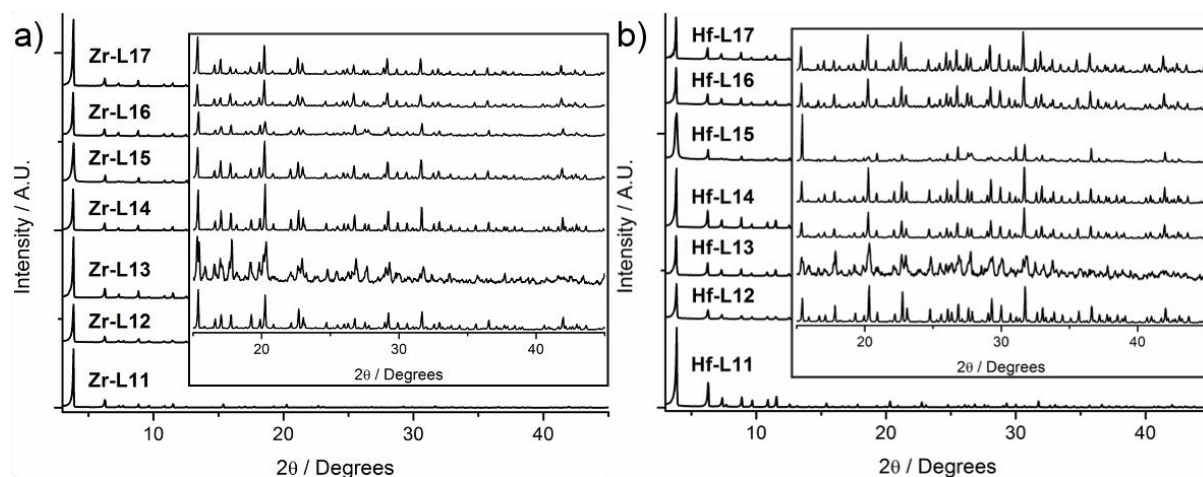


**Figure 4.5.** Stacked PXRD patterns of a) Zr and b) Hf MOFs containing L11-L17. The insets are expanded regions of the high angle data.

Upon inspecting the PXRD patterns of both series of MOFs, it is apparent that all fourteen materials are highly crystalline, and this is true even to high angles of  $2\theta$ . The high crystallinity of the MOFs is attributable to the use of synthetic modulators, which are routinely employed during the synthesis of Zr and Hf MOFs.<sup>30</sup> Twelve of the fourteen MOFs were successfully synthesised as microcrystalline powders using L-proline modulation, however this synthetic procedure did not produce phase pure **Zr-L15** or **Hf-L15**. There is no obvious reason why L-proline modulation fails during the synthesis of MOFs containing L15, although benzoic acid was effective and was used instead. There are a few observations which can be extracted from the PXRD patterns, with the first being that the patterns of **Zr-L12** and **Hf-L12** do not exactly match the patterns of the other MOFs. The PXRD pattern of **Hf-L15** is clearly in good agreement with the patterns of the other MOFs, albeit there are differences observed in the relative intensities. The MOFs are structurally very similar, and this is obvious from the similarity of their PXRD patterns. Comparing the experimental and calculated (from the single crystal model) patterns of two MOFs containing the same ligand the structural similarities of both series of MOFs is evident (Figure 4.6).

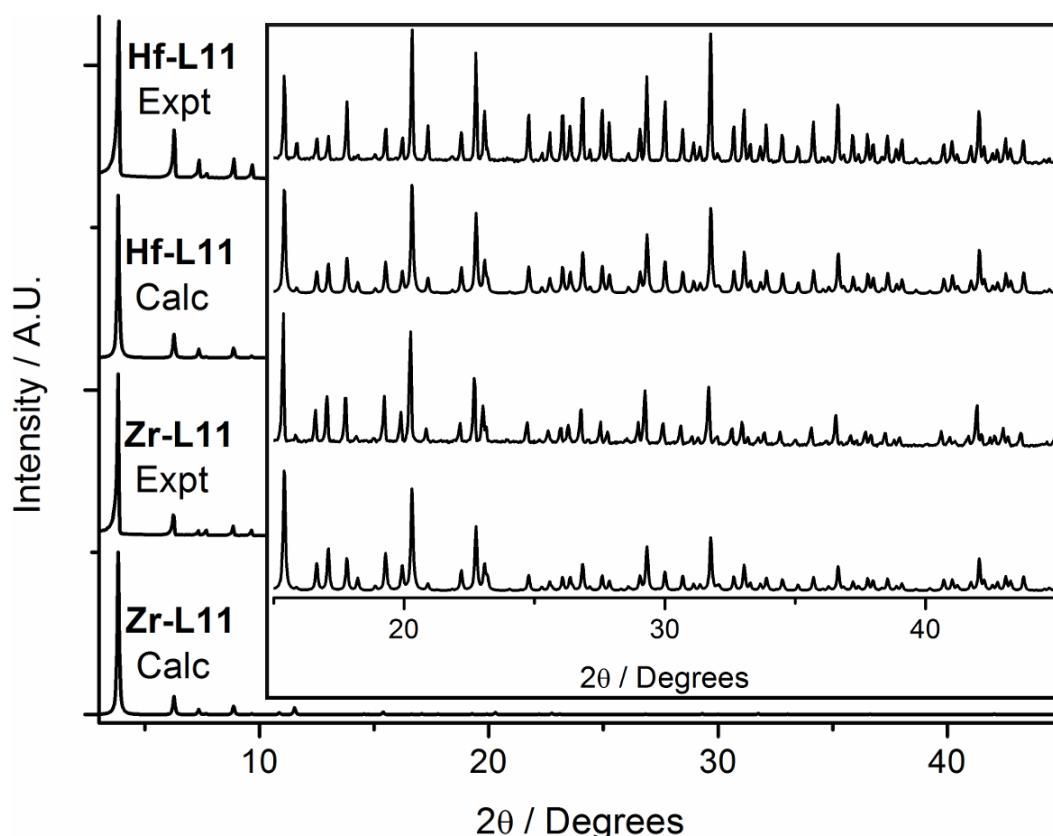


**Figure 4.6.** Comparison of the calculated and experimental PXRD patterns of **Zr-L11** and **Hf-L11**. The inset is an expanded region of the high angle data.

The bulk phase purities of **Zr-L11** and **Hf-L11** are confirmed by the excellent agreement between the PXRD patterns calculated from the single crystal models and the experimental patterns, even to high angles of  $2\theta$ . The very close agreement between the PXRD patterns of **Zr-L11** and **Hf-L11** proves that the MOFs are isostructural and this is true of all Zr and Hf MOFs containing each respective ligand. This suggests that ligand functionalisation does not disrupt framework interpenetration, as in the absence of interpenetrated structures PXRD patterns resembling UiO-66 type materials (non-interpenetrated) would be expected.<sup>1</sup> With bulk microcrystalline samples of all fourteen MOFs obtained, efforts were directed towards obtaining single crystals.

#### 4.5 Single Crystal Synthesis of Interpenetrated Zr and Hf MOFs

Reaction conditions were systematically adjusted and, upon refinement, thirteen of the MOFs were isolated as single crystals, allowing detailed structural information to be obtained. The exception is **Hf-L12** which could not be obtained as single crystals. Single crystals of the MOFs are not only useful for accurate structural analysis, but they are also required for our high pressure X-ray diffraction studies investigating the relationship between framework functionalisation and the corresponding host-host and host-guest interactions.

The crystal structures of the Zr and Hf analogues of individual ligands are very similar, as expected based on the close agreement between the PXRD patterns of **Zr-L11** and **Hf-L11** (Figure 4.6). The pendant functionality of the ligands does not disrupt formation of the MOFs with all materials displaying 2-fold interpenetration. In the crystal structures of the MOFs containing the difluorinated ligands, L13 and L14, there is positional disorder of the fluorine atoms across all four sites of the central phenylene core. On first inspection they all appear to be identical and resemble Zr and Hf MOFs containing L15, however the positional disorder is accounted for by adjusting chemical occupancies (Figure 4.7). Similarly, the benzothiadiazole unit of L17 is disordered across two orientations in the Zr and Hf MOFs, maintaining the cubic symmetry despite the lower symmetry of the ligand. Interestingly, differences are observed in the solid state structures of **Zr-L16** and **Hf-L16** which contain naphthalene units. In **Hf-L16** there is positional disorder of the naphthalene unit across both sides of the ligand, while in **Zr-L16** the same disorder is observed, however in this case the

naphthalene core twists out of the plane of conjugation by approximately  $23^\circ$ , presumably to minimise steric interactions between the interpenetrated frameworks. The reason for the different behaviour in the Zr and Hf analogues has not been established.

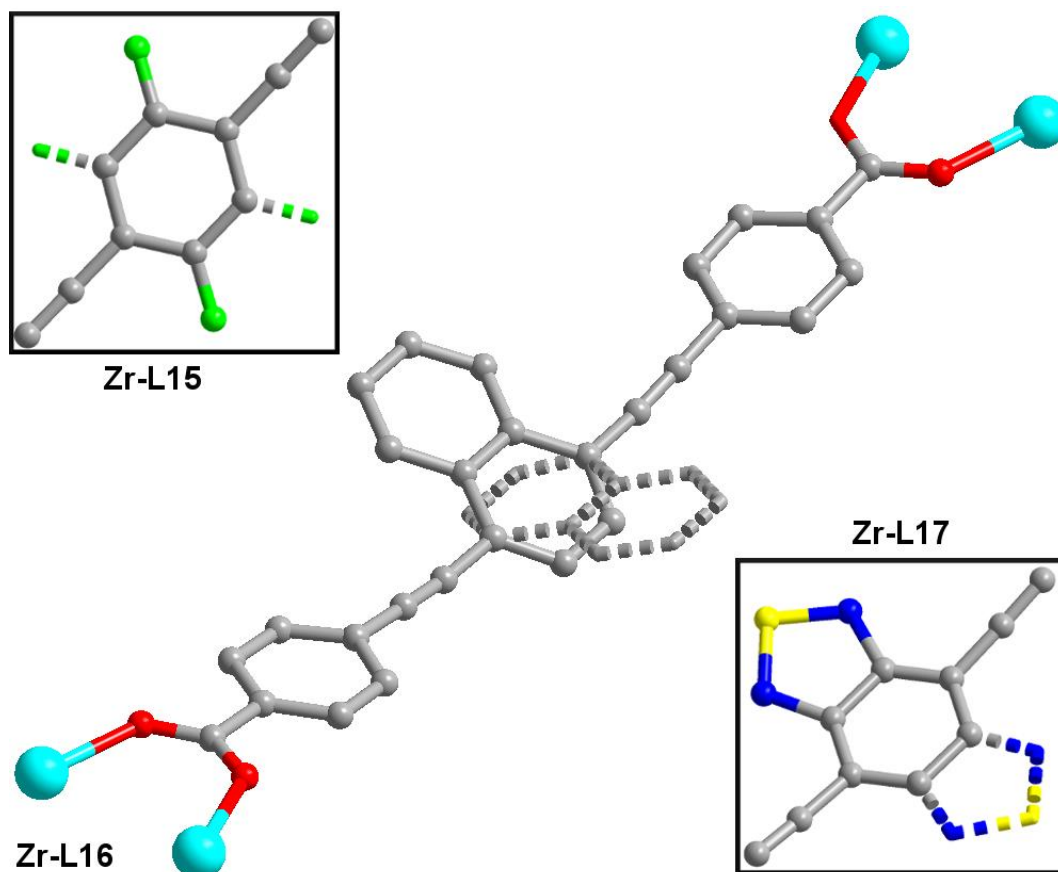


**Figure 4.7.** Portions of the solid state structures of **Zr-L15**, **Zr-L16** and **Zr-L17** highlighting the positional disorder observed in all three structures to maintain the cubic symmetry (disorder components are represented by dashed bonds). The orientation of **Zr-L16** shows twisting of the naphthalene core out of the plane of conjugation. Atom colour scheme: Zr, cyan; C, grey; O, red; F, green; N, blue; S, yellow. Hydrogen atoms are omitted for clarity.

All the functionalised MOFs discussed this far adopt the expected cubic symmetry and crystallise in the  $Fd-3m$  space group typical of the parent MOFs containing the unfunctionalised ligand, L11. However, there are differences observed in the PXRD patterns of the Zr and Hf MOFs containing L12 with additional peaks observed while some of the peaks also appear to be split. Viewing single crystals of **Zr-L12** by optical microscopy (Figure 4.8a) it is apparent that both lozenge and rounded crystal morphologies are obtained, unlike the well-defined octahedral shaped crystals typical of the other members of the series. Both

forms of **Zr-L12** crystallise in the lower symmetry orthorhombic *Imma* space group but have the same connectivity and composition as the other MOFs. The lower symmetry of **Zr-L12** is attributed to the presence of different ligand orientations (Figures 4.8b-d). Of the twelve ligands connected to each  $\text{Zr}_6$  cluster, four ligands in an equatorial plane are planar with disordered methyl units (Figure 4.8c) while the other eight ligands adopt a conformation where the central dimethylphenylene unit is twisted by  $\sim 40^\circ$  out of the plane of conjugation, and the methyl groups are fully ordered (Figure 4.8d). Twisting of the ligands in **Zr-L12** is believed to be the result of steric interactions between bulky methyl groups and adjacent phenyl units of the other interpenetrated net, which are in close proximity.

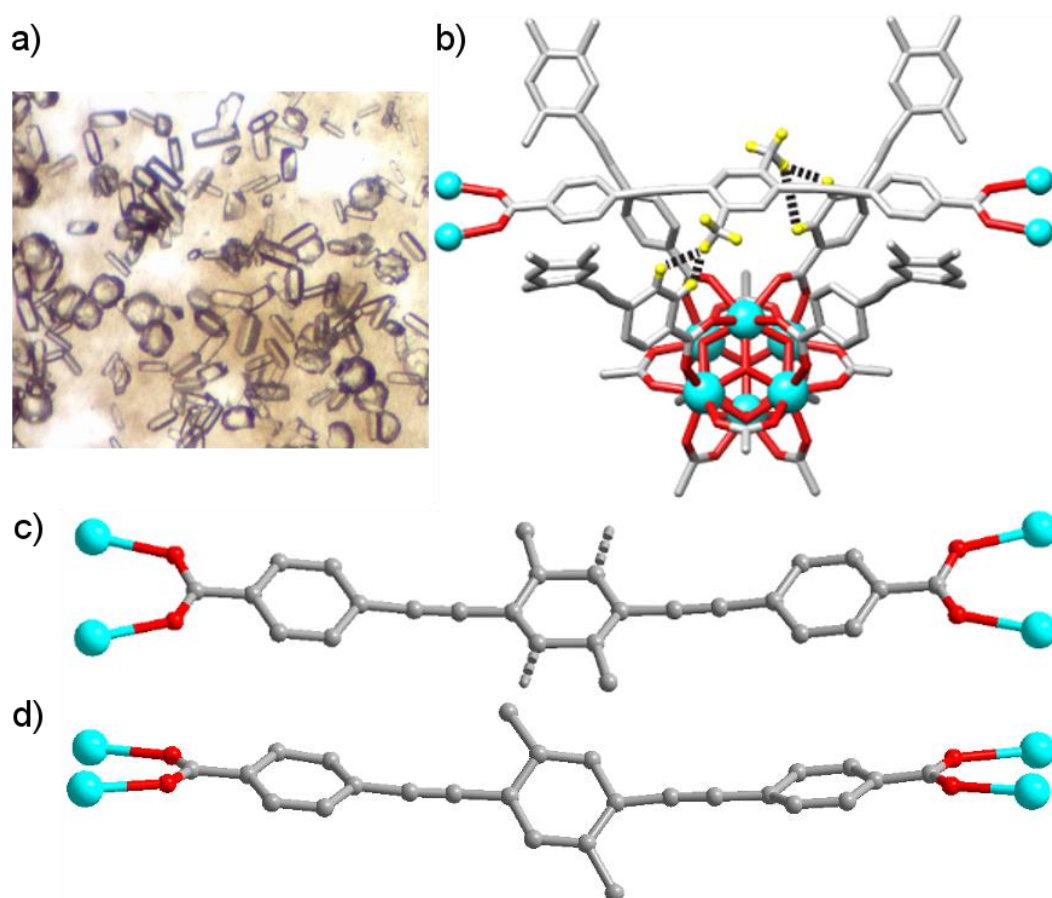


**Figure 4.8.** a) Optical microscope image of single crystals of **Zr-L12**. b) A portion of the solid state structure of **Zr-L12** with dashed lines representing the close proximity of the pendant methyl groups with the other framework. c) and d) represent the planar and twisted ligand conformations found within the solid state structure of **Zr-L12** respectively (disorder components are represented by dashed bonds). Atom colour scheme: Zr, cyan; C, grey; O, red; H, yellow. Some hydrogen atoms are omitted for clarity.



Interestingly, Zr and Hf MOFs containing L14, which have pendant fluorine atoms in the same positions that L12 contains methyl substituents, crystallise in the expected  $Fd-3m$  space group. The steric interactions imposed between the interpenetrating frameworks by the fluorine atoms are insufficient to drive a structural change and in this case the usual cubic symmetry is achievable. In the crystal structure of **Zr-L14** the ligands are all in the plane of conjugation and the fluorine atoms are disordered over all four positions of the central phenylene core. In **Zr-L12** the ligands can be observed to bow away from the  $Zr_6$  cluster (Figure 4.9a) while in **Zr-L14** and all the other members of the series the ligands bow in towards the  $Zr_6$  cluster (Figure 4.9b). The change in direction of ligand bowing is likely a consequence of the steric interactions of the bulky methyl substituents.

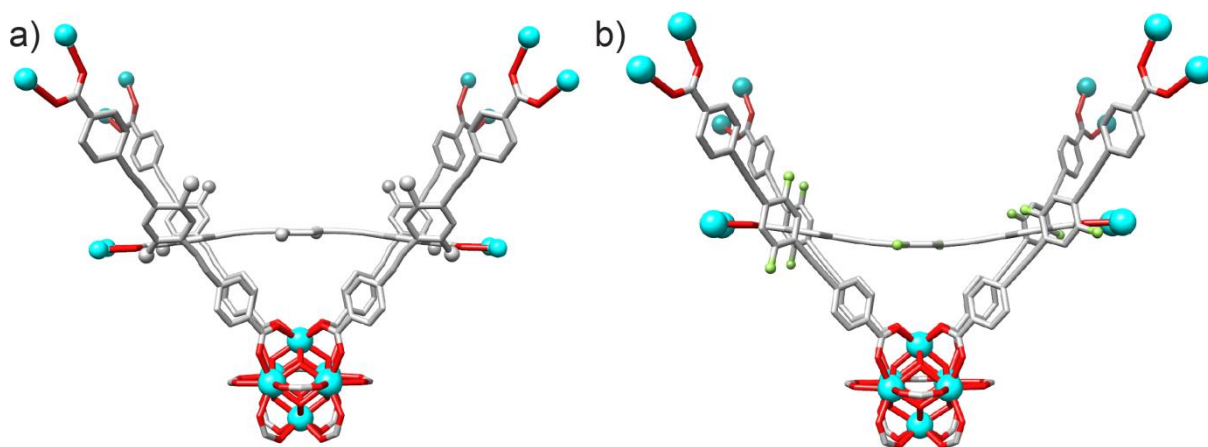


**Figure 4.9.** Portion of the solid state structure of a) **Zr-L12** and b) **Zr-L14** highlighting the direction of ligand bowing. Disordered methyl groups and fluorine atoms have been removed for clarity. Atom colour scheme: Zr, cyan; C, grey; O, red; F, green. Hydrogen atoms are omitted for clarity.

The differences observed in the solid state structure of **Zr-L12** results in alterations to the PXRD pattern compared with the other MOFs, however, the pattern of **Zr-L12** changes considerably upon activation prior to  $N_2$  uptake experiments (heating at 120 °C for 20 hours) suggesting a structural change.

#### 4.6 Zr-L12 Structural Investigation

The PXRD pattern of **Zr-L12** is different to the other members of the series as it crystallises in the lower symmetry orthorhombic *Imma* space group as a result of steric clashes between



the ligands of the two interpenetrating frameworks. The experimental PXRD pattern of chloroform exchanged **Zr-L12** resembles the calculated PXRD patterns (from the single crystal structures) of both **Zr-L12** (orthorhombic, *Imma*) and **Zr-L11** (cubic, *Fd-3m*) to a certain extent (Figure 4.10). This explains the splitting of the peaks in the PXRD pattern of **Zr-L12**, suggesting that a mixture of the two phases is obtained. The PXRD pattern of **Zr-L12** after N<sub>2</sub> uptake measurements is in close agreement with the predicted pattern of **Zr-L11**, confirming that the material transforms to the cubic phase (Figure 4.10).

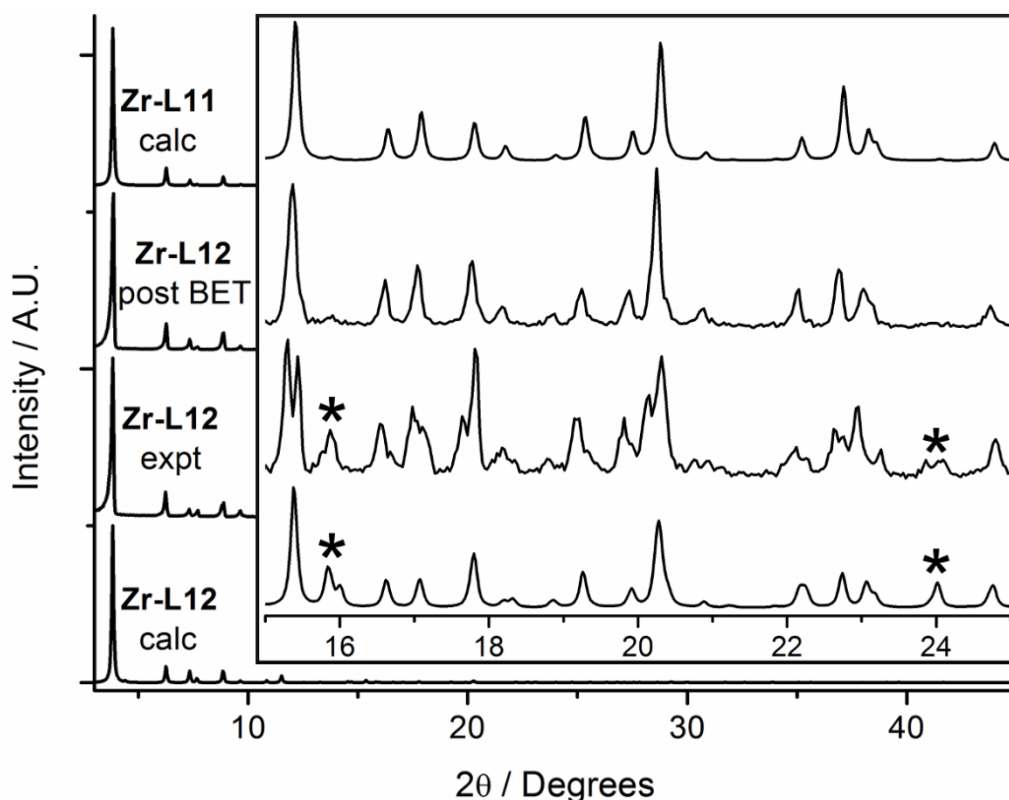


**Figure 4.10.** Stacked PXRD patterns of **Zr-L12** before (**Zr-L12 expt**) and after (**Zr-L12 post BET**) N<sub>2</sub> adsorption measurements compared with predicted patterns of orthorhombic (**Zr-L12 calc**) and cubic (**Zr-L11 calc**) symmetry. Peaks marked with an asterisk are lost upon activation, indicating a phase change. The inset is an expanded view of the deterministic region.

The ability of **Zr-L12** to transform from the orthorhombic to the cubic structure confirms that the material is dynamic as the dimethylphenylene core of the ligands must twist back into the plane of conjugation. Comparing the PXRD patterns of **Zr-L12** before and after N<sub>2</sub> uptake experiments, where the MOF is activated by heating at 120 °C under vacuum, it is obvious that some of the peaks are lost (marked with an asterisk in Figure 4.10), while the split peaks

also converge into single peaks, confirming that **Zr-L12** transforms to the cubic phase. Variable temperature PXRD patterns were collected at regular intervals from room temperature to 200 °C, and then once again when cooled to provide further details of the phase change and to confirm that heating definitely triggers the change (Figure 4.11).

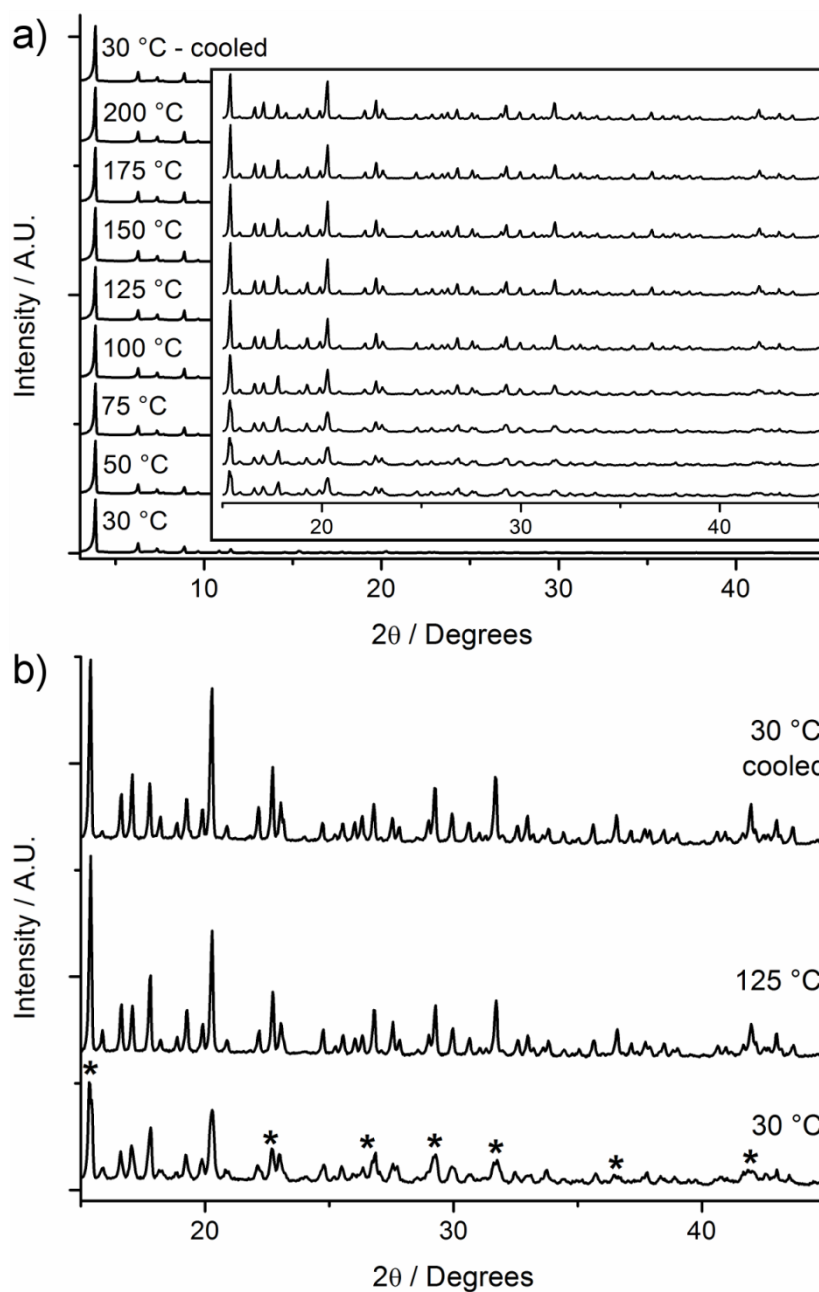


**Figure 4.11.** a) Stacked PXRD patterns of **Zr-L12** collected at a range of temperatures (the inset is an expanded view of the high angle data). b) Part of the PXRD patterns collected at 30 °C, 125 °C and 30 °C once cooled to allow the differences between the patterns to be more clearly visualised. The most pronounced regions where differences are observed are marked with an asterisk.

Comparing the PXRD patterns of **Zr-L12** at different temperatures it is clear that upon heating the split peaks merge to form single peaks, suggesting transformation to one single phase. The differences in the PXRD patterns are clearly viewed in Figure 4.11b with obvious differences in terms of both peak shapes and their relative intensities observed upon heating from 30 °C to 125 °C. The changes observed in the PXRD patterns further support transformation to the cubic phase upon heating, and the structural change does not appear to be reversible, with the PXRD pattern not changing upon cooling.

Combined SCXRD and PXRD analyses are useful for determination of the interesting structural features of **Zr-L12**, which is structurally different to the other members of the series despite only subtle differences in the pendant functionality of the bridging ligands. Furthermore, they have been useful for probing the phase change observed for **Zr-L12** which is believed to be the result of twisting of the dimethylphenylene core. The dynamic behaviour of **Zr-L12** suggests that this behaviour may also be possible for other interpenetrated Zr and Hf MOFs leading to interesting properties useful for switching or sensing applications if the phase change can be controlled by external stimulus.

## 4.7 Thermal Analysis

Having obtained bulk phase pure interpenetrated Zr and Hf MOFs containing L11-L17, thermogravimetric analysis (TGA) was used to determine the effect of both the metal cluster and the bridging organic ligand on the MOFs' thermal stabilities. TGA measurements were carried out under an air atmosphere, resulting in decomposition of the MOF to either ZrO<sub>2</sub> or HfO<sub>2</sub>. By using identical experimental parameters, the thermal stabilities of the Zr and Hf MOFs can be compared (Figure 4.12).

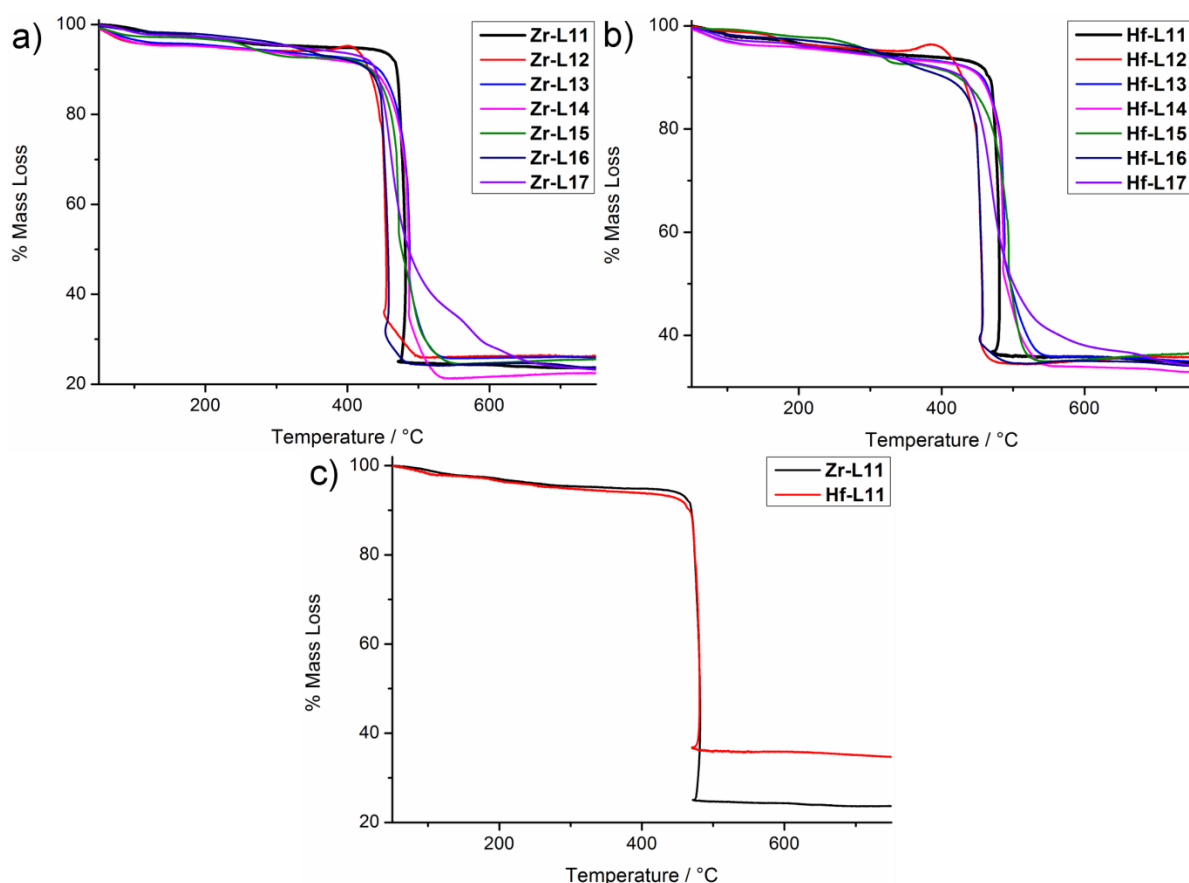


**Figure 4.12.** TGA profiles of a) Zr and b) Hf MOFs containing L11-L17. c) Comparison of the TGA profiles of **Zr-L11** and **Hf-L11**.

Comparing the TGA profiles of the Zr and Hf MOFs it is clear that ligand functionalisation results only in slight differences in the thermal properties of the materials. The functionalised MOFs undergo thermal decomposition at temperatures similar to the parent MOFs containing L11. The very similar thermal stabilities of the MOFs makes it difficult to visualise the individual thermal stability of each material, however the profiles of **Zr-L11** and **Hf-L11** are compared to understand the influence of  $\text{Zr}_6$  or  $\text{Hf}_6$  clusters on the MOFs thermal stabilities (Figure 4.12c). The TGA profiles of **Zr-L11** and **Hf-L11** are almost identical with the smaller percentage mass loss of **Hf-L11** compared with **Zr-L11** expected due to the increased mass of Hf relative to Zr. This confirms that Zr and Hf MOFs display similar thermal stabilities and as the thermal stabilities of Zr MOFs are one of their most promising features it is expected that interest in Hf MOFs will increase. Hf MOFs are especially useful for diffraction purposes due to the increased scattering power of Hf relative to Zr and this is desired for high pressure SCXRD studies where data collections become increasingly difficult at higher pressures. With all of the interpenetrated Zr and Hf MOFs displaying

promising thermal stabilities, the next stage in their characterisation was to measure their porosity by N<sub>2</sub> uptake experiments.

#### 4.8 Surface Area and Pore Size Distribution Analysis

N<sub>2</sub> adsorption and desorption isotherms were measured at 77 K to evaluate the effect of ligand functionalisation on the porosity of the MOFs (Figure 4.13).

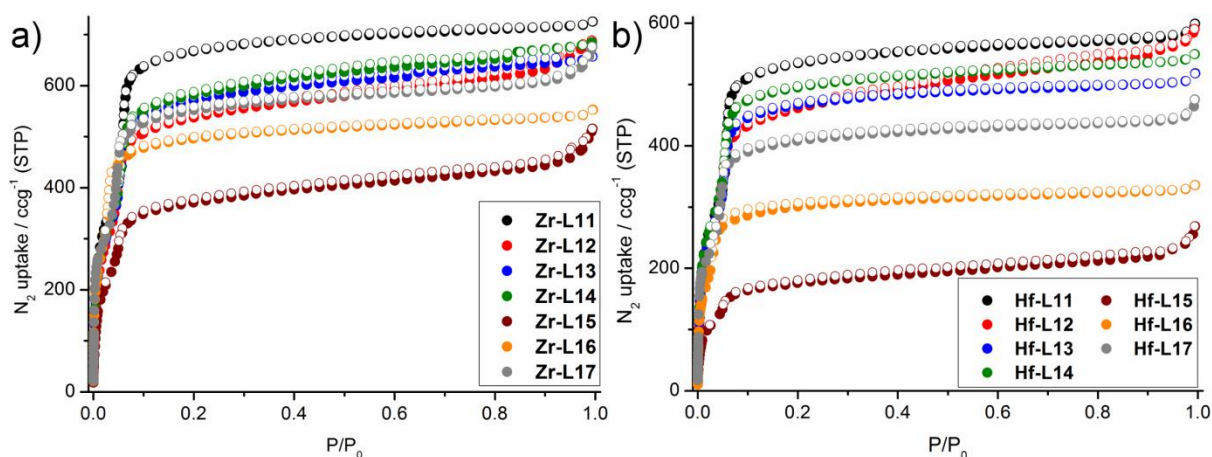


**Figure 4.13.** Comparison of the N<sub>2</sub> adsorption (closed circles) and desorption (open circles) isotherms of a) Zr and b) Hf MOFs containing L11-L17.

The BET surface areas of the fourteen MOFs were subsequently calculated and are summarised in Table 4.1.

**Table 4.1.** Calculated BET surface areas of the Zr and Hf MOFs containing L11-L17. All values are in m<sup>2</sup>g<sup>-1</sup>.

	<b>L11</b>	<b>L12</b>	<b>L13</b>	<b>L14</b>	<b>L15</b>	<b>L16</b>	<b>L17</b>
<b>Zr</b>	2680	2070	2195	2270	1420	1990	2130
<b>Hf</b>	2080	1775	1800	1960	675	1210	1660

Upon comparison of the N<sub>2</sub> isotherms of the Zr and Hf MOFs it is evident that ligand functionalisation results in reduced N<sub>2</sub> uptakes compared with **Zr-L11** and **Hf-L11**. This is reflected in their BET surface areas which decrease with increasing steric bulk. This is expected as (i) the increased molecular weight of the functionalised MOFs will result in

lower gravimetric N<sub>2</sub> uptake capacities, and (ii) the underlying MOFs structures are the same, and as the functionality occupies the pore space of the MOFs there is less free volume for the N<sub>2</sub> molecules to occupy. The N<sub>2</sub> uptake capacities of **Zr-L12**, **Zr-L13** and **Zr-L14** are similar, which is reassuring as all three MOFs contain two pendant moieties, either methyl groups or fluorine atoms. The porosity of **Zr-L17** is also similar to that of the MOFs containing difunctionalised phenylene cores, while **Zr-L16** displays a slightly lower uptake. All of these results are in line with what is expected, but combined with calculated BET surface areas (Table 4.1) it is clear that the uptake of **Zr-L15** is considerably lower than expected. The reason for the low N<sub>2</sub> uptake of **Zr-L15** is not immediately obvious, however this was consistently the case for multiple batches. It should be noted that the uptake of **Hf-L15** is also lower than expected, and therefore it may be plausible that the activation conditions used were ineffective for MOFs containing L15 or that during activation the MOFs were partially collapsing. The N<sub>2</sub> uptake and BET surface areas of the Hf MOFs are lower than the Zr MOFs due to their increased molecular weight, however this increase in mass does not fully account for the lower than expected N<sub>2</sub> uptakes of **Hf-L16** and **Hf-L17**. **Hf-L16** and **Hf-L17** were synthesised multiple times and subject to N<sub>2</sub> uptake experiments, however the values obtained were consistently low.

The N<sub>2</sub> adsorption isotherms of all fourteen MOFs reveal stepwise adsorption in the low pressure region. The stepwise adsorption (Figure 4.14) is due to preferential filling of the smaller tetrahedral pores with N<sub>2</sub> molecules prior to filling of the larger tetrahedral pores.

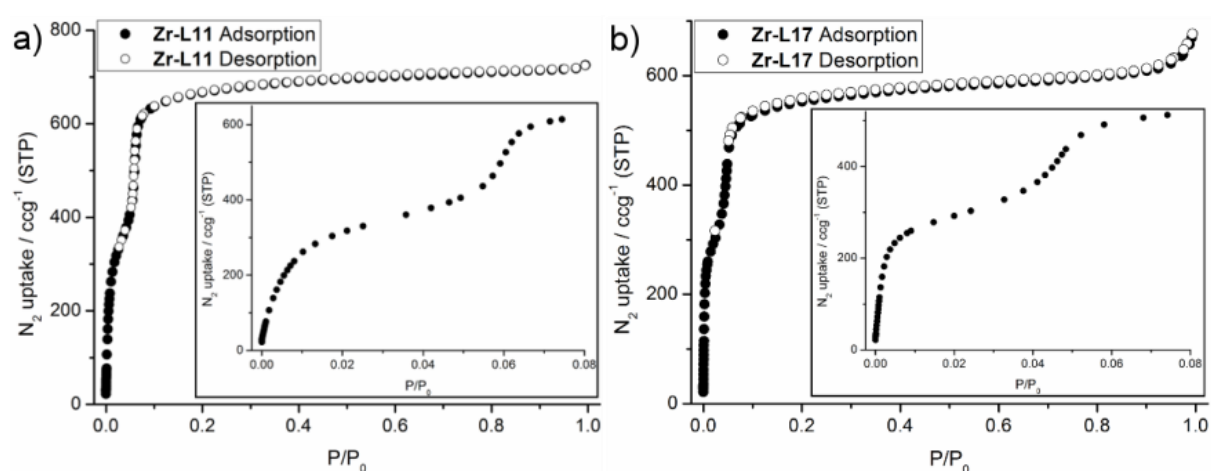


**Figure 4.14.** N<sub>2</sub> adsorption (closed circles) and desorption (open circles) isotherms collected at 77 K of a) **Zr-L11** and b) **Zr-L17**. The insets are expanded regions of the low P/P<sub>0</sub> adsorption data highlighting the stepwise adsorption.

The N<sub>2</sub> adsorption and desorption data of **Zr-L11** and **Zr-L17** are shown as two representative examples (Figure 4.14) of all the MOFs, highlighting the steps in their isotherms that are the result of preferential filling of the small pores prior to filling of the larger pores. Overall, the BET surface areas of the Zr and Hf MOFs containing L11-L17 are relatively high considering their 2-fold interpenetration.

Pore size distributions were calculated (slit pore, QSDFT equilibrium model) to visualise the effect of increasing steric bulk on the MOFs pore diameter (Figure 4.15).

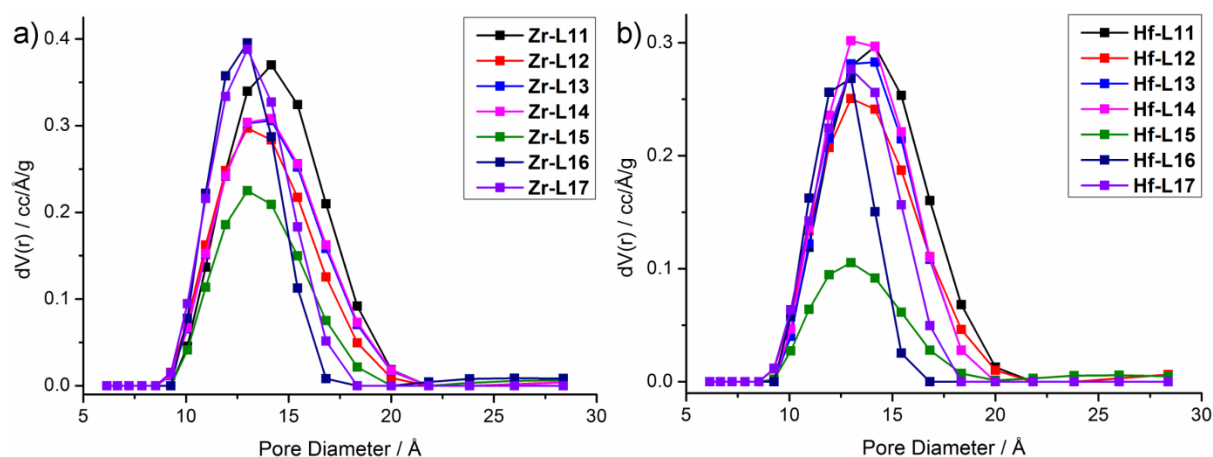


**Figure 4.15.** Pore size distributions of a) Zr and b) Hf MOFs containing L11-L17.

Pore size distributions of the Zr and Hf MOFs are consistent with decreasing pore diameters upon increasing steric bulk of the ligands. The main pore diameter decreases from ~14.2 Å for **Zr-L11** to ~13 Å for both **Zr-L16** and **Zr-L17**. The same pore size contraction is observed for the Hf MOFs, with the main pore diameter contracting by ~1.2 Å upon incorporation of naphthalene or benzothiadiazole units relative to the unfunctionalised ligand. The pore diameters of **Zr-L15** and **Hf-L15** are in line with what is expected, however the pore volumes of both MOFs are particularly low. The satisfactory pore diameter and reduction in pore volume further suggests that the low N<sub>2</sub> uptakes of these materials are due to incomplete activation rather than partial framework collapse.

The pore size distribution model only calculates the diameter of the main pore, however the frameworks contain two different types of tetrahedral pores. Alongside the larger tetrahedral pores, the smaller tetrahedral pores of the interpenetrated MOFs are unique to this topology and are not observed in the UiO-66 type frameworks which contain octahedral and



tetrahedral pores.<sup>1</sup> Interpenetration results in occupation of the octahedral pores observed in UiO-66 type MOFs by a second framework, splitting them into smaller tetrahedral pores. The smaller tetrahedral pores of the interpenetrated Zr MOFs have been highlighted to be beneficial for CO<sub>2</sub> capture, although it was found that functionalised ligands also varied the CO<sub>2</sub> capture performance.<sup>11</sup> CO<sub>2</sub> adsorption isotherms (Figure 4.16) were collected for the interpenetrated Zr and Hf MOFs to determine if the functionality incorporated within the MOFs would be beneficial for CO<sub>2</sub> uptake.

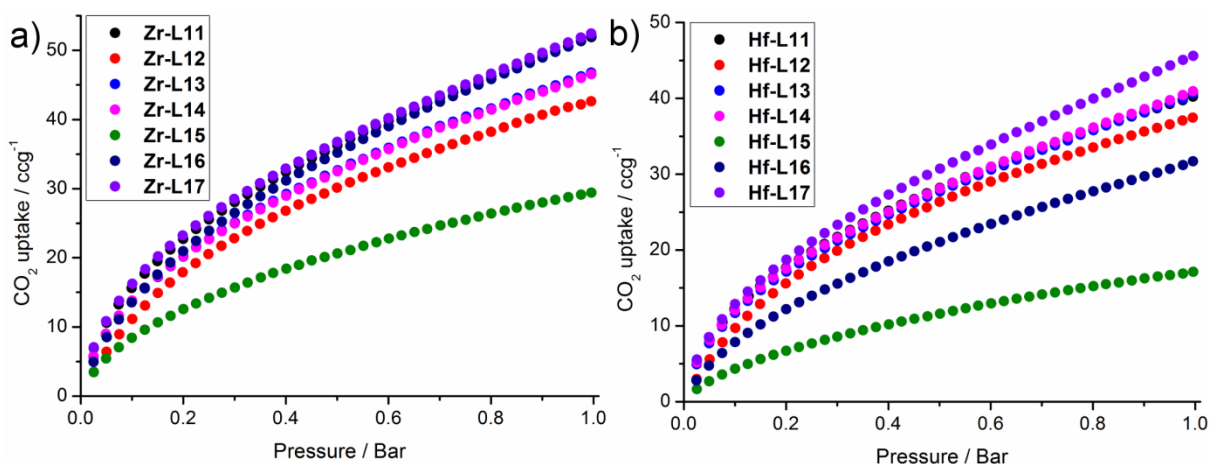


**Figure 4.16.** Comparison of the CO<sub>2</sub> isotherms (up to 1 bar, 273 K) of a) Zr and b) Hf MOFs containing L11-L17.

**Zr-L11**, **Zr-L16** and **Zr-L17** all display similar CO<sub>2</sub> uptake capacities (they are superimposed in Figure 4.16a), while the rest of the Zr MOFs all present lower uptakes. Incorporation of bulky aromatics/heterocycles in **Zr-L16** and **Zr-L17** would be expected to decrease CO<sub>2</sub> uptake as their N<sub>2</sub> uptakes are reduced relative to **Zr-L11**, however favourable interactions between CO<sub>2</sub> and the functionalised ligands results in similar CO<sub>2</sub> uptakes. Comparable results are observed for the Hf MOFs, although in this case incomplete activation of **Hf-L16** results in a lower than expected CO<sub>2</sub> uptake. The CO<sub>2</sub> uptake of **Hf-L17** is however the highest of the series, again inferring favourable interactions between CO<sub>2</sub> molecules and benzothiadiazole units. An increase in CO<sub>2</sub> uptake has previously been observed when benzothiadiazole moieties were incorporated into a Cu MOF.<sup>31</sup> There is only a slight increase in CO<sub>2</sub> uptake observed for **Hf-L17**, however the true increase in CO<sub>2</sub> uptake may only be fully elucidated at higher pressures. In this study the ligands contain pendant methyl, fluorine, naphthalene and benzothiadiazole units, however the wide range of



commercially available aryl dihalides presents scope for synthesis of other functionalised derivatives that could be beneficial for CO<sub>2</sub> uptake.

Considering the promising thermal stabilities and porosities of the MOFs, alternative methods of characterisation were sought. Incorporation of well-known chromophores (naphthalene and benzothiadiazole) within the MOFs prompted optical characterisation.

## **4.9 Solid State UV-Vis Spectroscopy**

It was expected that incorporation of functionalised ligands within interpenetrated Zr MOFs, especially the naphthalene and benzothiadiazole derivatives, would present interesting optical properties. Solid-state UV-Vis (SS-UV-Vis) absorption spectra were collected for all of the Zr MOFs as well as the free acids of their ligands. Comparing the absorption spectra of the MOFs with their respective ligands it is obvious that in most cases the optical properties of the MOFs are generally inherited from the incorporated ligand (Figures 4.17 and 4.19).

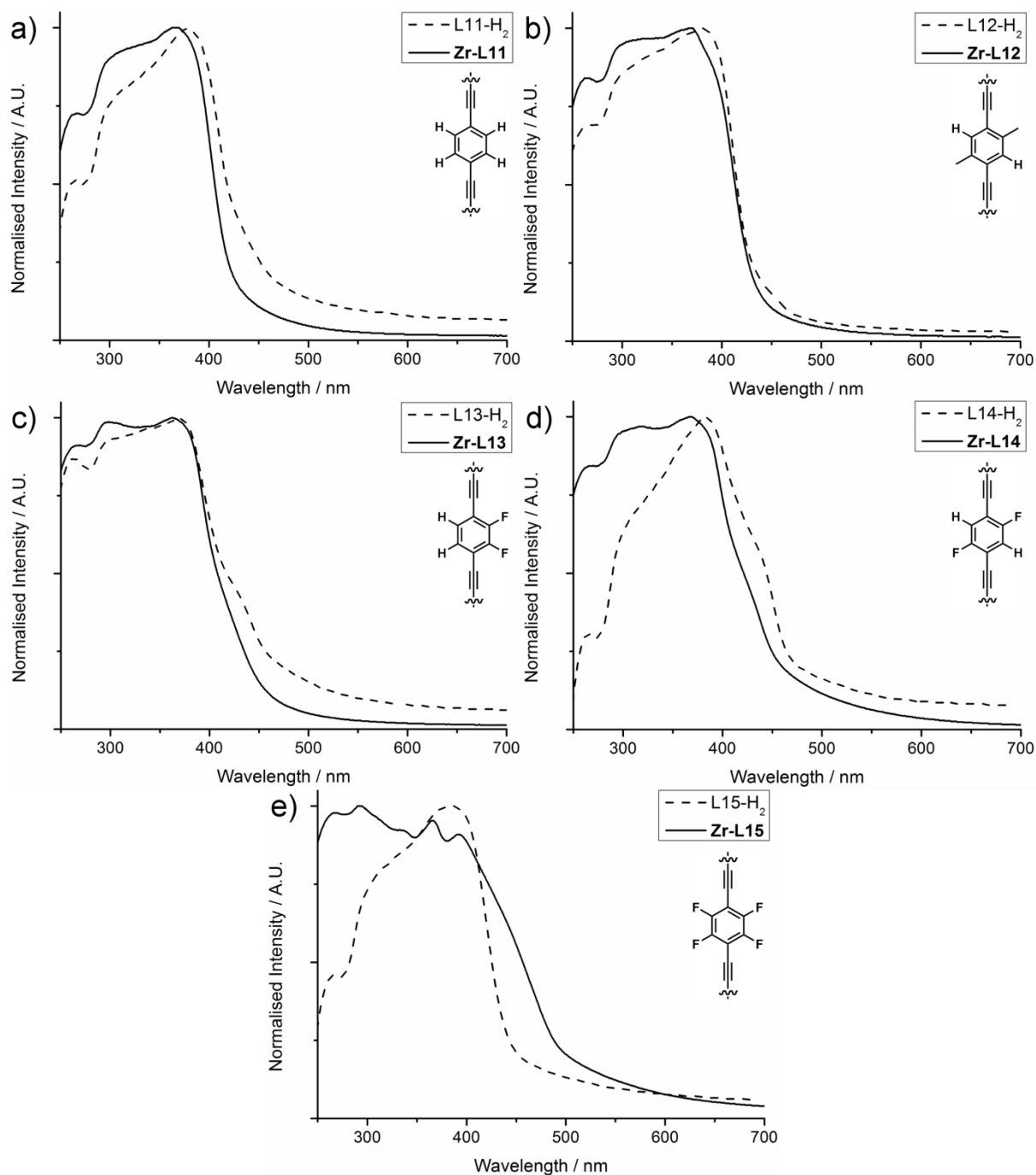


**Figure 4.17.** SS-UV-Vis absorption spectra of a) L11-H<sub>2</sub> and **Zr-L11**, b) L12-H<sub>2</sub> and **Zr-L12**, c) L13-H<sub>2</sub> and **Zr-L13**, d) L14-H<sub>2</sub> and **Zr-L14** and e) L15-H<sub>2</sub> and **Zr-L15**.

The absorption spectra of the ligands and the MOFs are generally in close agreement with some differences in intensity observed. The absorption of **Zr-L14** is more intense in the UV region compared with L14-H<sub>2</sub> while compared with L15-H<sub>2</sub> the absorption of **Zr-L15** is shifted into the visible region. The red-shift in absorbance of **Zr-L15** explains why bulk and single crystals samples of **Zr-L15** are a very intense yellow colour, compared with L15-H<sub>2</sub>

and **Zr-L11** which are white in appearance, thus proving the colour of **Zr-L15** is not typical of the interpenetrated MOFs or the tetrafluoro functionalised ligand. It should be noted that both bulk and single crystal samples of **Hf-L15** are also an intense yellow colour (Figure 4.18).

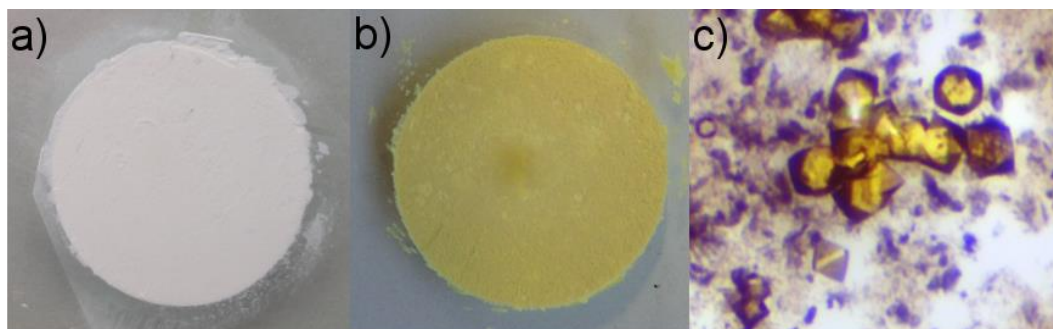


**Figure 4.18.** Photographs of bulk powders of a) **Zr-L11** and b) **Zr-L15** in glass sample holders for PXRD analysis and c) optical microscope image of single crystals ( $\sim 60\ \mu\text{m}$  in diameter) of **Hf-L15**.

It is not entirely obvious why Zr and Hf MOFs containing L15 are yellow; however, one hypothesis is that the solid state packing of L15- $\text{H}_2$  prevents absorption in the visible region. This is in contrast to the topological constraints of the Zr and Hf MOFs, where spatial separation of the ligands could effectively allow absorption in the visible region to occur. Characterisation of **Zr-L15** and **Hf-L15** does not suggest ligand degradation or the presence of impurities, and as the crystals do not lose their colour when immersed in fresh solvent it is apparent that the yellow colour of the MOFs is inherent. Bulk microcrystalline powders and single crystals of **Zr-L16** and **Zr-L17** are yellow in colour, although this is expected as the ligands contain well-known naphthalene and benzothiadiazole chromophores respectively.

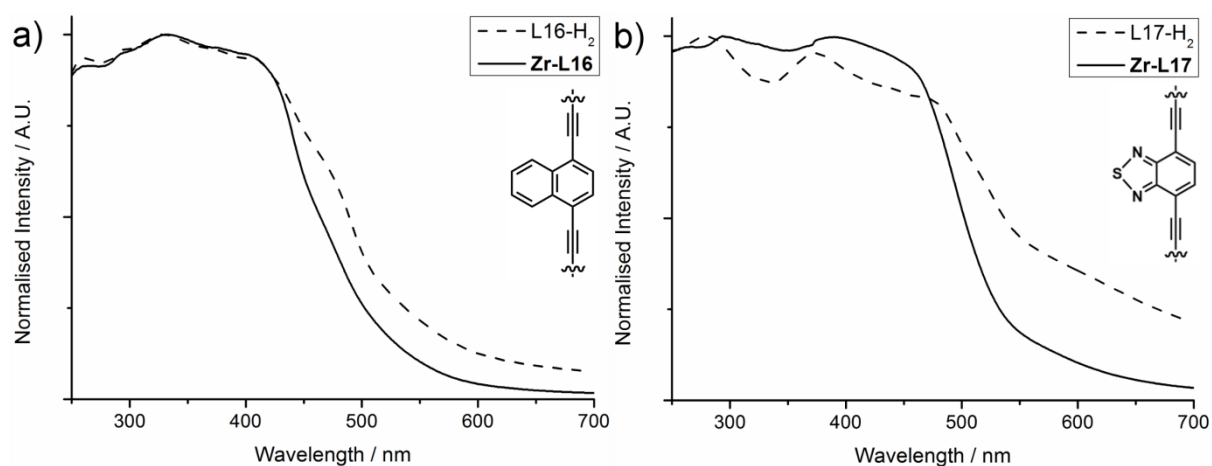


**Figure 4.19** Comparison of the SS-UV-Vis absorption spectra of a) L16-H<sub>2</sub> and **Zr-L16** and b) L17-H<sub>2</sub> and **Zr-L17**.

Comparison of the SS-UV-Vis spectra of **Zr-L16** and **Zr-L17** with the free acids of their respective ligands reveals that in both cases the absorbance of the MOFs is less intense in the visible region. However, both MOFs show broad absorption over the UV-Vis range and this is realised upon comparison of the SS-UV-Vis absorption spectra of the Zr MOFs (Figure 4.20).

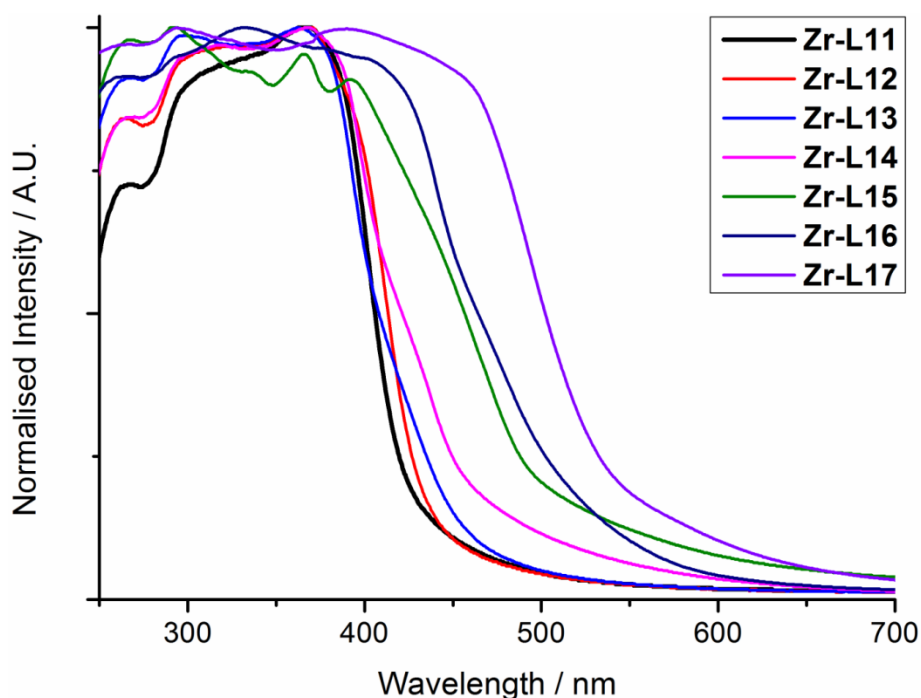


**Figure 4.20.** Comparison of the SS-UV-Vis absorption spectra of Zr MOFs containing L11-L17.

Comparing the UV-Vis absorption of the Zr MOFs it is clear that **Zr-L11**, **Zr-L12**, **Zr-L13** and **Zr-L14** do not absorb strongly in the visible region, and as the MOFs contain  $\text{Zr}^{4+}$  ions ( $d^0$ ) it is unsurprising that they are all lightly coloured. Meanwhile **Zr-L15**, **Zr-L16** and **Zr-L17** show broad absorption in the visible region with **Zr-L17** absorbing over the broadest range. The interesting optical properties of the Zr MOFs and the previously studied fluorescence of L11-Me<sub>2</sub><sup>16</sup> prompted us to investigate the solid state fluorescence behaviour of the MOFs under different experimental conditions.

#### 4.10 Solid State Fluorescence Emission Spectroscopy

Solid state fluorescence (herein termed fluorescence for simplification) emission spectroscopy was performed in collaboration with the Blight Group at the University of Kent. The materials were synthesised in Glasgow and shipped to the researchers who are experts in fluorescence spectroscopy. Both research groups were involved in the interpretation and presentation of the results. The interesting results obtained during this study are likely to lead to further collaboration as this technique has provided unprecedented levels of structural information that is discussed in detail throughout this section.

Fluorescence emission spectra of L11-H<sub>2</sub>, L12-H<sub>2</sub>, L15-H<sub>2</sub>, L16-H<sub>2</sub> and L17-H<sub>2</sub> were obtained under dry and wet conditions (Figure 4.21). Samples were wetted by addition of a drop of water onto solid samples and sandwiched between the slides of a quartz solid-state sample holder.

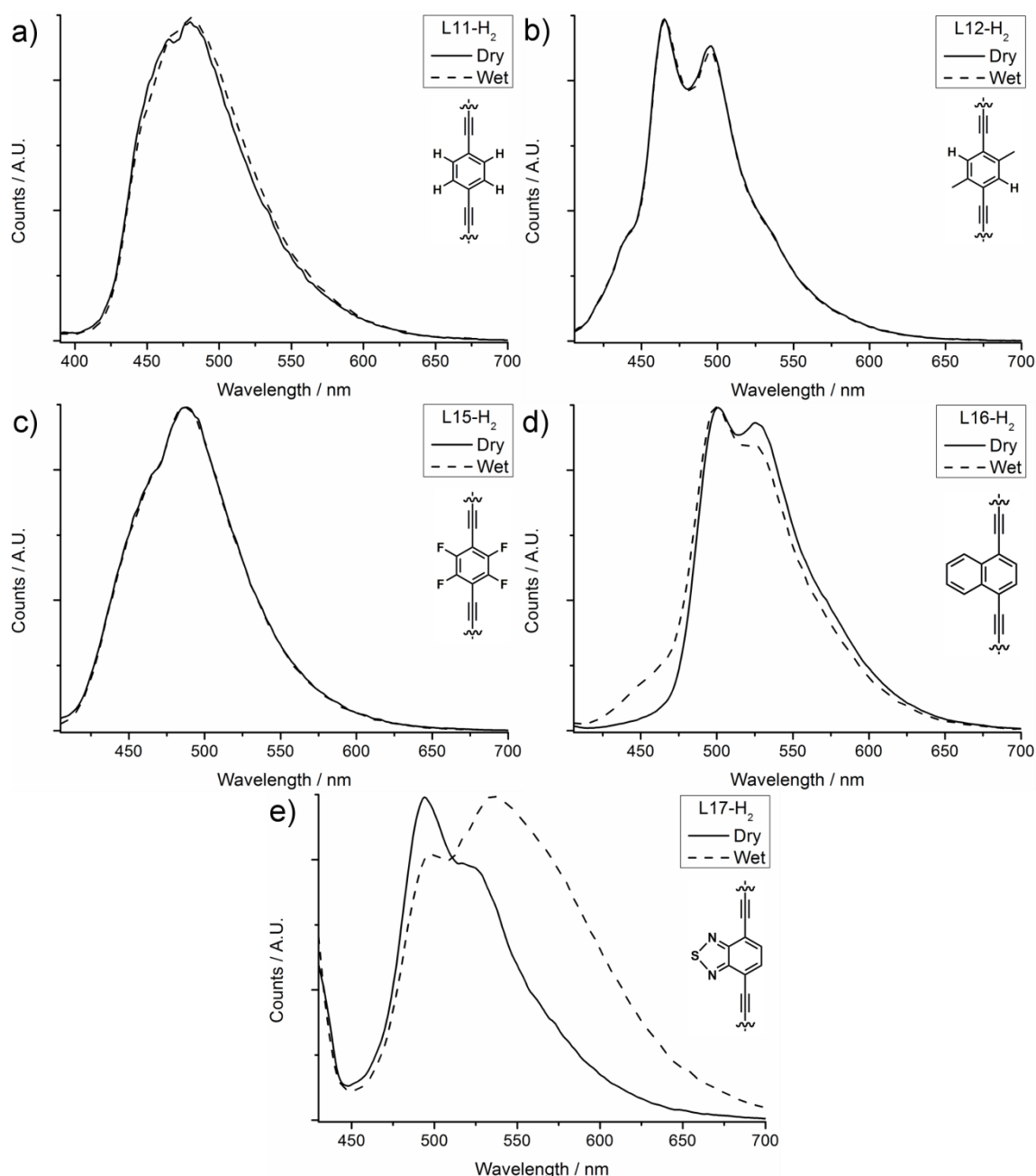


**Figure 4.21.** Fluorescence spectra of dry and wet samples of a) L11-H<sub>2</sub> ( $\lambda_{\text{ex}} = 380$  nm), b) L12-H<sub>2</sub> ( $\lambda_{\text{ex}} = 394$  nm), c) L15-H<sub>2</sub> ( $\lambda_{\text{ex}} = 395$  nm), d) L16-H<sub>2</sub> ( $\lambda_{\text{ex}} = 396$  nm) and e) L17-H<sub>2</sub> ( $\lambda_{\text{ex}} = 420$  nm).

There are only minor differences observed in the emission profiles of the ligands under dry and wet conditions. The intensity of one of the radiative processes of L16-H<sub>2</sub> decreased upon wetting, but overall both spectra closely resemble one another. In the case of L17-H<sub>2</sub>, which contains benzothiadiazole units that are well known fluorescent probes, direct wetting of the ligand results in a pronounced red-shift of the main fluorescence emission band from  $\lambda_{\text{max}} =$

494 nm to  $\lambda_{\text{max}} = 537$  nm. This is presumably due to differences in the solid state packing arrangement of the planar conjugated ligands or the interaction between water and the polar fluorophore. Fluorescence emission spectra were obtained for **Zr-L11**, **Zr-L12**, **Zr-L15**, **Zr-L16** and **Zr-L17** under a number of experimental conditions and in the presence of different chemical stimuli. Comparison of the fluorescence spectra of the dry Zr MOFs and their free ligands reveals that in some cases, coordination to the  $\text{Zr}_6$  clusters does not significantly affect the wavelengths of emission, while for **Zr-L11** and **Zr-L17** significant shifts are observed (see Appendix, Chapter 6, Figure 6.31).

The most pronounced differences in fluorescence emission of the MOFs, under the conditions examined, were observed between dry and wet samples of **Zr-L16** and **Zr-L17** (Figure 4.22). The emission spectra of the other MOFs are available in the Appendix, Chapter 6 Figure 6.32.

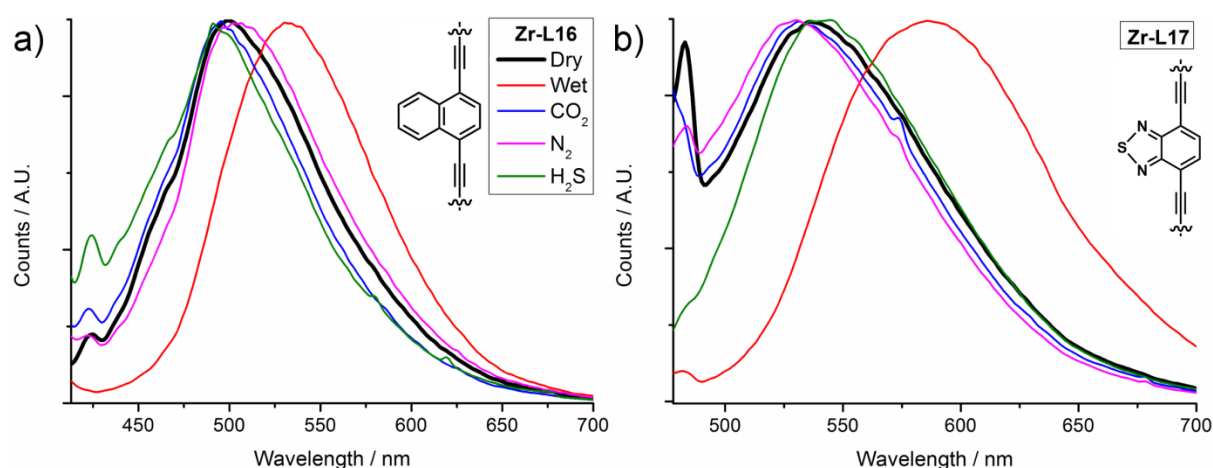


**Figure 4.22.** Fluorescence emission spectra of dry and wet samples of a) **Zr-L16** ( $\lambda_{\text{ex}} = 403$  nm) and b) **Zr-L17** ( $\lambda_{\text{ex}} = 468$  nm). Emission spectra were also recorded in the presence of gaseous  $\text{CO}_2$ ,  $\text{N}_2$  and  $\text{H}_2\text{S}$ . The legend is common to both comparisons.

**Zr-L16** shows pronounced changes in emission ( $\lambda_{\text{ex}} = 403$  nm) under dry and wet conditions, with an observed red-shift of  $\lambda_{\text{max}}$  from 499 nm to 531 nm (Figure 4.22a). **Zr-L17** also demonstrates dramatically different emission behaviour ( $\lambda_{\text{ex}} = 468$  nm) under dry and wet conditions, with a red-shift of  $\lambda_{\text{max}}$  from 537 nm to 586 nm (Figure 4.22b). Gaseous  $\text{CO}_2$ ,  $\text{N}_2$  and  $\text{H}_2\text{S}$  cause slight alterations to the fluorescence emission of **Zr-L16** and **Zr-L17**, however, for both MOFs the most sensitive response is observed upon wetting. Few studies have reported intrinsic fluorescence sensing of water by MOFs<sup>21,32,33</sup> although Zr MOFs are

ideal platforms for water sensing applications due to their well-known aqueous stability.<sup>34</sup> Comparing the fluorescence emission spectra of dry and wet samples of **Zr-L11** and **Zr-L15** it is clear that the two MOFs respond differently upon contact with water (Figure 4.23).

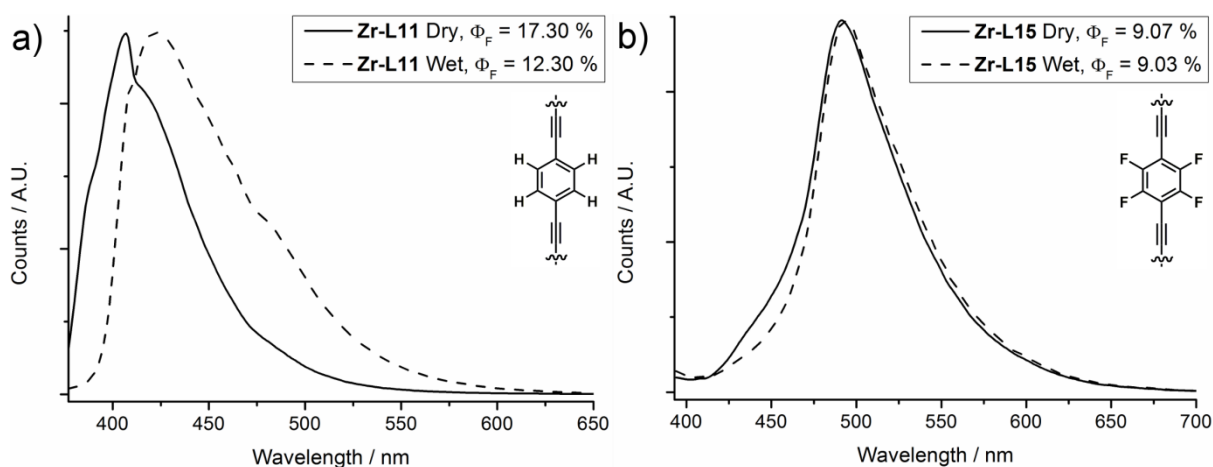


**Figure 4.23.** Fluorescence emission spectra of dry and wet samples of a) **Zr-L11** and b) **Zr-L15**.

The fluorescence emission of **Zr-L11** changes appreciably upon wetting with  $\lambda_{\text{max}}$  red-shifting from 407 nm to 423 nm and  $\Phi_F$  decreasing from 0.17 to 0.12. This is in stark contrast to **Zr-L15**, where the emission profiles are almost identical under dry and wet conditions and there is very little impact upon  $\Phi_F$ . **Zr-L15** contains pores partially lined with fluorine atoms and it is known that incorporation of fluorine atoms within MOFs can alter their hydrophobicity.<sup>35,36</sup> The fluorescence emission of **Zr-L15** likely does not change under dry and wet conditions due to the increased hydrophobicity of the material, preventing water from penetrating into and interacting with the framework. Contact angles were measured for **Zr-L11** and **Zr-L15** to determine whether differences in hydrophobicity are accountable for their different emission behaviours (Figure 4.24).



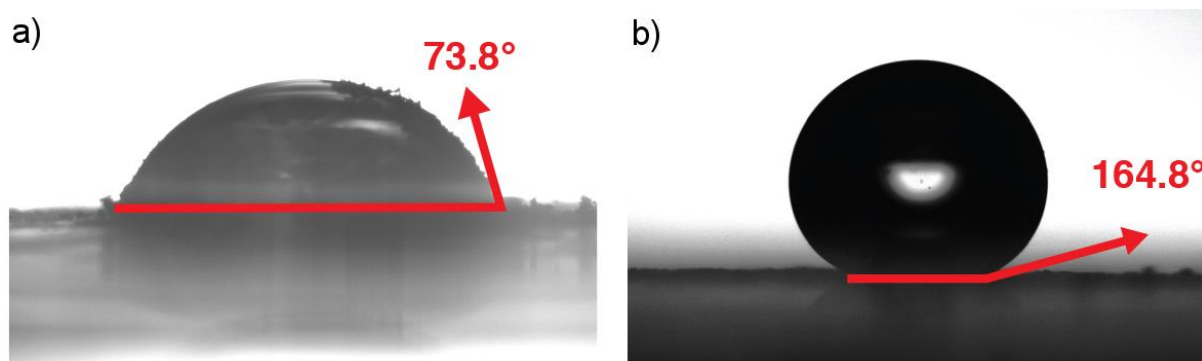


**Figure 4.24.** Contact angle measurements of water droplets on flattened surfaces of a) **Zr-L11** and b) **Zr-L15**.

**Zr-L11** has a contact angle of  $\sim 73.8^\circ$  indicative of a hydrophilic material, while **Zr-L15** has a contact angle of  $\sim 164.8^\circ$  typical of a superhydrophobic material (Figure 4.24).<sup>37</sup> These measurements show that small changes to the bridging organic ligand (substitution of only one third of the aromatic protons for fluorine's going from L11 to L15) can considerably alter the MOFs hydrophobicity. **Zr-L15** is a rare example of a stable carboxylate based fluorinated MOF<sup>38</sup> and other functionalised  $\text{peb}^{2-}$  ligands could be synthesised and incorporated into interpenetrated Zr MOFs to control their hydrophobicity.

The presence of two radiative transitions in the emission profile of **Zr-L12** (Figure 4.25) appears to be inherited from the ligand as two transitions are observed for L12-H<sub>2</sub> (Figure 4.21b). The two radiative transitions observed for **Zr-L12** are most likely due to different ligand conformations resulting from twisting of the central dimethylphenylene core as seen in its solid state structure (Figure 4.8), while the crystal structure of L12-Me<sub>2</sub> also reveals a twisting of the central dimethylphenylene core in the solid state (Figure 4.26, page 206).

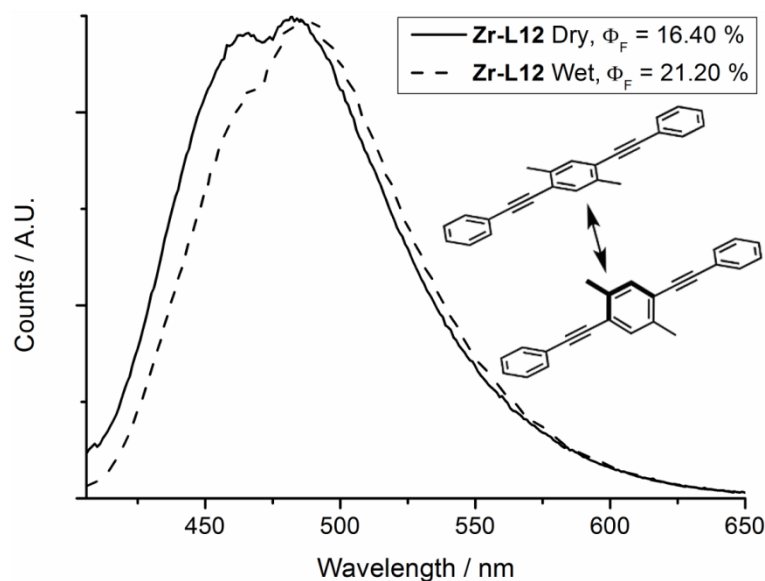


**Figure 4.25.** Solid state fluorescence emission of dry and wet samples of **Zr-L12** alongside a schematic representation of ligand twisting.

In comparison with the emission of **Zr-L12** when dry, the intensity of the transition at 465 nm decreases upon wetting. The decrease in intensity of the transition at 465 nm suggests that water causes a structural perturbation of the MOF, presumably by altering the degree of ligand twisting. The decrease in intensity of  $\lambda_{\text{max}} = 465$  nm and the increase in  $\Phi_F$  are indicative of a higher population of decay at  $\lambda_{\text{max}} = 486$  nm. Coupled with the observed transformation from the orthorhombic (twisted/planar ligands) to the cubic structure (planar ligands) under heating (see Section 4.6) this suggests that wetting results in an increase in population of the planar ligand conformation.

Solid state fluorescence emission spectroscopy has been used to probe the interpenetrated Zr MOFs, providing detailed information concerning their structures and properties. Fluorescence emission reveals differences in the MOFs hydrophobicity, whereby the fluorescence behaviour of **Zr-L15** does not change when hydrated due to its hydrophobic nature, while **Zr-L11** is hydrophilic and can be hydrated. These findings are confirmed by contact angle measurements. Incorporation of naphthalene and benzothiadiazole units within the MOFs results in large differences to their fluorescence behaviour upon wetting, suggesting their possible use as solid-state water sensors. Finally, rotation of the dimethylphenylene core in **Zr-L12** is detected using fluorescence, with changes to the relative intensities of the emission maxima observed upon hydration.

## 4.11 Conclusions and Future Work

In conclusion, a series of six functionalised ligands have been synthesised and incorporated into Zr and Hf MOFs isostructural with those containing the extended unfunctionalised  $\text{peb}^{2-}$  ligand (**Zr-L11** and **Hf-L11**). The ligands contain methyl, fluorine, naphthalene and benzothiadiazole functionality, resulting in interesting structural and physical properties. The L-proline modulation protocol successfully developed in Chapter 2 has been employed for the syntheses of the interpenetrated Zr and Hf MOFs, resulting in highly crystalline bulk powders and fine-tuning of conditions results in single crystals in most cases. Single crystal X-ray diffraction provides detailed structural analysis and allows interesting structural features of the MOFs to be observed. In the MOFs containing the difluorinated ligands disorder of the fluorine atoms across all 4 positions of the central phenylene core is observed, maintaining the cubic symmetry of the MOFs despite the lower symmetry of the ligands. In **Zr-L16** the central naphthalene core is disordered across two positions, while the ligand also twists out of the plane of conjugation by  $23^\circ$  presumably to minimise steric interactions. Interestingly, **Zr-L12** which contains pendant methyl groups does not crystallise with the expected octahedral symmetry, instead steric interactions between the frameworks results in 2/3 of the ligands adopting a twisted conformation.

$\text{N}_2$  uptake experiments reveal that the BET surface area of the MOFs decreases upon functional group incorporation, however **Zr-L16**, **Zr-L17** and **Hf-L17** demonstrate the potential to improve  $\text{CO}_2$  uptake. Solid state fluorescence spectroscopy has been used to determine the behaviour of the Zr MOFs in the presence of a number of analytes with highly sensitive emission changes of **Zr-L16** and **Zr-L17** upon wetting suggesting their possible use as water vapour sensors. The hydrophobicity/hydrophilicity of the MOFs results in different emission behaviours upon wetting and combined with contact angle measurements the superhydrophobicity of **Zr-L15** is confirmed.

Subtle differences to the ligand functionality have resulted in materials with a wide range of properties. Interestingly **Zr-L12** is dynamic and a twisting of the dimethylphenylene core is observed. The twisted conformation of the ligand is evident from the single crystal structure, resulting in a lowering of the symmetry from the expected  $Fd-3m$  space group to  $Imma$ . There are differences in the PXRD pattern of **Zr-L12** compared with the other MOFs to

reflect the change in symmetry, however upon heating the PXRD pattern transforms to match the expected cubic pattern indicating a phase change from the orthorhombic structure to the cubic structure. Variable temperature PXRD experiments confirm the change in structure upon heating and further that the process is not reversible upon cooling. The fluorescence emission of **Zr-L12** changes upon hydration, in terms of the relative intensity of emission maxima, and the change observed is indicative of a higher population of the planar ligand found in the cubic structure.

Solid-state fluorescence has rarely been used for the characterisation of MOFs, however we have found that it has been very effective for the characterisation of the interpenetrated Zr MOFs. To our surprise, fluorescence spectroscopy has revealed not only the potential of the MOFs for solid state sensing applications but it has also been used to map the structural perturbation of **Zr-L12** observed upon wetting. The unprecedented level of information obtained using this relatively simple technique highlights its potential use for the characterisation of MOFs and it is expected that it holds great potential for future studies.

Ligand functionalisation has altered the MOF's physical and structural properties, and it is therefore highly likely that the series of MOFs will display interesting host-host and host-guest behaviours. We have already discovered that **Hf-L11** undergoes a phase change in *n*-pentane at 1.4 GPa using high pressure single crystal X-ray diffraction (Figure 4.3). Together with the Moggach Group from the University of Edinburgh we are interested in probing the high pressure behaviours of the interpenetrated MOFs, both in contact with hydrostatic media and also in the presence of gases and investigations are currently underway.

## 4.12 Experimental

### 4.12.1 General Experimental Remarks

All chemicals and solvents were purchased from Alfa Aesar, Fisher Scientific, Maybridge, Fluorochem, Merck Millipore, Sigma-Aldrich, Strem Chemicals and VWR and used without further purification.

**Powder X-ray diffraction (PXRD):** PXRD measurements were carried out at 298 K using a PANalytical X'Pert PRO diffractometer ( $\lambda$  (CuK $\alpha$ ) = 1.5405 Å) on a mounted bracket sample stage. Data were collected over the range 3-45°. Variable temperature PXRD measurements were collected on the same diffractometer but equipped with an Anton Paar HTK 1200N high temperature oven chamber under a trickle flow of argon. PXRD patterns were predicted from single crystal data using Mercury 3.7.<sup>39</sup> (University of Glasgow)

**Single crystal X-ray diffraction (SCXRD):** Data for L11-Me<sub>2</sub>, L12-Me<sub>2</sub> and **Hf-L15** were collected using a Bruker ApexII CCD kappa goniometer with a Mo sealed tube source and equipped with an Oxford Cryosystems n-Helix device. Data for L13-Me<sub>2</sub>, L14-Me<sub>2</sub> and L15-Me<sub>2</sub> were collected using a Nonius Kappa CCD with a Mo sealed tube source and equipped with an Oxford Cryosystems cryostream device. (University of Glasgow)

Data for L14-H<sub>2</sub>, **Zr-L13**, **Hf-L13**, **Zr-L14**, **Hf-L14**, **Zr-L15**, **Zr-L16**, **Hf-L16**, **Zr-L17** and **Hf-L17** were collected using a Rigaku AFC12 goniometer equipped with an enhanced sensitivity (HG) Saturn724+ detector mounted at the window of an FR-E+ SuperBright molybdenum rotating anode generator with VHF Varimax optics (70 µm focus) equipped with an Oxford Cryosystems cryostream device. (EPSRC UK National Crystallography Service)

Data for **Zr-L12** was collected using a Rigaku Oxford Diffraction SuperNova goniometer equipped with a micro-focus Cu sealed tube source and a Pilatus 200K detector equipped with an Oxford Cryosystems cryostream device. (Rigaku Oxford Diffraction UK applications laboratory)

**Thermogravimetric analysis (TGA):** Measurements were carried out using a TA Instruments Q500 thermogravimetric analyser from room temperature to 800 °C with a heating rate of 10 °C/min under an air atmosphere. (University of Glasgow)

**Nuclear magnetic resonance spectroscopy (NMR):** NMR spectra were recorded on either a Bruker AVIII 400 MHz spectrometer or a Bruker AVI 500 MHz spectrometer and referenced to residual solvent peaks. (University of Glasgow)

**Gas uptake:** N<sub>2</sub> adsorption and desorption isotherms were carried out at 77 K on a Quantachrome Autosorb iQ gas sorption analyser. Samples were degassed under vacuum at 120 °C for 20 hours using the internal turbo pump. BET surface areas were calculated from the isotherms using the Micropore BET Assistant in the Quantachrome ASiQwin operating software. (University of Glasgow)

**Pore-size distribution:** Pore size distributions were calculated using the N<sub>2</sub> at 77 K on carbon (slit pore, QSDFT, equilibrium model) calculation model within the Quantachrome ASiQwin operating software. (University of Glasgow)

**Solid-state UV-Vis spectroscopy:** Solid-state UV-Vis spectra were recorded using a Shimadzu UV-2600 Spectrophotometer. Samples were prepared by evenly distributing small amounts of solid samples across a thin layer of BaSO<sub>4</sub>. Spectra were recorded over the range  $\lambda = 250\text{-}700$  nm. (University of Glasgow)

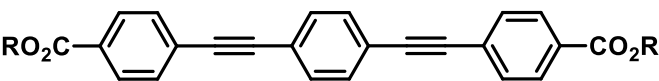
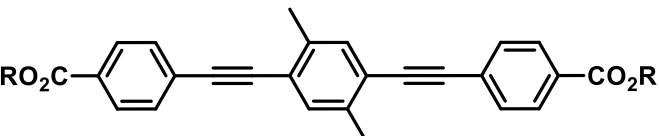
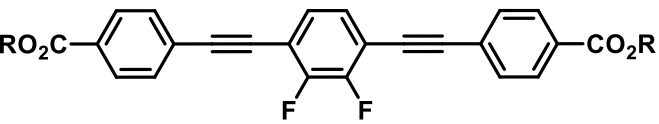
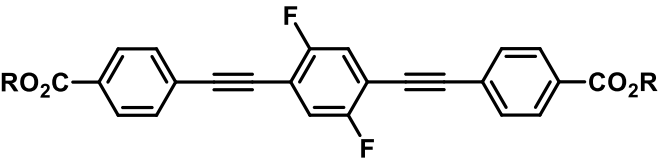
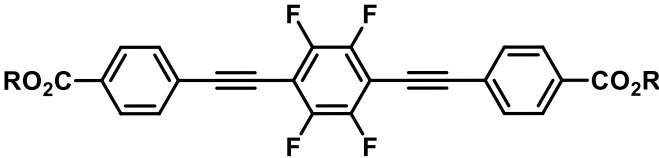
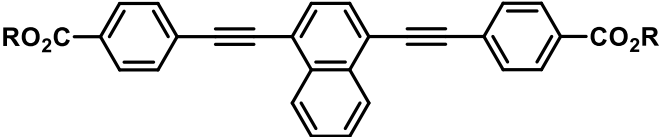
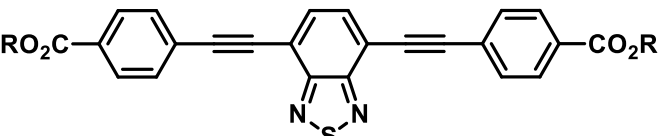
**Solid state fluorescence emission spectroscopy:** Fluorescence emission measurements were carried out using an Edinburgh Instruments FS5 Fluorescence Spectrometer. An SC-10 Front Face Sample Holder was used along with a solid-state cuvette. Solid-state quantum yields (QY) were also performed with the FS5, equipped with a standard xenon lamp (150 W) and a standard PMT detector (R928P, Hamamatsu). QY measurements were performed using SC-30 Integrating Sphere module, and reported values based on triple independent measurements. (University of Kent)

**Contact angle:** Contact angle measurements were performed using an Attension-Theta Optical Tensiometer (Biolin Scientific) at room temperature. Using a glass microscope slide

with a thin recess powdered sample was loaded into the recess and packed flat until level with the slide. Analysis was performed using the One-Attension software package. (University of Kent)

#### 4.12.2 Ligand Synthesis

The chemical structures and abbreviations of all ligands described throughout this chapter are detailed in Scheme 4.1.

	<b>R</b>	<b>Abbreviation</b>
	CH <sub>3</sub> H	L11-Me <sub>2</sub> L11-H <sub>2</sub>
	CH <sub>3</sub> H	L12-Me <sub>2</sub> L12-H <sub>2</sub>
	CH <sub>3</sub> H	L13-Me <sub>2</sub> L13-H <sub>2</sub>
	CH <sub>3</sub> H	L14-Me <sub>2</sub> L14-H <sub>2</sub>
	CH <sub>3</sub> H	L15-Me <sub>2</sub> L15-H <sub>2</sub>
	CH <sub>3</sub> H	L16-Me <sub>2</sub> L16-H <sub>2</sub>
	CH <sub>3</sub> H	L17-Me <sub>2</sub> L17-H <sub>2</sub>

**Scheme 4.1.** Schematic representation and abbreviations of the functionalised ligands synthesised for incorporation into interpenetrated Zr and Hf MOFs.

The syntheses of L11-Me<sub>2</sub>, L11-H<sub>2</sub>, methyl 4-(2-(trimethylsilyl)ethynyl)benzoate and methyl 4-ethynylbenzoate are described in detail in Chapter 2, Section 2.10.9. The dimethyl esters of L12-L17 were synthesised from commercially available aryl dihalides and methyl 4-ethynylbenzoate using conditions similar to those employed during the synthesis of L11-Me<sub>2</sub>.<sup>28</sup> Saponification of the esters resulted in the free acids of the ligands required for MOF syntheses.<sup>14</sup> Where possible <sup>13</sup>C NMR and high resolution mass spectrometry (HRMS) data are provided, however limited solubility in some cases prevented reliable spectra from being obtained.

### L12-Me<sub>2</sub>

Methyl 4-ethynylbenzoate (0.785 g, 4.90 mmol, 2.5 eq) and 1,4-diiodo-2,5-dimethylbenzene (0.700 g, 1.95 mmol, 1.0 eq) were dissolved in TEA (50 ml) by stirring. The solution was degassed for 20 minutes before bis(triphenylphosphine)palladium(II) dichloride (0.091 g, 0.13 mmol) and copper(I) iodide (0.021 g, 0.11 mmol) were added. The reaction mixture was left to stir at 50 °C overnight under an N<sub>2</sub> atmosphere. The mixture was removed from the heat and once cooled to room temperature the product was collected by vacuum filtration and washed with hexane until the washings were colourless. The product was stirred for ~2.5 hours in water (100 ml) then collected by vacuum filtration. The product was stirred in a minimal volume of DCM, collected by vacuum filtration and dried under vacuum (0.763 g, 1.81 mmol, 92%). <sup>1</sup>H NMR (CDCl<sub>3</sub>): δ/ppm 2.48 (s, 6H), 3.94 (s, 6H), 7.40 (s, 2H), 7.59 (d, 4H, *J* = 8.6 Hz), 8.03 (d, 4H, *J* = 8.6 Hz); HRMS (EI) calculated for C<sub>28</sub>H<sub>22</sub>O<sub>4</sub> (M)<sup>+</sup> 422.1518, found *m/z* 422.1514.

Single crystals of L12-Me<sub>2</sub> were isolated from an NMR solution upon slow evaporation of CDCl<sub>3</sub> (Figure 4.26).

Crystal data for L12-Me<sub>2</sub>. C<sub>28</sub>H<sub>22</sub>O<sub>4</sub>, *M<sub>r</sub>* = 422.45, crystal dimensions 0.80 x 0.15 x 0.06 mm, Monoclinic, *a* = 22.921 (8) Å, *b* = 3.8910 (12) Å, *c* = 11.720 (4) Å, β = 90.017 (9)°, *V* = 1045.3 (6) Å<sup>3</sup>, *T* = 100 K, space group *P*2<sub>1</sub>/*c* (no. 14), *Z* = 2, 9063 measured reflections, 1813 unique (*R*<sub>int</sub> = 0.087), which were used in all calculations. The final *R*<sub>I</sub> = 0.060 for 1561 observed data [*R*(*F*<sup>2</sup> > 2σ(*F*<sup>2</sup>))] and *wR*(*F*<sup>2</sup>) = 0.157 (all data). Crystal structure data for L12-Me<sub>2</sub> is available from the CCDC, deposition number 1516207.



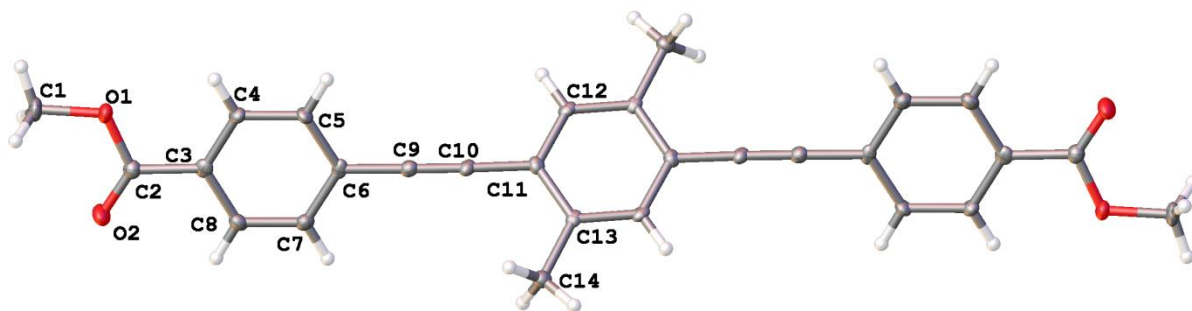


**Figure 4.26.** Solid state structure and atom labelling scheme (labels for asymmetric unit only) of L12-Me<sub>2</sub>. Displacement ellipsoids are drawn at 50% probability level.

### L12-H<sub>2</sub>

L12-Me<sub>2</sub> (1.091 g, 2.58 mmol, 1.0 eq) was suspended in THF (250 ml) by stirring. Sodium hydroxide (1.045 g, 26.10 mmol, 10.1 eq) was dissolved separately in water (250 ml) and added to the round bottom flask containing the diester. The resulting solution was allowed to reflux overnight at 85 °C. The transparent solution was removed from the heat and allowed to cool to room temperature then the volume was reduced by removing part of the THF under reduced pressure. The product was precipitated by addition of 6 M HCl (aq) and collected by centrifugation. The product was rinsed continuously with water until the washings were pH neutral and then washed with acetone (2 x 20 ml). The light coloured solid was dried under vacuum (0.916 g, 2.32 mmol, 90%). <sup>1</sup>H NMR (DMSO-*d*<sub>6</sub>): δ/ppm 2.45 (s, 6H), 7.52 (s, 2H), 7.68 (d, 4H, *J* = 8.4 Hz), 7.98 (d, 4H, *J* = 8.4 Hz) 13.2 (br s, 2H); <sup>13</sup>C NMR (DMSO-*d*<sub>6</sub>): δ/ppm 19.5 (CH<sub>3</sub>), 90.4 (C), 94.1 (C), 122.4 (C), 126.5 (C), 129.6 (CH), 130.9 (C), 131.5 (CH), 132.7 (CH), 137.5 (C), 166.7 (C); HRMS (EI) calculated for C<sub>26</sub>H<sub>18</sub>O<sub>4</sub> (M)<sup>+</sup> 394.1204, found *m/z* 394.1207.

### L13-Me<sub>2</sub>

Methyl 4-ethynylbenzoate (0.774 g, 4.83 mmol, 2.1 eq) was dissolved in DMF/TEA (1:1, 130 ml) by stirring. The solution was degassed for 20 minutes before bis(triphenylphosphine)palladium(II) dichloride (0.116 g, 0.17 mmol), copper(I) iodide (0.026 g, 0.14 mmol) and 1,4-dibromo-2,3-difluorobenzene (0.625 g, 2.30 mmol, 1.0 eq) were added. The solution was left to stir at 80 °C overnight under an N<sub>2</sub> atmosphere. The mixture was removed from the heat and once cooled to room temperature the product precipitated upon addition of water (100 ml). The product was collected by vacuum filtration, washing with water, hexane and a minimal volume of DCM. The product was dried under

vacuum (0.700 g, 1.63 mmol, 71%).  $^1\text{H}$  NMR ( $\text{CDCl}_3$ ):  $\delta/\text{ppm}$  3.94 (s, 6H), 7.27 (m, 2H), 7.63 (d, 4H,  $J = 8.3$  Hz), 8.05 (d, 4H,  $J = 8.3$  Hz);  $^{13}\text{C}$  NMR ( $\text{CDCl}_3$ ):  $\delta/\text{ppm}$  52.5 ( $\text{CH}_3$ ), 84.2 (C), 96.6 (C), 114.2 (C), 126.9 (C), 127.8 (CH), 129.8 (CH), 130.5 (C), 131.9 (CH), 151.2 (CF), 166.5 (C); HRMS (EI) calculated for  $\text{C}_{26}\text{H}_{16}\text{F}_2\text{O}_4$  ( $\text{M}$ ) $^+$  430.1017, found  $m/z$  430.1030.

Single crystals of L13-Me<sub>2</sub> were isolated from an NMR solution upon slow evaporation of  $\text{CDCl}_3$  (Figure 4.27).

Crystal data for L13-Me<sub>2</sub>.  $\text{C}_{26}\text{H}_{16}\text{F}_2\text{O}_4 \cdot \text{CHCl}_3$ ,  $M_r = 549.76$ , crystal dimensions 0.62 x 0.08 x 0.06 mm, Monoclinic,  $a = 22.110$  (4) Å,  $b = 8.8384$  (13) Å,  $c = 12.3459$  (19) Å,  $\beta = 96.987$  (6)°,  $V = 2394.6$  (6) Å<sup>3</sup>,  $T = 100$  K, space group  $P2_1/c$  (no. 14),  $Z = 4$ , 27885 measured reflections, 4269 unique ( $R_{\text{int}} = 0.052$ ), which were used in all calculations. The final  $R_1 = 0.047$  for 3388 observed data [ $F^2 > 2\sigma(F^2)$ ] and  $wR(F^2) = 0.123$  (all data). Crystal structure data for L13-Me<sub>2</sub> is available from the CCDC, deposition number 1516208.

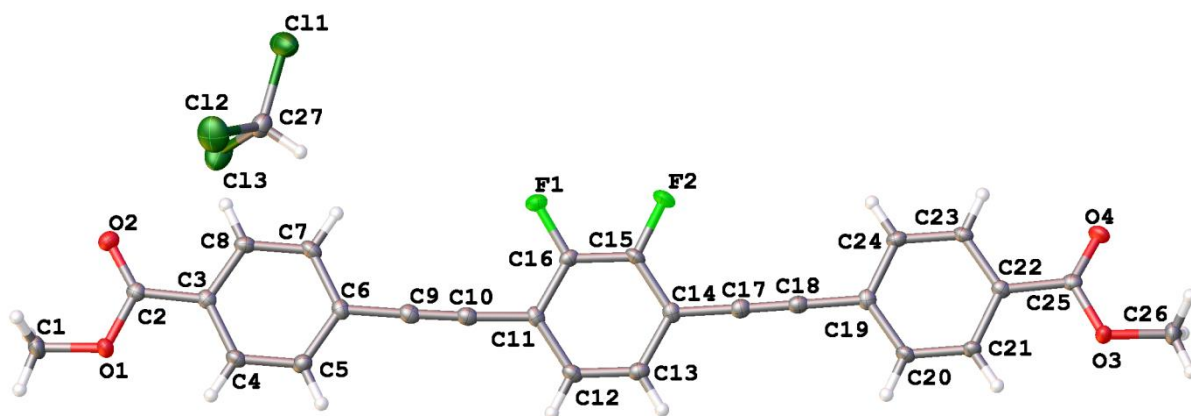


**Figure 4.27.** Solid state structure and atom labelling scheme of L13-Me<sub>2</sub>. Displacement ellipsoids are drawn at 50% probability level.

### L13-H<sub>2</sub>

L13-Me<sub>2</sub> (0.480 g, 1.12 mmol, 1.0 eq) was suspended in THF (125 ml) by stirring. Sodium hydroxide (0.490 g, 12.25 mmol, 10.9 eq) was dissolved separately in water (125 ml) and added to the round bottom flask containing the diester. The resulting solution was allowed to reflux overnight at 75 °C. The transparent solution was removed from the heat and allowed to cool to room temperature. The solution was gravity filtered and the product precipitated upon addition of 2 M HCl (aq). The product was isolated by centrifugation and rinsed multiple

times with water until the washings were pH neutral and then washed with acetone (10 ml). The product was dried under vacuum (0.427 g, 1.06 mmol, 95%).  $^1\text{H}$  NMR ( $\text{DMSO-}d_6$ ):  $\delta/\text{ppm}$  7.55 (dd, 2H,  $J = 3.0$  Hz, 1.6 Hz), 7.72 (d, 4H,  $J = 8.5$  Hz), 8.00 (d, 4H,  $J = 8.5$  Hz), 13.25 (br s, 2H);  $^{13}\text{C}$  NMR ( $\text{DMSO-}d_6$ ):  $\delta/\text{ppm}$  83.5 (C), 96.5 (C), 113.2 (C), 125.3 (C), 128.6 (CH), 129.7 (CH), 131.5 (C), 131.8 (CH), 150.0 (CF), 166.6 (C); HRMS (EI) calculated for  $\text{C}_{24}\text{H}_{12}\text{F}_2\text{O}_4$  ( $\text{M}$ ) $^+$  402.0704, found  $m/z$  402.0707.

### L14-Me<sub>2</sub>

Methyl 4-ethynylbenzoate (0.619 g, 3.86 mmol, 2.1 eq) was dissolved in DMF/TEA (1:1, 100 ml) by stirring. The solution was degassed for 20 minutes before bis(triphenylphosphine)palladium(II) dichloride (0.093 g, 0.13 mmol), copper(I) iodide (0.021 g, 0.11 mmol) and 1,4-dibromo-2,5-difluorobenzene (0.500 g, 1.84 mmol, 1.0 eq) were added. The solution was left to stir at 80 °C overnight under an  $\text{N}_2$  atmosphere. The mixture was removed from the heat and, once cooled to room temperature, the product precipitated upon addition of water (100 ml). The light coloured solid was collected by vacuum filtration, washing with water, hexane and a minimal volume of DCM. The product was dried under vacuum (0.573 g, 1.33 mmol, 72%).  $^1\text{H}$  NMR ( $\text{CDCl}_3$ ):  $\delta/\text{ppm}$  3.94 (s, 6H), 7.26 (m, 2H), 7.62 (d, 4H,  $J = 8.5$  Hz), 8.05 (d, 4H,  $J = 8.5$  Hz); HRMS (EI) calculated for  $\text{C}_{26}\text{H}_{16}\text{F}_2\text{O}_4$  ( $\text{M}$ ) $^+$  430.1017, found  $m/z$  430.1030.

Single crystals of L14-Me<sub>2</sub> were isolated from an NMR solution upon slow evaporation of  $\text{CDCl}_3$  (Figure 4.28).

Crystal data for L14-Me<sub>2</sub>.  $2(\text{C}_{13}\text{H}_8\text{FO}_2)$ ,  $M_r = 430.39$ , crystal dimensions 0.48 x 0.16 x 0.15 mm, Triclinic,  $a = 6.731$  (2) Å,  $b = 8.064$  (3) Å,  $c = 18.313$  (6) Å,  $\alpha = 88.061$  (10)°,  $\beta = 86.847$  (9)°,  $\gamma = 83.466$  (9)°,  $V = 985.6$  (6) Å<sup>3</sup>,  $T = 100$  K, space group  $P-1$  (no. 2),  $Z = 2$ , 15630 measured reflections, 15546 unique ( $R_{\text{int}} = 0.073$ ), which were used in all calculations. The final  $R_I = 0.092$  for 8625 observed data  $R[F^2 > 2\sigma(F^2)]$  and  $wR(F^2) = 0.265$  (all data). Crystal structure data for L14-Me<sub>2</sub> is available from the CCDC, deposition number 1516210.

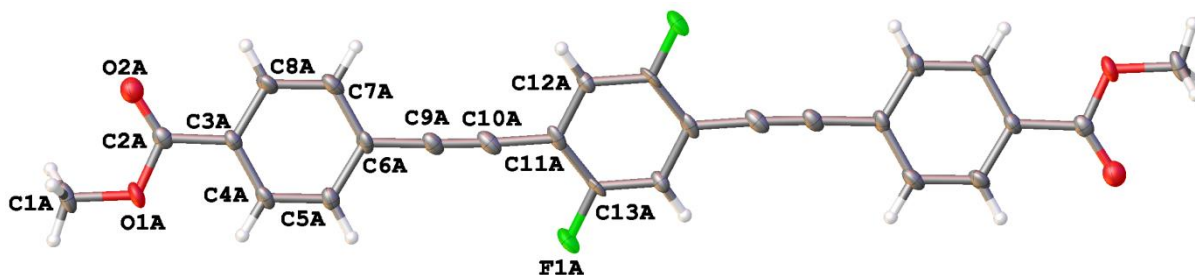


**Figure 4.28.** Solid state structure and atom labelling scheme of L14-Me<sub>2</sub>. The asymmetric unit contains two half molecules, labelling shown for independent atoms of one only, second molecule has label suffix B. Displacement ellipsoids are drawn at 50% probability level.

### L14-H<sub>2</sub>

L14-Me<sub>2</sub> (0.697 g, 1.62 mmol, 1.0 eq) was suspended in THF (185 ml) by stirring. Sodium hydroxide (0.648 g, 16.20 mmol, 10.0 eq) was dissolved separately in water (185 ml) and added to the round bottom flask containing the diester. The resulting solution was allowed to reflux overnight at 75 °C. The transparent solution was removed from the heat and allowed to cool to room temperature. The solution was gravity filtered and the product precipitated upon addition of 2 M HCl (aq). The product was isolated by centrifugation and rinsed multiple times with water until the washings were pH neutral. The pale yellow solid was then washed with acetone (2 x 25 ml), collected by centrifugation, and dried under vacuum (0.621 g, 1.54 mmol, 95%). <sup>1</sup>H NMR (DMSO-*d*<sub>6</sub>): δ/ppm 7.71 (d, 4H, *J* = 8.6 Hz), 7.76 (t, 2H, *J* = 7.6 Hz), 8.00 (d, 4H, *J* = 8.6 Hz), 13.22 (br s, 2H); <sup>13</sup>C NMR (DMSO-*d*<sub>6</sub>): δ/ppm 83.8 (C), 96.2 (C), 112.6 (C), 120.0 (CH), 125.3 (C), 129.7 (CH), 131.5 (C), 131.8 (CH), 157.8 (CF), 166.6 (C); HRMS (EI) calculated for C<sub>24</sub>H<sub>12</sub>F<sub>2</sub>O<sub>4</sub> (M)<sup>+</sup> 402.0704, found *m/z* 402.0703.

Single crystals of L14-H<sub>2</sub> were isolated from the DMF solution remaining after **Hf-L14** synthesis (Figure 4.29).

Crystal data for L14-H<sub>2</sub>. C<sub>24</sub>H<sub>12</sub>F<sub>2</sub>O<sub>4</sub>·2(C<sub>3</sub>H<sub>7</sub>NO), *M<sub>r</sub>* = 548.53, crystal dimensions 0.07 x 0.06 x 0.02 mm, Triclinic, *a* = 9.5707 (3) Å, *b* = 11.0072 (4) Å, *c* = 13.7230 (5) Å, α = 74.409 (3)°, β = 74.790 (3)°, γ = 75.265 (3)°, *V* = 1317.16 (9) Å<sup>3</sup>, *T* = 100 K, space group *P*-1 (no. 2), *Z* = 2, 22023 measured reflections, 6070 unique (*R*<sub>int</sub> = 0.041), which were used in all calculations. The final *R*<sub>*I*</sub> = 0.048 for 4437 observed data [*R*(*F*<sup>2</sup> > 2σ(*F*<sup>2</sup>))] and *wR*(*F*<sup>2</sup>) = 0.126 (all data). Crystal structure data for L14-H<sub>2</sub> is available from the CCDC, deposition number 1516209.

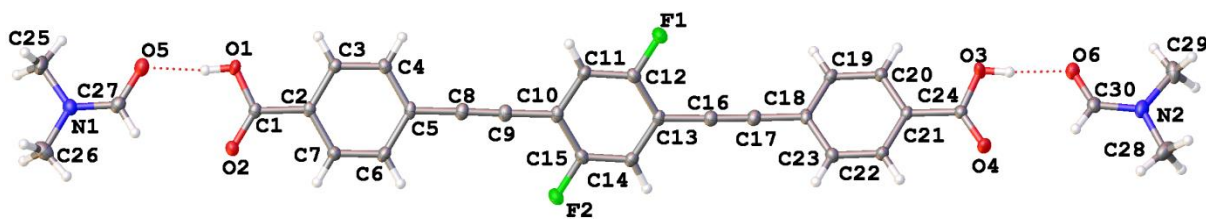


**Figure 4.29.** Solid state structure and atom labelling scheme of L14-H<sub>2</sub>. Displacement ellipsoids are drawn at 50% probability level.

### L15-Me<sub>2</sub>

Methyl 4-ethynylbenzoate (0.841 g, 5.25 mmol, 2.1 eq) was dissolved in TEA (100 ml) by stirring. The solution was degassed for 20 minutes before bis(triphenylphosphine)palladium(II) dichloride (0.126 g, 0.18 mmol), copper(I) iodide (0.029 g, 0.15 mmol) and 1,4-diiodotetrafluorobenzene (1.005 g, 2.50 mmol, 1.0 eq) were added. The reaction mixture was left to stir at 50 °C overnight under an N<sub>2</sub> atmosphere. The mixture was removed from the heat and once cooled to room temperature the product was collected by vacuum filtration, washing with water then hexane until the washings were colourless. The product was stirred in DCM (25 ml) then collected by vacuum filtration and dried under vacuum (1.057 g, 2.27 mmol, 91%). <sup>1</sup>H NMR (CDCl<sub>3</sub>): δ/ppm 3.95 (s, 6H), 7.67 (d, 4H, *J* = 8.5 Hz), 8.07 (d, 4H, *J* = 8.5 Hz); HRMS (EI) calculated for C<sub>26</sub>H<sub>14</sub>F<sub>4</sub>O<sub>4</sub> (M)<sup>+</sup> 466.0828, found *m/z* 466.0845.

Single crystals of L15-Me<sub>2</sub> were isolated from an NMR solution upon slow evaporation of CDCl<sub>3</sub> (Figure 4.30).

Crystal data for L15-Me<sub>2</sub>. C<sub>26</sub>H<sub>14</sub>F<sub>4</sub>O<sub>4</sub>, *M<sub>r</sub>* = 466.37, crystal dimensions 0.6 x 0.14 x 0.03 mm, Monoclinic, *a* = 17.248 (12) Å, *b* = 4.784 (3) Å, *c* = 12.021 (8) Å, β = 93.881 (19)°, *V* = 989.6 (11) Å<sup>3</sup>, *T* = 100 K, space group *P*2<sub>1</sub>/*c* (no. 14), *Z* = 2, 8314 measured reflections, 1450 unique (*R*<sub>int</sub> = 0.0728), which were used in all calculations. The final *R*<sub>*I*</sub> = 0.130 for 869 observed data [*R*[*F*<sup>2</sup> > 2σ(*F*<sup>2</sup>)] and *wR*(*F*<sup>2</sup>) = 0.406 (all data). Crystal structure data for L15-Me<sub>2</sub> is available from the CCDC, deposition number 1516211.



**Figure 4.30.** Solid state structure and atom labelling scheme (labels for asymmetric unit only) of L15-Me<sub>2</sub>. Displacement ellipsoids are drawn at 50% probability level.

### L15-H<sub>2</sub>

L15-Me<sub>2</sub> (0.950 g, 2.04 mmol, 1.0 eq) was suspended in THF (250 ml) by stirring. Sodium hydroxide (0.839 g, 20.98 mmol, 10.3 eq) was dissolved separately in water (250 ml) and added to the round bottom flask containing the diester. The resulting solution was allowed to reflux overnight at 75 °C. The transparent solution was removed from the heat and allowed to cool to room temperature. The solution was gravity filtered and the product precipitated upon addition of 6 M HCl (aq). The product was isolated by centrifugation and rinsed multiple times with water until the washings were pH neutral. The light coloured solid was washed with acetone (2 x 20 ml), collected by centrifugation, and dried under vacuum (0.864 g, 1.97 mmol, 97%). <sup>1</sup>H NMR (DMSO-*d*<sub>6</sub>): δ/ppm 7.77 (d, 4H, *J* = 8.3 Hz), 8.03 (d, 4H, *J* = 8.3 Hz), 13.32 (br s, 2H); HRMS (EI) calculated for C<sub>24</sub>H<sub>10</sub>F<sub>4</sub>O<sub>4</sub> (M)<sup>+</sup> 438.0515, found *m/z* 438.0521.

### L16-Me<sub>2</sub>

Methyl 4-ethynylbenzoate (0.618 g, 3.86 mmol, 2.1 eq) was dissolved in DMF/TEA (1:1, 100 ml) by stirring. The solution was degassed for 20 minutes before bis(triphenylphosphine)palladium(II) dichloride (0.093 g, 0.13 mmol), copper(I) iodide (0.021 g, 0.11 mmol) and 1,4-dibromonaphthalene (0.526 g, 1.84 mmol, 1.0 eq) were added. The solution was left to stir at 80 °C overnight under an N<sub>2</sub> atmosphere. The mixture was removed from the heat and, once cooled to room temperature, the product precipitated upon addition of water (100 ml). The product was collected by vacuum filtration, washing with water then hexane. The product was dried under vacuum (0.604 g, 1.36 mmol, 74%). <sup>1</sup>H NMR (CDCl<sub>3</sub>): δ/ppm 3.95 (s, 6H), 7.68 (dd, 2H, *J* = 6.4 Hz, 3.3 Hz), 7.71 (4H, d, *J* = 8.5 Hz), 7.76 (s, 2H), 8.08 (d, 4H, *J* = 8.5 Hz), 8.46 (dd, 2H, *J* = 6.4 Hz, 3.3 Hz); <sup>13</sup>C NMR (CDCl<sub>3</sub>): δ/ppm 52.4 (CH<sub>3</sub>), 90.5 (C), 95.5 (C), 121.6 (C), 126.7 (CH), 127.7 (CH), 127.9

(C), 129.8 (CH), 130.0 (C), 130.2 (CH), 131.7 (CH), 133.1 (C), 166.7 (C); HRMS (EI) calculated for  $C_{30}H_{20}O_4$  (M)<sup>+</sup> 444.1362, found  $m/z$  444.1363.

### L16-H<sub>2</sub>

L16-Me<sub>2</sub> (0.590 g, 1.33 mmol, 1.0 eq) was suspended in THF (140 ml) by stirring. Sodium hydroxide (0.551 g, 13.78 mmol, 10.4 eq) was dissolved separately in water (140 ml) and added to the round bottom flask containing the diester. The resulting solution was allowed to reflux overnight at 75 °C. The transparent solution was removed from the heat and allowed to cool to room temperature. The solution was gravity filtered and the product precipitated upon addition of 2 M HCl (aq). The product was isolated by centrifugation and rinsed multiple times with water until the washings were pH neutral. The yellow solid was washed with acetone (2 x 20 ml), collected by centrifugation, and dried under vacuum (0.479 g, 1.15 mmol, 86%). <sup>1</sup>H NMR (DMSO-*d*<sub>6</sub>): δ/ppm 7.81 (dd, 2H, *J* = 6.4 Hz, 3.3 Hz), 7.84 (d, 4H, *J* = 8.5 Hz), 7.90 (s, 2H), 8.03 (d, 4H, *J* = 8.5 Hz), 8.47 (dd, 2H, *J* = 6.4 Hz, 3.3 Hz), 13.22 (br s, 2H); <sup>13</sup>C NMR (DMSO-*d*<sub>6</sub>): δ/ppm 89.5 (C), 95.6 (C), 120.7 (C), 126.2 (CH), 126.3 (C), 128.4 (CH), 129.7 (CH), 130.4 (CH), 131.0 (C), 131.8 (CH), 132.3 (C), 166.7 (C).

### L17-Me<sub>2</sub>

Methyl 4-ethynylbenzoate (0.629 g, 3.93 mmol, 2.1 eq) was dissolved in DMF/TEA (1:1, 110 ml) by stirring. The solution was degassed for 20 minutes before bis(triphenylphosphine)palladium(II) dichloride (0.095 g, 0.14 mmol), copper(I) iodide (0.022 g, 0.12 mmol) and 4,7-dibromo-2,1,3-benzothiadiazole (0.550 g, 1.87 mmol, 1.0 eq) were added. The solution was left to stir at 80 °C overnight under an N<sub>2</sub> atmosphere. The mixture was removed from the heat and, once cooled to room temperature, the product precipitated upon addition of water (100 ml). The product was collected by vacuum filtration, washing with water, hexane and a minimal volume of DCM. The product was dried under vacuum (0.737 g, 1.63 mmol, 87%). <sup>1</sup>H NMR (CDCl<sub>3</sub>): δ/ppm 3.95 (s, 6H), 7.74 (d, 4H, *J* = 8.4 Hz), 7.84 (s, 2H), 8.08 (d, 2H, *J* = 8.4 Hz); <sup>13</sup>C NMR (CDCl<sub>3</sub>): δ/ppm 52.5 (CH<sub>3</sub>), 88.0 (C), 96.9 (C), 117.3 (C), 127.2 (C), 129.8 (CH), 130.5 (C), 132.1 (CH), 132.9 (CH), 154.4 (C), 166.6 (C); HRMS (EI) calculated for  $C_{26}H_{16}N_2O_4S$  (M)<sup>+</sup> 452.0831, found  $m/z$  452.0840.

### L17-H<sub>2</sub>

L17-Me<sub>2</sub> (0.737 g, 1.63 mmol, 1.0 eq) was suspended in THF (275 ml) by stirring. Sodium hydroxide (0.652 g, 16.30 mmol, 10.0 eq) was dissolved separately in water (275 ml) and

added to the round bottom flask containing the diester. The resulting solution was allowed to reflux overnight at 75 °C. The transparent solution was removed from the heat and allowed to cool to room temperature. The solution was gravity filtered and the product precipitated upon addition of 2 M HCl (aq). The product was isolated by centrifugation and rinsed multiple times with water until the washings were pH neutral. The yellow solid was washed with acetone (2 x 20 ml), collected by centrifugation and dried under vacuum (0.685 g, 1.61 mmol, 99%).  $^1\text{H}$  NMR (DMSO- $d_6$ ):  $\delta$ /ppm 7.78 (d, 4H,  $J$  = 8.4 Hz), 8.04 (d, 4H,  $J$  = 8.4 Hz), 8.04 (s, 2H), 13.21 (br s, 2H);  $^{13}\text{C}$  NMR (DMSO- $d_6$ ):  $\delta$ /ppm 87.9 (C), 96.1 (C), 116.1 (C), 125.8 (C), 129.7 (CH), 131.3 (C), 131.8 (CH), 133.3 (CH), 153.6 (C), 166.6 (C).

#### 4.12.3 Bulk Synthesis of Zr and Hf MOFs Containing L12-L17

Zr and Hf MOFs were synthesised using L12-H<sub>2</sub>-L17-H<sub>2</sub>, resulting in an isorecticular series of interpenetrated 3-dimensional frameworks containing M<sub>6</sub>O<sub>4</sub>(OH)<sub>4</sub> clusters (M = Zr or Hf) 12-connected by bridging organic ligands. A general naming scheme of the format **M-L<sub>n</sub>**, where **M** represents the metal cluster and **L<sub>n</sub>** corresponds to the ligand is used for convenience. The amino acid modulated syntheses of Zr and Hf MOFs containing L11 as bulk microcrystalline powders are described in detail in Chapter 2, Section 2.10.10. Similar synthetic procedures are employed for bulk syntheses of the other MOFs of the series, although Zr and Hf MOFs containing L15 could not be obtained using this method and an alternative benzoic acid modulation procedure was used.<sup>7</sup>

##### Zr-L12

L-proline (0.130 g, 1.13 mmol, 5 eq), L12-H<sub>2</sub> (0.089 g, 0.23 mmol, 1 eq), zirconium chloride (0.052 g, 0.22 mmol, 1 eq) and DMF (10 ml) were added to a 50 ml Pyrex reagent bottle and sonicated for 10 minutes. Concentrated HCl (0.02 ml) was added and the suspension was sonicated for a further 10 minutes before being placed in the oven at 120 °C for 24 hours. The bulk material was collected from the bottle upon completion, centrifuged once with fresh DMF (30 ml) and twice with acetone (2 x 30 ml), before being dried under vacuum ([Zr<sub>6</sub>O<sub>4</sub>(OH)<sub>4</sub>(L12)<sub>6</sub>]<sub>n</sub>, 0.104 g, 0.034 mmol, 93%).



**Hf-L12**

L-proline (0.130 g, 1.13 mmol, 5 eq), L12-H<sub>2</sub> (0.089 g, 0.23 mmol, 1 eq), hafnium chloride (0.072 g, 0.22 mmol, 1 eq) and DMF (10 ml) were added to a 50 ml Pyrex reagent bottle and sonicated for 10 minutes. Concentrated HCl (0.02 ml) was added and the suspension was sonicated for a further 10 minutes before being placed in the oven at 100 °C for 48 hours. The bulk material was collected from the bottle upon completion, centrifuged once with fresh DMF (30 ml) and twice with acetone (2 x 30 ml), before being dried under vacuum ([Hf<sub>6</sub>O<sub>4</sub>(OH)<sub>4</sub>(L12)<sub>6</sub>]<sub>n</sub>, 0.121 g, 0.034 mmol, 91%).

**Zr-L13**

L-proline (0.052 g, 0.45 mmol, 4 eq), L13-H<sub>2</sub> (0.045 g, 0.11 mmol, 1 eq), zirconium chloride (0.026 g, 0.11 mmol, 1 eq) and DMF (5 ml) were added to a 50 ml Pyrex reagent bottle and sonicated for 10 minutes. Concentrated HCl (0.01 ml) was added and the suspension was sonicated for a further 10 minutes before being placed in the oven at 120 °C for 24 hours. The bulk material was collected from the bottle upon completion, centrifuged once with fresh DMF (30 ml) and twice with acetone (2 x 30 ml), before being dried under vacuum ([Zr<sub>6</sub>O<sub>4</sub>(OH)<sub>4</sub>(L13)<sub>6</sub>]<sub>n</sub>, 0.056 g, 0.018 mmol, 98%).

**Hf-L13**

L-proline (0.052 g, 0.45 mmol, 4 eq), L13-H<sub>2</sub> (0.045 g, 0.11 mmol, 1 eq), hafnium chloride (0.036 g, 0.11 mmol, 1 eq) and DMF (5 ml) were added to a 50 ml Pyrex reagent bottle and sonicated for 10 minutes. Concentrated HCl (0.01 ml) was added and the suspension was sonicated for a further 10 minutes before being placed in the oven at 120 °C for 24 hours. The bulk material was collected from the bottle upon completion, centrifuged once with fresh DMF (30 ml) and twice with acetone (2 x 30 ml), before being dried under vacuum ([Hf<sub>6</sub>O<sub>4</sub>(OH)<sub>4</sub>(L13)<sub>6</sub>]<sub>n</sub>, 0.066 g, 0.018 mmol, 98%).

**Zr-L14**

L-proline (0.052 g, 0.45 mmol, 4 eq), L14-H<sub>2</sub> (0.045 g, 0.11 mmol, 1 eq), zirconium chloride (0.026 g, 0.11 mmol, 1 eq) and DMF (5 ml) were added to a 50 ml Pyrex reagent bottle and sonicated for 10 minutes. Concentrated HCl (0.01 ml) was added and the suspension was sonicated for a further 10 minutes before being placed in the oven at 120 °C for 24 hours. The bulk material was collected from the bottle upon completion, centrifuged once with fresh

DMF (30 ml) and twice with acetone (2 x 30 ml), before being dried under vacuum ( $[\text{Zr}_6\text{O}_4(\text{OH})_4(\text{L14})_6]_n$ , 0.057 g, 0.016 mmol, 98%).

#### Hf-L14

L-proline (0.052 g, 0.45 mmol, 4 eq), L14- $\text{H}_2$  (0.045 g, 0.11 mmol, 1 eq), hafnium chloride (0.036 g, 0.11 mmol, 1 eq) and DMF (5 ml) were added to a 50 ml Pyrex reagent bottle and sonicated for 10 minutes. Concentrated HCl (0.01 ml) was added and the suspension was sonicated for a further 10 minutes before being placed in the oven at 120 °C for 24 hours. The bulk material was collected from the bottle upon completion, centrifuged once with fresh DMF (30 ml) and twice with acetone (2 x 30 ml), before being dried under vacuum ( $[\text{Hf}_6\text{O}_4(\text{OH})_4(\text{L14})_6]_n$ , 0.067 g, 0.019 mmol, 100%).

#### Zr-L15

Benzoic acid (0.618 g, 5.06 mmol, 30 eq), zirconium chloride (0.039 g, 0.17 mmol, 1 eq) and DMF (10 ml) were added to a 50 ml Pyrex reagent bottle and sonicated for 10 minutes. L15- $\text{H}_2$  (0.074 g, 0.17 mmol, 1 eq) and HCl (0.015 ml) were added and the suspension was sonicated for a further 10 minutes before being placed in the oven at 120 °C for 24 hours. The bulk material was collected from the bottle upon completion, centrifuged once with fresh DMF (30 ml) and twice with acetone (2 x 30 ml), before being dried under vacuum ( $[\text{Zr}_6\text{O}_4(\text{OH})_4(\text{L15})_6]_n$ , 0.085 g, 0.026 mmol, 92%).

#### Hf-L15

Benzoic acid (0.618 g, 5.06 mmol, 30 eq), hafnium chloride (0.054 g, 0.17 mmol, 1 eq) and DMF (10 ml) were added to a 50 ml Pyrex reagent bottle and sonicated for 10 minutes. L15- $\text{H}_2$  (0.074 g, 0.17 mmol, 1 eq) and HCl (0.015 ml) were added and the suspension was sonicated for a further 10 minutes before being placed in the oven at 120 °C for 24 hours. The bulk material was collected from the bottle upon completion, centrifuged once with fresh DMF (30 ml) and twice with acetone (2 x 30 ml), before being dried under vacuum ( $[\text{Hf}_6\text{O}_4(\text{OH})_4(\text{L15})_6]_n$ , 0.101 g, 0.026 mmol, 92%).

#### Zr-L16

L-proline (0.052 g, 0.45 mmol, 4 eq), L16- $\text{H}_2$  (0.047 g, 0.11 mmol, 1 eq), zirconium chloride (0.026 g, 0.11 mmol, 1 eq) and DMF (5 ml) were added to a 50 ml Pyrex reagent bottle and sonicated for 10 minutes. Concentrated HCl (0.01 ml) was added and the mixture was

sonicated for a further 10 minutes before being placed in the oven at 120 °C for 24 hours. The bulk material was collected from the bottle upon completion, centrifuged once with fresh DMF (30 ml) and twice with acetone (2 x 30 ml), before being dried under vacuum ( $[\text{Zr}_6\text{O}_4(\text{OH})_4(\text{L16})_6]_n$ , 0.062 g, 82%).

#### **Hf-L16**

L-proline (0.052 g, 0.45 mmol, 4 eq), L16- $\text{H}_2$  (0.047 g, 0.11 mmol, 1 eq), hafnium chloride (0.036 g, 0.11 mmol, 1 eq) and DMF (5 ml) were added to a 50 ml Pyrex reagent bottle and sonicated for 10 minutes. Concentrated HCl (0.01 ml) was added and the suspension was sonicated for a further 10 minutes before being placed in the oven at 120 °C for 24 hours. The bulk material was collected from the bottle upon completion, centrifuged once with fresh DMF (30 ml) and twice with acetone (2 x 30 ml), before being dried under vacuum ( $[\text{Hf}_6\text{O}_4(\text{OH})_4(\text{L16})_6]_n$ , 0.058 g, 0.016 mmol, 87%).

#### **Zr-L17**

L-proline (0.052 g, 0.45 mmol, 4 eq), L17- $\text{H}_2$  (0.048 g, 0.11 mmol, 1 eq), zirconium chloride (0.026 g, 0.11 mmol, 1 eq) and DMF (5 ml) were added to a 50 ml Pyrex reagent bottle and sonicated for 10 minutes. Concentrated HCl (0.01 ml) was added and the mixture was sonicated for a further 10 minutes before being placed in the oven at 120 °C for 24 hours. The bulk material was collected from the bottle upon completion, centrifuged once with fresh DMF (30 ml) and twice with acetone (2 x 30 ml), before being dried under vacuum ( $[\text{Zr}_6\text{O}_4(\text{OH})_4(\text{L17})_6]_n$ , 0.058 g, 0.018 mmol, 98%).

#### **Hf-L17**

L-proline (0.052 g, 0.45 mmol, 4 eq), L17- $\text{H}_2$  (0.048 g, 0.11 mmol, 1 eq), hafnium chloride (0.026 g, 0.11 mmol, 1 eq) and DMF (5 ml) were added to a 50 ml Pyrex reagent bottle and sonicated for 10 minutes. Concentrated HCl (0.01 ml) was added and the suspension was sonicated for a further 10 minutes before being placed in the oven at 120 °C for 24 hours. The bulk material was collected from the bottle upon completion, centrifuged once with fresh DMF (30 ml) and twice with acetone (2 x 30 ml), before being dried under vacuum ( $[\text{Hf}_6\text{O}_4(\text{OH})_4(\text{L17})_6]_n$ , 0.064 g, 0.017 mmol, 93%).

**Activation:** Bulk MOF samples were added to 50 ml Pyrex reagent bottles and left to stand in  $\text{CHCl}_3$ . The  $\text{CHCl}_3$  was exchanged for fresh  $\text{CHCl}_3$  at least 3 times over 3 days, before being dried under vacuum.

#### 4.12.4 Single Crystal Synthesis of Zr and Hf MOFs Containing L12-L17

Single crystals of Zr and Hf MOFs containing L11 were synthesised using benzoic acid modulation and their syntheses are described in Chapter 2 Section 2.10.11. Single crystals of the functionalised MOFs have been synthesised using either benzoic acid modulation or L-proline modulation similar to bulk synthesis conditions (see Section 4.12.3). A slightly modified L-proline modulation protocol was employed during the synthesis of single crystals of **Zr-L17**.<sup>40</sup>

##### Zr-L12

L-proline (0.052 g, 0.45 mmol, 4 eq), L12- $\text{H}_2$  (0.044 g, 0.11 mmol, 1 eq), zirconium chloride (0.026 g, 0.11 mmol, 1 eq) and DMF (5 ml) were added to a 50 ml Pyrex reagent bottle and sonicated for 10 minutes. Concentrated HCl (0.01 ml) was added and the suspension was sonicated for a further 10 minutes before being placed in the oven at 100 °C for 48 hours. The bottle was removed from the oven after this period and allowed to cool to room temperature. The crystals were left to stand in their mother solution.

**Crystal data for Zr-L12.**  $\text{C}_{156}\text{H}_{96}\text{O}_{32}\text{Zr}_6$ ,  $M_r = 3029.64$ , crystal dimensions 0.07 x 0.04 x 0.04 mm, Orthorhombic,  $a = 28.1510$  (2) Å,  $b = 28.1718$  (3) Å,  $c = 39.9493$  (4) Å,  $V = 31682.3$  (5) Å<sup>3</sup>,  $T = 100$  K, space group *Imma* (no. 74),  $Z = 4$ , 122767 measured reflections, 14629 unique ( $R_{\text{int}} = 0.065$ ), which were used in all calculations. The final  $R_I = 0.089$  for 12990 observed data  $R[F^2 > 2\sigma(F^2)]$  and  $wR(F^2) = 0.255$  (all data). Approximately 66% of the cell volume is not occupied by the framework and contains diffuse and disordered solvent molecules. This electron density was accounted for using SQUEEZE within PLATON<sup>41</sup> which calculated a solvent accessible volume of 20904 Å<sup>3</sup> containing 6114 electrons (the equivalent of ~153 molecules of DMF) per unit cell. Crystal structure data for **Zr-L12** is available from the CCDC, deposition number 1516193.

**Zr-L13**

Benzoic acid (0.275 g, 2.25 mmol, 40 eq), zirconium chloride (0.013 g, 0.056 mmol, 1 eq) and DMF (5 ml) were added to a 25 ml Pyrex reagent bottle and sonicated for 10 minutes. L13-H<sub>2</sub> (0.023 g, 0.057 mmol, 1 eq) and HCl (0.01 ml) were added and the suspension was sonicated for a further 10 minutes before being placed in the oven at 120 °C for 24 hours. The bottle was removed from the oven after this period and allowed to cool to room temperature. The crystals were left to stand in their mother solution.

**Crystal data for Zr-L13.** C<sub>144</sub>H<sub>64</sub>F<sub>12</sub>O<sub>32</sub>Zr<sub>6</sub>,  $M_r = 3081.27$ , crystal dimensions 0.06 x 0.06 x 0.06 mm, Cubic,  $a = 39.8364$  (2) Å,  $V = 63217.9$  (10) Å<sup>3</sup>,  $T = 100$  K, space group  $Fd-3m$  (no. 227),  $Z = 8$ , 94790 measured reflections, 3410 unique ( $R_{int} = 0.074$ ), which were used in all calculations. The final  $R_I = 0.056$  for 2807 observed data  $R[F^2 > 2\sigma(F^2)]$  and  $wR(F^2) = 0.151$  (all data). Approximately 66% of the cell volume is not occupied by the framework and contains diffuse and disordered solvent molecules. This electron density was accounted for using SQUEEZE within PLATON<sup>41</sup> which calculated a solvent accessible volume of 41827 Å<sup>3</sup> containing 8506 electrons (the equivalent of ~213 molecules of DMF) per unit cell. Crystal structure data for **Zr-L13** is available from the CCDC, deposition number 1516194.

**Hf-L13**

Benzoic acid (0.275 g, 2.25 mmol, 40 eq), hafnium chloride (0.018 g, 0.056 mmol, 1 eq) and DMF (5 ml) were added to a 25 ml Pyrex reagent bottle and sonicated for 10 minutes. L13-H<sub>2</sub> (0.023 g, 0.057 mmol, 1 eq) and HCl (0.01 ml) were added and the suspension was sonicated for a further 10 minutes before being placed in the oven at 120 °C for 24 hours. The bottle was removed from the oven after this period and allowed to cool to room temperature. The crystals were left to stand in their mother solution.

**Crystal data for Hf-L13.** C<sub>144</sub>H<sub>64</sub>F<sub>12</sub>Hf<sub>6</sub>O<sub>32</sub>,  $M_r = 3604.89$ , crystal dimensions 0.06 x 0.05 x 0.04 mm, Cubic,  $a = 39.7405$  (2) Å,  $V = 62762.5$  (9) Å<sup>3</sup>,  $T = 100$  K, space group  $Fd-3m$  (no. 227),  $Z = 8$ , 74076 measured reflections, 3409 unique ( $R_{int} = 0.065$ ), which were used in all calculations. The final  $R_I = 0.043$  for 2767 observed data  $R[F^2 > 2\sigma(F^2)]$  and  $wR(F^2) = 0.101$  (all data). Approximately 66% of the cell volume is not occupied by the framework and contains diffuse and disordered solvent molecules. This electron density was accounted for using SQUEEZE within PLATON<sup>41</sup> which calculated a solvent accessible volume of 41460

$\text{\AA}^3$  containing 10890 electrons (the equivalent of ~272 molecules of DMF) per unit cell. Crystal structure data for **Hf-L13** is available from the CCDC, deposition number 1516199.

#### Zr-L14

Benzoic acid (0.206 g, 1.69 mmol, 30 eq), zirconium chloride (0.013 g, 0.056 mmol, 1 eq) and DMF (5 ml) were added to a 25 ml Pyrex reagent bottle and sonicated for 10 minutes. L14-H<sub>2</sub> (0.023 g, 0.057 mmol, 1 eq) and HCl (0.01 ml) were added and the suspension was sonicated for a further 10 minutes before being placed in the oven at 100 °C for 24 hours, then the temperature was increased to 120 °C for a further 24 hours. The bottle was removed from the oven after this period and allowed to cool to room temperature. The crystals were left to stand in their mother solution.

**Crystal data for Zr-L14.** C<sub>144</sub>H<sub>64</sub>F<sub>12</sub>O<sub>32</sub>Zr<sub>6</sub>,  $M_r = 3081.27$ , crystal dimensions 0.05 x 0.05 x 0.05 mm, Cubic,  $a = 39.83167$  (14)  $\text{\AA}$ ,  $V = 63195.4$  (7)  $\text{\AA}^3$ ,  $T = 100$  K, space group  $Fd-3m$  (no. 227),  $Z = 8$ , 125385 measured reflections, 3410 unique ( $R_{\text{int}} = 0.073$ ), which were used in all calculations. The final  $R_I = 0.070$  for 2956 observed data  $R[F^2 > 2\sigma(F^2)]$  and  $wR(F^2) = 0.191$  (all data). Approximately 66% of the cell volume is not occupied by the framework and contains diffuse and disordered solvent molecules. This electron density was accounted for using SQUEEZE within PLATON<sup>41</sup> which calculated a solvent accessible volume of 41816  $\text{\AA}^3$  containing 9131 electrons (the equivalent of ~228 molecules of DMF) per unit cell. Crystal structure data for **Zr-L14** is available from the CCDC, deposition number 1516195.

#### Hf-L14

Benzoic acid (0.206 g, 1.69 mmol, 30 eq), hafnium chloride (0.018 g, 0.056 mmol, 1 eq) and DMF (5 ml) were added to a 25 ml Pyrex reagent bottle and sonicated for 10 minutes. L14-H<sub>2</sub> (0.023 g, 0.057 mmol, 1 eq) and HCl (0.01 ml) were added and the suspension was sonicated for a further 10 minutes before being placed in the oven at 120 °C for 24 hours. The bottle was removed from the oven after this period and allowed to cool to room temperature. The crystals were left to stand in their mother solution.

**Crystal data for Hf-L14.** C<sub>144</sub>H<sub>64</sub>F<sub>12</sub>Hf<sub>6</sub>O<sub>32</sub>,  $M_r = 3604.89$ , crystal dimensions 0.04 x 0.03 x 0.03 mm, Cubic,  $a = 39.7709$  (2)  $\text{\AA}$ ,  $V = 62906.6$  (9)  $\text{\AA}^3$ ,  $T = 100$  K, space group  $Fd-3m$  (no. 227),  $Z = 8$ , 133574 measured reflections, 3396 unique ( $R_{\text{int}} = 0.103$ ), which were used in all

calculations. The final  $R_I = 0.052$  for 2635 observed data  $R[F^2 > 2\sigma(F^2)]$  and  $wR(F^2) = 0.127$  (all data). Approximately 66% of the cell volume is not occupied by the framework and contains diffuse and disordered solvent molecules. This electron density was accounted for using SQUEEZE within PLATON<sup>41</sup> which calculated a solvent accessible volume of 41450 Å<sup>3</sup> containing 12622 electrons (the equivalent of ~316 molecules of DMF) per unit cell. Crystal structure data for **Hf-L14** is available from the CCDC, deposition number 1516200.

### Zr-L15

Single crystals were synthesised according to bulk **Zr-L15** synthesis conditions (see Section 4.12.3). The crystals were left to stand in their mother solution prior to analysis.

**Crystal data for Zr-L15.** C<sub>144</sub>H<sub>52</sub>F<sub>24</sub>O<sub>32</sub>Zr<sub>6</sub>,  $M_r = 3297.17$ , crystal dimensions 0.05 x 0.05 x 0.05 mm, Cubic,  $a = 39.8334$  (2) Å,  $V = 63203.6$  (10) Å<sup>3</sup>,  $T = 100$  K, space group  $Fd-3m$  (no. 227),  $Z = 8$ , 101888 measured reflections, 3413 unique ( $R_{\text{int}} = 0.090$ ), which were used in all calculations. The final  $R_I = 0.075$  for 2895 observed data  $R[F^2 > 2\sigma(F^2)]$  and  $wR(F^2) = 0.206$  (all data). Approximately 66% of the cell volume is not occupied by the framework and contains diffuse and disordered solvent molecules. This electron density was accounted for using SQUEEZE within PLATON<sup>41</sup> which calculated a solvent accessible volume of 41775 Å<sup>3</sup> containing 11166 electrons (the equivalent of ~279 molecules of DMF) per unit cell. Crystal structure data for **Zr-L15** is available from the CCDC, deposition number 1516196.

### Hf-L15

Single crystals were synthesised according to bulk **Hf-L15** synthesis conditions (see Section 4.12.3). The crystals were left to stand in their mother solution prior to analysis.

**Crystal data for Hf-L15.** C<sub>144</sub>H<sub>52</sub>F<sub>24</sub>Hf<sub>6</sub>O<sub>32</sub>,  $M_r = 3820.79$ , crystal dimensions 0.05 x 0.05 x 0.05 mm, Cubic,  $a = 39.828$  (14) Å,  $V = 63180$  (64) Å<sup>3</sup>,  $T = 100$  K, space group  $Fd-3m$  (no. 227),  $Z = 8$ , 58657 measured reflections, 2636 unique ( $R_{\text{int}} = 0.391$ ), which were used in all calculations. The final  $R_I = 0.074$  for 1214 observed data  $R[F^2 > 2\sigma(F^2)]$  and  $wR(F^2) = 0.266$  (all data). Approximately 65% of the cell volume is not occupied by the framework and contains diffuse and disordered solvent molecules. This electron density was accounted for using SQUEEZE within PLATON<sup>41</sup> which calculated a solvent accessible volume of 40929

$\text{\AA}^3$  containing 19791 electrons (the equivalent of ~495 molecules of DMF) per unit cell. Crystal structure data for **Hf-L15** is available from the CCDC, deposition number 1516201.

### Zr-L16

Benzoic acid (0.206 g, 1.69 mmol, 30 eq), zirconium chloride (0.013 g, 0.056 mmol, 1 eq) and DMF (5 ml) were added to a 25 ml Pyrex reagent bottle and sonicated for 10 minutes. L16-H<sub>2</sub> (0.024 g, 0.057 mmol, 1 eq) and HCl (0.01 ml) were added and the suspension was sonicated for a further 10 minutes before being placed in the oven at 120 °C for 24 hours. The bottle was removed from the oven after this period and allowed to cool to room temperature. The crystals were left to stand in their mother solution.

**Crystal data for Zr-L16.** C<sub>168</sub>H<sub>88</sub>O<sub>32</sub>Zr<sub>6</sub>,  $M_r = 3165.70$ , crystal dimensions 0.04 x 0.04 x 0.04 mm, Cubic,  $a = 39.8785$  (3)  $\text{\AA}$ ,  $V = 63418.6$  (16)  $\text{\AA}^3$ ,  $T = 100$  K, space group  $Fd-3m$  (no. 227),  $Z = 8$ , 73411 measured reflections, 3415 unique ( $R_{\text{int}} = 0.167$ ), which were used in all calculations. The final  $R_I = 0.074$  for 2274 observed data  $R[F^2 > 2\sigma(F^2)]$  and  $wR(F^2) = 0.224$  (all data). Approximately 58% of the cell volume is not occupied by the framework and contains diffuse and disordered solvent molecules. This electron density was accounted for using SQUEEZE within PLATON<sup>41</sup> which calculated a solvent accessible volume of 37012  $\text{\AA}^3$  containing 10404 electrons (the equivalent of ~260 molecules of DMF) per unit cell. Crystal structure data for **Zr-L16** is available from the CCDC, deposition number 1516197.

### Hf-L16

Single crystals were synthesised according to bulk **Hf-L16** synthesis conditions (see Section 4.12.3). The crystals were left to stand in their mother solution prior to analysis.

**Crystal data for Hf-L16.** C<sub>168</sub>H<sub>88</sub>Hf<sub>6</sub>O<sub>32</sub>,  $M_r = 3689.32$ , crystal dimensions 0.04 x 0.04 x 0.04 mm, Cubic,  $a = 39.8509$  (2)  $\text{\AA}$ ,  $V = 63287.0$  (10)  $\text{\AA}^3$ ,  $T = 100$  K, space group  $Fd-3m$  (no. 227),  $Z = 8$ , 84534 measured reflections, 3434 unique ( $R_{\text{int}} = 0.110$ ), which were used in all calculations. The final  $R_I = 0.069$  for 2483 observed data  $R[F^2 > 2\sigma(F^2)]$  and  $wR(F^2) = 0.175$  (all data). Approximately 60% of the cell volume is not occupied by the framework and contains diffuse and disordered solvent molecules. This electron density was accounted for using SQUEEZE within PLATON<sup>41</sup> which calculated a solvent accessible volume of 38041



$\text{\AA}^3$  containing 9752 electrons (the equivalent of ~244 molecules of DMF) per unit cell. Crystal structure data for **Hf-L16** is available from the CCDC, deposition number 1516202.

### Zr-L17

L-proline (0.054 g, 0.47 mmol, 5 eq) was dissolved in concentrated HCl (0.063 ml) and subsequently evaporated to dryness. The obtained solid was dissolved in DMF (3 ml), added to a 25 ml Pyrex reagent bottle containing zirconium chloride (0.022 g, 0.094 mmol, 1 eq) and sonicated for 10 minutes. L17-H<sub>2</sub> (0.040 g, 0.094 mmol, 1 eq) was added and the mixture was sonicated for a further 10 minutes before being placed in the oven at 120 °C for 48 hours. The bottle was removed from the oven after this period and allowed to cool to room temperature. The crystals were left to stand in their mother solution.

**Crystal data for Zr-L17.** C<sub>144</sub>H<sub>64</sub>N<sub>12</sub>O<sub>32</sub>S<sub>6</sub>Zr<sub>6</sub>,  $M_r = 3213.75$ , crystal dimensions 0.03 x 0.03 x 0.03 mm, Cubic,  $a = 40.0341$  (6)  $\text{\AA}$ ,  $V = 64164$  (3)  $\text{\AA}^3$ ,  $T = 100$  K, space group  $Fd-3m$  (no. 227),  $Z = 8$ , 19071 measured reflections, 3450 unique ( $R_{\text{int}} = 0.109$ ), which were used in all calculations. The final  $R_I = 0.061$  for 2051 observed data  $R[F^2 > 2\sigma(F^2)]$  and  $wR(F^2) = 0.183$  (all data). Approximately 64% of the cell volume is not occupied by the framework and contains diffuse and disordered solvent molecules. This electron density was accounted for using SQUEEZE within PLATON<sup>41</sup> which calculated a solvent accessible volume of 40922  $\text{\AA}^3$  containing 7855 electrons (the equivalent of ~196 molecules of DMF) per unit cell. Crystal structure data for **Zr-L17** is available from the CCDC, deposition number 1516198.

### Hf-L17

L-proline (0.026 g, 0.23 mmol, 4 eq), hafnium chloride (0.018 g, 0.056 mmol, 1 eq), L17-H<sub>2</sub> (0.024 g, 0.057 mmol, 1 eq) and DMF (2.5 ml) were added to a 25 ml Pyrex reagent bottle and sonicated for 10 minutes. HCl (0.01 ml) was added and the suspension was sonicated for a further 10 minutes before being placed in the oven at 100 °C for 48 hours. The bottle was removed from the oven after this period and allowed to cool to room temperature. The crystals were left to stand in their mother solution.

**Crystal data for Hf-L17.** C<sub>144</sub>H<sub>64</sub>Hf<sub>6</sub>N<sub>12</sub>O<sub>32</sub>S<sub>6</sub>,  $M_r = 3737.37$ , crystal dimensions 0.03 x 0.03 x 0.03 mm, Cubic,  $a = 39.867$  (2)  $\text{\AA}$ ,  $V = 63362$  (10)  $\text{\AA}^3$ ,  $T = 100$  K, space group  $Fd-3m$  (no. 227),  $Z = 8$ , 20748 measured reflections, 2658 unique ( $R_{\text{int}} = 0.103$ ), which were used in all

calculations. The final  $R_I = 0.043$  for 1667 observed data  $R[F^2 > 2\sigma(F^2)]$  and  $wR(F^2) = 0.119$  (all data). Approximately 63% of the cell volume is not occupied by the framework and contains diffuse and disordered solvent molecules. This electron density was accounted for using SQUEEZE within PLATON<sup>41</sup> which calculated a solvent accessible volume of 39996 Å<sup>3</sup> containing 9285 electrons (the equivalent of ~232 molecules of DMF) per unit cell. Crystal structure data for **Hf-L17** is available from the CCDC, deposition number 1516203.

### 4.13 References

- (1) Cavka, J. H.; Jakobsen, S.; Olsbye, U.; Guillou, N.; Lamberti, C.; Bordiga, S.; Lillerud, K. P. *J. Am. Chem. Soc.* **2008**, *130*, 13850.
- (2) Ma, J.; Wong-Foy, A. G.; Matzger, A. J. *Inorg. Chem.* **2015**, *54*, 4591.
- (3) Wang, R.; Wang, Z.; Xu, Y.; Dai, F.; Zhang, L.; Sun, D. *Inorg. Chem.* **2014**, *53*, 7086.
- (4) Feng, D.; Gu, Z.-Y.; Li, J.-R.; Jiang, H.-L.; Wei, Z.; Zhou, H.-C. *Angew. Chem. Int. Ed.* **2012**, *51*, 10307.
- (5) Morris, W.; Voloskiy, B.; Demir, S.; Gándara, F.; McGrier, P. L.; Furukawa, H.; Cascio, D.; Stoddart, J. F.; Yaghi, O. M. *Inorg. Chem.* **2012**, *51*, 6443.
- (6) Mondloch, J. E.; Bury, W.; Fairen-Jimenez, D.; Kwon, S.; DeMarco, E. J.; Weston, M. H.; Sarjeant, A. A.; Nguyen, S. T.; Stair, P. C.; Snurr, R. Q.; Farha, O. K.; Hupp, J. T. *J. Am. Chem. Soc.* **2013**, *135*, 10294.
- (7) Schaate, A.; Roy, P.; Preuße, T.; Lohmeier, S. J.; Godt, A.; Behrens, P. *Chem. Eur. J.* **2011**, *17*, 9320.
- (8) Chen, D.; Xing, H.; Wang, C.; Su, Z. *J. Mater. Chem. A* **2016**, *4*, 2657.
- (9) Doan, T. L. H.; Nguyen, H. L.; Pham, H. Q.; Pham-Tran, N.-N.; Le, T. N.; Cordova, K. E. *Chem. Asian J.* **2015**, *10*, 2660.
- (10) Doan, T. L. H.; Dao, T. Q.; Tran, H. N.; Tran, P. H.; Le, T. N. *Dalton Trans.* **2016**, *45*, 7875.
- (11) Babarao, R.; Rubio-Martinez, M.; Hill, M. R.; Thornton, A. W. *J. Phys. Chem. C* **2016**, *120*, 13013.
- (12) Roy, P.; Schaate, A.; Behrens, P.; Godt, A. *Chem. Eur. J.* **2012**, *18*, 6979.
- (13) Jones, S. C.; Bauer, C. A. *J. Am. Chem. Soc.* **2009**, *131*, 12516.
- (14) Frahm, D.; Hoffmann, F.; Fröba, M. *Cryst. Growth Des.* **2014**, *14*, 1719.
- (15) Marshall, R. J.; Griffin, S. L.; Wilson, C.; Forgan, R. S. *Chem. Eur. J.* **2016**, *22*, 4870.
- (16) Fasina, T. M.; Collings, J. C.; Burke, J. M.; Batsanov, A. S.; Ward, R. M.; Albesa-Jove, D.; Porres, L.; Beeby, A.; Howard, J. A. K.; Scott, A. J.; Clegg, W.; Watt, S. W.; Viney, C.; Marder, T. B. *J. Mater. Chem.* **2005**, *15*, 690.
- (17) Carboni, M.; Lin, Z.; Abney, C. W.; Zhang, T.; Lin, W. *Chem. Eur. J.* **2014**, *20*, 14965.
- (18) Nagarkar, S. S.; Desai, A. V.; Ghosh, S. K. *Chem. Commun.* **2014**, *50*, 8915.
- (19) Nagarkar, S. S.; Desai, A. V.; Ghosh, S. K. *Chem. Eur. J.* **2015**, *21*, 9994.

- (20) Desai, A. V.; Samanta, P.; Manna, B.; Ghosh, S. K. *Chem. Commun.* **2015**, 51, 6111.
- (21) Drache, F.; Bon, V.; Senkovska, I.; Adam, M.; Eychmüller, A.; Kaskel, S. *Eur. J. Inorg. Chem.* **2016**, 2016, 4483.
- (22) Wang, B.; Lv, X.-L.; Feng, D.; Xie, L.-H.; Zhang, J.; Li, M.; Xie, Y.; Li, J.-R.; Zhou, H.-C. *J. Am. Chem. Soc.* **2016**, 138, 6204.
- (23) Jiang, H.-L.; Feng, D.; Wang, K.; Gu, Z.-Y.; Wei, Z.; Chen, Y.-P.; Zhou, H.-C. *J. Am. Chem. Soc.* **2013**, 135, 13934.
- (24) Aguilera-Sigalat, J.; Bradshaw, D. *Chem. Commun.* **2014**, 50, 4711.
- (25) Wei, Z.; Gu, Z.-Y.; Arvapally, R. K.; Chen, Y.-P.; McDougald, R. N.; Ivy, J. F.; Yakovenko, A. A.; Feng, D.; Omary, M. A.; Zhou, H.-C. *J. Am. Chem. Soc.* **2014**, 136, 8269.
- (26) Deria, P.; Yu, J.; Balaraman, R. P.; Mashni, J.; White, S. N. *Chem. Commun.* **2016**.
- (27) Ko, N.; Hong, J.; Sung, S.; Cordova, K. E.; Park, H. J.; Yang, J. K.; Kim, J. *Dalton Trans.* **2015**, 44, 2047.
- (28) Ballesteros, L. M.; Martín, S.; Cortés, J.; Marqués-González, S.; Higgins, S. J.; Nichols, R. J.; Low, P. J.; Cea, P. *Chem. Eur. J.* **2013**, 19, 5352.
- (29) Marshall, R. J.; Hobday, C. L.; Murphie, C. F.; Griffin, S. L.; Morrison, C. A.; Moggach, S. A.; Forgan, R. S. *J. Mater. Chem. A* **2016**, 4, 6955.
- (30) Schaate, A.; Roy, P.; Godt, A.; Lippke, J.; Waltz, F.; Wiebcke, M.; Behrens, P. *Chem. Eur. J.* **2011**, 17, 6643.
- (31) Song, C.; He, Y.; Li, B.; Ling, Y.; Wang, H.; Feng, Y.; Krishna, R.; Chen, B. *Chem. Commun.* **2014**, 50, 12105.
- (32) Douvali, A.; Tsipis, A. C.; Eliseeva, S. V.; Petoud, S.; Papaefstathiou, G. S.; Malliakas, C. D.; Papadas, I.; Armatas, G. S.; Margiolaki, I.; Kanatzidis, M. G.; Lazarides, T.; Manos, M. J. *Angew. Chem. Int. Ed.* **2015**, 54, 1651.
- (33) Yu, Y.; Zhang, X.-M.; Ma, J.-P.; Liu, Q.-K.; Wang, P.; Dong, Y.-B. *Chem. Commun.* **2014**, 50, 1444.
- (34) Mondloch, J. E.; Katz, M. J.; Planas, N.; Semrouni, D.; Gagliardi, L.; Hupp, J. T.; Farha, O. K. *Chem. Commun.* **2014**, 50, 8944.
- (35) Chen, T.-H.; Popov, I.; Zenasni, O.; Daugulis, O.; Miljanic, O. S. *Chem. Commun.* **2013**, 49, 6846.
- (36) Drache, F.; Bon, V.; Senkovska, I.; Marschelke, C.; Synytska, A.; Kaskel, S. *Inorg. Chem.* **2016**, 55, 7206.
- (37) Law, K.-Y. *J. Phys. Chem. Lett.* **2014**, 5, 686.

- (38) Chen, T.-H.; Popov, I.; Kaveevivitchai, W.; Chuang, Y.-C.; Chen, Y.-S.; Jacobson, A. J.; Miljanić, O. Š. *Angew. Chem. Int. Ed.* **2015**, *54*, 13902.
- (39) Macrae, C. F.; Bruno, I. J.; Chisholm, J. A.; Edgington, P. R.; McCabe, P.; Pidcock, E.; Rodriguez-Monge, L.; Taylor, R.; van de Streek, J.; Wood, P. A. *J. Appl. Crystallogr.* **2008**, *41*, 466.
- (40) Gutov, O. V.; Molina, S.; Escudero-Adán, E. C.; Shafir, A. *Chem. Eur. J.* **2016**, *22*, 13582.
- (41) Spek, A. *Acta Crystallogr. Sect. C* **2015**, *71*, 9.

## **Chapter 5**

## **Conclusions**

## Contents

<b>Chapter 5 .....</b>	<b>227</b>
<b>5.1 Conclusions .....</b>	<b>229</b>
<b>5.2 References .....</b>	<b>235</b>

## 5.1 Conclusions

The aims of each chapter of this thesis are outlined below:

- Chapter 2 – Evaluate the use of amino acids as modulators for the syntheses of Zr and Hf MOFs with UiO-66 topology.
- Chapter 3 – Determine the feasibility of integral postsynthetic modifications at unsaturated sites within Zr and Hf MOFs.
- Chapter 4 – Expand the series of interpenetrated Zr and Hf MOFs through incorporation of alternative functionality.

In the main, the aims of each chapter have been achieved. The results reported in Chapter 2 are vital for the success of the work carried out during the chapters that follow. A comprehensive approach was taken towards the amino acid modulation of Zr and Hf MOFs, with a wide variety of modulators and bridging organic ligands enabling a large parameter space to be examined.<sup>1</sup> Initially the results obtained were discouraging and despite the necessary prerequisites (e.g. carboxylic acid functionality for competitive attachment to the Zr clusters) it appeared that amino acids were not effective modulators. This was true for Zr and Hf MOFs containing terephthalate based ligands (L1-L4), with amino acids providing no improvement in the materials' crystallinity, although fortunately it was found that adding HCl alone to their syntheses was enough to reliably produce phase pure samples. The true modulating ability of amino acids, in particular L-proline (in concert with HCl), was obvious when MOFs containing longer ligands (L5-L8) were examined, resulting in great improvements in crystallinity. The materials were characterised using a number of experimental techniques, and in all cases it was found that they were of high quality. Initially, 5 equivalents of L-proline were added to the syntheses, although further studies varying the concentration revealed that 4 equivalents were sufficient to produce highly crystalline samples. This represents a major reduction in comparison to the amount of conventional modulator (e.g. formic, acetic or benzoic acid) typically required for effective modulation (usually no less than 30 equivalents although often much larger excesses are used). Synthesising single crystals of Zr and Hf MOFs is typically a troublesome task however, the efficacy of L-proline as a modulator enabled 5 of the MOFs to be obtained as single crystals and subsequently their crystal structures were successfully determined using laboratory X-ray



sources. Accessing single crystals has been a major advancement for Zr and Hf MOFs, not only to gain improved structural information but also they have enabled specialised techniques to be used to investigate their mechanical properties. Using high-pressure single crystal X-ray diffraction and nanoindentation alongside computational studies it was revealed that subtle changes in ligand flexibility results in dramatically different mechanical behaviours of Zr MOFs.<sup>2</sup> This work was performed in collaboration with researchers from the Universities of Edinburgh and Cambridge and is not discussed in detail in this thesis.

In an attempt to further modulate the mechanical properties of Zr and Hf MOFs by controlling the degree of ligand flexibility a series of extended ligands containing alkyne and butadiyne units were designed, synthesised and reported in Chapter 2.<sup>3</sup> Butadiyne units are highly flexible, as shown by Anderson and co-workers who have used them for the construction of nanoring-based structures where the cyclic strain is adopted by the butadiyne units.<sup>4</sup> In-depth studies are currently underway to extend the initial collaborative investigation into the mechanical properties of Zr MOFs, to include the extended derivatives while the Hf derivatives are also being examined.

The L-proline modulation protocol developed in Chapter 2 has been imperative for the successful syntheses of Zr and Hf MOFs containing the extended ligands as both bulk microcrystalline powders and single crystals. All the ligands examined throughout this thesis are linear, and L-proline appears to be an effective modulator for these systems however, it would be useful to try and adapt these conditions to the synthesis of Zr MOFs with alternative topologies.

The extended MOFs are structurally very interesting, and it was revealed that **Zr-L10** is the most porous UiO-66 type MOF reported to date as the longer ligand, L11, results in a 2-fold interpenetrated structure.<sup>5</sup> The flexible nature of L11 when contained within Zr and Hf MOFs is evident from their single crystal structures, which reveal that the ligand adopts a bowed geometry. Aside from flexibility, it is expected that interpenetration will affect the mechanical properties of the MOFs and this phenomenon will also be investigated in the future.

However, with the MOFs in hand it was realised that the integral alkene and alkyne units present sites for potential covalent transformation, hence this was investigated and

subsequently reported in Chapter 3. Unlike previous unsuccessful attempts to brominate stilbene units within a Zn MOF,<sup>6</sup> **Zr-L8** could be quantitatively brominated by immersion in a chloroform solution containing neat Br<sub>2</sub> and stored in the dark for 48 hours.<sup>7</sup> The quantitative nature of the transformation was confirmed using a number of experimental techniques, including <sup>1</sup>H and <sup>13</sup>C NMR spectroscopies, thermogravimetric analysis, elemental bromine analysis and N<sub>2</sub> uptake measurements. The transformation could also be performed in a single-crystal to single-crystal manner, proving the high mechanical and chemical stability of **Zr-L8**, while combined with NMR analysis exclusive formation of the *meso*-dibromoalkane product was confirmed. In contrast, the corresponding solution phase reaction of L8-Me<sub>2</sub> is non-stereoselective and the enhanced stereoselectivity observed is due to the restricted conformational freedom of the ligand when contained within the MOF, confirming that the transformation occurs on the solid-phase material.<sup>6</sup> Upon transforming the alkene units to dibromoalkane units, the hybridisation of the integral carbon atoms changes from sp<sup>2</sup> to sp<sup>3</sup>. An alkane bridged ligand was synthesised and investigated for its ability to be incorporated into a Zr MOF, however the high conformational freedom of the ligand disrupted MOF formation, proving that postsynthetic modification (PSM) has been used to provide access to otherwise inaccessible MOF structures. The reactivity of the double bond was also examined using *N*-bromosuccinimide as a bromine source and it was found that both brominated and bromohydrinated products were obtained.<sup>3</sup> Bromohydration (dual addition of Br and OH across the double bond) is an interesting route for the introduction of OH groups within MOFs as they can be difficult to introduce during direct synthesis as they often compete for attachment to the metal clusters.<sup>8</sup>

It is the high mechanical and chemical stability of **Zr-L8** that enabled the alkene units to be quantitatively brominated, and so the alkyne containing MOFs were then considered for their ability to undergo similar transformations.<sup>3,9</sup> The reaction conditions proved to be successful for the PSM of alkyne units to dibromoalkene units within the MOFs. During the transformation, the hybridisation of the integral carbon atoms changes from sp to sp<sup>2</sup>, resulting in changes to both ligand length and geometry. Again, the transformations were observed to be stereoselective within the MOF, resulting exclusively in the *trans*-dibromoalkene products, in comparison to the mixture of *cis* and *trans* products obtained from the corresponding reaction on the esters of the ligands. The transformation from alkyne to *trans*-dibromoalkene results in a mechanical contraction of the MOFs, and single crystal X-ray diffraction reveals that during bromination of **Zr-L11** and **Hf-L11** (containing 2

alkyne units per ligand) the unit cell edge  $a$  contracts by  $\sim 0.75$  Å. The ability of the MOFs to withstand such large mechanical contractions again demonstrates their high mechanical stabilities, while the ability to tolerate highly corrosive bromine solutions proves their high chemical stabilities.

Integral postsynthetic bromination of alkene and alkyne units within Zr MOFs demonstrated their ability to undergo covalent modification and so their reactivity with vapour phase iodine was investigated. Using both gravimetric uptake measurements and  $^1\text{H}$  NMR analysis of digested MOF samples it was possible to determine both physisorption (reversible) and chemisorption (irreversible) storage capacities. The double bonds in **Zr-L8** did not undergo covalent modification with vapour phase iodine however, the alkyne units were able to be iodinated. The 2-fold interpenetrated MOF, **Zr-L11**, was able to take up as much as 279%  $w/w$   $\text{I}_2$ , which is a considerable amount and suggests the possible use of these MOFs for the capture and sequestration of radioactive iodine released during nuclear accidents. It has been demonstrated that the unsaturated functionality, despite being a structural component of the MOFs, are able to be postsynthetically modified, however future studies could aim to introduce a wider range of functionality for instance using thiol-ene or thiol-yne type additions.

In Chapter 4, six 4,4'-[1,4-phenylene-bis(ethyne-2,1-diyl)]-dibenzoate ( $\text{peb}^{2-}$ ) derivatives (**L12-L17**) containing a range of functionality, including pendent methyl, fluorine, naphthalene and benzothiadiazole moieties were synthesised and incorporated into Zr and Hf MOFs.<sup>10</sup> Using either L-proline or benzoic acid modulation, 12 functionalised MOFs were obtained as highly crystalline powders, while fine-tuning reaction conditions resulted in the isolation of 11 of them as single crystals. Single crystal X-ray diffraction reveals that all but one of the MOFs crystallise in the  $Fd-3m$  space group while they all maintain the 2-fold interpenetration observed in the parent structures (**Zr-L11** and **Hf-L11**). Cubic symmetry is maintained in the MOFs containing the unsymmetrical ligands as the pendant functionality is disordered across both sides of the ligand. The most structurally interesting of the MOFs are **Zr-L16**, where the central naphthalene core twists out of the plane of conjugation by  $23^\circ$ , presumably to minimise steric interactions, and **Zr-L12** which is the exception and crystallises in the lower symmetry  $Imma$  space group. The lower symmetry of **Zr-L12** is attributed to steric clashes between pendant methyl groups and adjacent phenyl units of the other interpenetrated net, which are in close proximity, causing the central phenylene ring of

some of the ligands to adopt a twisted conformation. However, variable temperature powder X-ray diffraction reveals that **Zr-L12** is dynamic – the MOF transforms from orthorhombic to cubic symmetry upon heating.

The interpenetrated MOFs appear to be dynamic and in collaboration with the Moggach Group at the University of Edinburgh we have found that upon applying pressure to **Hf-L11** (diamond anvil cell, 1.4 GPa, *n*-pentane) the MOF undergoes a phase change, caused by a twisting of the central phenylene core of the ligands by  $\sim 90^\circ$ . It is interesting that in the case of **Zr-L12** host-host interactions perturb the usual MOF structure while in **Hf-L11** host-guest interactions cause a similar structural change. The dynamic behaviour of the functionalised derivatives is currently being investigated.

Lastly, solid state fluorescence emission spectroscopy, a technique that has rarely been used for the characterisation of MOFs, has provided insight into the ability of the functionalised MOFs to act as solid state sensors. **Zr-L16** and in particular **Zr-L17** have been shown to be highly sensitive to water, resulting in significant changes in their fluorescence emission profiles. This is in contrast to **Zr-L15** that does not appear to be affected by wetting. Contact angle measurements revealed that incorporating fluorine atoms onto the ligand scaffold results in a superhydrophobic MOF, meaning that water cannot penetrate into the pores and hence no change in fluorescence emission is observed.

MOFs are receiving widespread attention by the scientific community and Zr MOFs are amongst the most typically studied materials as a result of their high chemical<sup>11</sup> and mechanical<sup>12</sup> stabilities, which have been proven by their ability to undergo integral postsynthetic modifications. It has been shown within this thesis that L-proline has successfully modulated Zr and Hf MOFs containing a variety of ligands, both in terms of their length and chemical functionality, and therefore it is reasonable to assume that other researchers will now consider L-proline as a modulator.<sup>13</sup> Hf MOFs are reported less frequently than Zr MOFs, although it has been shown that these MOFs possess many of the desired properties of their Zr counterparts and therefore it is anticipated that interest in Hf MOFs will increase in the future. The interpenetrated family of MOFs had received little interest since their discovery until recently,<sup>14,15</sup> while we have found that they are much more dynamic than may be anticipated and that they hold great potential for sensing applications.

To conclude, this thesis presents a significant advancement towards the synthetic capabilities of Zr and Hf MOFs. It has been shown that Zr and Hf MOFs are prime candidates for the introduction of functionality by postsynthetic modification. Finally, the improved synthetic procedure has been used to synthesise a range of functionalised 2-fold interpenetrated Zr and Hf MOFs that demonstrate interesting structural and physical properties. Therefore, as a whole this thesis details aspects concerning the synthesis, postsynthetic modification and functionalisation of highly interesting Zr and Hf MOFs.

## 5.2 References

- (1) Marshall, R. J.; Hobday, C. L.; Murphie, C. F.; Griffin, S. L.; Morrison, C. A.; Moggach, S. A.; Forgan, R. S. *J. Mater. Chem. A* **2016**, *4*, 6955.
- (2) Hobday, C. L.; Marshall, R. J.; Murphie, C. F.; Sotelo, J.; Richards, T.; Allan, D. R.; Düren, T.; Coudert, F.-X.; Forgan, R. S.; Morrison, C. A.; Moggach, S. A.; Bennett, T. D. *Angew. Chem. Int. Ed.* **2016**, *55*, 2401.
- (3) Marshall, R. J.; Griffin, S. L.; Wilson, C.; Forgan, R. S. *Chem. Eur. J.* **2016**, *22*, 4870.
- (4) O'Sullivan, M. C.; Sprafke, J. K.; Kondratuk, D. V.; Rinfray, C.; Claridge, T. D. W.; Saywell, A.; Blunt, M. O.; O'Shea, J. N.; Beton, P. H.; Malfois, M.; Anderson, H. L. *Nature* **2011**, *469*, 72.
- (5) Schaate, A.; Roy, P.; Preuße, T.; Lohmeier, S. J.; Godt, A.; Behrens, P. *Chem. Eur. J.* **2011**, *17*, 9320.
- (6) Jones, S. C.; Bauer, C. A. *J. Am. Chem. Soc.* **2009**, *131*, 12516.
- (7) Marshall, R. J.; Richards, T.; Hobday, C. L.; Murphie, C. F.; Wilson, C.; Moggach, S. A.; Bennett, T. D.; Forgan, R. S. *Dalton Trans.* **2016**, *45*, 4132.
- (8) Dietzel, P. D. C.; Johnsen, R. E.; Blom, R.; Fjellvåg, H. *Chem. Eur. J.* **2008**, *14*, 2389.
- (9) Marshall, R. J.; Griffin, S. L.; Wilson, C.; Forgan, R. S. *J. Am. Chem. Soc.* **2015**, *137*, 9527.
- (10) Marshall, R. J.; Kalinovsky, Y.; Griffin, S. L.; Wilson, C.; Blight, B. A.; Forgan, R. S. *J. Am. Chem. Soc.* **2017**, DOI: 10.1021/jacs.7b02184.
- (11) Kandiah, M.; Nilsen, M. H.; Usseglio, S.; Jakobsen, S.; Olsbye, U.; Tilset, M.; Larabi, C.; Quadrelli, E. A.; Bonino, F.; Lillerud, K. P. *Chem. Mater.* **2010**, *22*, 6632.
- (12) Wu, H.; Yildirim, T.; Zhou, W. *J. Phys. Chem. Lett.* **2013**, *4*, 925.
- (13) Gutov, O. V.; Molina, S.; Escudero-Adán, E. C.; Shafir, A. *Chem. Eur. J.* **2016**, *22*, 13582.
- (14) Babarao, R.; Rubio-Martinez, M.; Hill, M. R.; Thornton, A. W. *J. Phys. Chem. C* **2016**, *120*, 13013.
- (15) Chen, D.; Xing, H.; Wang, C.; Su, Z. *J. Mater. Chem. A* **2016**, *4*, 2657.

## **Chapter 6**

## **Appendix**

## Contents

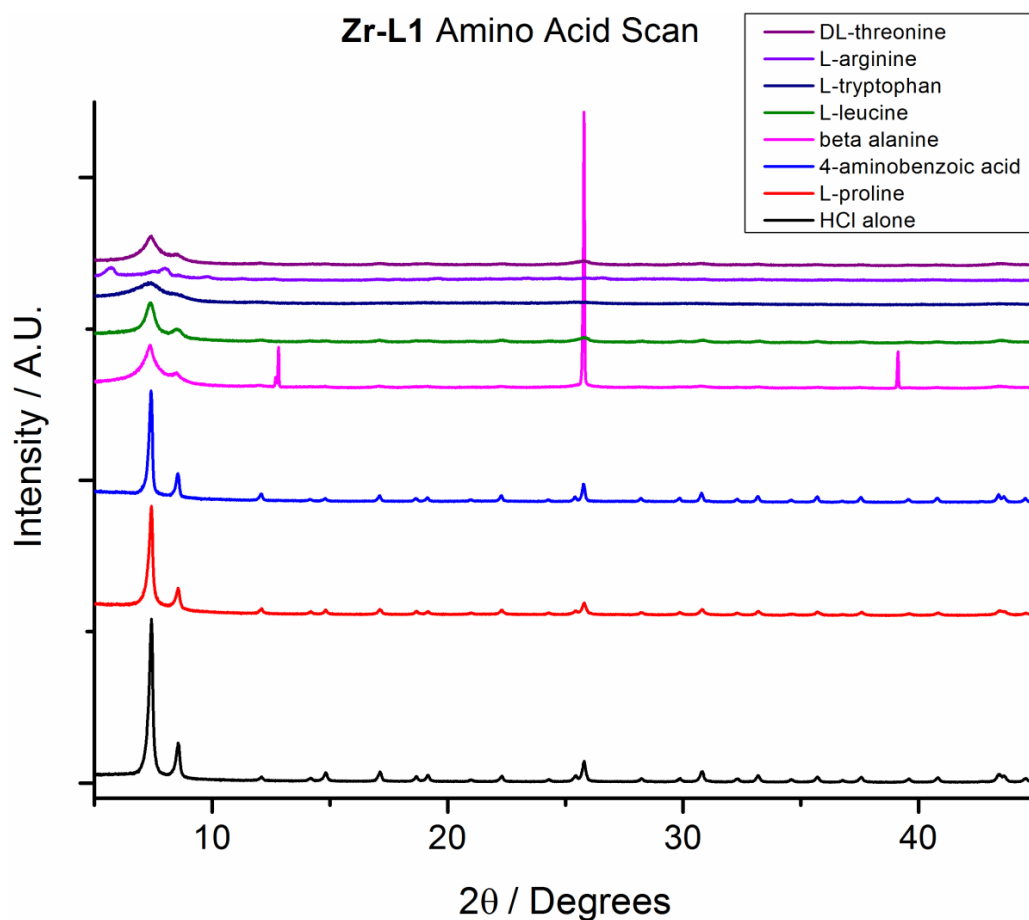
<b>Chapter 6 .....</b>	<b>236</b>
<b>6.1 Chapter 2 Supplementary Material .....</b>	<b>238</b>
<b>6.2 Chapter 3 Supplementary Material .....</b>	<b>258</b>
<b>6.3 Chapter 4 Supplementary Material .....</b>	<b>264</b>



## 6.1 Chapter 2 Supplementary Material

**Table 6.1.** Amino acid modulated synthesis of **Zr-L1**.

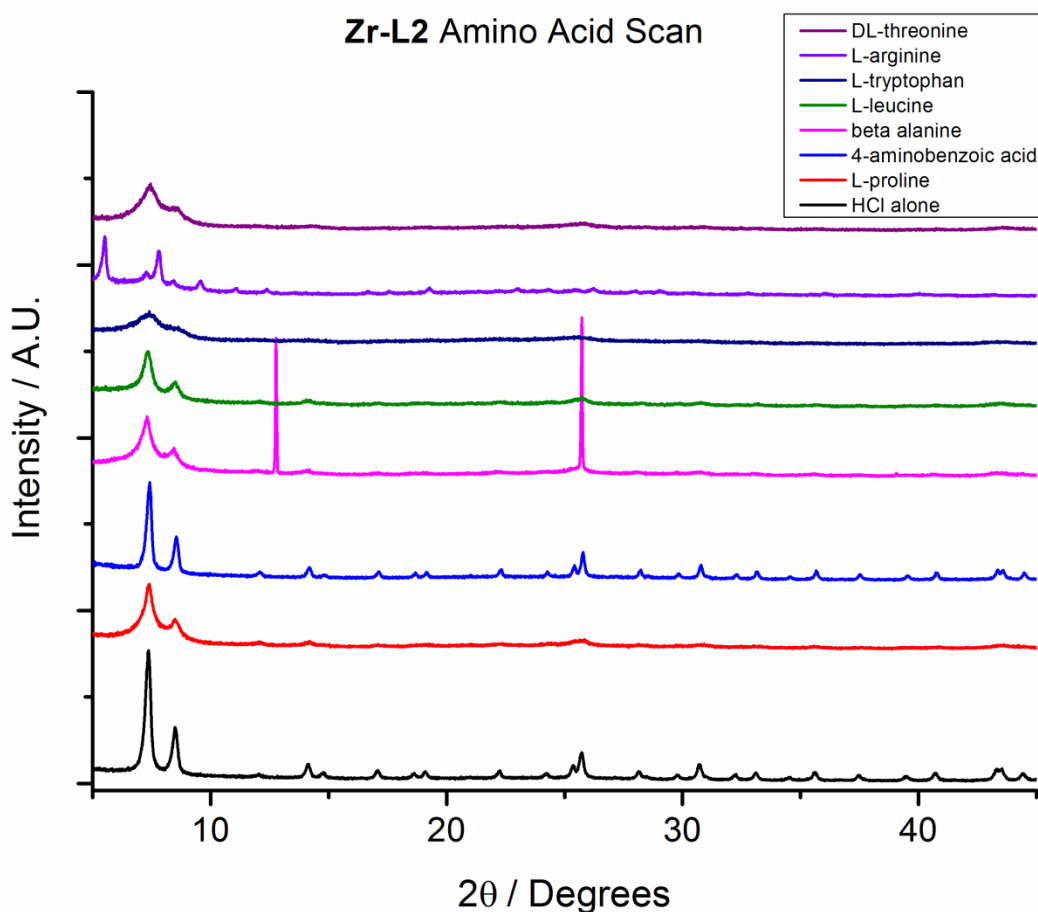
L1		ZrCl <sub>4</sub>		HCl	Modulator		
Moles (mmol)	Mass (g)	Moles (mmol)	Mass (g)	Volume (ml)	Amino Acid	Moles (mmol)	Mass (g)
0.45	0.0748	0.45	0.1049	0.04	unmodulated		
0.45	0.0748	0.45	0.1049	0.04	L-proline	2.25	0.2590
0.45	0.0748	0.45	0.1049	0.04	PABA	2.25	0.3086
0.45	0.0748	0.45	0.1049	0.04	beta alanine	2.25	0.2005
0.45	0.0748	0.45	0.1049	0.04	L-leucine	2.25	0.2952
0.45	0.0748	0.45	0.1049	0.04	L-tryptophan	2.25	0.4595
0.45	0.0748	0.45	0.1049	0.04	L-arginine	2.25	0.3920
0.45	0.0748	0.45	0.1049	0.04	DL-threonine	2.25	0.2680



**Figure 6.1.** Stacked PXRD patterns for amino acid modulated syntheses of **Zr-L1**.

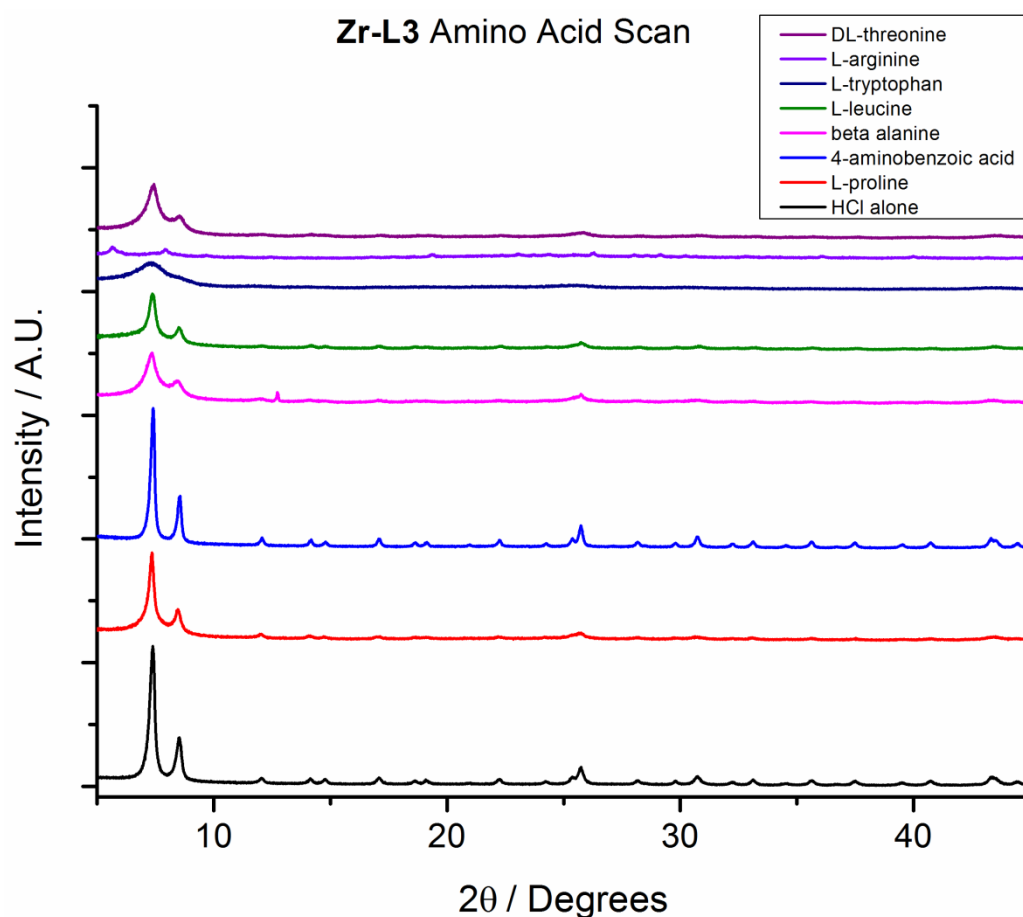
**Table 6.2.** Amino acid modulated synthesis of **Zr-L2**.

<b>L2</b>		<b>ZrCl<sub>4</sub></b>		<b>HCl</b>	<b>Modulator</b>		
<b>Moles (mmol)</b>	<b>Mass (g)</b>	<b>Moles (mmol)</b>	<b>Mass (g)</b>	<b>Volume (ml)</b>	<b>Amino Acid</b>	<b>Moles (mmol)</b>	<b>Mass (g)</b>
0.45	0.1103	0.45	0.1049	0.04	unmodulated		
0.45	0.1103	0.45	0.1049	0.04	L-proline	2.25	0.2590
0.45	0.1103	0.45	0.1049	0.04	PABA	2.25	0.3086
0.45	0.1103	0.45	0.1049	0.04	beta alanine	2.25	0.2005
0.45	0.1103	0.45	0.1049	0.04	L-leucine	2.25	0.2952
0.45	0.1103	0.45	0.1049	0.04	L-tryptophan	2.25	0.4595
0.45	0.1103	0.45	0.1049	0.04	L-arginine	2.25	0.3920
0.45	0.1103	0.45	0.1049	0.04	DL-threonine	2.25	0.2680

**Figure 6.2.** Stacked PXRD patterns for amino acid modulated syntheses of **Zr-L2**.

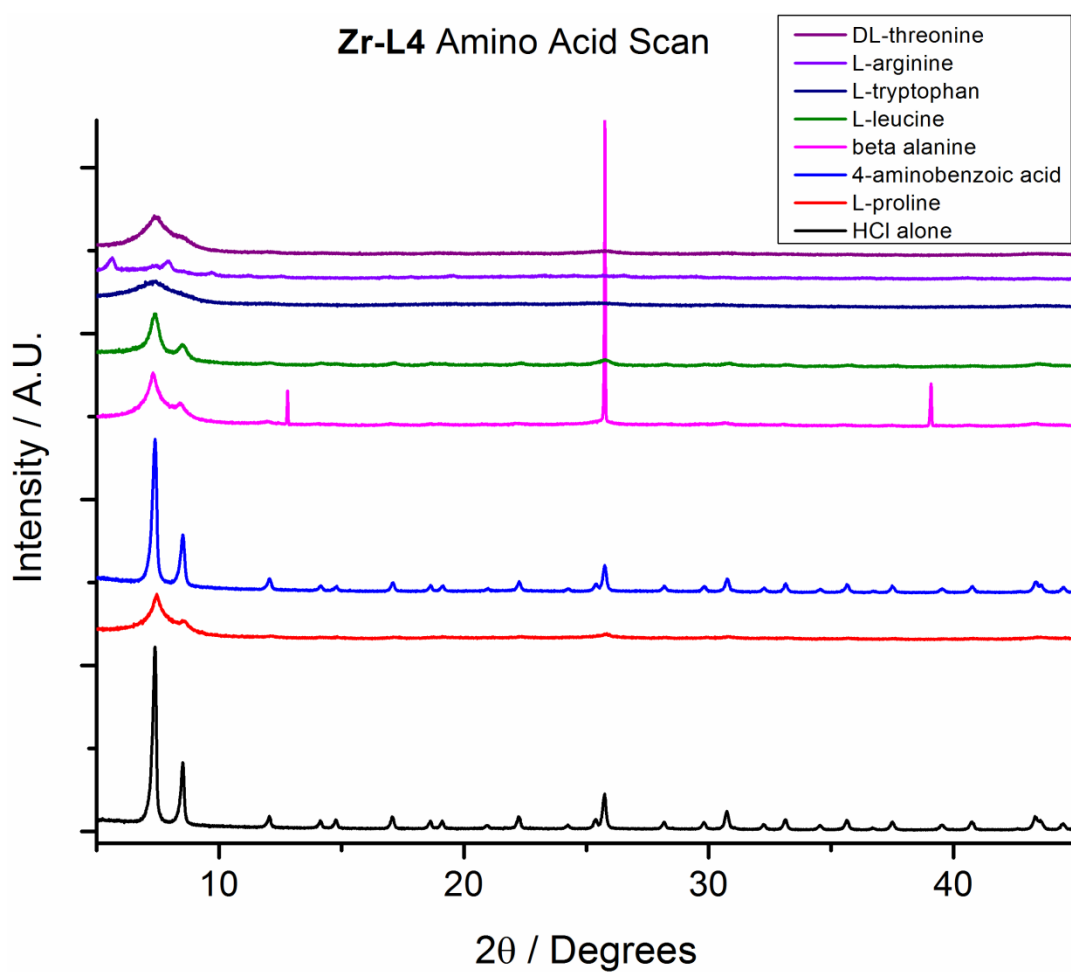
**Table 6.3.** Amino acid modulated synthesis of **Zr-L3**.

L3		ZrCl <sub>4</sub>		HCl	Modulator		
Moles (mmol)	Mass (g)	Moles (mmol)	Mass (g)	Volume (ml)	Amino Acid	Moles (mmol)	Mass (g)
0.45	0.0950	0.45	0.1049	0.04	unmodulated		
0.45	0.0950	0.45	0.1049	0.04	L-proline	2.25	0.2590
0.45	0.0950	0.45	0.1049	0.04	PABA	2.25	0.3086
0.45	0.0950	0.45	0.1049	0.04	beta alanine	2.25	0.2005
0.45	0.0950	0.45	0.1049	0.04	L-leucine	2.25	0.2952
0.45	0.0950	0.45	0.1049	0.04	L-tryptophan	2.25	0.4595
0.45	0.0950	0.45	0.1049	0.04	L-arginine	2.25	0.3920
0.45	0.0950	0.45	0.1049	0.04	DL-threonine	2.25	0.2680

**Figure 6.3.** Stacked PXRD patterns for amino acid modulated syntheses of **Zr-L3**.

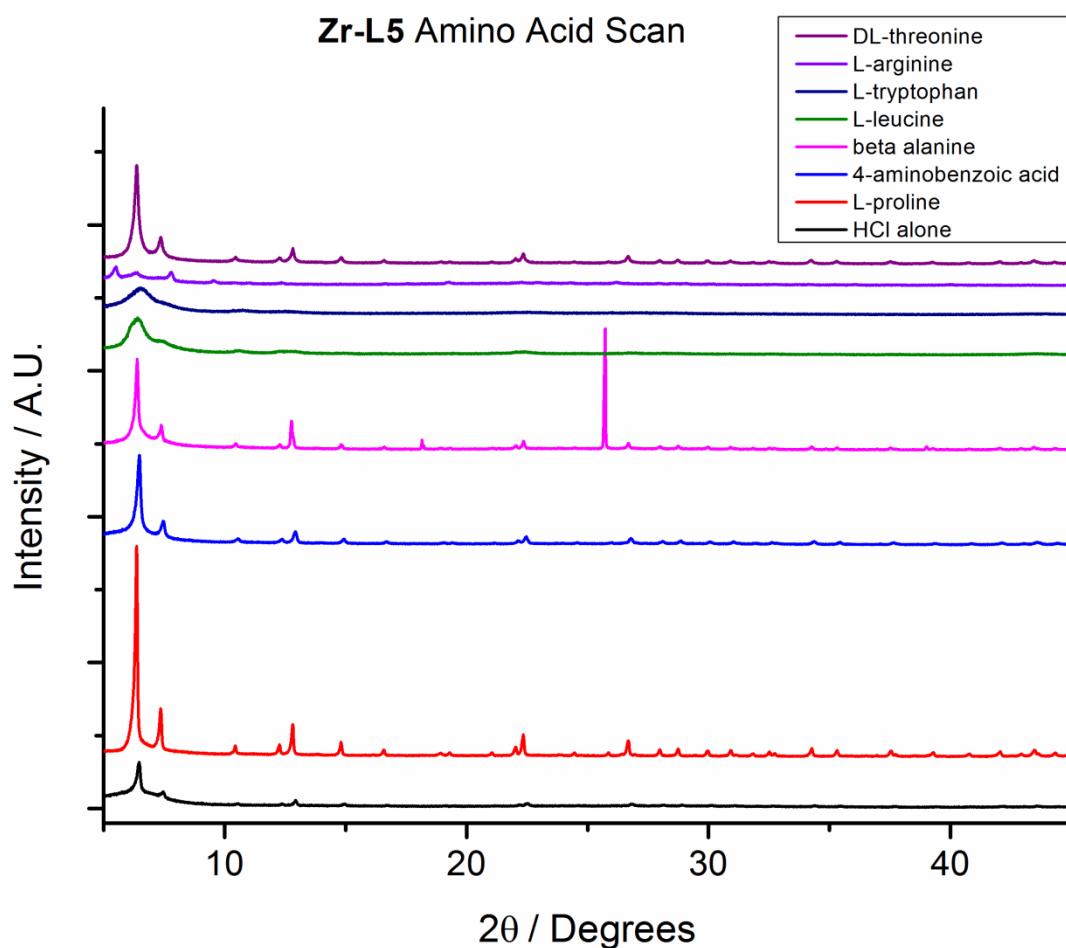
**Table 6.4.** Amino acid modulated synthesis of **Zr-L4**.

<b>L4</b>		<b>ZrCl<sub>4</sub></b>		<b>HCl</b>	<b>Modulator</b>		
<b>Moles (mmol)</b>	<b>Mass (g)</b>	<b>Moles (mmol)</b>	<b>Mass (g)</b>	<b>Volume (ml)</b>	<b>Amino Acid</b>	<b>Moles (mmol)</b>	<b>Mass (g)</b>
0.45	0.0815	0.45	0.1049	0.04	unmodulated		
0.45	0.0815	0.45	0.1049	0.04	L-proline	2.25	0.2590
0.45	0.0815	0.45	0.1049	0.04	PABA	2.25	0.3086
0.45	0.0815	0.45	0.1049	0.04	beta alanine	2.25	0.2005
0.45	0.0815	0.45	0.1049	0.04	L-leucine	2.25	0.2952
0.45	0.0815	0.45	0.1049	0.04	L-tryptophan	2.25	0.4595
0.45	0.0815	0.45	0.1049	0.04	L-arginine	2.25	0.3920
0.45	0.0815	0.45	0.1049	0.04	DL-threonine	2.25	0.2680

**Figure 6.4.** Stacked PXRD patterns for amino acid modulated syntheses of **Zr-L4**.

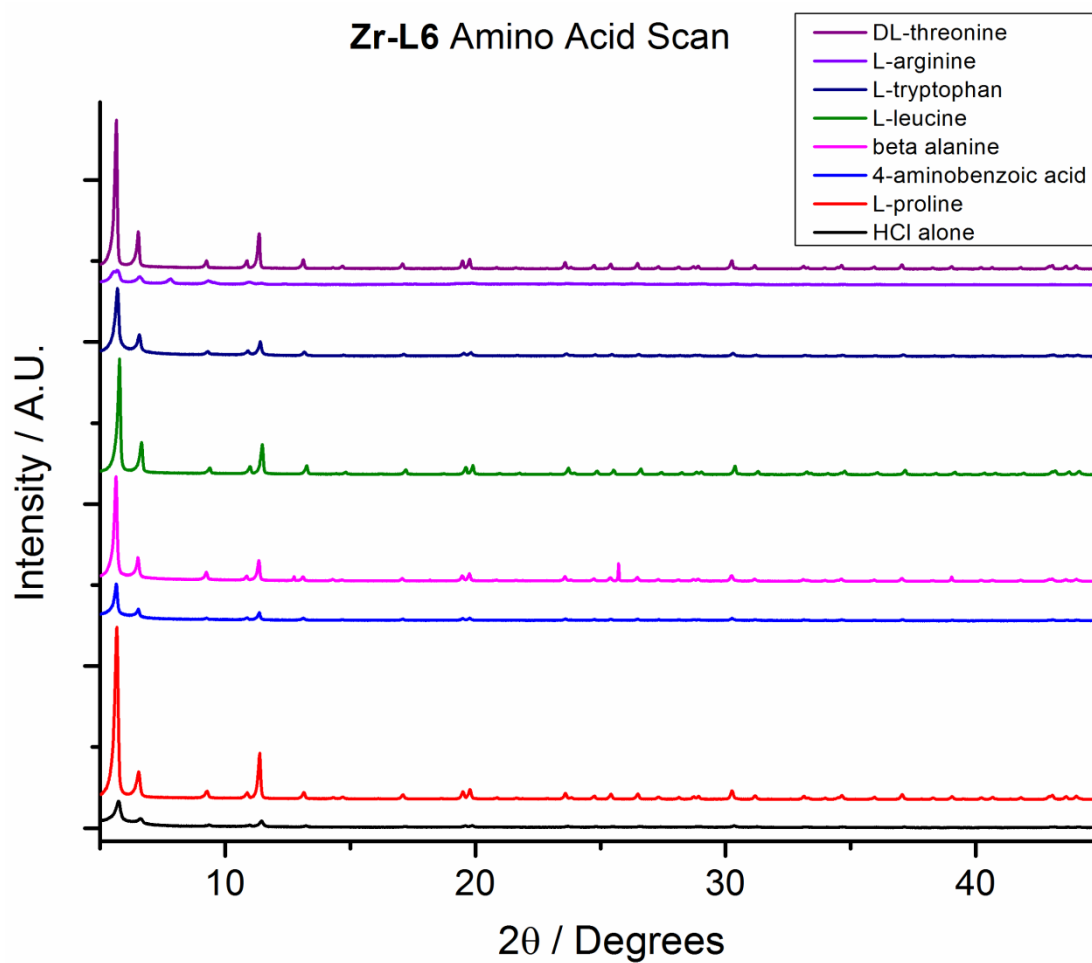
**Table 6.5.** Amino acid modulated synthesis of **Zr-L5**.

<b>L5</b>		<b>ZrCl<sub>4</sub></b>		<b>HCl</b>	<b>Modulator</b>		
<b>Moles (mmol)</b>	<b>Mass (g)</b>	<b>Moles (mmol)</b>	<b>Mass (g)</b>	<b>Volume (ml)</b>	<b>Amino Acid</b>	<b>Moles (mmol)</b>	<b>Mass (g)</b>
0.45	0.0973	0.45	0.1049	0.04	unmodulated		
0.45	0.0973	0.45	0.1049	0.04	L-proline	2.25	0.2590
0.45	0.0973	0.45	0.1049	0.04	PABA	2.25	0.3086
0.45	0.0973	0.45	0.1049	0.04	beta alanine	2.25	0.2005
0.45	0.0973	0.45	0.1049	0.04	L-leucine	2.25	0.2952
0.45	0.0973	0.45	0.1049	0.04	L-tryptophan	2.25	0.4595
0.45	0.0973	0.45	0.1049	0.04	L-arginine	2.25	0.3920
0.45	0.0973	0.45	0.1049	0.04	DL-threonine	2.25	0.2680

**Figure 6.5.** Stacked PXRD patterns for amino acid modulated syntheses of **Zr-L5**.

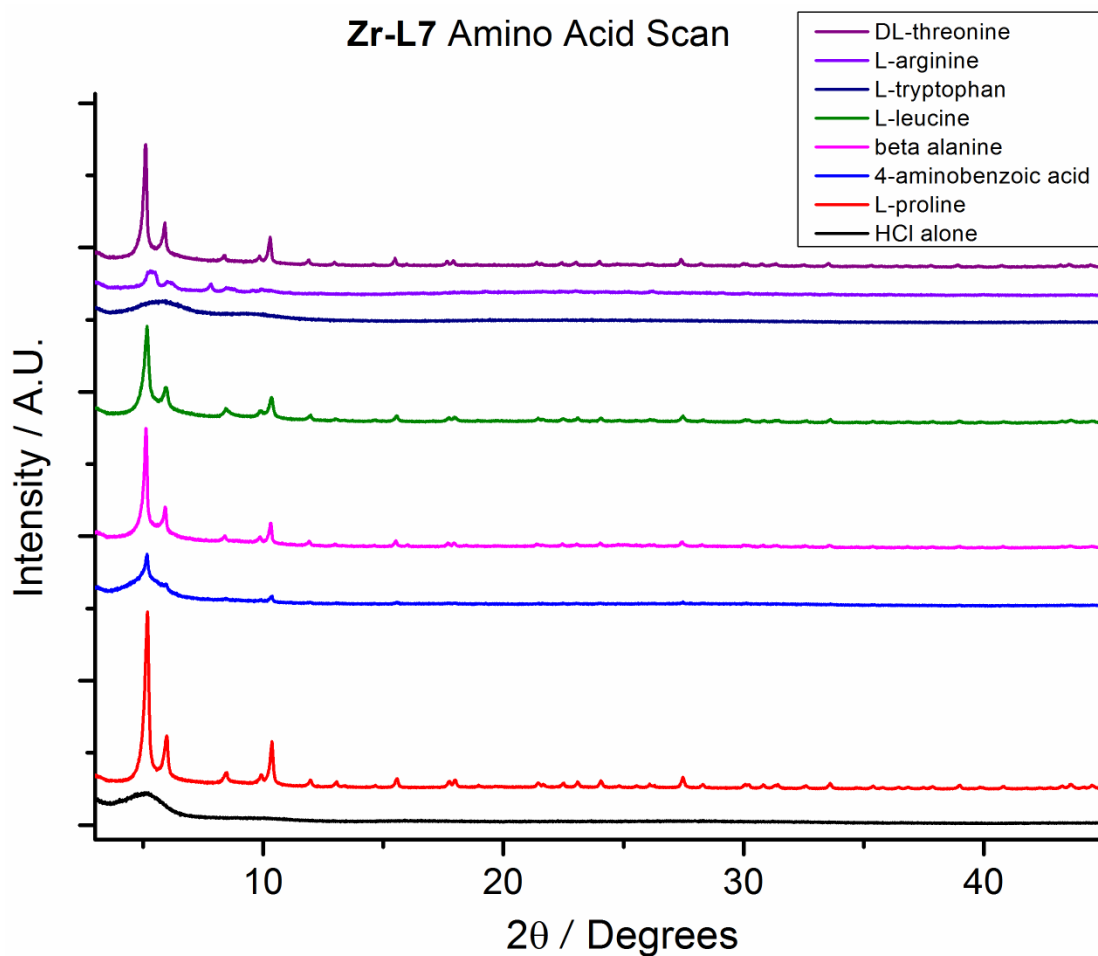
**Table 6.6.** Amino acid modulated synthesis of **Zr-L6**.

<b>L6</b>		<b>ZrCl<sub>4</sub></b>		<b>HCl</b>	<b>Modulator</b>		
<b>Moles (mmol)</b>	<b>Mass (g)</b>	<b>Moles (mmol)</b>	<b>Mass (g)</b>	<b>Volume (ml)</b>	<b>Amino Acid</b>	<b>Moles (mmol)</b>	<b>Mass (g)</b>
0.45	0.1090	0.45	0.1049	0.04	unmodulated		
0.45	0.1090	0.45	0.1049	0.04	L-proline	2.25	0.2590
0.45	0.1090	0.45	0.1049	0.04	PABA	2.25	0.3086
0.45	0.1090	0.45	0.1049	0.04	beta alanine	2.25	0.2005
0.45	0.1090	0.45	0.1049	0.04	L-leucine	2.25	0.2952
0.45	0.1090	0.45	0.1049	0.04	L-tryptophan	2.25	0.4595
0.45	0.1090	0.45	0.1049	0.04	L-arginine	2.25	0.3920
0.45	0.1090	0.45	0.1049	0.04	DL-threonine	2.25	0.2680

**Figure 6.6.** Stacked PXRD patterns for amino acid modulated syntheses of **Zr-L6**.

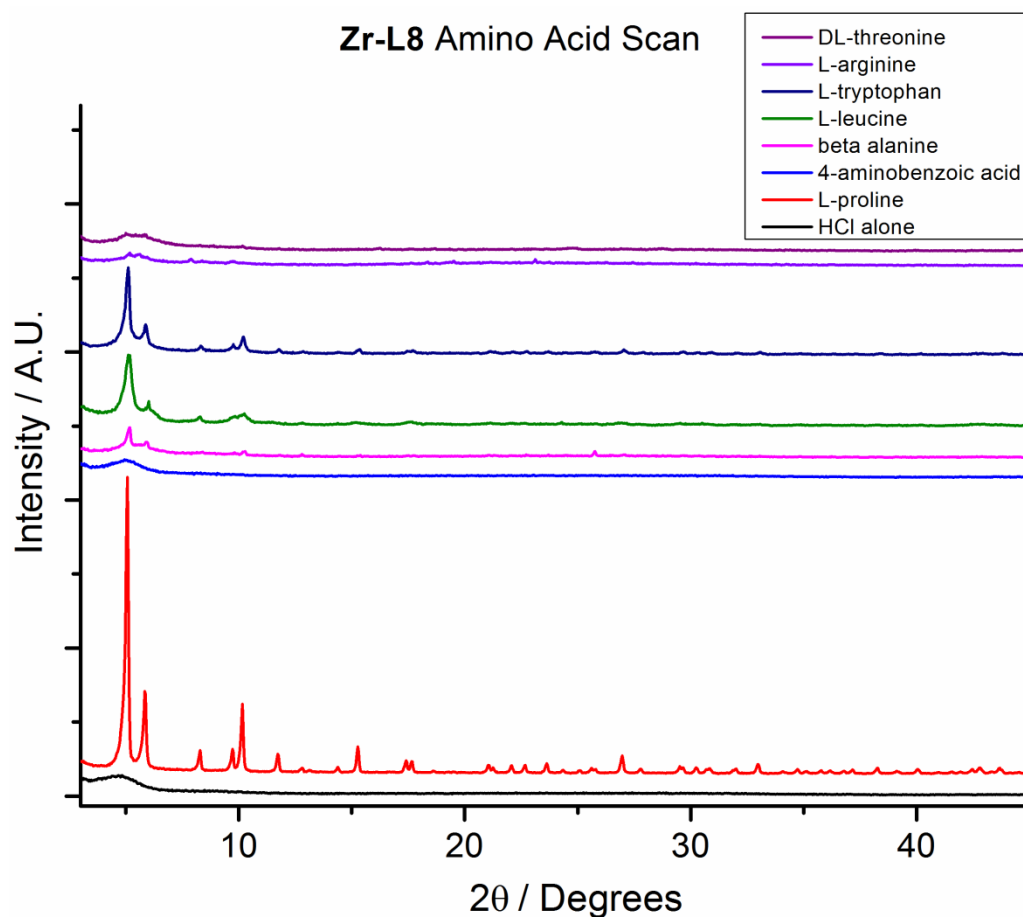
**Table 6.7.** Amino acid modulated synthesis of **Zr-L7**.

<b>L7</b>		<b>ZrCl<sub>4</sub></b>		<b>HCl</b>	<b>Modulator</b>		
<b>Moles (mmol)</b>	<b>Mass (g)</b>	<b>Moles (mmol)</b>	<b>Mass (g)</b>	<b>Volume (ml)</b>	<b>Amino Acid</b>	<b>Moles (mmol)</b>	<b>Mass (g)</b>
0.45	0.1216	0.45	0.1049	0.04	unmodulated		
0.45	0.1216	0.45	0.1049	0.04	L-proline	2.25	0.2590
0.45	0.1216	0.45	0.1049	0.04	PABA	2.25	0.3086
0.45	0.1216	0.45	0.1049	0.04	beta alanine	2.25	0.2005
0.45	0.1216	0.45	0.1049	0.04	L-leucine	2.25	0.2952
0.45	0.1216	0.45	0.1049	0.04	L-tryptophan	2.25	0.4595
0.45	0.1216	0.45	0.1049	0.04	L-arginine	2.25	0.3920
0.45	0.1216	0.45	0.1049	0.04	DL-threonine	2.25	0.2680

**Figure 6.7.** Stacked PXRD patterns for amino acid modulated syntheses of **Zr-L7**.

**Table 6.8.** Amino acid modulated synthesis of **Zr-L8**.

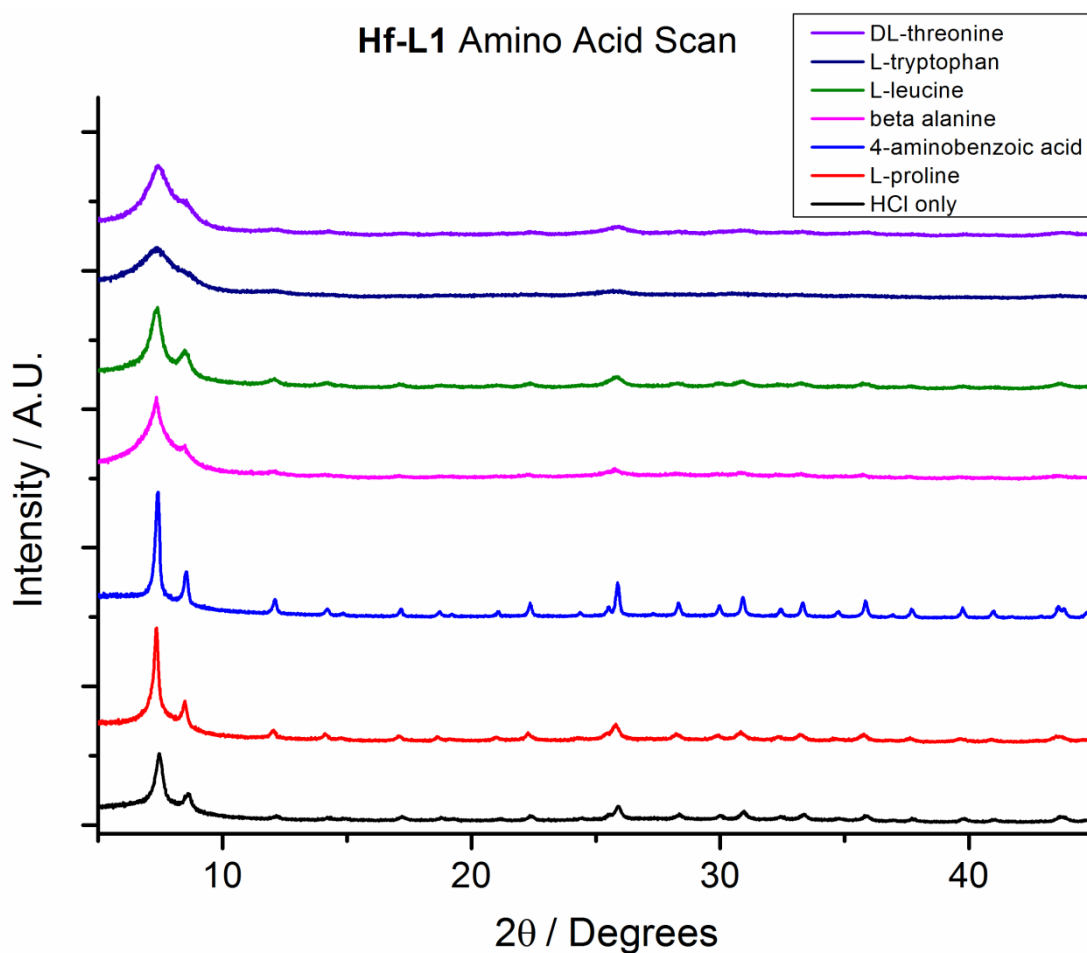
L8		ZrCl <sub>4</sub>		HCl	Modulator		
Moles (mmol)	Mass (g)	Moles (mmol)	Mass (g)	Volume (ml)	Amino Acid	Moles (mmol)	Mass (g)
0.45	0.1207	0.45	0.1049	0.04	unmodulated		
0.45	0.1207	0.45	0.1049	0.04	L-proline	2.25	0.2590
0.45	0.1207	0.45	0.1049	0.04	PABA	2.25	0.3086
0.45	0.1207	0.45	0.1049	0.04	beta alanine	2.25	0.2005
0.45	0.1207	0.45	0.1049	0.04	L-leucine	2.25	0.2952
0.45	0.1207	0.45	0.1049	0.04	L-tryptophan	2.25	0.4595
0.45	0.1207	0.45	0.1049	0.04	L-arginine	2.25	0.3920
0.45	0.1207	0.45	0.1049	0.04	DL-threonine	2.25	0.2680

**Figure 6.8.** Stacked PXRD patterns for amino acid modulated syntheses of **Zr-L8**.



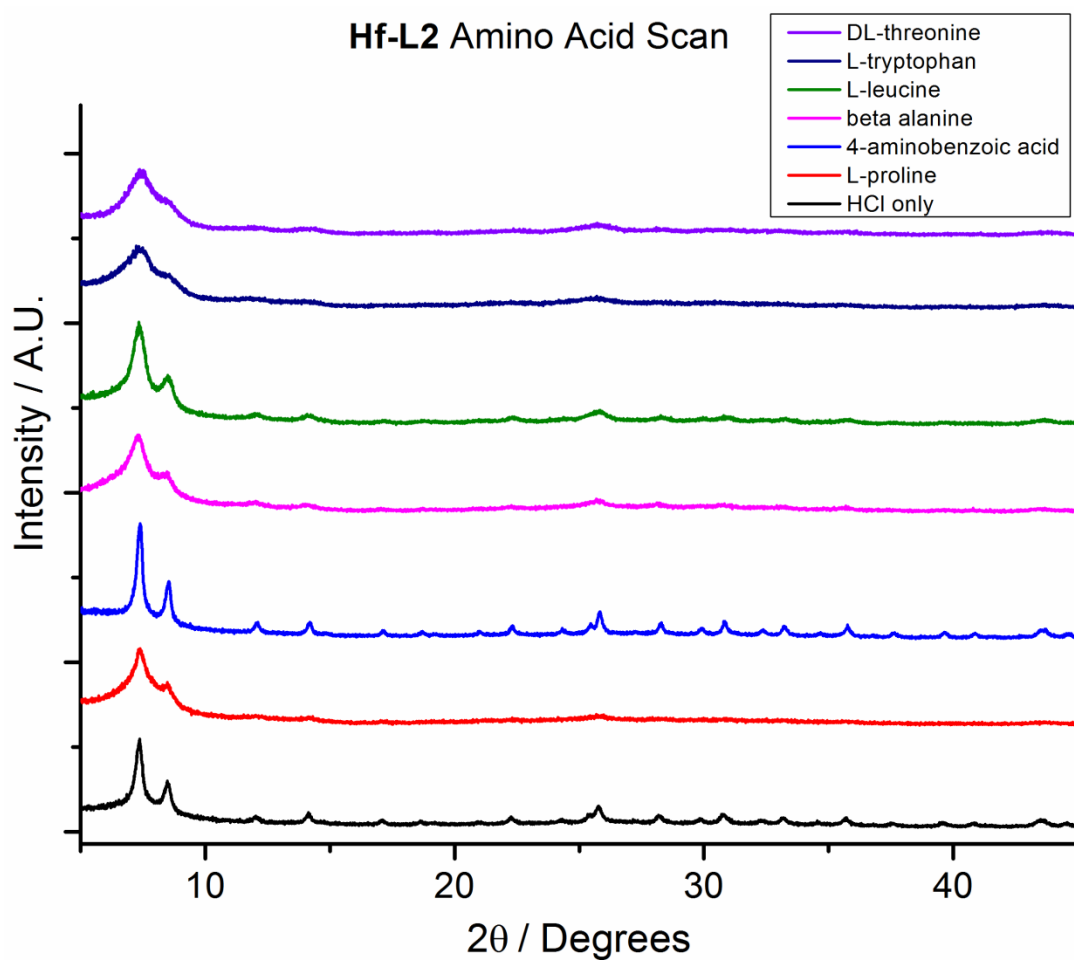
**Table 6.9.** Amino acid modulated synthesis of **Hf-L1**.

L1		HfCl <sub>4</sub>		HCl	Modulator		
Moles (mmol)	Mass (g)	Moles (mmol)	Mass (g)	Volume (ml)	Amino Acid	Moles (mmol)	Mass (g)
0.45	0.0748	0.45	0.1441	0.04	unmodulated		
0.45	0.0748	0.45	0.1441	0.04	L-proline	2.25	0.2590
0.45	0.0748	0.45	0.1441	0.04	PABA	2.25	0.3086
0.45	0.0748	0.45	0.1441	0.04	beta alanine	2.25	0.2005
0.45	0.0748	0.45	0.1441	0.04	L-leucine	2.25	0.2952
0.45	0.0748	0.45	0.1441	0.04	L-tryptophan	2.25	0.4595
0.45	0.0748	0.45	0.1441	0.04	L-arginine	2.25	0.3920
0.45	0.0748	0.45	0.1441	0.04	DL-threonine	2.25	0.2680

**Figure 6.9.** Stacked PXRD patterns for amino acid modulated syntheses of **Hf-L1**.

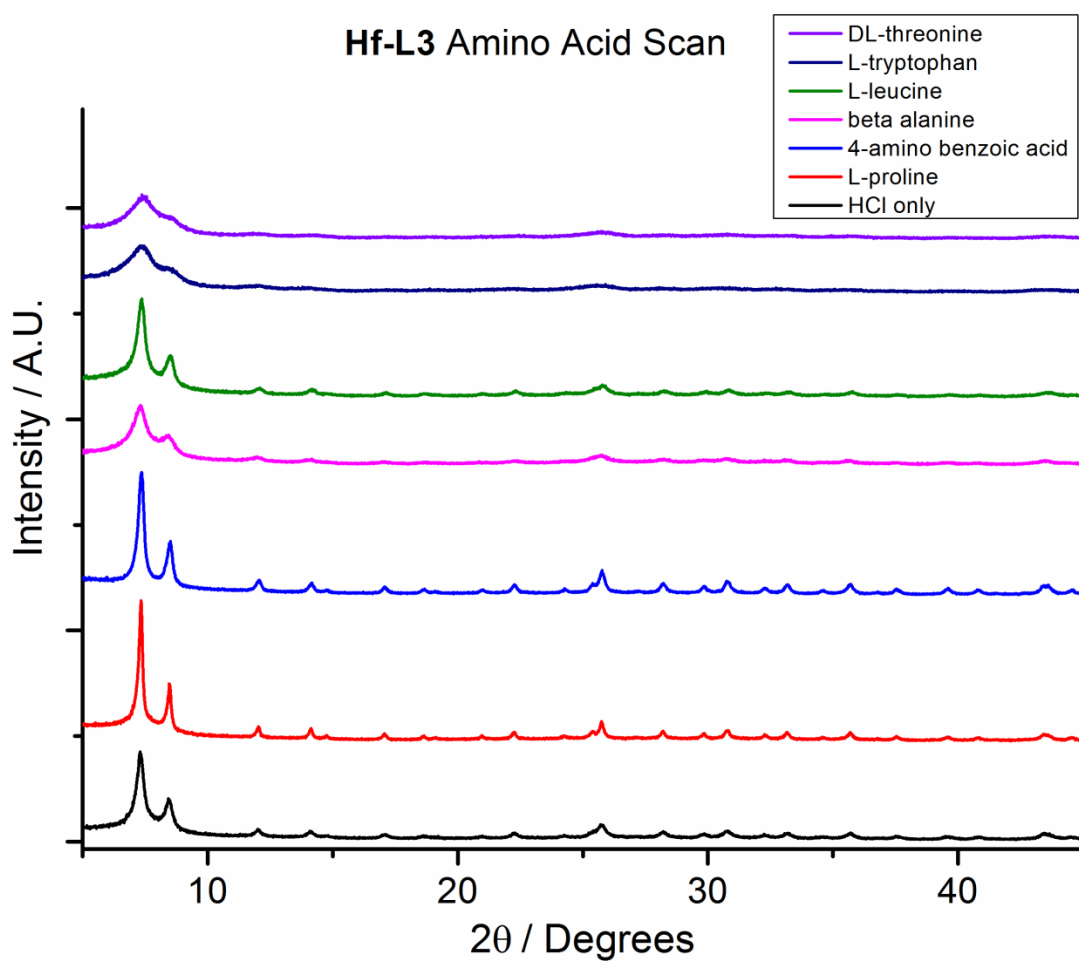
**Table 6.10.** Amino acid modulated synthesis of **Hf-L2**.

L2		HfCl <sub>4</sub>		HCl	Modulator		
Moles (mmol)	Mass (g)	Moles (mmol)	Mass (g)	Volume (ml)	Amino Acid	Moles (mmol)	Mass (g)
0.45	0.1103	0.45	0.1441	0.04	unmodulated		
0.45	0.1103	0.45	0.1441	0.04	L-proline	2.25	0.2590
0.45	0.1103	0.45	0.1441	0.04	PABA	2.25	0.3086
0.45	0.1103	0.45	0.1441	0.04	beta alanine	2.25	0.2005
0.45	0.1103	0.45	0.1441	0.04	L-leucine	2.25	0.2952
0.45	0.1103	0.45	0.1441	0.04	L-tryptophan	2.25	0.4595
0.45	0.1103	0.45	0.1441	0.04	L-arginine	2.25	0.3920
0.45	0.1103	0.45	0.1441	0.04	DL-threonine	2.25	0.2680

**Figure 6.10.** Stacked PXRD patterns for amino acid modulated syntheses of **Hf-L2**.

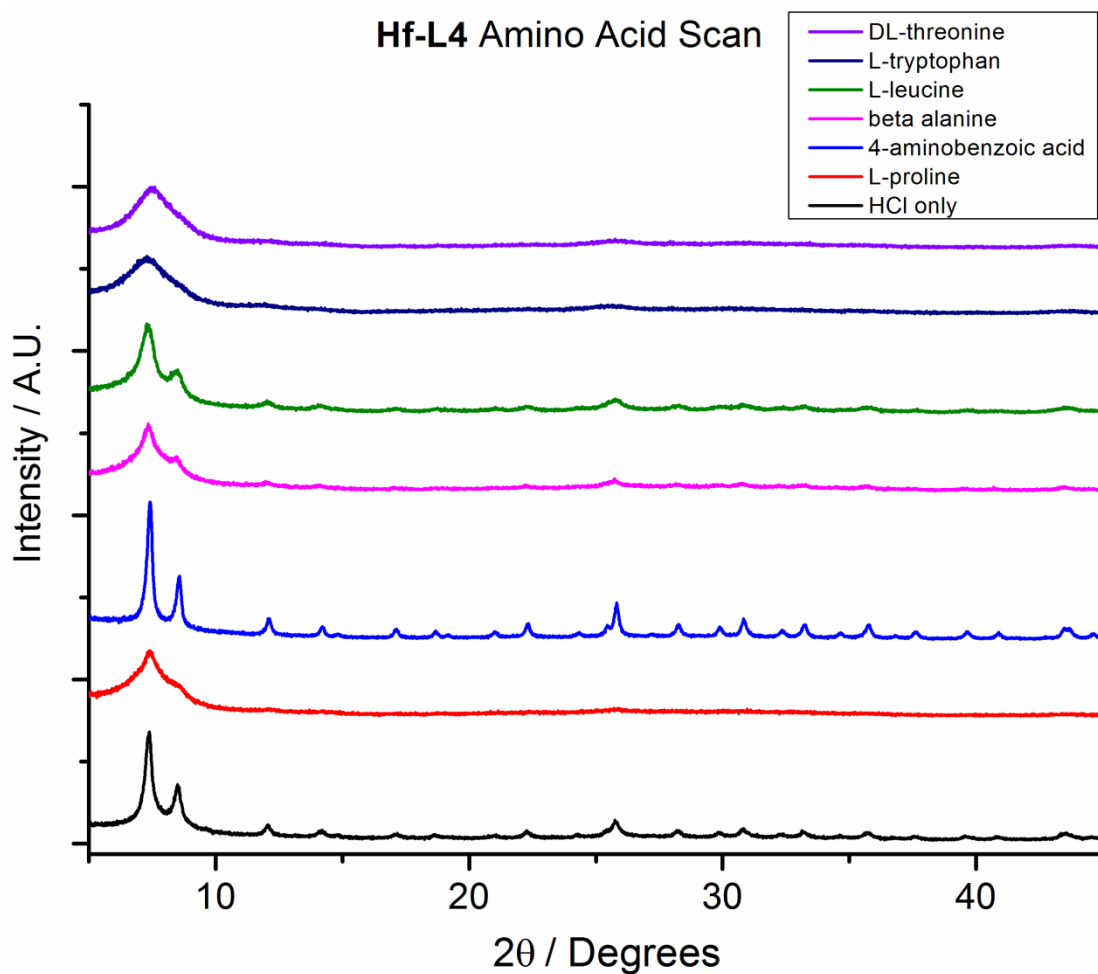
**Table 6.11.** Amino acid modulated synthesis of **Hf-L3**.

L3		HfCl <sub>4</sub>		HCl	Modulator		
Moles (mmol)	Mass (g)	Moles (mmol)	Mass (g)	Volume (ml)	Amino Acid	Moles (mmol)	Mass (g)
0.45	0.0950	0.45	0.1441	0.04	unmodulated		
0.45	0.0950	0.45	0.1441	0.04	L-proline	2.25	0.2590
0.45	0.0950	0.45	0.1441	0.04	PABA	2.25	0.3086
0.45	0.0950	0.45	0.1441	0.04	beta alanine	2.25	0.2005
0.45	0.0950	0.45	0.1441	0.04	L-leucine	2.25	0.2952
0.45	0.0950	0.45	0.1441	0.04	L-tryptophan	2.25	0.4595
0.45	0.0950	0.45	0.1441	0.04	L-arginine	2.25	0.3920
0.45	0.0950	0.45	0.1441	0.04	DL-threonine	2.25	0.2680

**Figure 6.11.** Stacked PXRD patterns for amino acid modulated syntheses of **Hf-L3**.

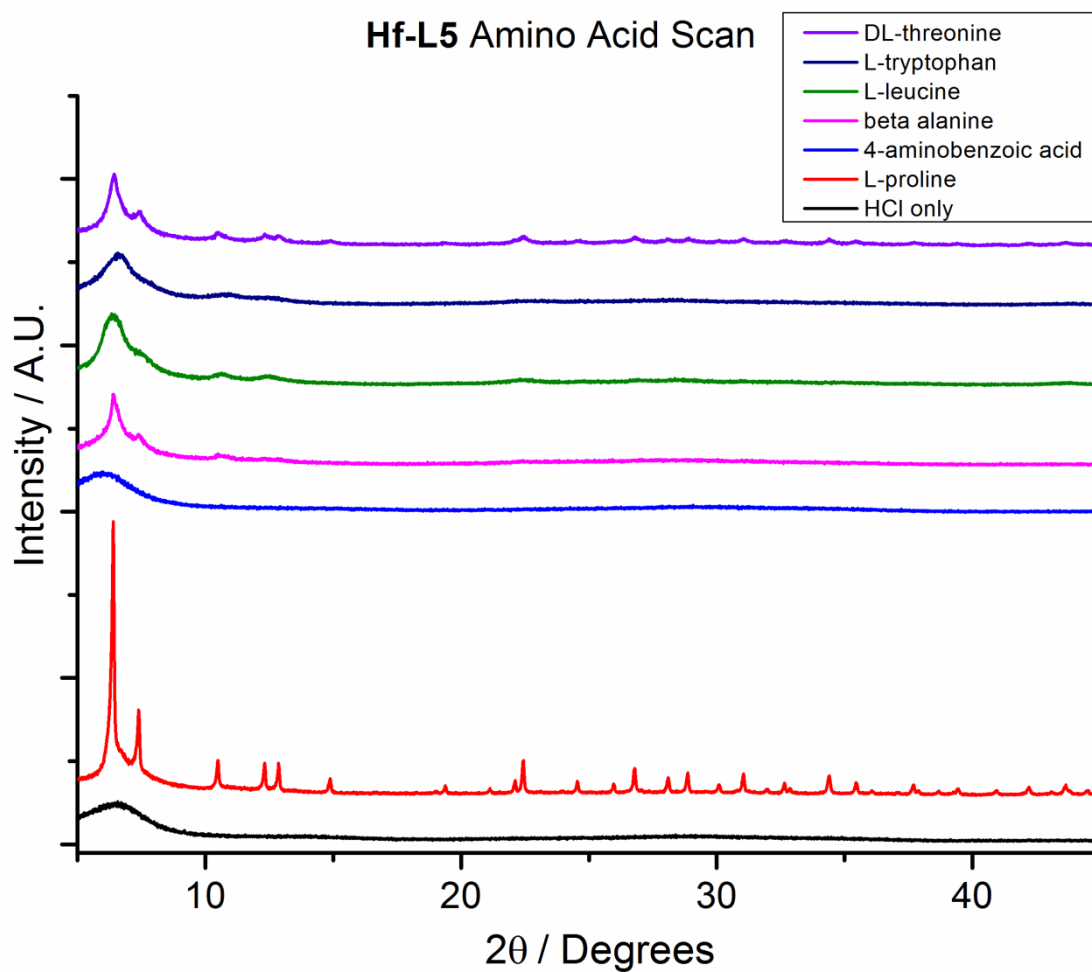
**Table 6.12.** Amino acid modulated synthesis of **Hf-L4**.

<b>L4</b>		<b>HfCl<sub>4</sub></b>		<b>HCl</b>	<b>Modulator</b>		
<b>Moles (mmol)</b>	<b>Mass (g)</b>	<b>Moles (mmol)</b>	<b>Mass (g)</b>	<b>Volume (ml)</b>	<b>Amino Acid</b>	<b>Moles (mmol)</b>	<b>Mass (g)</b>
0.45	0.0815	0.45	0.1441	0.04	unmodulated		
0.45	0.0815	0.45	0.1441	0.04	L-proline	2.25	0.2590
0.45	0.0815	0.45	0.1441	0.04	PABA	2.25	0.3086
0.45	0.0815	0.45	0.1441	0.04	beta alanine	2.25	0.2005
0.45	0.0815	0.45	0.1441	0.04	L-leucine	2.25	0.2952
0.45	0.0815	0.45	0.1441	0.04	L-tryptophan	2.25	0.4595
0.45	0.0815	0.45	0.1441	0.04	L-arginine	2.25	0.3920
0.45	0.0815	0.45	0.1441	0.04	DL-threonine	2.25	0.2680

**Figure 6.12.** Stacked PXRD patterns for amino acid modulated syntheses of **Hf-L4**.

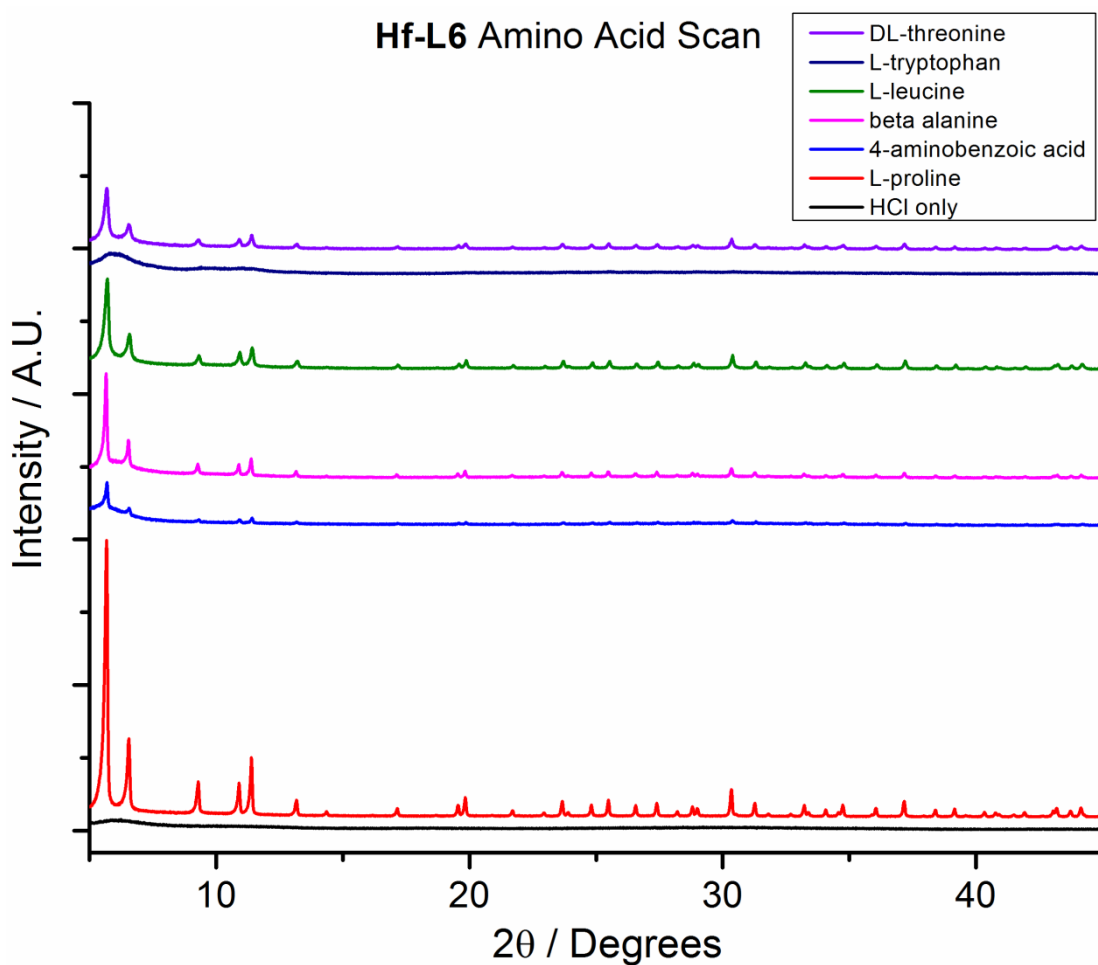
**Table 6.13.** Amino acid modulated synthesis of **Hf-L5**.

L5		HfCl <sub>4</sub>		HCl	Modulator		
Moles (mmol)	Mass (g)	Moles (mmol)	Mass (g)	Volume (ml)	Amino Acid	Moles (mmol)	Mass (g)
0.45	0.0973	0.45	0.1441	0.04	unmodulated		
0.45	0.0973	0.45	0.1441	0.04	L-proline	2.25	0.2590
0.45	0.0973	0.45	0.1441	0.04	PABA	2.25	0.3086
0.45	0.0973	0.45	0.1441	0.04	beta alanine	2.25	0.2005
0.45	0.0973	0.45	0.1441	0.04	L-leucine	2.25	0.2952
0.45	0.0973	0.45	0.1441	0.04	L-tryptophan	2.25	0.4595
0.45	0.0973	0.45	0.1441	0.04	L-arginine	2.25	0.3920
0.45	0.0973	0.45	0.1441	0.04	DL-threonine	2.25	0.2680

**Figure 6.13.** Stacked PXRD patterns for amino acid modulated syntheses of **Hf-L5**.

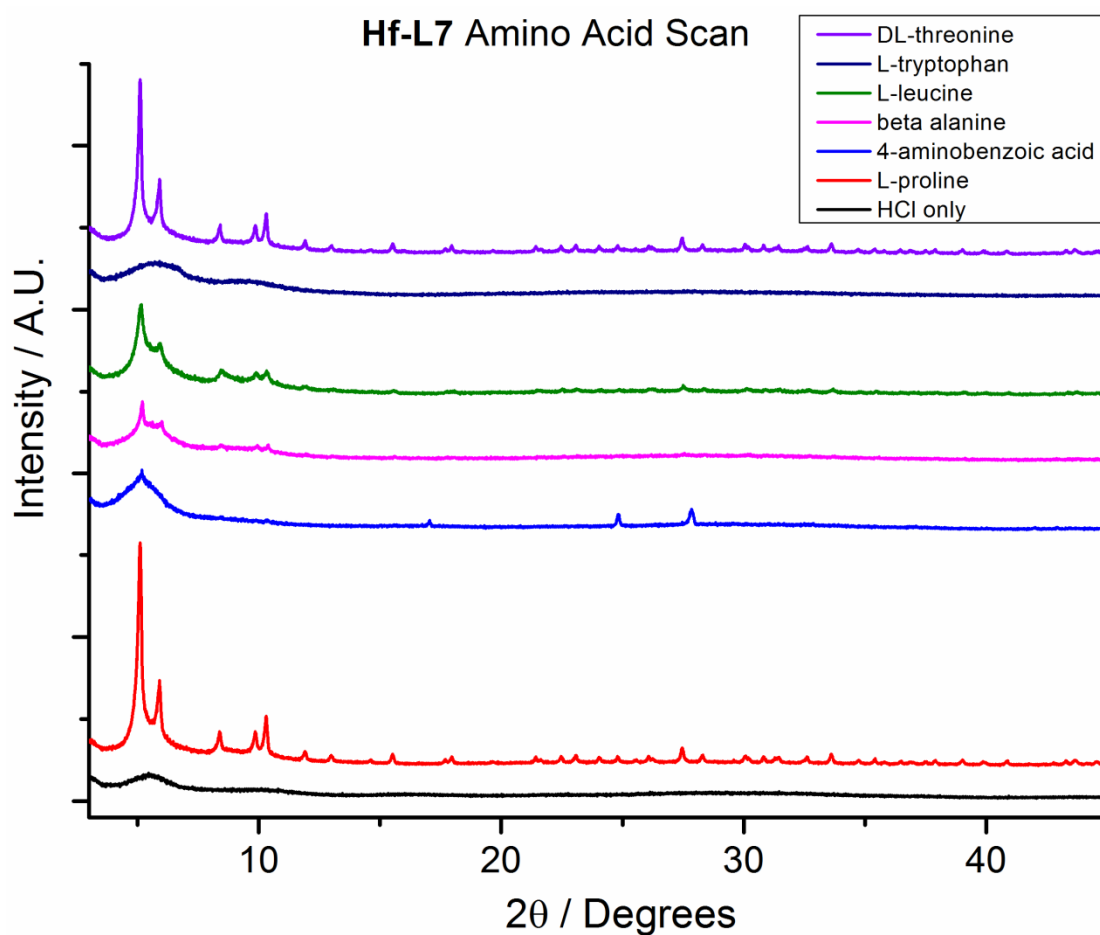
**Table 6.14.** Amino acid modulated synthesis of **Hf-L6**.

L6		HfCl <sub>4</sub>		HCl	Modulator		
Moles (mmol)	Mass (g)	Moles (mmol)	Mass (g)	Volume (ml)	Amino Acid	Moles (mmol)	Mass (g)
0.45	0.1090	0.45	0.1441	0.04	unmodulated		
0.45	0.1090	0.45	0.1441	0.04	L-proline	2.25	0.2590
0.45	0.1090	0.45	0.1441	0.04	PABA	2.25	0.3086
0.45	0.1090	0.45	0.1441	0.04	beta alanine	2.25	0.2005
0.45	0.1090	0.45	0.1441	0.04	L-leucine	2.25	0.2952
0.45	0.1090	0.45	0.1441	0.04	L-tryptophan	2.25	0.4595
0.45	0.1090	0.45	0.1441	0.04	L-arginine	2.25	0.3920
0.45	0.1090	0.45	0.1441	0.04	DL-threonine	2.25	0.2680

**Figure 6.14.** Stacked PXRD patterns for amino acid modulated syntheses of **Hf-L6**.

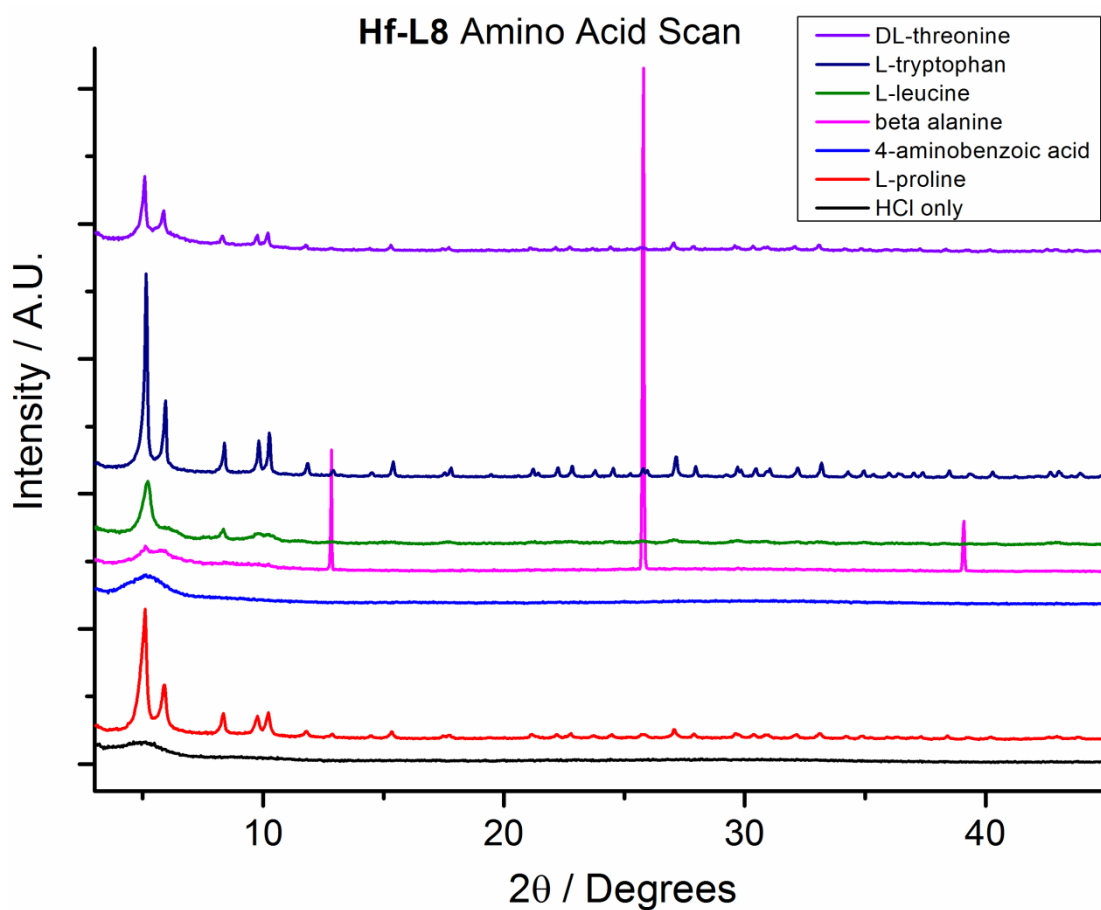
**Table 6.15.** Amino acid modulated synthesis of **Hf-L7**.

<b>L7</b>		<b>HfCl<sub>4</sub></b>		<b>HCl</b>	<b>Modulator</b>		
<b>Moles (mmol)</b>	<b>Mass (g)</b>	<b>Moles (mmol)</b>	<b>Mass (g)</b>	<b>Volume (ml)</b>	<b>Amino Acid</b>	<b>Moles (mmol)</b>	<b>Mass (g)</b>
0.45	0.1216	0.45	0.1441	0.04	unmodulated		
0.45	0.1216	0.45	0.1441	0.04	L-proline	2.25	0.2590
0.45	0.1216	0.45	0.1441	0.04	PABA	2.25	0.3086
0.45	0.1216	0.45	0.1441	0.04	beta alanine	2.25	0.2005
0.45	0.1216	0.45	0.1441	0.04	L-leucine	2.25	0.2952
0.45	0.1216	0.45	0.1441	0.04	L-tryptophan	2.25	0.4595
0.45	0.1216	0.45	0.1441	0.04	L-arginine	2.25	0.3920
0.45	0.1216	0.45	0.1441	0.04	DL-threonine	2.25	0.2680

**Figure 6.15.** Stacked PXRD patterns for amino acid modulated syntheses of **Hf-L7**.

**Table 6.16.** Amino acid modulated synthesis of **Hf-L8**.

L8		HfCl <sub>4</sub>		HCl	Modulator		
Moles (mmol)	Mass (g)	Moles (mmol)	Mass (g)	Volume (ml)	Amino Acid	Moles (mmol)	Mass (g)
0.45	0.1207	0.45	0.1441	0.04	unmodulated		
0.45	0.1207	0.45	0.1441	0.04	L-proline	2.25	0.2590
0.45	0.1207	0.45	0.1441	0.04	PABA	2.25	0.3086
0.45	0.1207	0.45	0.1441	0.04	beta alanine	2.25	0.2005
0.45	0.1207	0.45	0.1441	0.04	L-leucine	2.25	0.2952
0.45	0.1207	0.45	0.1441	0.04	L-tryptophan	2.25	0.4595
0.45	0.1207	0.45	0.1441	0.04	L-arginine	2.25	0.3920
0.45	0.1207	0.45	0.1441	0.04	DL-threonine	2.25	0.2680

**Figure 6.16.** Stacked PXRD patterns for amino acid modulated syntheses of **Hf-L8**.



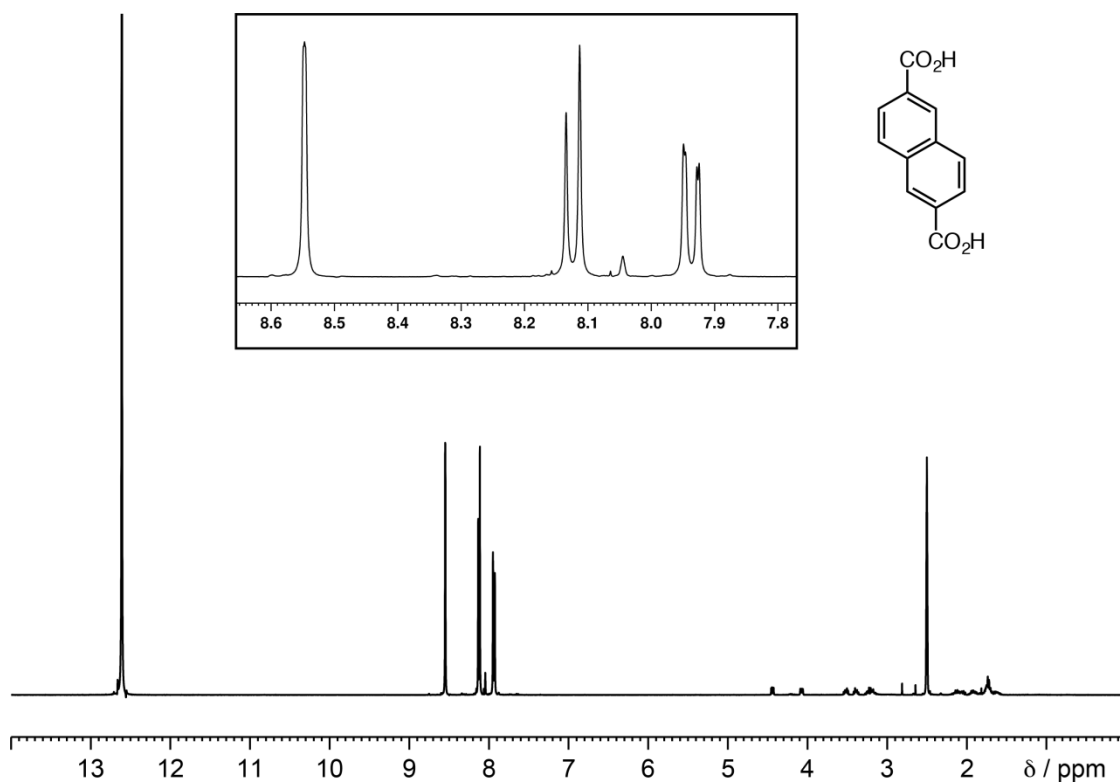


**Figure 6.17.**  $^1\text{H}$  NMR ( $\text{DMSO-}d_6/\text{D}_2\text{SO}_4$ ) of **Zr-L5** prepared by L-proline modulation.

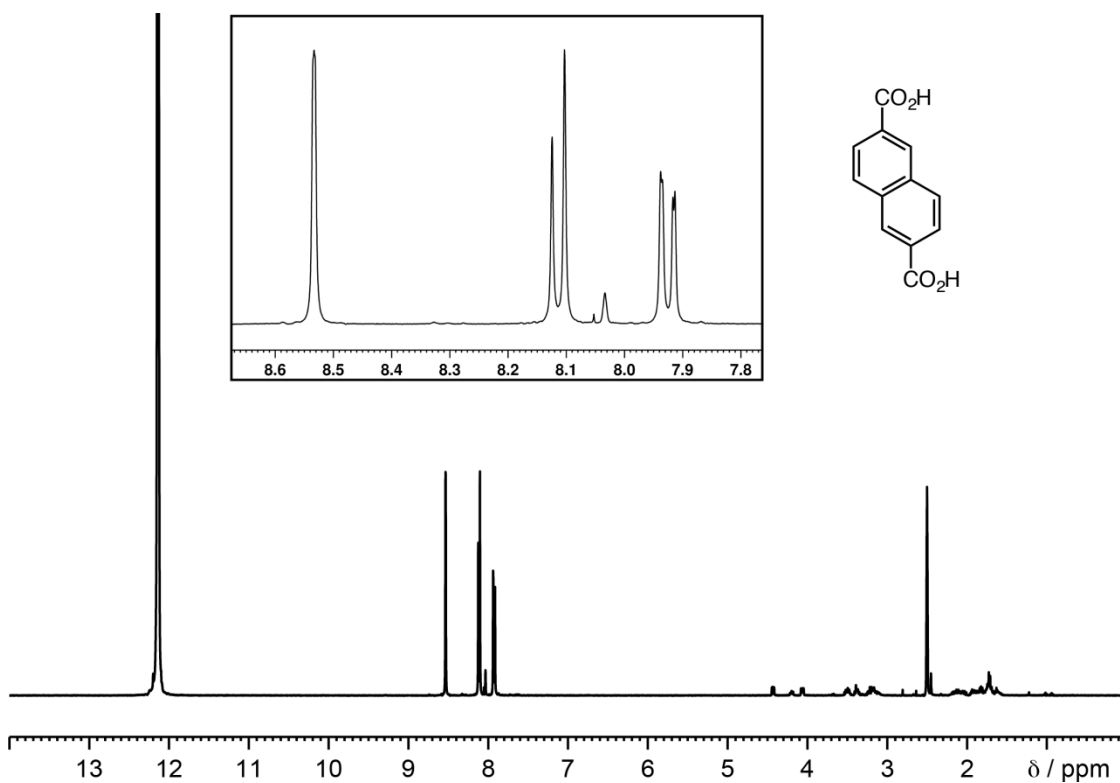


**Figure 6.18.**  $^1\text{H}$  NMR ( $\text{DMSO-}d_6/\text{D}_2\text{SO}_4$ ) of **Hf-L5** prepared by L-proline modulation.

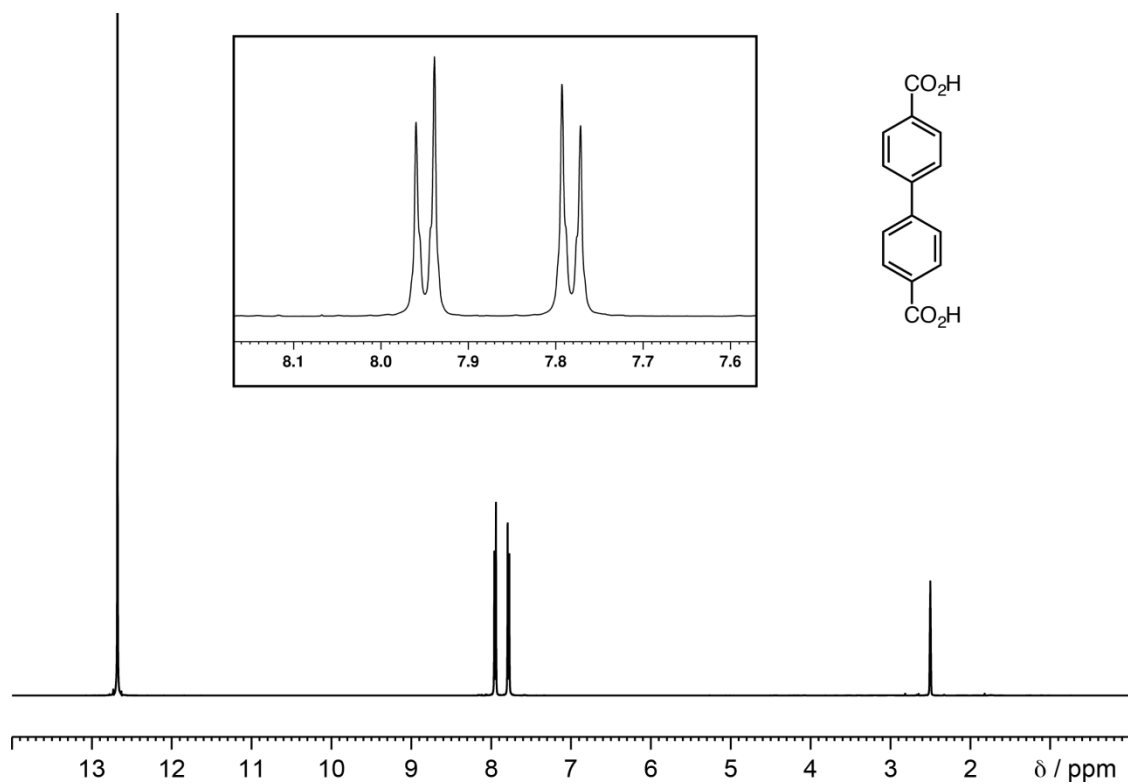


**Figure 6.19.**  $^1\text{H}$  NMR ( $\text{DMSO-}d_6/\text{D}_2\text{SO}_4$ ) of **Zr-L6** prepared by L-proline modulation.

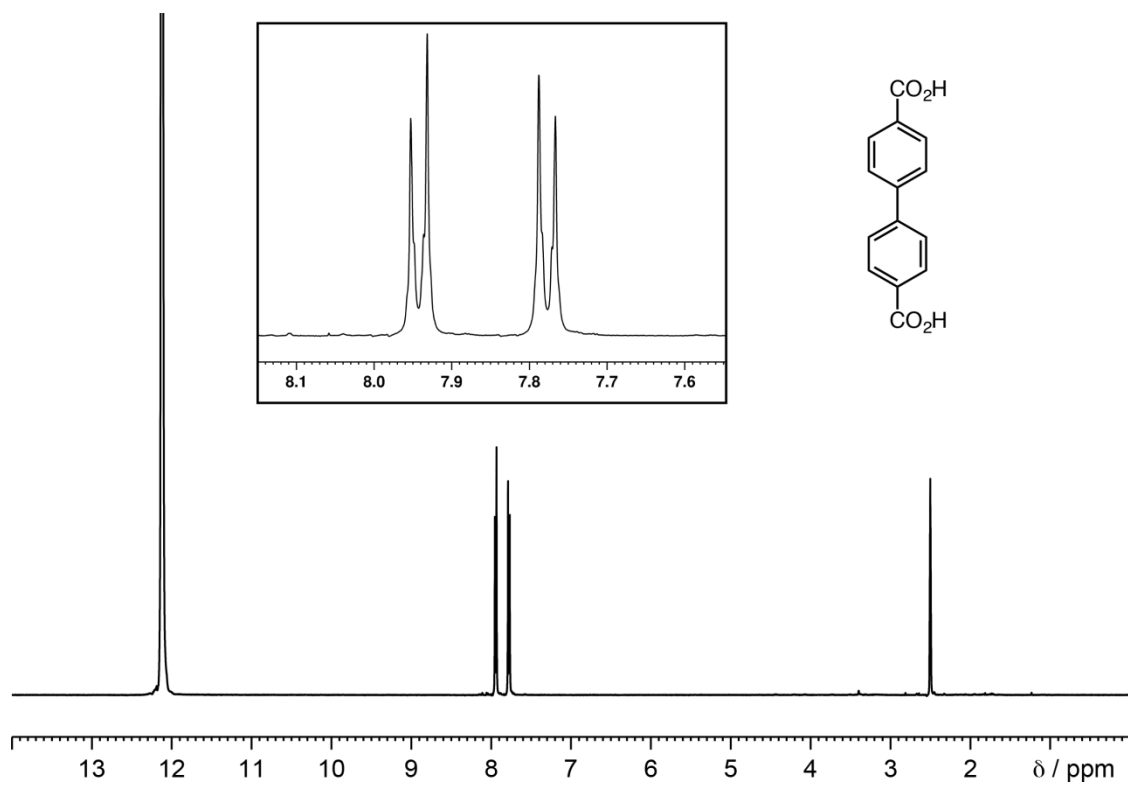


**Figure 6.20.**  $^1\text{H}$  NMR ( $\text{DMSO-}d_6/\text{D}_2\text{SO}_4$ ) of **Hf-L6** prepared by L-proline modulation.

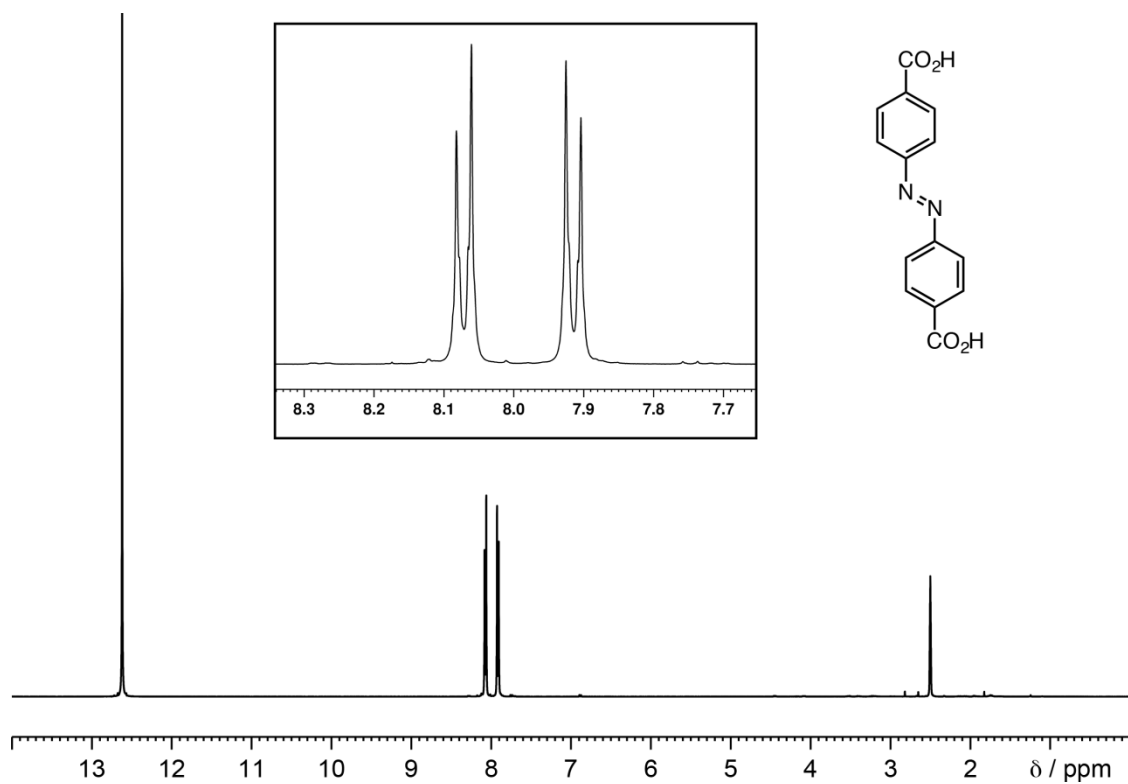


**Figure 6.21.**  $^1\text{H}$  NMR ( $\text{DMSO-}d_6/\text{D}_2\text{SO}_4$ ) of **Zr-L7** prepared by L-proline modulation.

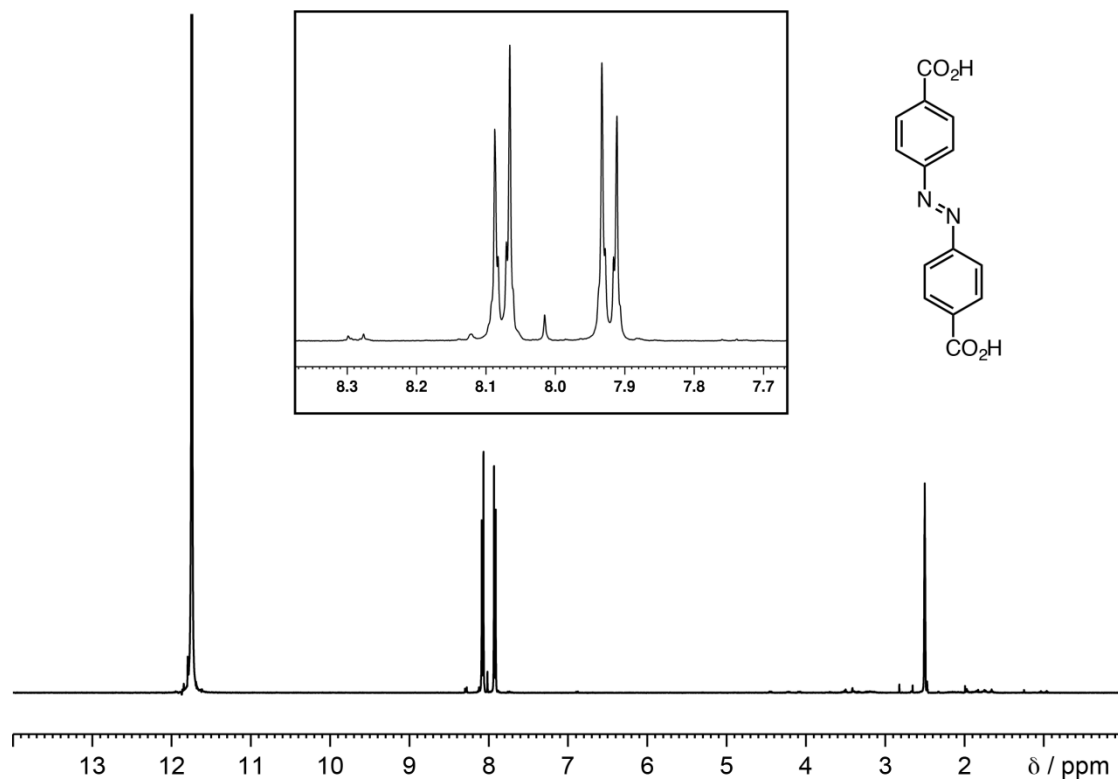


**Figure 6.22.**  $^1\text{H}$  NMR ( $\text{DMSO-}d_6/\text{D}_2\text{SO}_4$ ) of **Hf-L7** prepared by L-proline modulation.

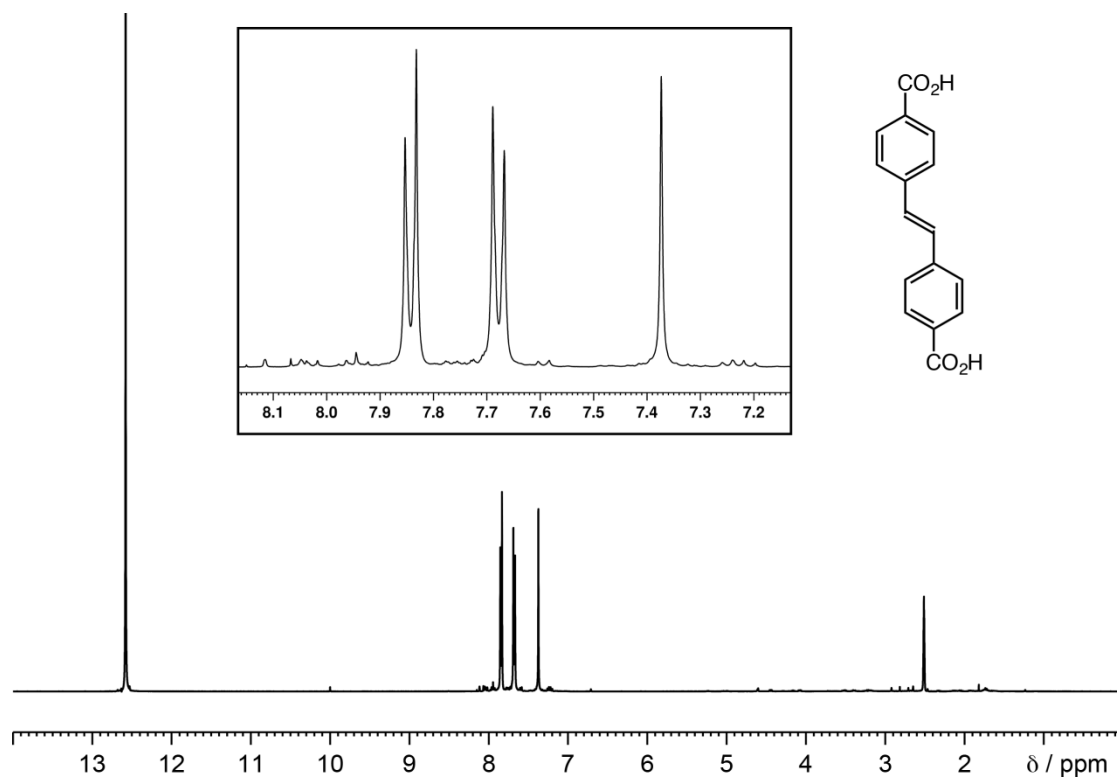


**Figure 6.23.**  $^1\text{H}$  NMR ( $\text{DMSO-}d_6/\text{D}_2\text{SO}_4$ ) of **Zr-L8** prepared by L-proline modulation.

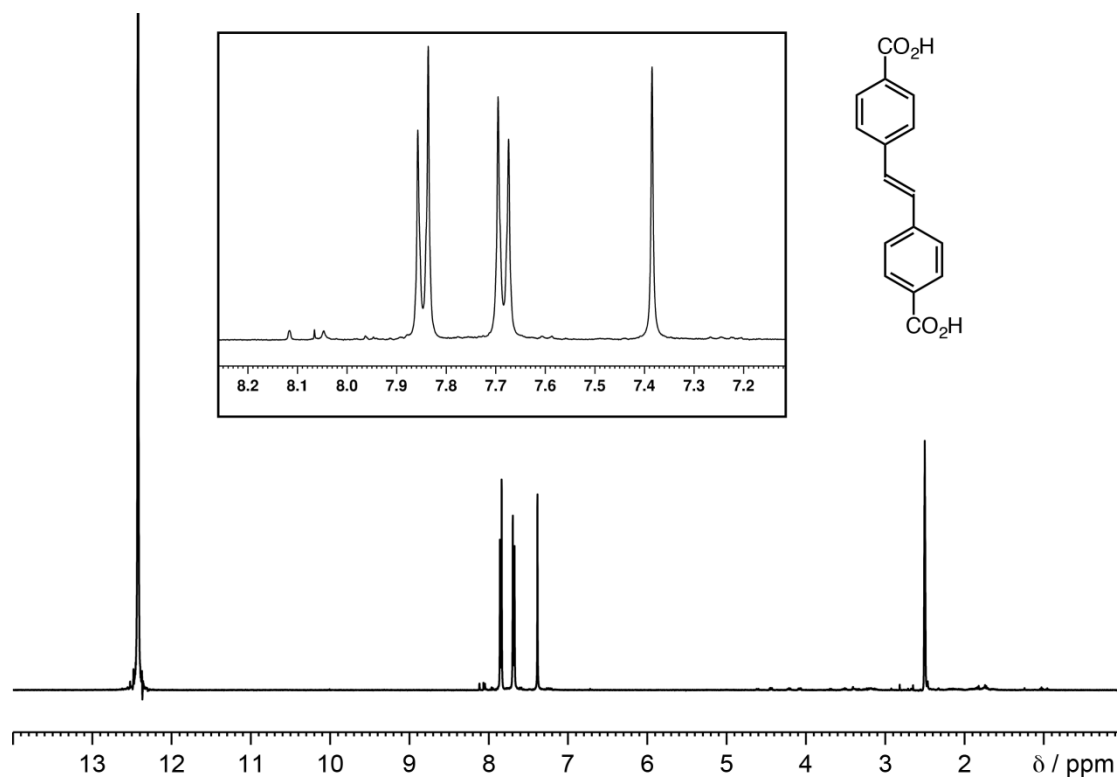


**Figure 6.24.**  $^1\text{H}$  NMR ( $\text{DMSO-}d_6/\text{D}_2\text{SO}_4$ ) of **Hf-L8** prepared by L-proline modulation.

## 6.2 Chapter 3 Supplementary Material

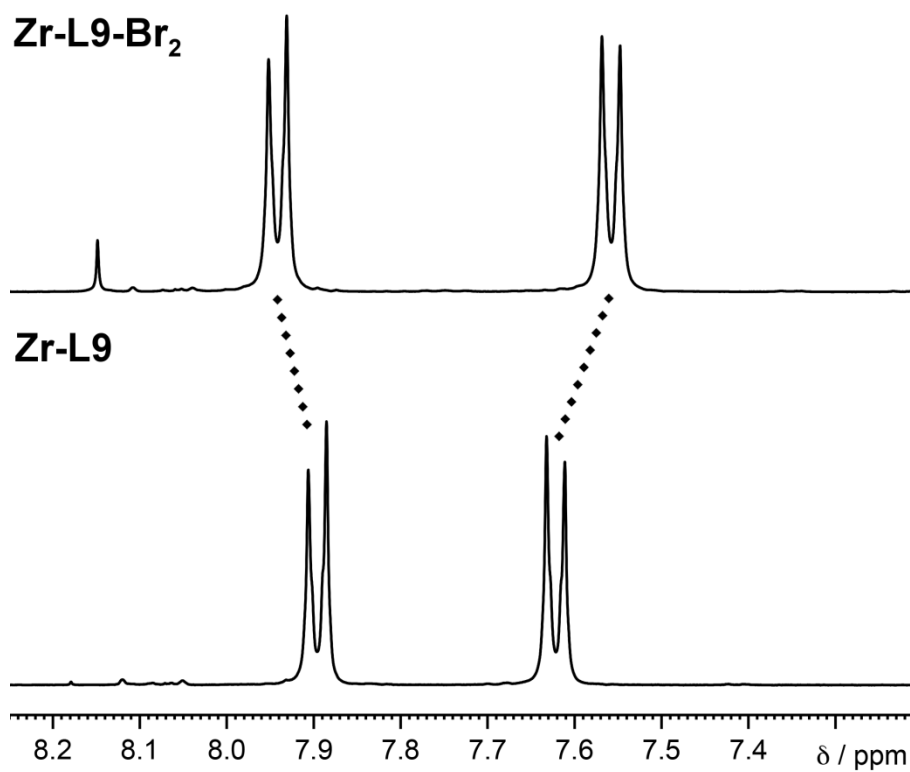


**Figure 6.25.** Partial  $^1\text{H}$  NMR spectra (DMSO- $d_6$ /D $_2$ SO $_4$ ) of **Zr-L9** and **Zr-L9-Br<sub>2</sub>**, showing an increased splitting of the doublets on bromination.

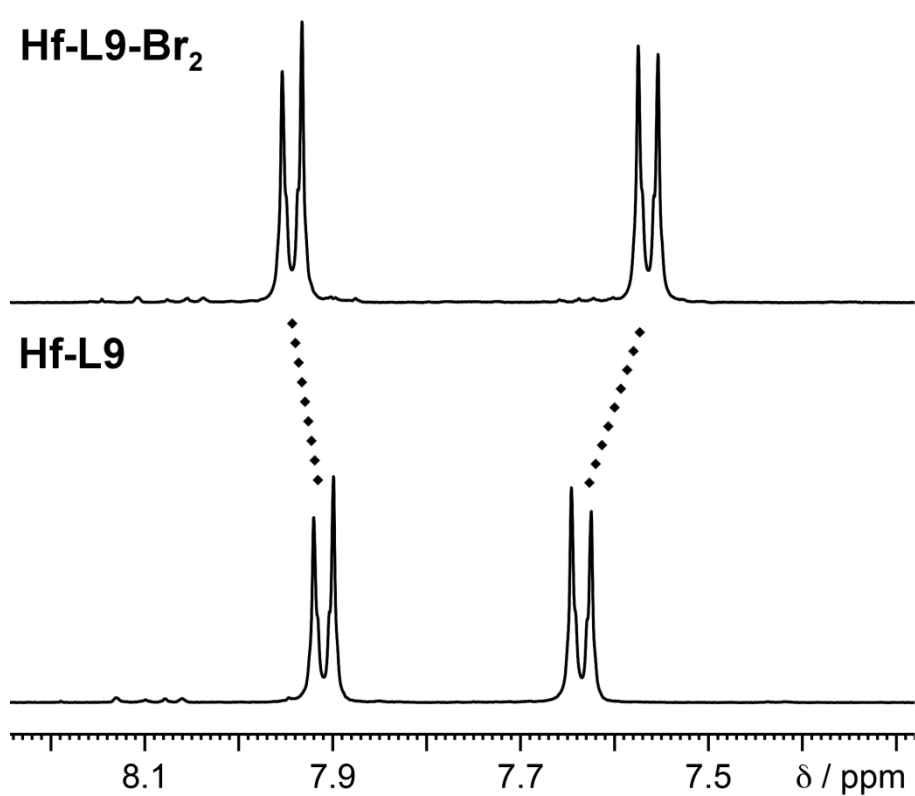


**Figure 6.26.** Partial  $^1\text{H}$  NMR spectra (DMSO- $d_6$ /D $_2$ SO $_4$ ) of **Hf-L9** and **Hf-L9-Br<sub>2</sub>**, showing an increased splitting of the doublets on bromination.

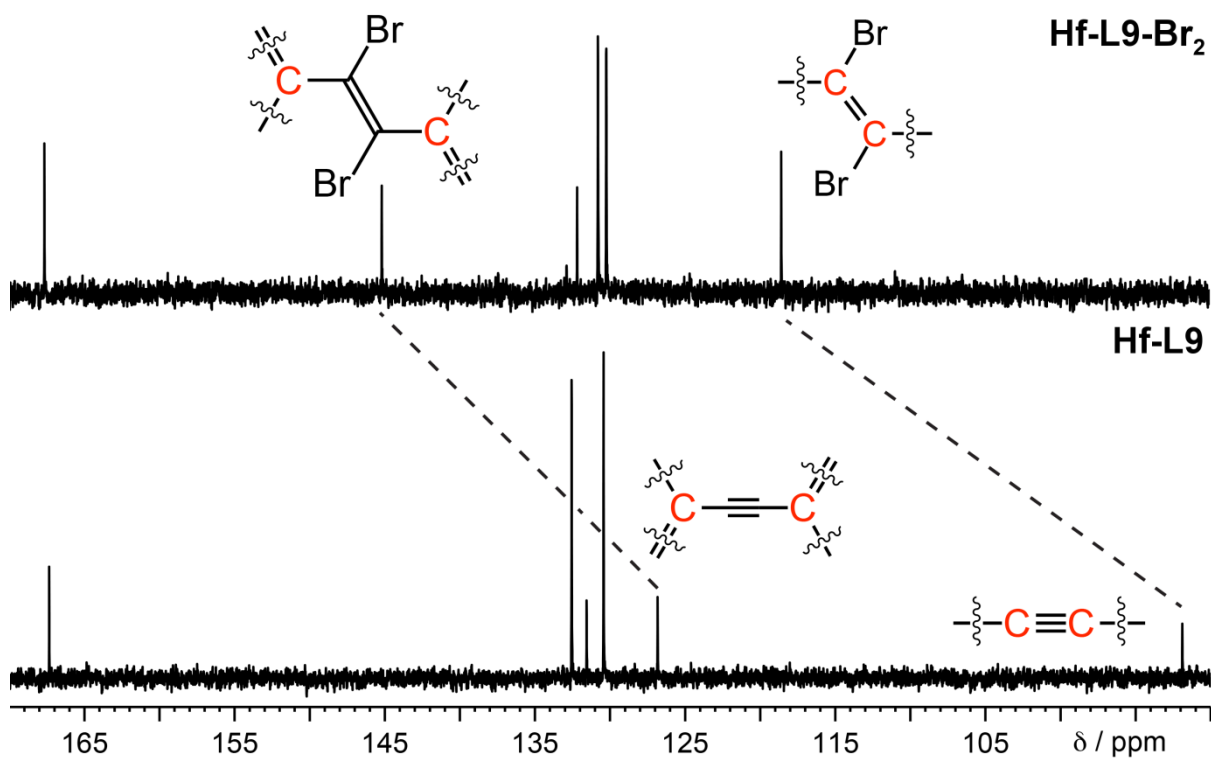


**Figure 6.27.** Stacked partial  $^{13}\text{C}$  NMR ( $\text{DMSO-}d_6/\text{D}_2\text{SO}_4$ ) spectra of **Hf-L9** and **Hf-L9-Br<sub>2</sub>** highlighting the characteristic downfield shift of deterministic carbon atoms upon bromination.

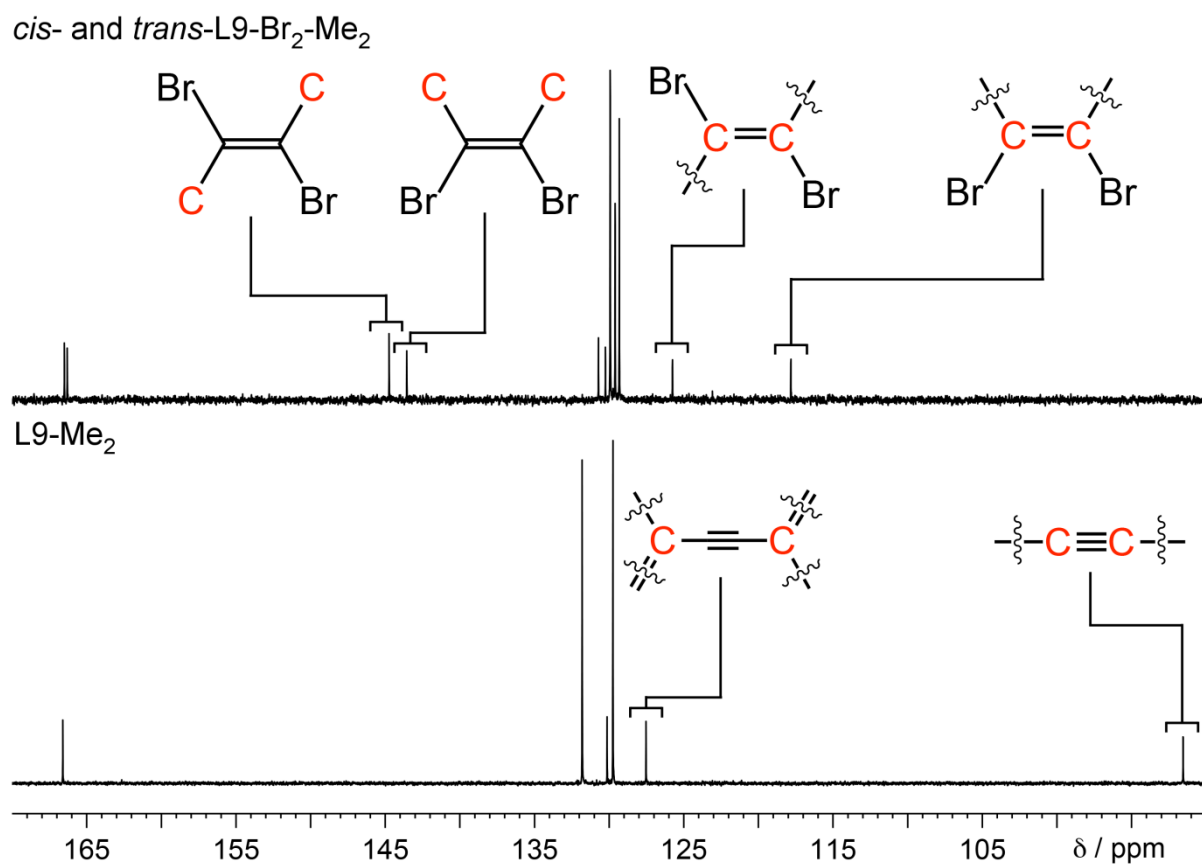


**Figure 6.28.** Stacked partial <sup>13</sup>C NMR (CDCl<sub>3</sub>) spectra of L9-Me<sub>2</sub> and its brominated products, *cis*- and *trans*-L9-Br<sub>2</sub>-Me<sub>2</sub>.



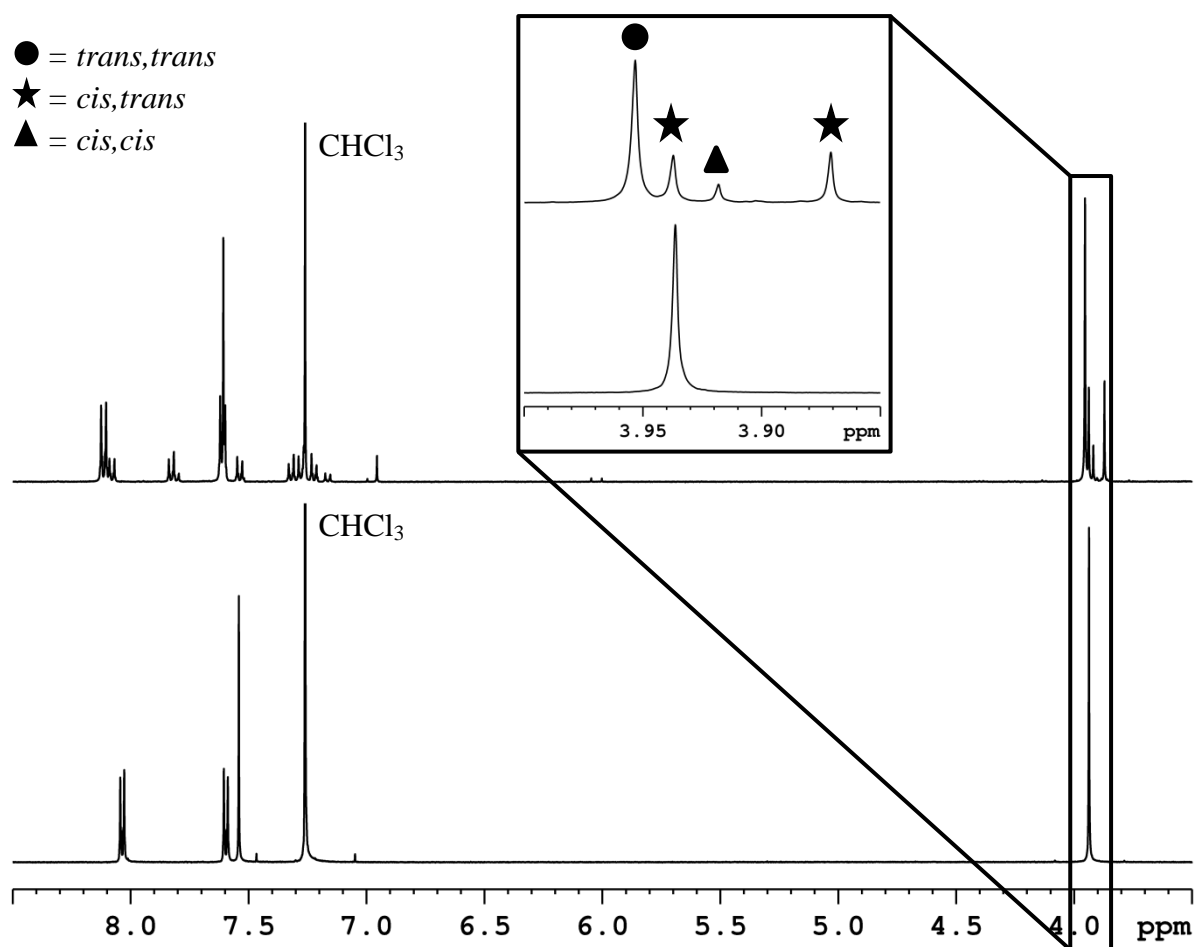


**Figure 6.29.** Stacked partial  $^1\text{H}$  NMR spectra ( $\text{CDCl}_3$ ) of  $\text{L11-Me}_2$  (bottom) and its brominated products (top), the isomers of  $\text{L11-Br}_4\text{-Me}_2$ .

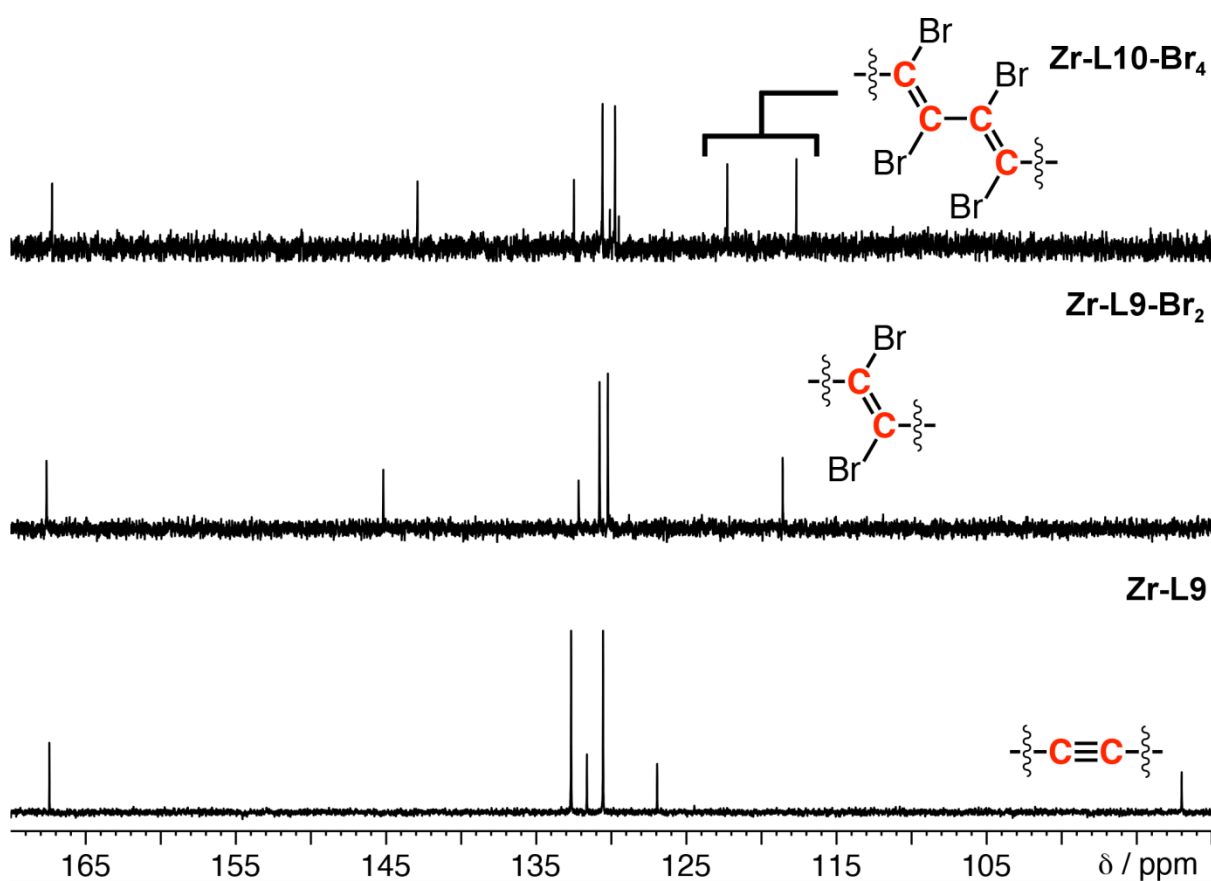


**Figure 6.30.** Stacked partial  $^{13}\text{C}$  NMR spectra of digested samples ( $\text{DMSO}-d_6/\text{D}_2\text{SO}_4$ ) of **Zr-L9**, **Zr-L9-Br<sub>2</sub>** and **Zr-L10-Br<sub>4</sub>**.

### 6.3 Chapter 4 Supplementary Material

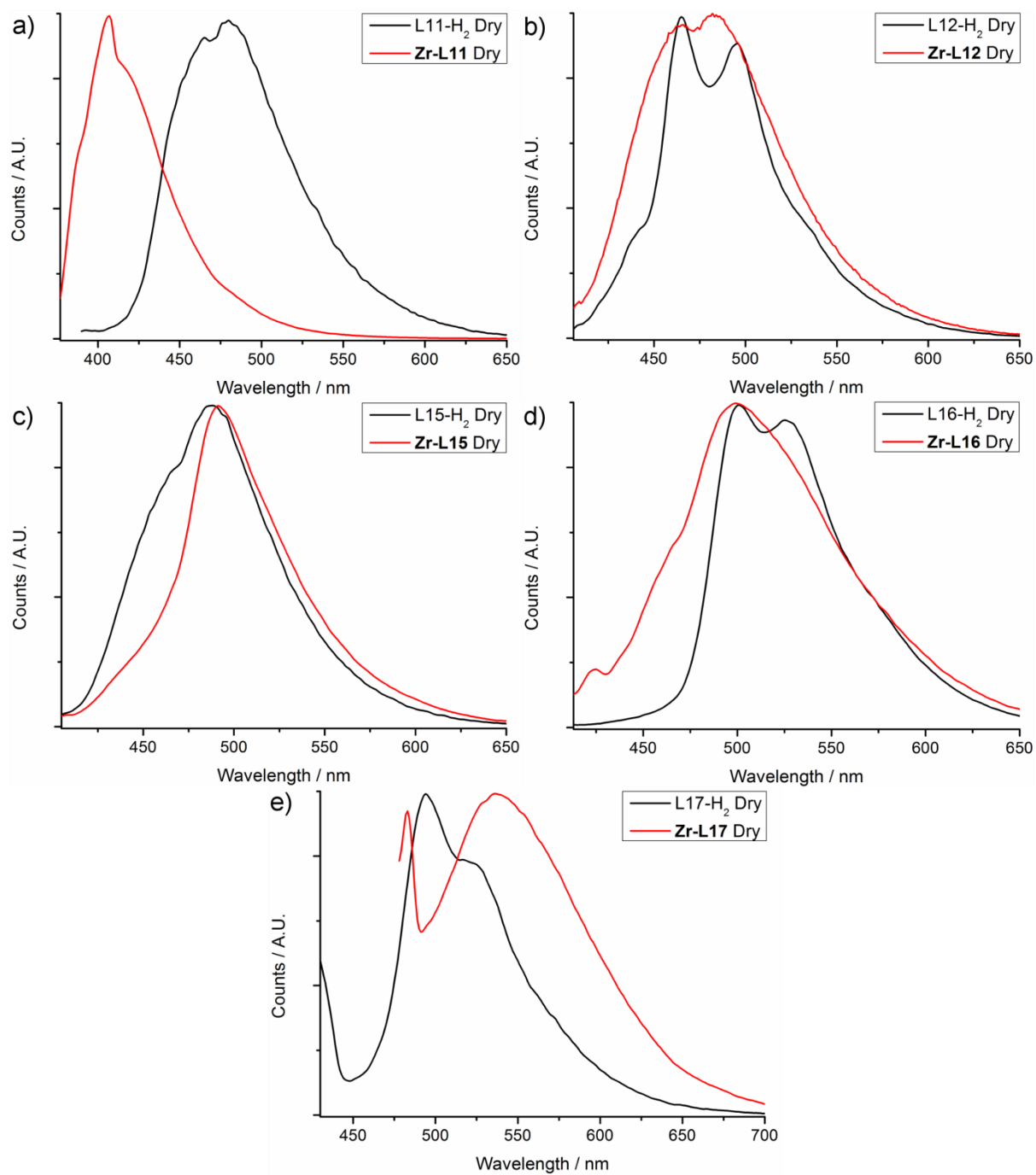


**Figure 6.31.** Comparison of normalised solid-state fluorescence emission spectra of dry samples of ligands and their Zr MOFs for a) L11, b) L12, c) L15, d) L16 and e) L17.

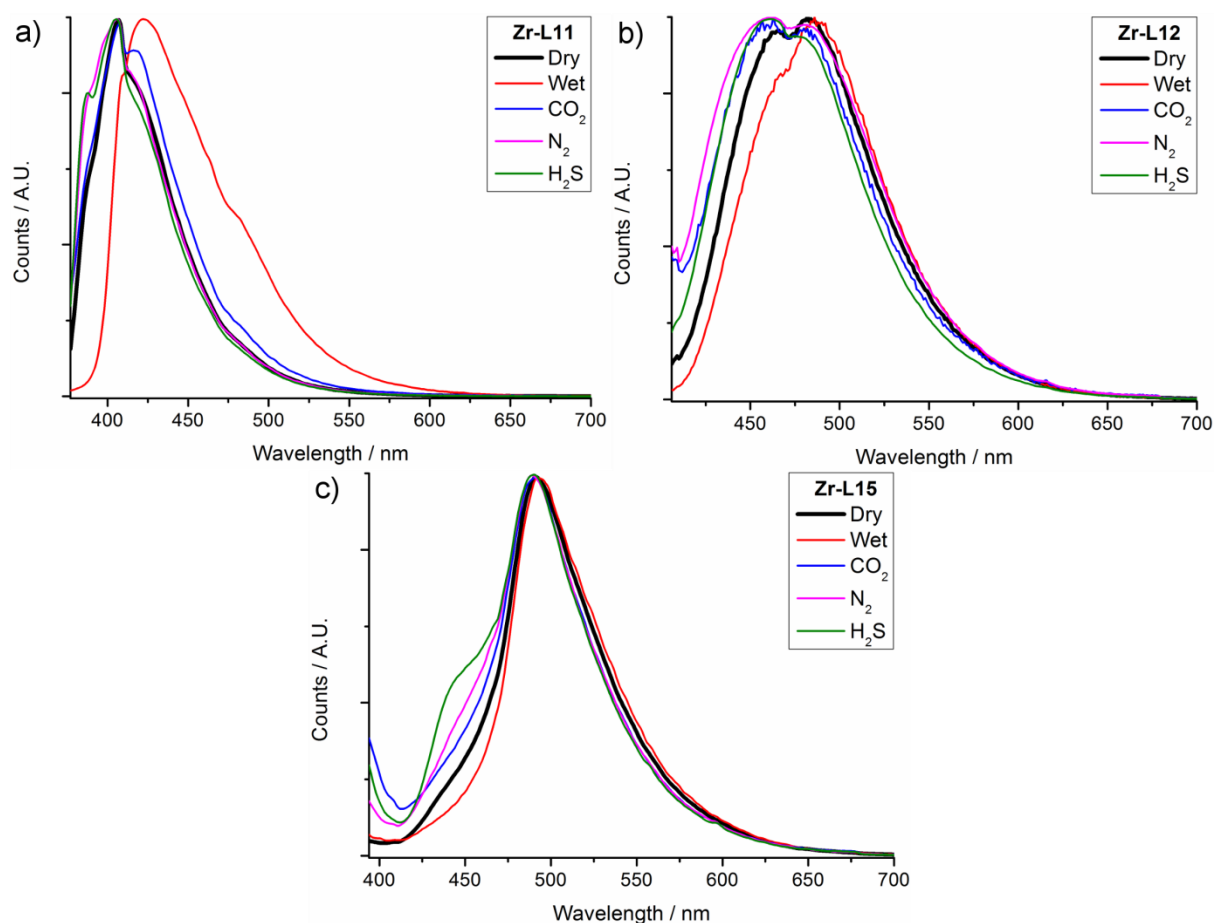


**Figure 6.32.** Comparison of normalised solid-state fluorescence emission spectra of a) **Zr-L11** ( $\lambda_{\text{ex}} = 367$  nm), b) **Zr-L12** ( $\lambda_{\text{ex}} = 396$  nm) and c) **Zr-L15** ( $\lambda_{\text{ex}} = 384$  nm) under a variety of conditions including gas phase reagents.